Journal of Nanomaterials

Advanced Nanoporous Materials for Sustainable Environment

Lead Guest Editor: Fei Ke
Guest Editors: Yunpan Ying and Xiufang Wang

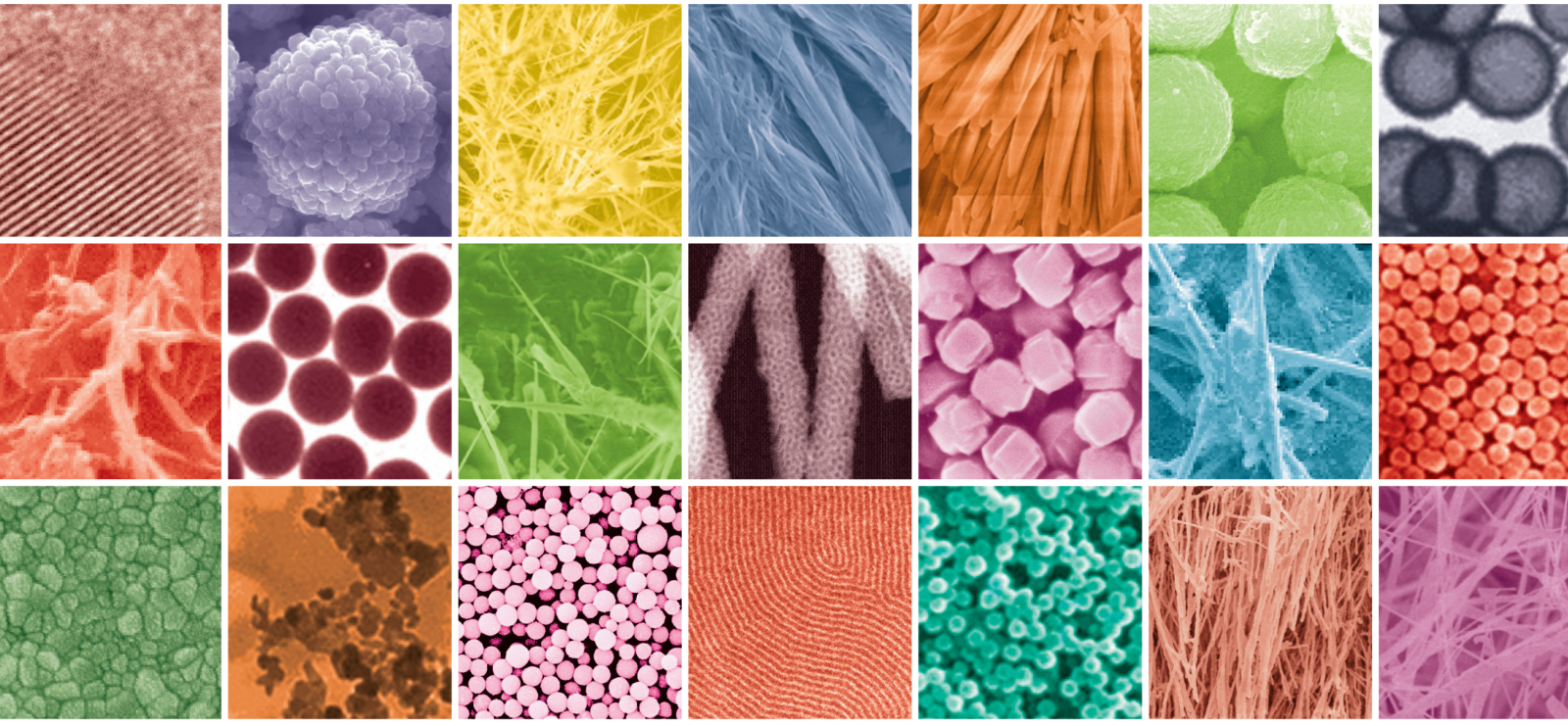

Advanced Nanoporous Materials for Sustainable Environment

Journal of Nanomaterials

Advanced Nanoporous Materials for Sustainable Environment

Lead Guest Editor: Fei Ke
Guest Editors: Yunpan Ying and Xiufang Wang

Contents

Hindawi
Journal of Nanomaterials
Volume 2020, Article ID 7593048, 2 pages
https://doi.org/10.1155/2020/7593048

Erratum

Erratum to "Study on Photocatalytic Antibacterial and Sustained-Release Properties of Cellulose/TiO_2/β-CD Composite Hydrogel"

Hui Zhang, Jiangying Zhu, Yanqiang Hu, Aonan Chen, Liang Zhou, Hui Gao, Yamei Liu, and Shengquan Liu

School of Forestry and Landscape Architecture, Anhui Agricultural University, Hefei 230036, China

Correspondence should be addressed to Shengquan Liu; liusq@ahau.edu.cn

Received 9 January 2020; Accepted 10 January 2020; Published 3 April 2020

In the article titled "Study on Photocatalytic Antibacterial and Sustained-Release Properties of Cellulose/TiO_2/β-CD Composite Hydrogel" [1], there was an error in Figure 3, whereby panel b was a duplicate of panel a. The publisher apologises for this error that occurred during the production of the article, and the corrected figure is shown below as Figure 1:

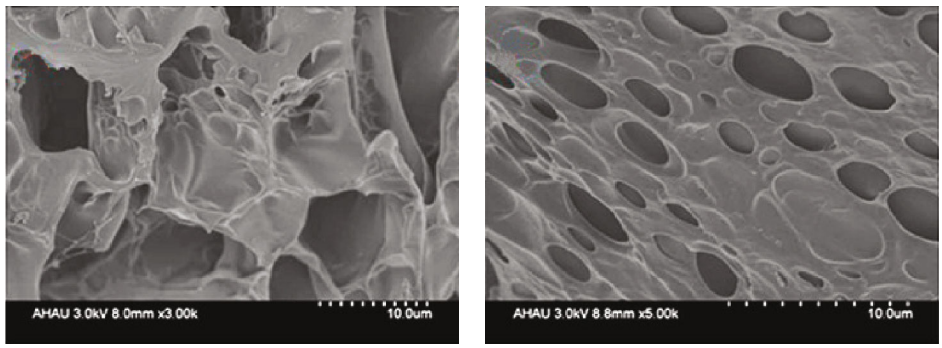

(a) (b)

Figure 1: SEM images of the cellulose/TiO_2 hydrogel (a) and cellulose/TiO_2/β-CD hydrogel (b).

References

[1] H. Zhang, J. Zhu, Y. Hu et al., "Study on photocatalytic antibacterial and sustained-release properties of cellulose/TiO_2/β-CD composite hydrogel," *Journal of Nanomaterials*, vol. 2019, Article ID 2326042, 12 pages, 2019.

Hindawi
Journal of Nanomaterials
Volume 2019, Article ID 6130152, 11 pages
https://doi.org/10.1155/2019/6130152

Research Article

Adsorption of Carbon Dioxide, Methane, and Nitrogen Gases onto ZIF Compounds with Zinc, Cobalt, and Zinc/Cobalt Metal Centers

Ahmed Awadallah-F,[1] Febrian Hillman,[2] Shaheen A. Al-Muhtaseb,[1] and Hae-Kwon Jeong[2,3]

[1]*Department of Chemical Engineering, Qatar University, P.O. Box 2713, Doha, Qatar*
[2]*Artie McFerrin Department of Chemical Engineering, Texas A&M University, College Station, TX 77843-3122, USA*
[3]*Department of Materials Science and Engineering, Texas A&M University, College Station, TX 77843-3122, USA*

Correspondence should be addressed to Shaheen A. Al-Muhtaseb; s.almuhtaseb@qu.edu.qa

Received 14 May 2019; Revised 10 November 2019; Accepted 18 November 2019; Published 23 December 2019

Guest Editor: Fei Ke

ZIF-8, Co-ZIF-8, and Zn/Co-ZIF-8 are utilized in adsorbing nitrogen (N_2), methane (CH_4), and carbon dioxide (CO_2) gases at temperatures between 25 and 55°C and pressures up to ~1 MPa. Equilibrium adsorption isotherms and adsorption kinetics are studied. The dual-site Langmuir equation is employed to correlate the nonisothermal adsorption equilibrium behavior. Generally, N_2 showed the lowest equilibrium adsorption quantity on the three samples, whereas CO_2 showed the highest equilibrium adsorption capacity. Amid the ZIF samples, the biggest adsorption quantities of N_2 and CH_4 were onto Zn/Co-ZIF-8, whereas the highest adsorption quantity of CO_2 was on ZIF-8. The isosteric heats of adsorbing these gases on ZIF-8, Co-ZIF-8, and Zn/Co-ZIF-8 were examined. Moreover, the overall mass transfer coefficients of adsorption at different temperatures were investigated.

1. Introduction

Zeolitic imidazolate frameworks (ZIFs) are convenient substances for gas separation and purification applications. The main reason is their outstanding properties such as excellent chemical and thermal stabilities, surface areas, microporous structures, and synthesis controllability [1, 2]. ZIF-8 possesses a large pore size of 11.6 Å and a small aperture size of 3.4 Å with a zinc metal center linked by an imidazole-type of organic linkers, which looks like a neutral zeolitic sodalite topology [3].

Microwave technology attracted attention in the last decade for the chemical fabrication of nanoporous materials [4, 5]. The microwave-irradiation technique is featured with homogenous and rapid heating with controllable rates [6], which significantly decreases the synthesis time and increases the product yield [7]. To the authors' knowledge, only few works have tackled the subject of the microwave-assisted fabrication of ZIF-8 [8, 9]. The preparation of ZIF-8 products involves several stages of crystal growth, which starts with unstable clusters under super-saturation conditions [10]. Different variables (e.g., heat, diluent vaporization, and molar ratios) influence the product formation in the microwave-assisted preparation process [11].

The climate change phenomenon, which is driven highly by the CO_2 discharge into the atmosphere, draws the concern of the scientific community from different fields. Therefore, the reduction of the anthropogenic CO_2 gas emissions in the atmosphere has become one of the most urgent climate problems to be confronted [12]. Therefore, the improvement of a proficient adsorbent for carbon dioxide gas is a dire need and a necessary step to alleviate this problem [13]. Approximately 30% of CO_2 gas emitted to the atmosphere emerges from fossil-fuel-based power plants and different human life activities [12]. Hence, it is necessary to separate the CO_2 found in flue gases before being exhausted to the atmosphere. Natural gas is known as an alternative and cleaner energy source to replace coal and petroleum. Nonetheless, it involves undesired impurities of CO_2 and N_2, which cause a corrosive impact in pipelines and lower the calorific value of natural gas [14]. Therefore, natural gas requires a pretreatment to remove these impurities before industrial applications [15].

Overall, worldwide research has exerted extreme efforts to develop concise and decisive methods for removing post combustion CO_2 from gas mixtures [16–18]. Methods involving absorption, cryogenic distillation, and physical adsorption are developed to split up carbon dioxide, methane, and nitrogen gas mixtures [19–22].

The aim of this paper is to utilize ZIF compounds, in its virgin shape and after fractional and complete replacement of zinc by cobalt (to form Co-ZIF-8 and Zn/Co-ZIF-8), in order to adsorb CH_4, N_2, and CO_2 gases at four temperatures (ranging from 25 to 55°C) and pressures up to ~1 MPa. The influence of conformational metal content (zinc, cobalt, or zinc/cobalt) of ZIFs on their adsorption behaviors will be studied. The dual-site Langmuir equation will be applied to correlate the adsorption equilibrium data at various temperatures collectively, and the corresponding adsorption isosteric heats of CH_4, N_2, and CO_2 will be estimated. Moreover, the overall mass transfer coefficients for the adsorption of these gases on ZIFs will be examined at various temperatures.

2. Materials and Methods

2.1. Materials. Zinc nitrate hexahydrate (98%, Sigma Aldrich), cobalt nitrate hexahydrate (≥99.99%), and 2-methylimidazole (97%) were purchased from Sigma-Aldrich. Methanol (99.8%) was supplied from Alfa Aesar. Gases (CH_4, N_2, and CO_2) were of high purity (99.999%) and were supplied from the National Industrial Gas Plants (NIGP, Doha, Qatar). All chemical reagents were utilized without further purification.

2.2. ZIF Compound Preparation. Various ZIF compounds (Zn-ZIF (i.e., ZIF-8), Co-ZIF-8, and Zn/Co-ZIF-8) were synthesized by a microwave-assisted method as detailed elsewhere [23].

2.3. Characterization. The characterization results of these ZIFs are found in a previous work [23]. Adsorption equilibrium isotherms of CH_4, N_2, and CO_2 gases were measured via a Hygra magnetic suspension microbalance (MSB, Rubotherm), with microgram sensitivity, following the same procedures described elsewhere [24].

2.4. Theory

2.4.1. Adsorption. The multisite Langmuir model supposes that a heterogeneous surface of an adsorbent is composed of patches with distinctive adsorption energies. Each patch is thus considered as a homogeneous portion of the adsorbent surface, and the total quantity adsorbed of a gas component can be correlated as

$$n_{\text{ads}} = \sum_{j=1}^{J} \frac{m_j b_j P}{1 + b_j P}, \tag{1}$$

where J is the number of homogeneous adsorption patches and it depends on the extent of surface heterogeneity (usually, J is set to 2, corresponding to the dual-site Langmuir (DSL) model), j refers to adsorption patch number, P indicates pressure, m_j refers to the quantity of monolayer saturation on patch j, and b_j indicates the tendency (affinity) for adsorbing the molecules on patch j as estimated by

$$b_j = b_j^0 \exp\left(\frac{\varepsilon_j}{RT}\right), \tag{2}$$

where b_j^0 refers to the adsorption affinity on patch j at infinite temperature, ε_j refers to the characteristic adsorption energy on patch j, R refers to the universal gas constant, and T refers to absolute temperature.

2.4.2. Isosteric Heat of Adsorption. The isosteric heat of adsorption (Q_{st}) can be estimated by the Clausius-Clapeyron approximation [25] as

$$Q_{\text{st}} = -R \left[\frac{\partial lnP}{\partial(1/T)}\right]_n. \tag{3}$$

The dependence of Q_{st} on surface coverage is an implicit indicator of energetic characteristics between the adsorbed molecules and the adsorbent [26].

2.4.3. Adsorption Kinetics. The adsorption rate is determined by the linear driving force (LDF) approximation as [27]

$$\left(\frac{n_t}{n_e}\right) = \left(1 - e^{-kt}\right), \tag{4}$$

where n_t (mole/kg) refers to the adsorbed quantity at time t (sec), n_e (mole/kg) refers to the adsorbed equilibrium quantity at the corresponding temperature and pressure, and k denotes the overall mass transfer coefficient (sec^{-1}). The k-value can be estimated from experimental dynamic adsorption results at a specific temperature and pressure by plotting the $-\ln(1 - n_t/n_e)$ against t until reaching the equilibrium state.

2.4.4. Regression Analysis. Regression was used to obtain the optimum fitting parameters. The least sum of squared errors (LSSE) is widely utilized for regression as [28]

$$\text{LSSE} = \text{Minimum}\left[\sum_{i=1}^{N} \left(n_{i,\text{Calc}} - n_{i,\text{meas}}\right)^2\right], \tag{5}$$

where i indicates measured data point numbers, N denotes the total number of measured data points, and $n_{i,\text{Calc}}$ and $n_{i,\text{meas}}$ refer, respectively, to the calculated and measured quantities adsorbed.

The averaged relative error (ARE, %) was utilized in order to estimate the accuracy of fitting to describe measured data as [29]

$$\text{ARE}\,(\%) = \frac{100\%}{N} \sum_{i=1}^{N} \frac{\left|n_{i,\text{Calc}} - n_{i,\text{meas}}\right|}{n_{i,\text{meas}}}. \tag{6}$$

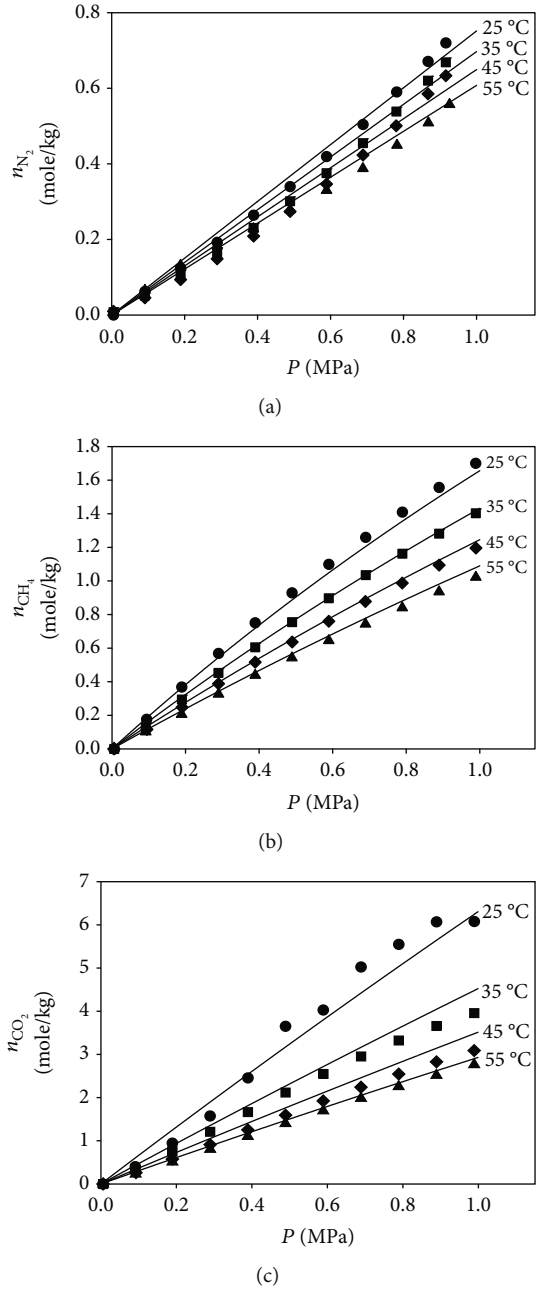

Figure 1: The adsorption equilibria of (a) nitrogen, (b) methane, and (c) carbon dioxide gases on ZIF-8 at different temperatures. The symbols indicate measured results and the lines indicate DSL fitting.

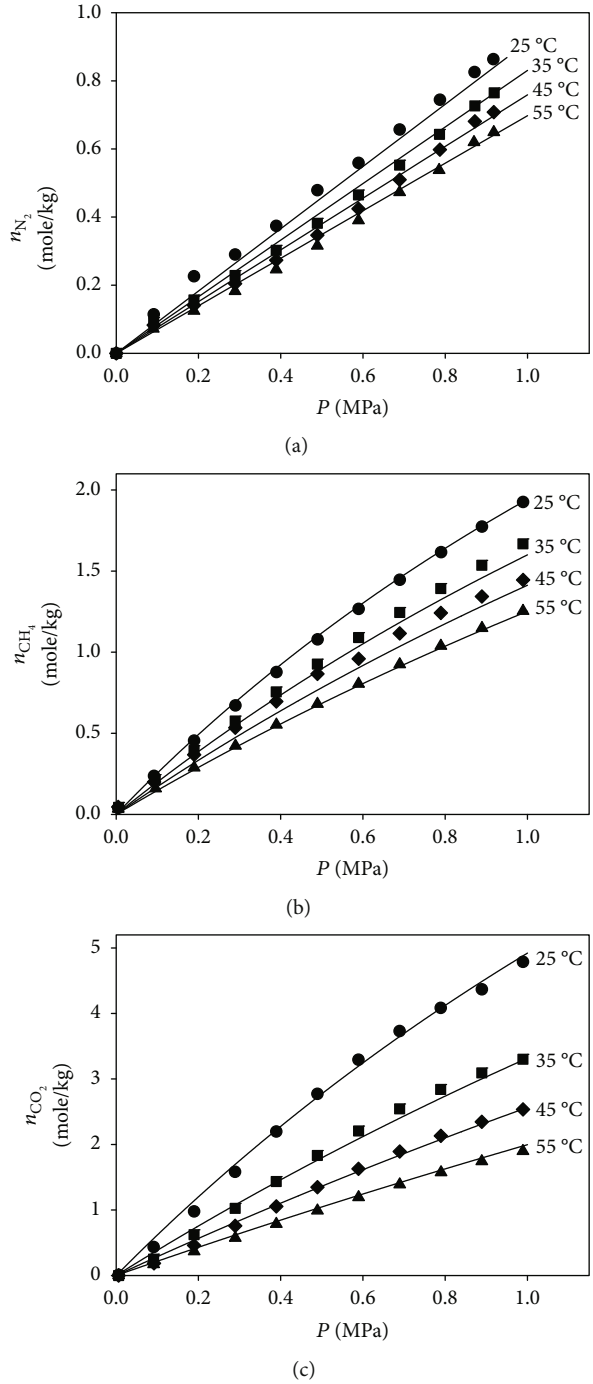

Figure 2: The adsorption equilibria of (a) nitrogen, (b) methane, and (c) carbon dioxide on gases Co-ZIF-8 at different temperatures. The symbols indicate measured results and the lines indicate DSL fitting.

3. Results and Discussion

3.1. Adsorption Equilibrium Isotherms. The adsorption of nitrogen, methane, and carbon dioxide gases onto ZIF-8, Co-ZIF-8, and Zn/Co-ZIF-8 at different temperatures is presented in Figures 1–3, respectively. Broadly, it is seen that the adsorption quantity decreases at higher temperatures. Overall, N_2 gas exposes the lowest adsorbed quantity, whereas CO_2 shows the highest adsorbed quantity. The DSL equation is applied to fit the experimentation results of nitrogen, methane, and carbon dioxide as a function of both temperature and pressure. The fitting parameters registered in Table 1 exposed a good relation with measured results as seen in the solid lines in Figures 1(a)–1(c) to Figures 3(a)–3(c) and by values of ARE (%) in Table 1. Figures 1(a)–1(c) exhibit the adsorption results of nitrogen, methane, and carbon dioxide, respectively, on ZIF-8. It is observed that adsorption

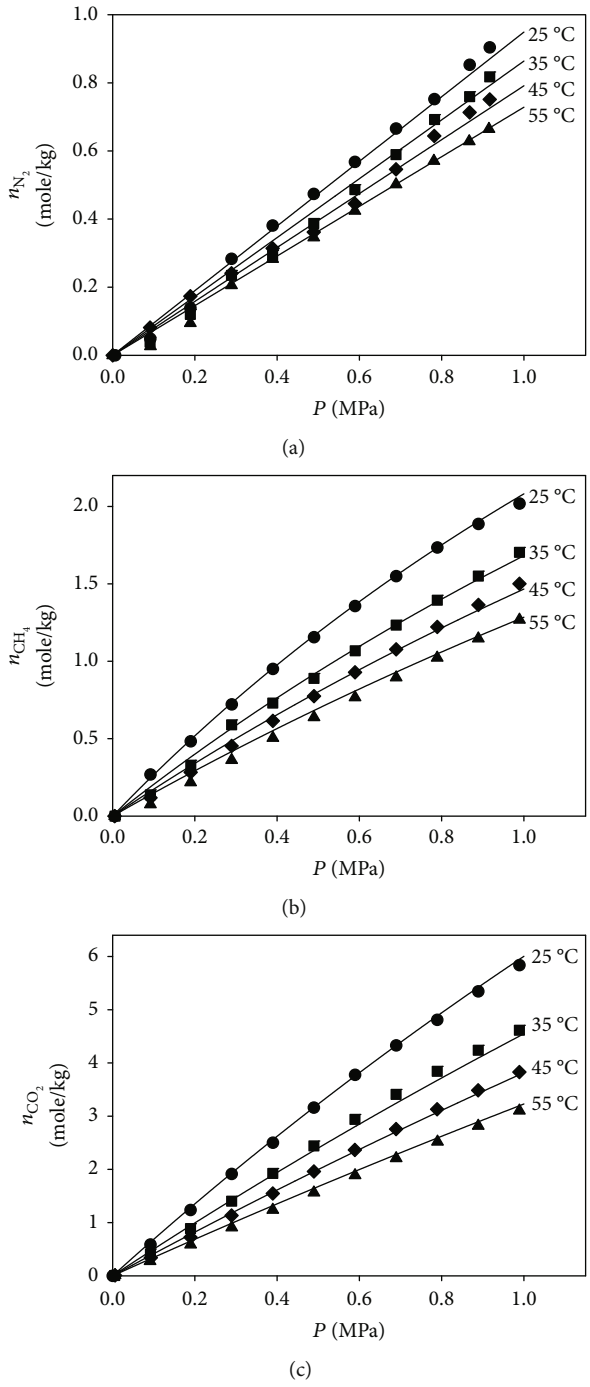

Figure 3: The adsorption equilibria of (a) nitrogen, (b) methane, and (c) carbon dioxide gases on Zn/Co-ZIF-8 at different temperatures. The symbols indicate measured results and the lines indicate DSL fitting.

equilibria of these gases were fitted perfectly, with a minor deviation, by DSL formula for the whole range of pressures and temperatures. Further, the adsorption equilibria of various gases on the ZIF-8 sample exhibited a Henry's law trend that did not seem to reach the saturation limit within the examined pressure scale. Figures 2(a)–2(c) display adsorption equilibrium isotherms of nitrogen, methane, and carbon dioxide, respectively, on Co-ZIF-8. It is observed that the DSL model has deviated slightly from experimental points of nitrogen, methane, and carbon dioxide adsorption isotherms. Figures 3(a)–3(c) show, respectively, the adsorption equilibrium of nitrogen, methane, and carbon dioxide adsorptions on Zn/Co-ZIF-8. Excellent fit of the DSL model to experimental data points is observed in the entire range of temperatures. Furthermore, Table 1 shows that for variety of the studied adsorption systems, one adsorption site was sufficient to describe the corresponding isotherm data (as exhibited by the sufficiency of $J = 1$), which reduces to the regular Langmuir adsorption isotherm and refers to an energetically homogeneous adsorbent surface towards the corresponding gas. It is noted that the results of ZIF-8 reported in Awadallah-F et al. [30] are used here for the purpose of comparison.

Figures 4(a)–4(c) illustrates the influence of various adsorbents (i.e., ZIF-8, Co-ZIF-8, and Zn/Co-ZIF-8) on the adsorption equilibria of nitrogen, methane, and carbon dioxide, respectively, at 25°C (25°C was selected as an illustration for the purpose of briefness). It is observed that the quantity adsorbed on Zn/Co-ZIF-8 is the largest in the case of N_2 and CH_4 gases, whereas ZIF-8 exhibits the biggest adsorption capacity of CO_2 gas (and the lowest adsorption capacity in the case of N_2 and CH_4 gases). Therefore, it can be said that insertion of cobalt ions into ZIF-8 leads to a noticeable change in adsorption equilibrium quantities of CH_4, N_2, and CO_2 gases.

3.2. Rate of Adsorption. Figures 5–7 illustrate the correlation between the overall mass transfer coefficient (k, sec^{-1}) of adsorbing nitrogen, methane, and carbon dioxide on ZIF-8, Co-ZIF-8, and Zn/Co-ZIF-8, correspondingly, against the reciprocal pressure ($1/P$) at different temperatures. Symbols and lines denote, correspondingly, measured data and linear regression. The regression constants were recorded in Table S1 (see Supplementary File Data). As an overview, it was noticed that k-values rise via rising temperature and via diminishing pressure (or rising reciprocal pressure). Furthermore, the k-values approach zero at extreme pressures (i.e., as $1/P \rightarrow 0$), and the influence of temperature in this case is nil. Otherwise, at mild pressures, the k-values were in the rough order of 10^{-3} s^{-1}.

Figures 5(a)–5(c) display the k-values for adsorbing nitrogen, methane, and carbon dioxide, respectively, on ZIF-8. It is noted that the adsorption of carbon dioxide on ZIF-8 is slowest, whereas the adsorption of methane is the fastest. The sequence of gas adsorption rates on ZIF-8 is $CH_4 > N_2 > CO_2$. Figures 6(a)–6(c) elucidate the k results of adsorption on Co-ZIF-8 against $1/P$. It is noted that the adsorption of nitrogen on Co-ZIF-8 is quicker than that of both carbon dioxide and methane. Moreover, the adsorption of CH_4 is faster than the adsorption of CO_2. The sequence of gas adsorption rates on Co-ZIF-8 is $N_2 > CH_4 > CO_2$. Figures 7(a)–7(c) expose that the adsorption of CH_4 on Zn/Co-ZIF-8 is the most rapid amid the gases used, whereas carbon dioxide gas was the slowest. The sequence of gas adsorption rates on Zn/Co-ZIF-8 is $CH_4 > N_2 > CO_2$.

Table 1: The fitting constants of the DSL equation for CH_4, N_2, and CO_2 on ZIF-8, Co-ZIF-8, and Zn/Co-ZIF-8.

Constants	Specimens								
	ZIF-8			Co-ZIF-8			Zn/Co-ZIF-8		
	Gas								
	Nitrogen	Methane	Carbon dioxide	Nitrogen	Methane	Carbon dioxide	Nitrogen	Methane	Carbon dioxide
m_1 (mole/kg)	38359	9.58	97.28	12139	7.37	21.83	13139	8.45	42.85
b_0 (MPa^{-1})	1.84×10^{-6}	9.98×10^{-4}	2.14×10^{-9}	3.91×10^{-6}	1.90×10^{-3}	1.38×10^{-5}	40.10×10^{-6}	1.17×10^{-3}	2.45×10^{-4}
ε/R (K)	693.55	1582	5038	881.97	1535.11	2917.13	861.97	1649.61	1904.60
m_2 (mole/kg)	0	0	27.89	0	0	0	0	0	0
b_0 (MPa^{-1})	0	0	7.61×10^{-2}	0	0	0	0	0	0
ε/R (K)	0	0	0	0	0	0	0	0	0
SSE	0.020	0.0082	1.07	2.04	0.13	0.22	1.52	0.11	0.22
ARE (%)	8.82	3.54	7.46	34.61	12.15	27.98	45.30	9.32	18.26

Figure 8 shows the influence of the ZIF sample type (i.e., ZIF-8, Co-ZIF-8, and Zn/Co-ZIF-8) on the k results of nitrogen, methane, and carbon dioxide gases at the temperatures of 25 and 55°C (note that these temperatures were selected as examples for the purpose of briefness). It was observed from Figures 8(a) and 8(b) that, at both temperatures, adsorbing N_2 is fastest onto the Co-ZIF-8 sample, followed by Zn/Co-ZIF-8 and then ZIF-8. Figures 8(c) and 8(d) indicate that the adsorption rate of the CH_4 gas at both temperatures followed the trend of ZIF-8 > Co-ZIF-8 > Zn/Co-ZIF-8. Additionally, it is noted from Figures 8(e) and 8(f) that the rate of CO_2 adsorption follows the order of Zn/Co-ZIF-8 > ZIF-8 > ZIF-8. It is noted that the results of ZIF-8 reported in Awadallah-F et al. [30] were used here for the purpose of comparison.

3.3. Isosteric Heat of Adsorption. Isosteric heats of adsorption (Q_{st}) were determined from the numerical differentiation of the experimental adsorption data at various temperatures in accordance to Clausius-Clapeyron's equation (Equation (3)). Figures 9(a)–9(c) expose the isosteric heats (Q_{st}) of nitrogen, methane, and carbon dioxide adsorbed on ZIF-8, Co-ZIF-8, and Zn/Co-ZIF-8, respectively. In general, it was observed that the Q_{st} of different components rises to various levels when the loading of each gas on the ZIF surface rises. This is a sign of auspicious interactions amid the molecules adsorbed to the ZIF surface [26]. The consequent trend of adsorption isosteric heats of different components (at similar gas loadings) is methane > carbon dioxide > nitrogen, which reflects their affinity for adsorption.

Nevertheless, it is noticed from Figure 9(a) that the Q_{st} of nitrogen on ZIF-8 augments from ~9 kJ/mole at a loading of 0.048 mole/kg up to ~11 kJ/mole at 0.3 mole/kg. Then, it settles at about this amount, which reveals either adsorption on a nearly nonheterogeneous surface of ZIF [26] or an equivalence between positive and negative interactions. The Q_{st} of carbon dioxide augments from ~14 kJ/mole at 0.36 mole/kg to ~33 kJ/mole at 2.81 mole/kg. Further, the Q_{st} of methane rose from ~16 kJ/mole at a loading of 0.10 mole/kg up to ~31 kJ/mole at 1.2 mole/kg.

Figure 9(b) displays that the Q_{st} of nitrogen adsorbed on Co-ZIF-8 settled at ~10 kJ/mole for loadings up to ~0.75 mole/kg. The Q_{st} of carbon dioxide gas rises from ~24 kJ/mole to ~31 kJ/mole when augmenting its loading from 0.25 to 2.56 kg/mole. Furthermore, it is seen that the Q_{st} of CH_4 rises from ~32 kJ/mole at ~0.23 mole/kg to ~41 kJ/mole at 1.40 mole/kg.

Figure 9(c) exposes that the Q_{st} of the adsorption of nitrogen on Zn/Co-ZIF-8 augments from ~8 kJ/mole up to ~11 kJ/mole when increasing the corresponding loading from 0.05 mole/kg to 0.76 mole/kg. The Q_{st} of carbon dioxide gas remains at around ~20-21 kJ/mole for the entire range of its loading. In contrast, the Q_{st} of methane rises from ~20 kJ/mole at an adsorbed amount of 0.14 mole/kg up to ~27 kJ/mole at 1.51 mole/kg.

Figures 10(a)–10(c) elucidate a disparity between the isosteric heat values of nitrogen, methane, and carbon dioxide, respectively, on various ZIFs. Overall, it was noticed from Figure 10(a) that the Q_{st} values of N_2 obeys the trend ZIF-8 > Zn/Co-ZIF-8 > Co-ZIF-8. Additionally, the Q_{st} of the adsorption of nitrogen augments with the adsorbed amount of gas on Zn/Co-ZIF-8, ZIF-8, and to a lesser extent on Co-ZIF-8. Figure 10(b) displays that the order of Q_{st} for CH_4 is Co-ZIF-8 > Zn/Co-ZIF-8 > ZIF-8 in the range from 0.15 to 0.97 mole/kg. After 0.97 mole/kg, the order of Q_{st} for CH_4 turns out to be Co-ZIF-8 > ZIF-8 > Zn/Co-ZIF-8. It is seen from Figure 10(c) that the Q_{st} value of CO_2 was always highest for Co-ZIF-8. The Q_{st} for CO_2 on Zn/Co-ZIF-8 was nearly constant at values higher than that on ZIF-8 up to a loading of 1.57 mole/kg, after which the isosteric heat on ZIF-8 becomes greater than that on Zn/Co-ZIF-8. It is noted that the results of ZIF-8 reported in Awadallah-F et al. [30] were used for the purpose of comparison.

4. Conclusions

ZIF-8, Co-ZIF-8, and Zn/Co-ZIF-8 were produced by a microwave-irradiation technique. The adsorption of CH_4, N_2, and CO_2 on ZIF-8, Co-ZIF-8, and Zn/Co-ZIF-8 was

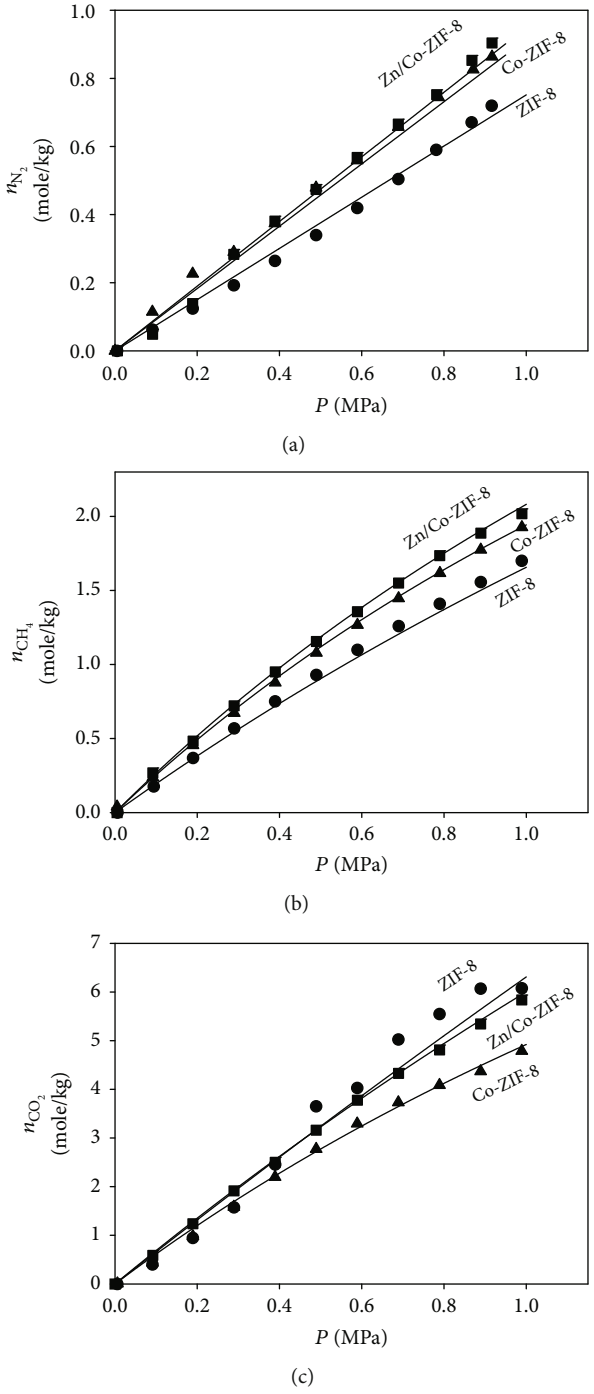

Figure 4: Influence of ZIF types (ZIF-8, Co-ZIF-8, and Zn/Co-ZIF-8) on their adsorption of (a) nitrogen, (b) methane, and (c) carbon dioxide at the temperature of 25°C. The symbols indicate measured data and the lines indicate DSL fitting.

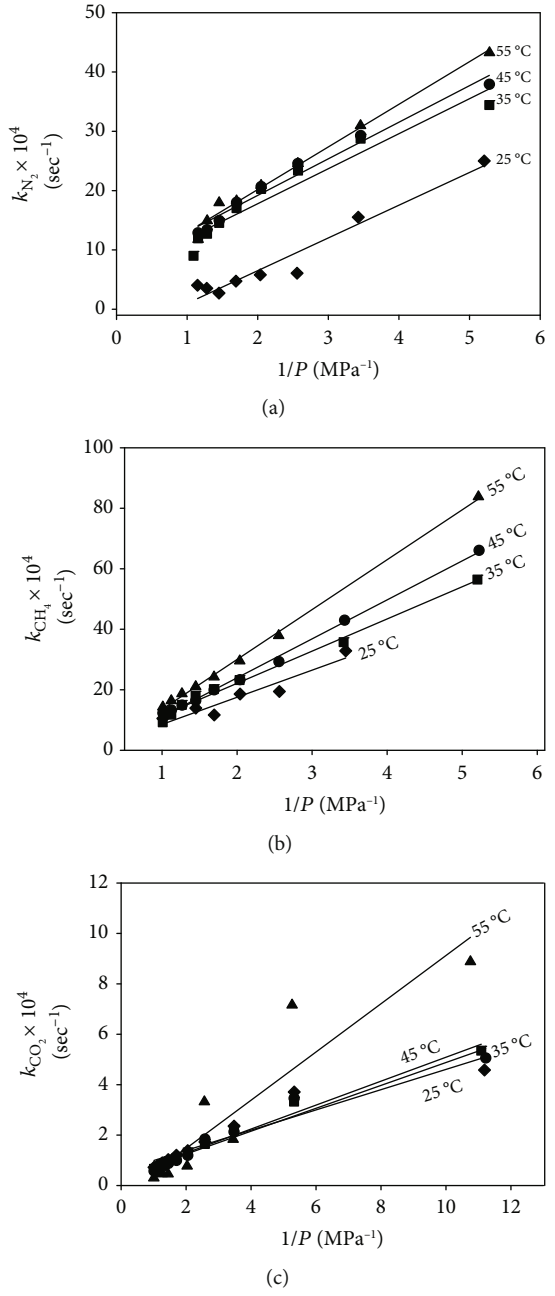

Figure 5: k-values for adsorbing (a) nitrogen, (b) methane, and (c) carbon dioxide gases on ZIF-8 samples at diverse temperatures. Symbols and lines indicate, respectively, estimated data and linear regression.

studied at a range of temperatures (25 to 55°C) and pressures (~0 to ~1 MPa). The dual-site Langmuir (DSL) model was used to describe experimental adsorption equilibria at different pressures and temperatures. Zn/Co-ZIF-8 displays the largest capacity to adsorb nitrogen and methane at various temperatures, while ZIF-8 shows the largest capacity to adsorb carbon dioxide. The order of adsorption quantities of nitrogen and methane gases on different ZIFs is Zn/Co-ZIF-8 > Co-ZIF-8 > ZIF-8. Moreover, the order of adsorption capacities of carbon dioxide gas onto different ZIFs is ZIF-8 > Zn/Co-ZIF-8 > Co-ZIF-8. The overall mass transfer coefficients have been evaluated to indicate the rates of adsorbing CH_4, N_2, and CO_2 gases on various ZIFs. Overall, the mass transfer coefficients were augmented when raising the temperature or reducing the pressure. Furthermore, the

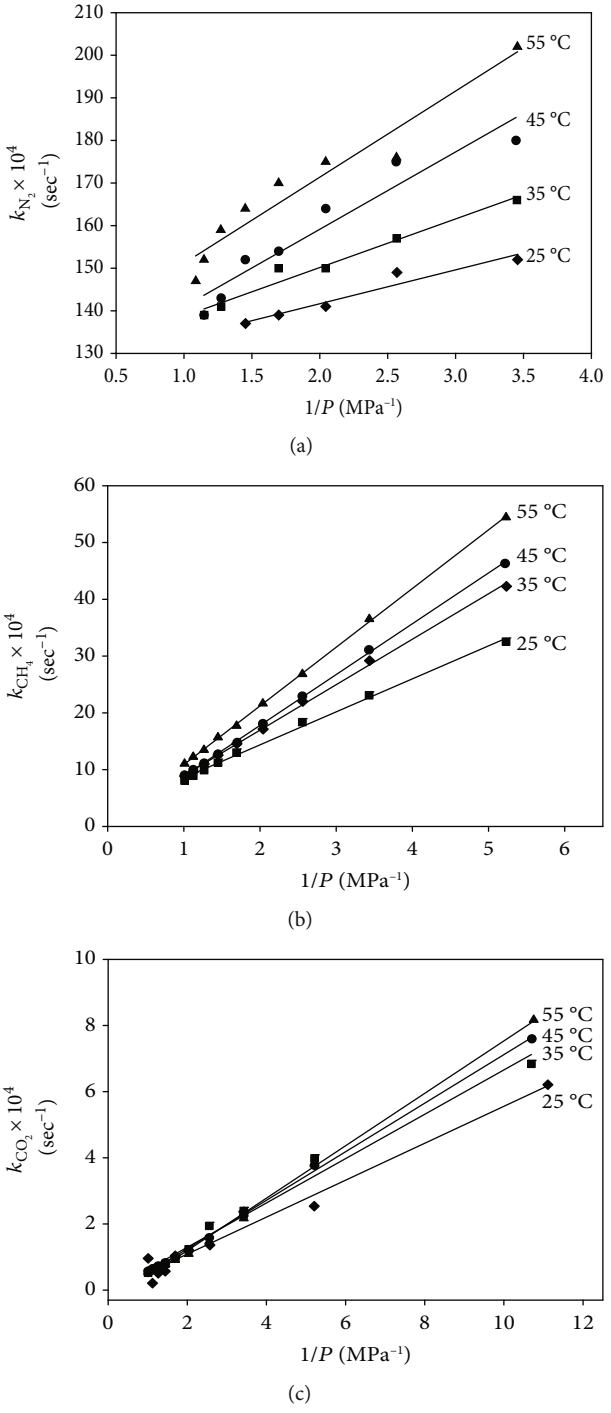

Figure 6: k-values for adsorbing (a) nitrogen, (b) methane, and (c) carbon dioxide gases on Co-ZIF-8 samples at diverse temperatures. Symbols and lines denote, respectively, estimated data and linear regression.

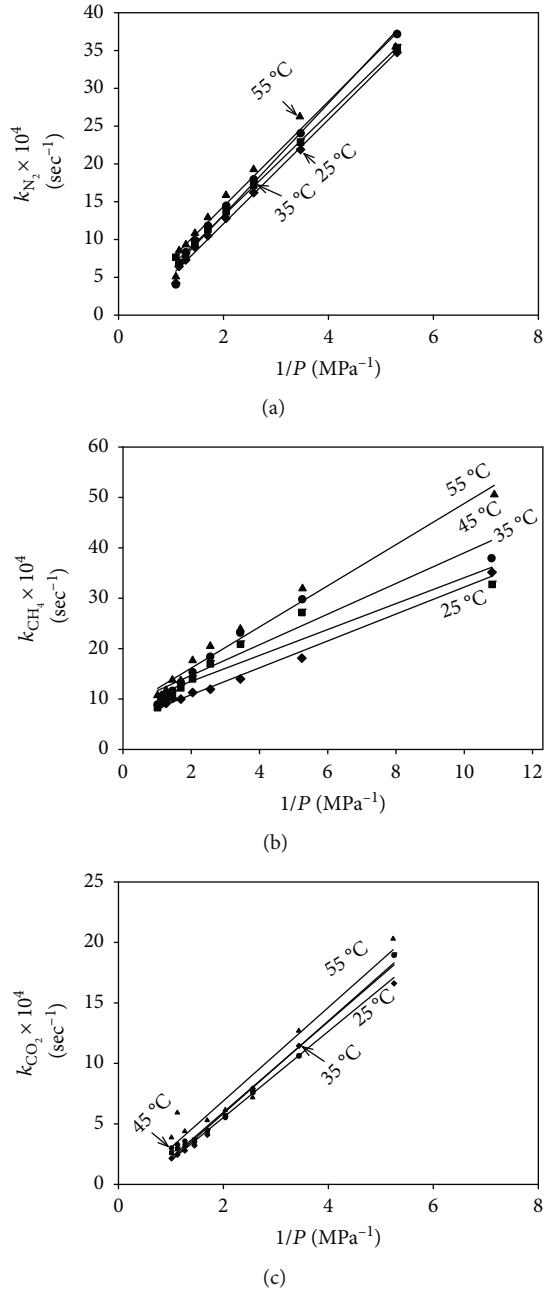

Figure 7: k-values for adsorbing (a) nitrogen, (b) methane, and (c) carbon dioxide gases on Zn/Co-ZIF-8 samples at diverse temperatures. Symbols and lines denote, respectively, estimated data and linear regression.

adsorption of CO_2 gas was slowest on all ZIFs. On the other hand, the adsorption of CH_4 gas was the fastest on ZIF-8 and Co/Zn-ZIF-8, while nitrogen adsorption was fastest on Co-ZIF-8. These disparities, which are due to the existence of cobalt into the matrix of ZIFs, can be utilized to boost the kinetic separations of CH_4, N_2, and CO_2 mixtures. Additionally, the isosteric heats of adsorbing CH_4, N_2, and CO_2 gases on ZIF-8, Co-ZIF-8, and Zn/Co-ZIF-8 were estimated. Across study findings, it has been noticed that the isosteric heats vary in accordance with the ZIF type utilized, but they were mostly highest for CH_4 and lowest for N_2.

Data Availability

The data used to support the findings of this study are included within the article.

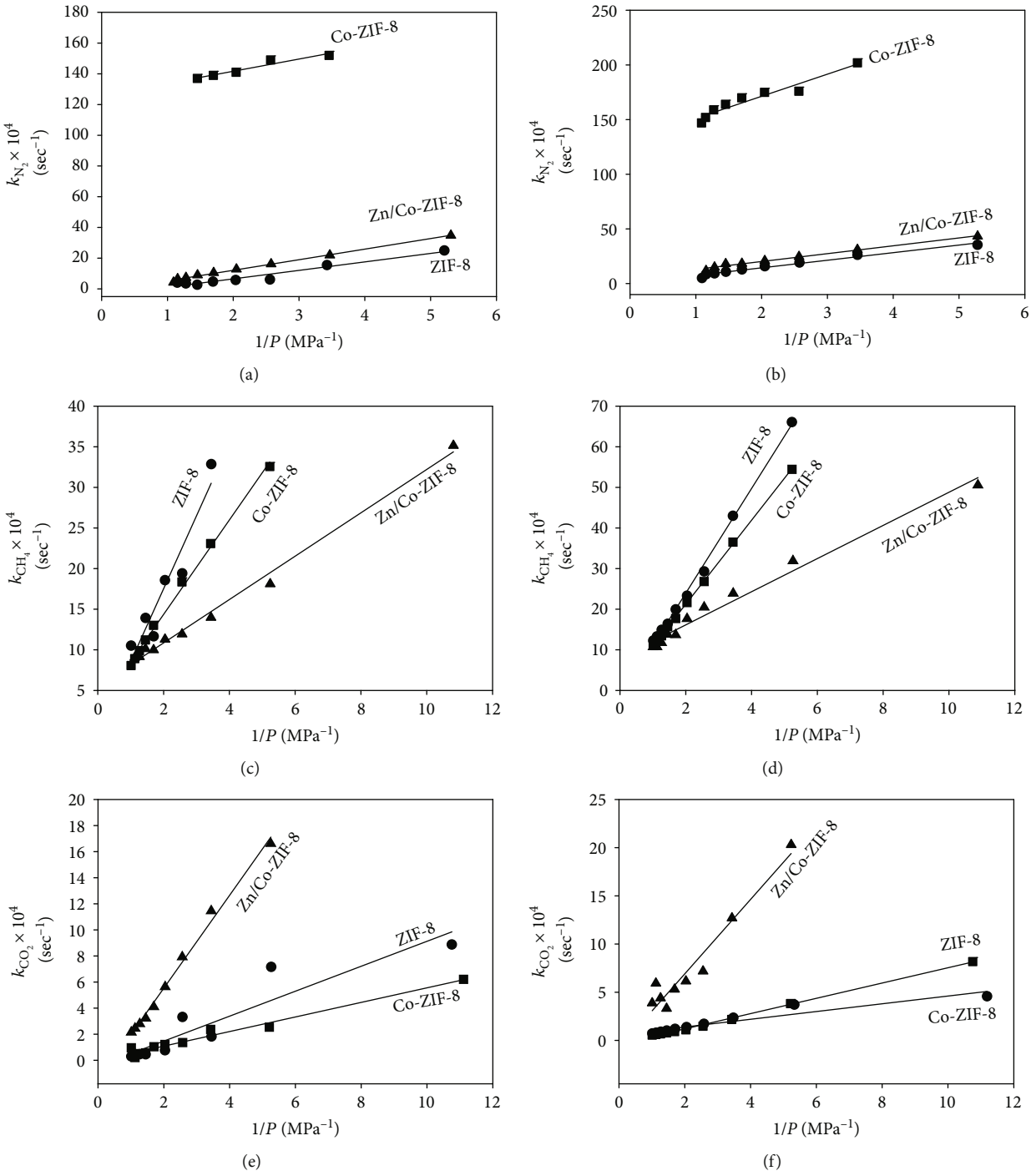

Figure 8: Impact of ZIF types (i.e., ZIF-8, Co-ZIF-8, and Zn/Co-ZIF-8) on k for (a, b) nitrogen, (c, d) methane, and (e, f) carbon dioxide at 25°C (a, c, e) and 55°C (b, d, f). Symbols and lines denote to estimated data and linear regression, correspondingly.

Disclosure

Ahmed Awadallah-F is on leave from the Radiation Research of Polymer Department, National Centre for Radiation Research and Technology, Atomic Energy Authority, P.O. Box 29, Nasr City, Cairo, Egypt. The sponsors had no role in the design, execution, interpretation, or writing of the study.

Conflicts of Interest

The authors declare no conflict of interest.

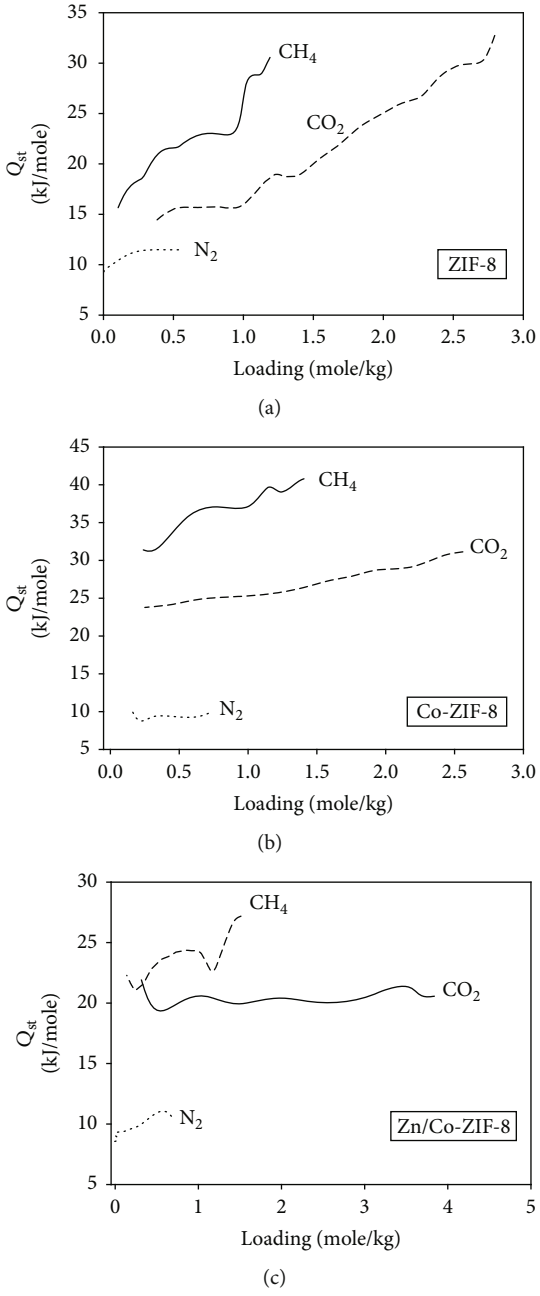

FIGURE 9: Q_{st} of adsorption of nitrogen, methane, and carbon dioxide gases upon (a) ZIF-8, (b) Co-ZIF-8, and (c) Zn/Co-ZIF-8.

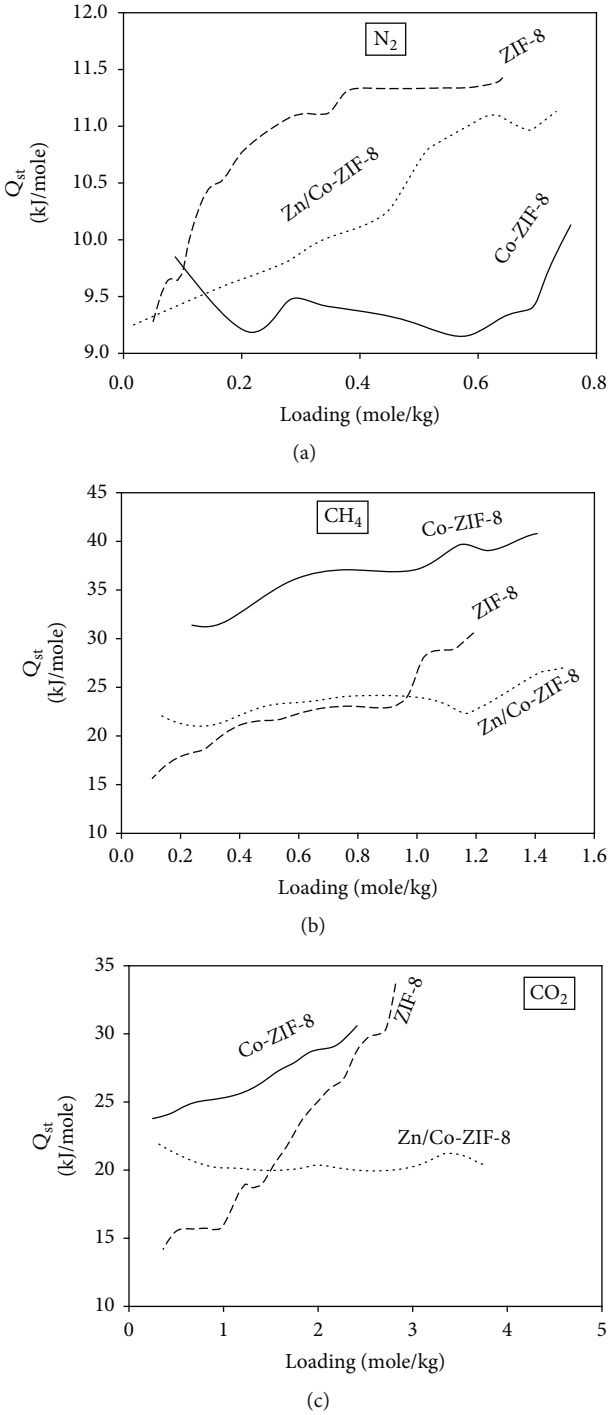

FIGURE 10: The Q_{st} of adsorption for (a) N_2, (b) CH_4, and (c) CO_2 on various ZIFs.

Acknowledgments

This publication was made possible by the NPRP awards (NPRP 08-014-2-003 and NPRP-8-001-2-001) from the Qatar National Research Fund (a member of The Qatar Foundation). H.-K.J. acknowledges support from the National Science Foundation (CMMI-1561897). The statements made herein are solely the responsibility of the authors. Technical support from the Department of Chemical Engineering, the Central Laboratory Unit (CLU), and the Gas Processing Centre (GPC) at Qatar University is also acknowledged. The publication of this article was funded by the Qatar National Library.

Supplementary Materials

S1: regression of mass transfer coefficients. Table S1 summarizes the regression of mass transfer coefficients for the adsorption of nitrogen, methane, and carbon dioxide gases onto different adsorbents of ZIFs: ZIF, Co-ZIF-8, and Zn/Co-ZIF-8. Table S1: regression and the coefficients of determination (R^2) for the overall mass transfer coefficient

$10^4 \times k$ (s^{-1}) against $1/P$ (MPa^{-1}) for adsorption of methane, nitrogen, and carbon dioxide gases on ZIF-8, Co-ZIF-8, and Zn/Co-ZIF-8 adsorbents at different temperatures. *(Supplementary Materials)*

References

[1] J. Duan, Y. Pan, G. Liu, and W. Jin, "Metal-organic framework adsorbents and membranes for separation applications," *Current Opinion in Chemical Engineering*, vol. 20, pp. 122–131, 2018.

[2] A. Awadallah-F, F. Hillman, S. A. Al-Muhtaseb, and H. K. Jeong, "Influence of doped metal center on morphology and pore structure of ZIF-8," *Material Research Society Communications*, vol. 9, no. 01, pp. 288–291, 2019.

[3] W. Li, Y. Zhang, Q. Li, and G. Zhang, "Metal–organic framework composite membranes: synthesis and separation applications," *Chemical Engineering Science*, vol. 135, pp. 232–257, 2015.

[4] L. S. Lai, Y. F. Yeong, K. K. Lau, and A. M. Shariff, "Effect of synthesis parameters on the formation of ZIF-8 under microwave-assisted solvothermal," *Procedia engineering*, vol. 148, pp. 35–42, 2016.

[5] V. V. Butova, A. P. Budnik, E. A. Bulanova, and A. V. Soldatov, "New microwave-assisted synthesis of ZIF-8," *Mendeleev Communications*, vol. 26, no. 1, pp. 43-44, 2016.

[6] A. A. Oladipo, "Microwave-assisted synthesis of high-performance polymer-based nanoadsorbents for pollution control," in *New polymer nanocomposites for environmental remediation*, C. M. Hussain and A. K. Mishra, Eds., pp. 337–359, Elsevier Inc, Amsterdam, 2018.

[7] A. Mirzaei and G. Neri, "Microwave-assisted synthesis of metal oxide nanostructures for gas sensing application: a review," *Sensors and Actuators B: Chemical*, vol. 237, pp. 749–775, 2016.

[8] H. Zhang, C. Duan, F. Li, X. Yan, and H. Xi, "Green and rapid synthesis of hierarchical porous zeolitic imidazolate frameworks for enhanced CO_2 capture," *Inorganica Chimica Acta*, vol. 482, pp. 358–363, 2018.

[9] A. Awadallah-F, F. Hillman, S. A. Al-Muhtaseb, and H.-K. Jeong, "On the nanogate-opening pressures of copper-doped zeolitic imidazolate framework ZIF-8 for the adsorption of propane, propylene, isobutane, and N-butane," *Journal of Materials Science*, vol. 54, no. 7, pp. 5513–5527, 2019.

[10] J. Peng, X. Sun, Y. Li et al., "Controllable growth of ZIF-8 layers with nanometer-level precision on SiO_2 nanopowders via liquid phase epitaxy stepwise growth approach," *Microporous and Mesoporous Materials*, vol. 268, pp. 268–275, 2018.

[11] J. H. ter Horst, C. Schmidt, and J. Ulrich, "Fundamentals of industrial crystallization," in *Handbook of Crystal Growth*, pp. 1317–1349, Bulk Crystal Growth Handbook of Crystal Growth, 2015.

[12] X. Wang, B. Yuan, X. Zhou et al., "Novel glucose-based adsorbents (Glc-Cs) with high CO_2 capacity and excellent $CO_2/CH_4/N_2$ adsorption selectivity," *Chemical Engineering Journal*, vol. 327, pp. 51–59, 2017.

[13] M. Yang, W. Jing, J. Zhao, Z. Ling, and Y. Song, "Promotion of hydrate-based CO_2 capture from flue gas by additive mixtures (THF (tetrahydrofuran) + TBAB (tetra-n-butyl ammonium bromide))," *Energy*, vol. 106, pp. 546–553, 2016.

[14] A. Dugstad, M. Halseid, and B. Morland, "Testing of CO_2 specifications with respect to corrosion and bulk phase reactions," *Energy Procedia*, vol. 63, pp. 2547–2556, 2014.

[15] K. Dalane, H. F. Svendsen, M. Hillestad, and L. Deng, "Membrane contactor for subsea natural gas dehydration: model development and sensitivity study," *Journal of Membrane Science*, vol. 556, pp. 263–276, 2018.

[16] A. Kumar and K. A. Subramanian, "Control of greenhouse gas emissions (CO_2, CH_4 and N_2O) of a biodiesel (B100) fueled automotive diesel engine using increased compression ratio," *Applied Thermal Engineering*, vol. 127, pp. 95–105, 2017.

[17] S. Rani, B. K. Prusty, and S. K. Pal, "Adsorption kinetics and diffusion modeling of CH_4 and CO_2 in Indian shales," *Fuel*, vol. 216, pp. 61–70, 2018.

[18] X. He, T. J. Kim, and M. B. Hägg, "Hybrid fixed-site-carrier membranes for CO_2 removal from high pressure natural gas: membrane optimization and process condition investigation," *Journal of Membrane Science*, vol. 470, pp. 266–274, 2014.

[19] S. K. Das, X. Wang, M. M. Ostwal, and Z. Lai, "A highly stable microporous covalent imine network adsorbent for natural gas upgrading and flue gas CO_2 capture," *Separation and Purification Technology*, vol. 170, pp. 68–77, 2016.

[20] B. Wu, X. Zhang, Y. Xu, D. Bao, and S. Zhang, "Assessment of the energy consumption of the biogas upgrading process with pressure swing adsorption using novel adsorbents," *Journal of Cleaner Production*, vol. 101, pp. 251–261, 2015.

[21] S. Yu, J. Bo, and L. Fengjuan, "Competitive adsorption of $CO_2/N_2/CH_4$ onto coal vitrinite macromolecular: effects of electrostatic interactions and oxygen functionalities," *Fuel*, vol. 235, pp. 23–38, 2019.

[22] L. Chong and E. M. Myshakin, "Molecular simulations of competitive adsorption of carbon dioxide - methane mixture on illitic clay surfaces," *Fluid Phase Equilibria*, vol. 472, pp. 185–195, 2018.

[23] F. Hillman, J. M. Zimmerman, S. M. Paek, M. R. A. Hamid, W. T. Lim, and H. K. Jeong, "Rapid microwave-assisted synthesis of hybrid zeolitic–imidazolate frameworks with mixed metals and mixed linkers," *Journal of Materials Chemistry A*, vol. 5, no. 13, pp. 6090–6099, 2017.

[24] A. Awadallah-F, S. A. al-Muhtaseb, and H. K. Jeong, "Selective adsorption of carbon dioxide, methane and nitrogen using resorcinol-formaldehyde-xerogel activated carbon," *Adsorption*, vol. 23, no. 7-8, pp. 933–944, 2017.

[25] A. Awadallah-F and S. A. Al-Muhtaseb, "Carbon dioxide sequestration and methane removal from exhaust gases using resorcinol–formaldehyde activated carbon xerogel," *Adsorption*, vol. 19, no. 5, pp. 967–977, 2013.

[26] H. Li, J. Kang, F. Zhou, Z. Qiang, and G. Li, "Adsorption heat features of coalbed methane based on microcalorimeter," *Journal of Loss Prevention in the Process Industries*, vol. 55, pp. 437–449, 2018.

[27] D. Leinekugel-le-Cocq, M. Tayakout-Fayolle, Y. Le Gorrec, and C. Jallut, "A double linear driving force approximation for non-isothermal mass transfer modeling through bi-

disperse adsorbents," *Chemical Engineering Science*, vol. 62, no. 15, pp. 4040–4053, 2007.

[28] M. Li and X. Liu, "The least squares based iterative algorithms for parameter estimation of a bilinear system with autoregressive noise using the data filtering technique," *Signal Process*, vol. 147, pp. 23–34, 2018.

[29] V. S. Mane and P. V. V. Babu, "Studies on the adsorption of brilliant green dye from aqueous solution onto low-cost NaOH treated saw dust," *Desalination*, vol. 273, no. 2-3, pp. 321–329, 2011.

[30] A. Awadallah-F, F. Hillman, S. A. al-Muhtaseb, and H. K. Jeong, "Adsorption equilibrium and kinetics of nitrogen, methane and carbon dioxide gases onto ZIF-8, Cu10%/ZIF-8, and Cu30%/ZIF-8," *Industrial & Engineering Chemistry Research*, vol. 58, no. 16, pp. 6653–6661, 2019.

Hindawi
Journal of Nanomaterials
Volume 2019, Article ID 8318260, 7 pages
https://doi.org/10.1155/2019/8318260

Research Article

Effect of Cellulose Nanocrystals on the Properties of Cement Paste

Qiaoling Liu,[1,2] **Yujiao Peng**,[1,2] **Long Liang**,[1,2] **Xiaobin Dong**,[3] **and Hancai Li**[1,2]

[1]*School of Civil Engineering, Shandong Jianzhu University, Jinan 250101, China*
[2]*Key Laboratory of Building Structural Retrofitting and Underground Space Engineering of Ministry of Education, Jinan 250101, China*
[3]*School of Materials Science and Engineering, Shandon Jianzhu University, Jinan 250101, China*

Correspondence should be addressed to Qiaoling Liu; lql263@163.com

Received 20 July 2019; Revised 24 September 2019; Accepted 3 October 2019; Published 16 December 2019

Guest Editor: Yunpan Ying

The effect of the addition of cellulose nanocrystals (CNCs) on the properties of cement pastes is studied herein. The compressive strength of CNC/cement paste was investigated under the curing conditions defined in this study. Two-dimensional micrographs and pore size distributions were obtained by scanning electron microscopy, X-ray computed tomography (XCT), and nitrogen adsorption. The addition of CNCs was found to significantly enhance the mechanical properties of cement pastes with a rapid decrease in temperature and humidity. XCT and nitrogen adsorption analyses show that the addition of CNCs leads to a refinement of the pore structure in the cement matrix. Almost no hydration products, including C-S-H, are formed in the cement matrix without CNCs under extreme conditions. This is in contrast with the results for the cement paste with 0.5% CNCs.

1. Introduction

In recent decades, research on nanocrystals including organic and inorganic materials has become a promising topic. Owing to their excellent properties, nanocrystals have been applied in medicine, catalysis, biology, and composites. However, most nanocrystals have been prepared by chemical synthesis, such as SiC nanocrystals, ZnO nanocrystals, GaAs nanocrystals, and poly (butylene carbonate). Although the size and shape of synthetic nanocrystals can be controlled when compared to CNCs, the preparation of nanocrystals will lead to the destruction of resources and result in environmental pollution [1–9]. However, CNCs are manufactured from natural sources such as trees and plants. Thus, CNCs have developed rapidly in recent years as nanofibers that are environmentally friendly and renewable. Furthermore, they have many extraordinary properties when compared to other nanofibers, such as an ultrafine diameter, low density, and low cost. They also show good water dispersibility without the need of any modification or the addition of any surfactant [10, 11].

Cellulose nanocrystals (CNCs) have become a potential nanofiber material that can improve the properties of cement paste. Previous research has shown that the addition of CNCs can prevent microcracking and improve the mechanical properties of cement paste [12–16]. An addition of only 0.2% volume of CNCs can increase the flexural strength of cement by approximately 30% [15]. After ultrasonication, this can reach up to 50% [16]. Furthermore, the degree of hydration (DOH) of cement pastes can be improved by employing CNCs. Short-circuit diffusion mechanism is more dominant than steric stabilization; this explains the increase in DOH caused by CNCs [15]. Cao et al. [16] found that when a simulated pore solution of cement paste replaces deionized water, CNCs will be more probable to agglomeration at a lower concentration. This shows that the dispersion of CNCs plays a key role in improving the flexural strength of the cement paste, particularly at a high concentration of CNCs.

This study investigated the tremendous influence of CNCs on cement pastes under the curing conditions defined, which is detrimental to cement hydration.

2. Materials and Methods

2.1. Materials. Ordinary Portland cement is used in this study. Table 1 lists the chemical composition and physical

Table 1: Chemical composition and physical properties of cement.

Chemical composition (wt.%)							Special surface area, Blaine ($m^2 \cdot kg^{-1}$)	Compressive strength (MPa)
CaO	SiO_2	Al_2O_3	Fe_2O_3	MgO	SO_3	Ignition loss		
63.6	21.2	3.2	3.0	1.0	2.5	2.3	385	52.1

wt.% represents mass fraction.

Table 2: Mixture proportions.

No.	Cement/g	CNCs/g	Water/g
C1	100	0	50
C2	100	0.2	50
C3	100	0.5	50
C4	100	0.2	40

properties of this type of cement. The CNC materials are manufactured by the laboratory of Nanjing Forestry University. The CNCs are extracted from cotton cellulose fibers. Firstly, the microcrystalline cellulose of cotton is hydrolyzed with 64 wt.% H_2SO_4, after which the solution is diluted with distilled water and the suspension is centrifuged. After repeating the dilution and centrifugation, the precipitates collected are further dialyzed with distilled water from a dialysis tube (Biosharp; molecular mass cutoff = 14400, USA) until its pH becomes 7.0. Subsequently, the CNC suspension is ultrasonically dispersed for 30 min. Therefore, the CNC material is a suspension at a concentration of 1.1 wt.%. The width and length of CNCs are 4–9 nm and 100–400 nm, respectively.

2.2. Mixing and Specimen Preparation. Table 2 shows the proportion of cement paste mixtures. The cement pastes are created in a rotary mixer. Cement is added first, after which water and the CNC solution are introduced and the pastes are mixed. The pastes are then poured into 30 × 30 × 30 mm molds. All samples are demolded after 24 h and then cured at 20 ± 2°C and a relative humidity (RH) ≥ 95% for 7 d. Subsequently, these samples were moved to a curing room and treated at 4 ± 2°C and RH of 55 ± 5% for 21 d.

2.3. Testing. The micromorphology of CNCs in water was observed by transmission electron microscopy (TEM) (JEM-1400, Japan). The compressive strength of cement pastes was measured at defined ages. To study the 2D microstructure and pore size distribution of cement pastes, the samples were crushed into pieces and soaked in ethanol for 48 h to stop the hydration of cement. The samples were then dried in an oven at 45 ± 5°C for 48 h, and the dried samples were stored in a dryer. Scanning electron microscopy (SEM) was used to characterize the 2D microstructure of the samples. The samples, after curing for a defined number of days, were cut into 1.5 ± 0.5 cm thick slices; central cylinders with a diameter of 1 cm were obtained using a water saw. Then, three-dimensional (3D) images were obtained, and the defect distributions of cement pastes without any prior damaging preparation were tested via X-ray computed tomography (XCT; Xradia 510 Versa, Zeiss, Germany). The voltage and current of the X-ray tubes were 80 kV and 87 μA, respectively. The pore size distributions of the cement paste were determined by nitrogen adsorption via the Barrett–Joyner–Halenda (BJH) analysis.

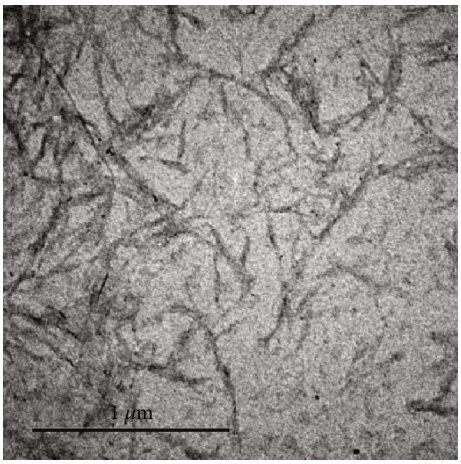

Figure 1: Micromorphology of CNCs.

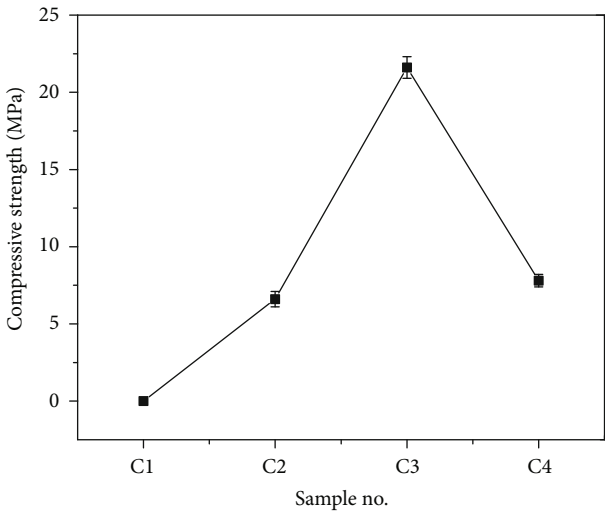

Figure 2: Effect of CNCs on compressive strength of cement pastes.

3. Results and Discussion

3.1. Micromorphology of CNCs. Figure 1 shows the micromorphology of CNCs in water. It is observed that CNCs are dispersed well in deionized water.

3.2. Mechanical Properties. Figure 2 shows the compressive strength of the cement pastes. The compressive strength of cement pastes without CNCs cannot be obtained because of the cracking destruction of specimens. Firstly, cement pastes

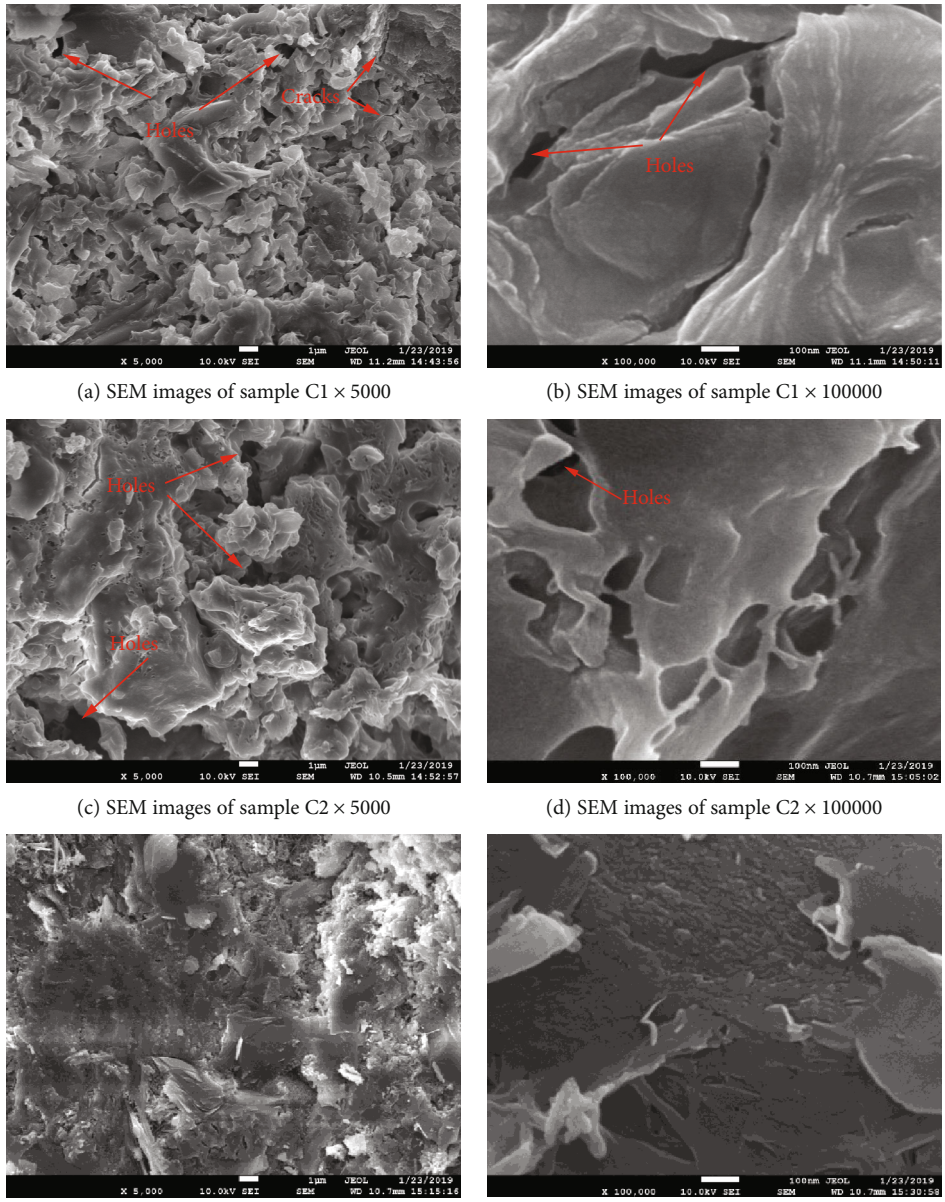

(a) SEM images of sample C1 × 5000

(b) SEM images of sample C1 × 100000

(c) SEM images of sample C2 × 5000

(d) SEM images of sample C2 × 100000

(e) SEM images of sample C3 × 5000

(f) SEM images of sample C3 × 100000

Figure 3: SEM images of samples C1, C2 and C3.

without aggregates have higher shrinkage and the higher water-cement ratio increases the shrinkage and brittleness of cement pastes. Secondly, the rapid decrease in temperature and humidity causes higher temperature and dry shrinkage deformation and worsens the hydration process of cement. Most surprisingly, it was found that a mere 0.5% CNCs addition could improve the mechanical properties of cement pastes significantly under the detrimental curing system. It was seen that CNC addition has excellent effect in preventing cement pastes from cracking. This notable result indicates that CNCs have exciting application prospects in concrete construction under lower temperatures, but not freezing environments.

3.3. Micrographs. In order to avoid the interference caused by the selected areas, several photos were taken with different magnifications in different zones of the cement pastes. The effect of CNC addition on the microstructure of cement pastes is very evident. Figures 3(a) and 3(b) show the SEM images of cement pastes without CNCs; Figures 3(c) and 3(d) show the SEM images of cement pastes with 0.2% CNCs; and Figures 3(e) and 3(f) show the SEM images of cement pastes with 0.5% CNCs. It is observed that the cement paste without CNCs has many gas holes and loosing structures. The microstructure of cement pastes is enhanced when CNCs are introduced into the samples. Figures 3(e)–3(f) show that 0.5% CNCs compact the cement paste and evidently reduce pores and cracks.

3.4. XCT. Figures 4(a) and 4(b), Figures 5(a) and 5(b), Figures 6(a) and 6(b), and Figures 7(a) and 7(b) show the 3D defect images of CNC/cement pastes with different

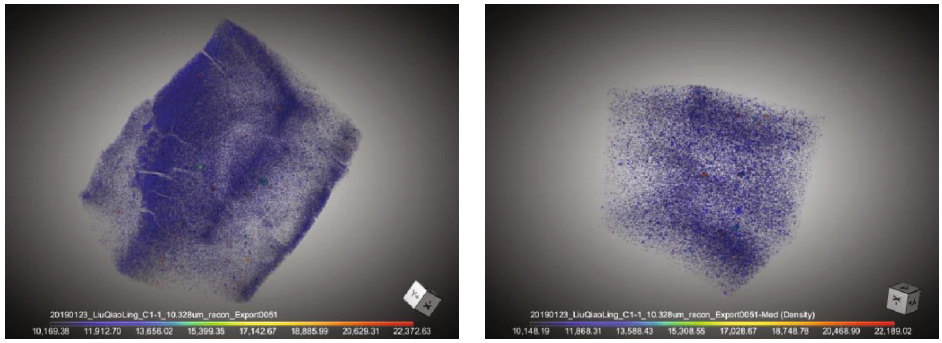

(a) Initial image (b) Cropped image

Figure 4: 3D images of sample C1 with 0.0% CNCs.

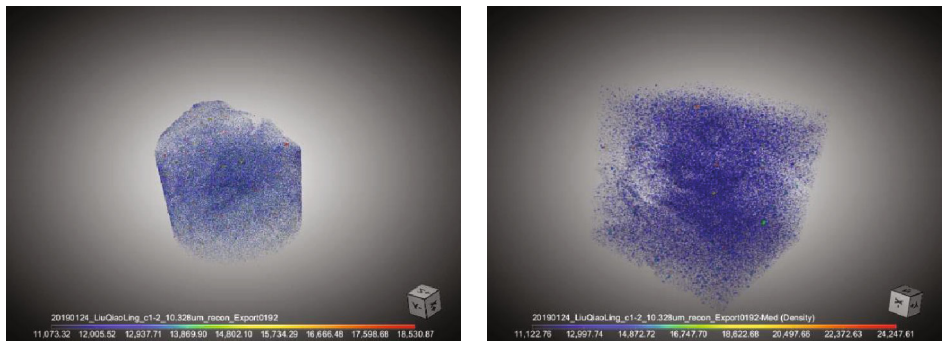

(a) Initial image (b) Cropped image

Figure 5: 3D images of sample C2 with 0.2% CNCs.

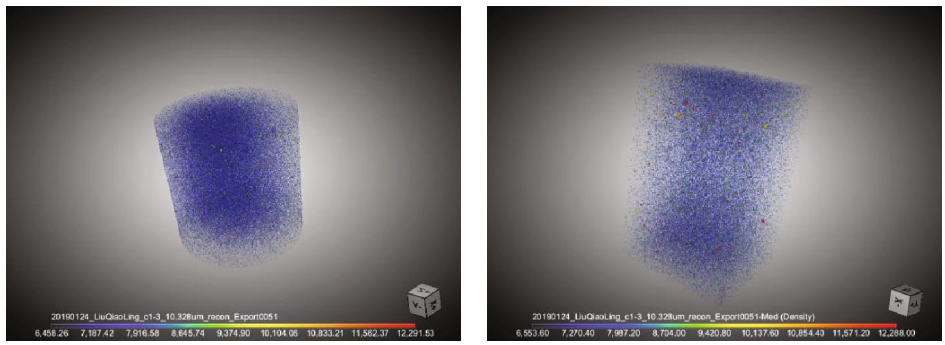

(a) Initial image (b) Cropped image

Figure 6: 3D images of sample C3 with 0.5% CNCs.

amounts of CNCs. Figure 8 shows the two-dimensional (2D) images of the defect segmentation. It is evident that the shape of sample C1 is irregular because it is so fragile that the central cylinders cannot be obtained with a water saw. A box has been cropped from the initial 3D images in order to avoid the boundary layer interaction. It is observed that the defects in sample C3 reduce; 0.5% CNC addition can improve the mesoscopic structure significantly under a detrimental environment.

In order to check the effect of CNCs on 3D defect distribution of cement pastes, the defect counts of the same volume (309, 550, 999, and 395.70 μm^3) were statistically studied. Figures 9(a) and 9(b) show the effect of CNCs on 3D defect distribution of cement pastes. Figures 9(a) and 9(b) show that the count of the total 3D defects reduces when CNCs are introduced into the cement pastes. When the amount of CNCs is 0.5% of cement by weight, the 3D defect count is the lowest between 1000 μm^3 and 10000 μm^3; however, the 3D defect count greater than 10000 μm^3 is slightly higher than that in sample C4. It is observed that CNCs play an important role in decreasing 3D defects between 1000 μm^3 and 10000 μm^3 of cement pastes.

3.5. Pore Size Analysis by Nitrogen Adsorption. Figure 10 shows the effect of the addition of CNCs on micropore and mesopore distribution in cement pastes. It is seen that sample C3 has the highest volume of pores between 0 and 250 nm. In comparison, Figure 10 shows that the count of 3D defects

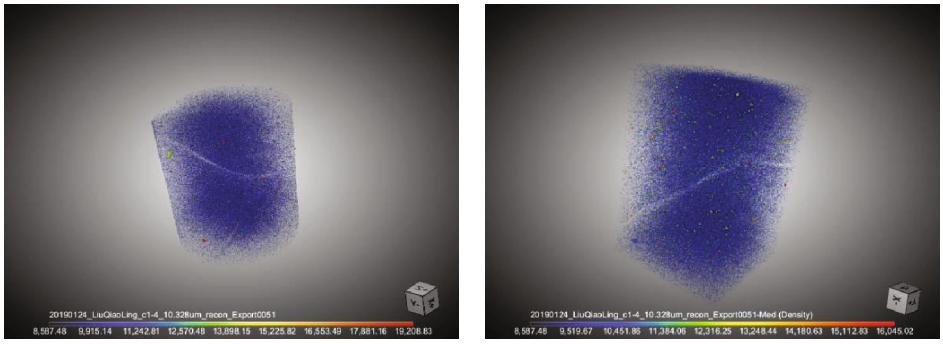

(a) Initial image (b) Cropped image

Figure 7: 3D images of sample C4 with 0.2% CNCs.

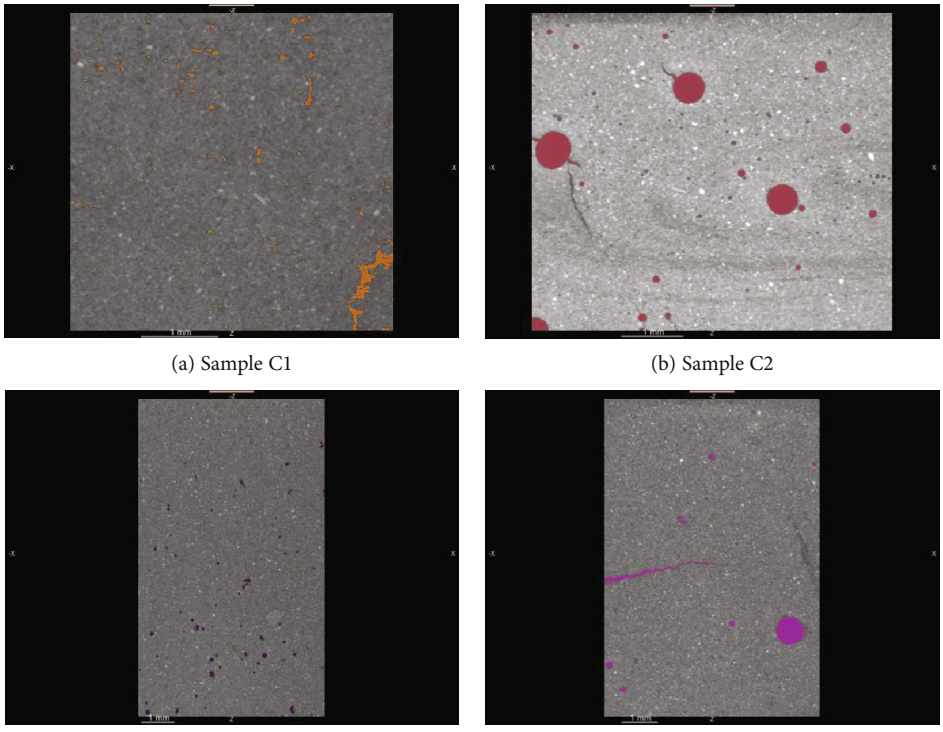

(a) Sample C1 (b) Sample C2

(c) Sample C3 (d) Sample C4

Figure 8: 2D images of the defect segmentation.

between 1000 and 10000 μm^3 (the pore size is approximately 10–20 μm) in sample C3 is the lowest. Thus, the addition of CNCs has a positive effect on the pore size distribution of cement pastes; this addition also leads to a pore structure refinement.

Furthermore, a very interesting discovery was made. In order to avoid the possibility of this being an accidental finding, repetitiveness of the nitrogen adsorption test was validated. It was found that 4–12 nm pores in sample C1, 3–7 nm pores in sample C2, and 3–8 nm pores in sample C4 disappeared.

Numerous studies show that there is no obvious separation between the C–S–H interlayer space width, gel pore width, and the sizes of interhydrate and capillary pores of cement pastes [17–20]. However, Valori et al. [21] and Muller et al. [22, 23] do define the interhydrate pore width in cement matrix and the size of the C–S–H interlayer space and gel pore size. The size of the pores that disappeared in sample C1 is in good agreement with the C–S–H interlayer space size, gel pore size, and interhydrate pore size obtained in their research results. When the CNC content is increased to 0.5% (sample C3), 3–10 nm pores appear completely. Figure 1 shows that the compressive strengths of samples C1 and C3 are 0 MPa and 21.6 ± 0.7 MPa, respectively. Therefore, almost no hydration products including C-S-H gel were formed in sample C1 under extreme conditions. The absence of 3–7(8) nm pores in samples C2 and C4 shows that almost no C-S-H gel is formed in those samples either. It is possible that a rapid decrease in temperature and humidity leads to a difficulty in the formation of CSH.

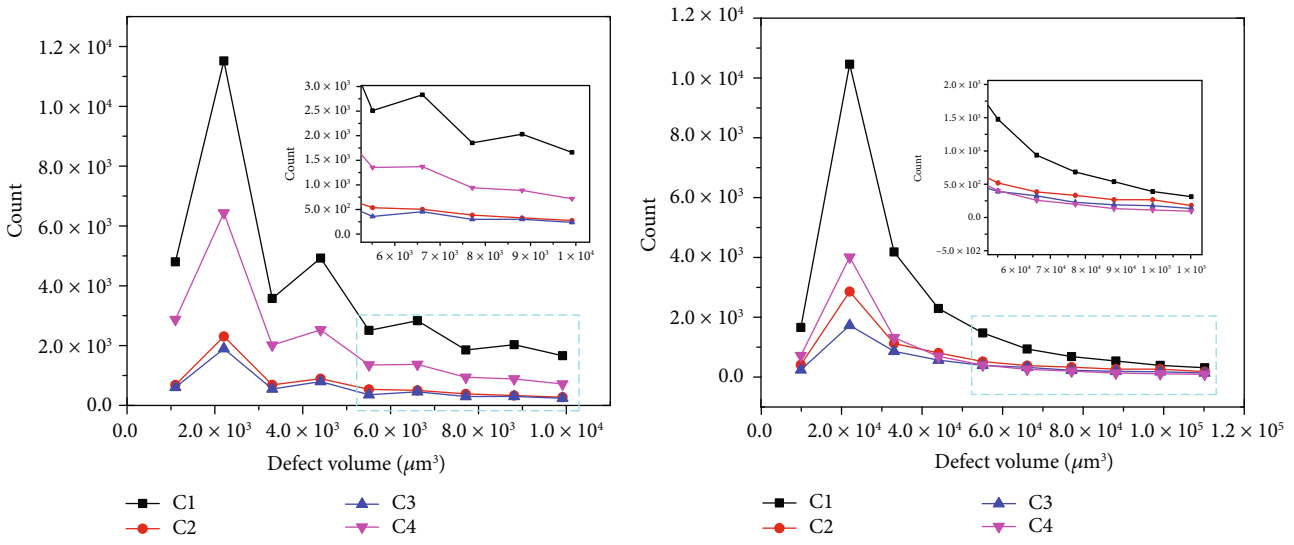

(a) 3D defect distribution

(b) 3D defect distribution

Figure 9: 3D defect distribution in cement pastes.

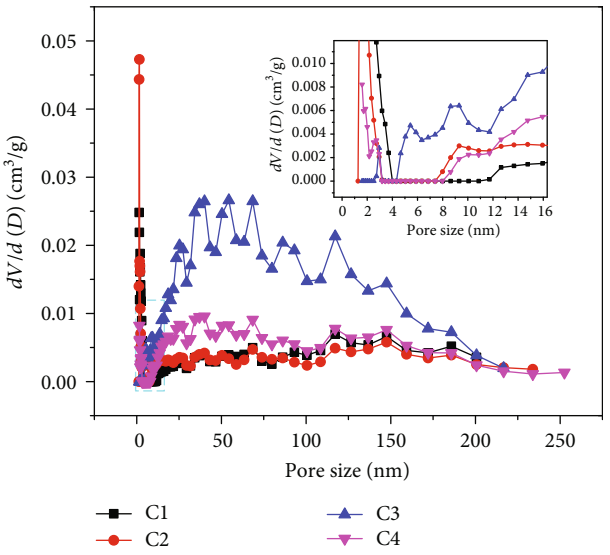

Figure 10: Pore size distribution in cement pastes.

4. Conclusions

The effect of the addition of CNCs on the properties of cement composites has been studied in this work. Encouragingly, we find that this addition can improve the properties of cement pastes significantly under the curing conditions defined when a rapid decrease in temperature and humidity occurs.

The pore distributions of cement pastes show that the addition of CNCs improves the microstructure of cement paste; the pore structure refinement in the cement matrix has happened. The nitrogen adsorption results show that almost no hydration products, including C-S-H gel, are formed in cement pastes without any addition of CNCs under extreme conditions. A rapid decrease in temperature and humidity leads to a difficulty in the formation of CSH.

The addition of CNCs has an excellent effect in promoting the hydration of cement and preventing cement pastes from cracking under extreme conditions. CNCs have potential application prospects in concrete construction under lower temperature but not in an environment that promotes freezing.

Data Availability

The data in our manuscript is available. The data used to support the findings of this study are included within the supplementary information file.

Conflicts of Interest

We declare that we do not have any commercial or associative interest that represents a conflict of interest in connection with the work submitted.

Acknowledgments

This work was supported by the National Natural Science Foundation of China (grant number 51608311); the Program for Changjiang Scholars and Innovative Research Team from the University of China (grant number IRT_17R69); and a Jiangsu Key Laboratory of Construction Materials Open Fund (grant number CM2016-07). We thank Editage (http://www.editage.cn) for its linguistic assistance during the preparation of this manuscript.

Supplementary Materials

The original figures are in the file of "Tiff". The original data of Fig.2, Fig.9 a, Fig.9 b and Fig.10 is in the file of "opj". The original nitrogen adsorption data of sample C1, C2, C3 and C4 are in the file of "nitrogen adsorption. *(Supplementary Materials)*

References

[1] L. Wang, J. Bao, L. Wang, F. Zhang, and Y. Li, "One-pot synthesis and bioapplication of amine-functionalized magnetite nanoparticles and hollow nanospheres," *Chemistry – A European Journal*, vol. 12, no. 24, pp. 6341–6347, 2006.

[2] K. Zhou, X. Wang, X. Sun, Q. Peng, and Y. Li, "Enhanced catalytic activity of ceria nanorods from well-defined reactive crystal planes," *Journal of Catalysis*, vol. 229, no. 1, pp. 206–212, 2005.

[3] S. Hu and X. Wang, "Ultrathin nanostructures: smaller size with new phenomena," *Chemical Society Review*, vol. 42, no. 12, pp. 5577–5594, 2013.

[4] Y. Long, J. Hui, P. Wang et al., "Hydrogen bond nanoscale networks showing switchable transport performance," *Scientific Reports*, vol. 2, pp. 612–617, 2012.

[5] L. Luo, P. Wang, D. Jing, and X. Wang, "Self-assembly of TiO_2 nanoparticles into chains, films and honeycomb networks," *CrystEngComm*, vol. 16, no. 8, pp. 1584–1591, 2014.

[6] F. Saleem, Z. Zhang, B. Xu, X. Xu, P. He, and X. Wang, "Ultrathin Pt–Cu nanosheets and nanocones," *Journal of the American Chemical Society*, vol. 135, no. 49, pp. 18304–18307, 2013.

[7] P. Wang, H. Sun, Y. Ji, W. Li, and X. Wang, "Three-dimensional assembly of single-layered MoS_2," *Advanced Materials*, vol. 26, no. 6, pp. 964–969, 2014.

[8] B. Xu, P. He, H. Liu, P. Wang, G. Zhou, and X. Wang, "A 1D/2D helical $CdS/ZnIn_2S_4$ nano-heterostructure," *Angewandte Chemie International Edition*, vol. 53, no. 9, pp. 2339–2343, 2014.

[9] K. Wang, Z. Zhang, X. Wang, and Y. Li, "Inorganic nanocrystals: from molecular design to systematic engineering," *Particuology*, vol. 17, pp. 1–10, 2014.

[10] P. N. Balaguru and S. P. Shah, *Fiber-Reinforced Cement Composites*, McGraw-Hill, New York, NY, USA, 1992.

[11] R. J. Moon, A. Martini, J. Nairn, J. Simonsen, and J. Youngblood, "Cellulose nanomaterials review: structure, properties and nanocomposites," *Chemical Society Reviews*, vol. 40, no. 7, pp. 3941–3994, 2011.

[12] J. E. Goodsell, R. J. Moon, A. Huizar, and R. B. Pipes, "A strategy for prediction of the elastic properties of epoxy-cellulose nanocrystal-reinforced fiber networks," *Nordic Pulp & Paper Research Journal*, vol. 29, no. 1, pp. 85–94, 2014.

[13] Y. Habibi and A. Dufresne, "Highly filled bionanocomposites from functionalized polysaccharide nanocrystals," *Biomacromolecules*, vol. 9, no. 7, pp. 1974–1980, 2008.

[14] Y. Habibi, L. A. Lucia, and O. J. Rojas, "Cellulose nanocrystals: chemistry, self-assembly, and applications," *Chemical Reviews*, vol. 110, no. 6, pp. 3479–3500, 2010.

[15] Y. Cao, P. D. Zavaterri, J. Youngblood, R. J. Moon, and J. Weiss, "The influence of cellulose nanocrystal additions on the performance of cement paste," *Cement and Concrete Composites*, vol. 56, pp. 73–83, 2015.

[16] Y. Cao, P. Zavattieri, J. Youngblood, R. Moon, and J. Weiss, "The relationship between cellulose nanocrystal dispersion and strength," *Construction and Building Materials*, vol. 119, pp. 71–79, 2016.

[17] H. M. Jennings, "A model for the microstructure of calcium silicate hydrate in cement paste," *Cement and Concrete Research*, vol. 30, pp. 101–116, 2000.

[18] H. M. Jennings, "Refinements to colloid model of C-S-H in cement: CM-II," *Cement and Concrete Research*, vol. 38, pp. 275–289, 2008.

[19] H. Roper, "Dimensional change and water sorption studies of cement paste," in *Symposium on structure of Portland cement paste and concrete*, pp. 74–83, Highway Research Board Special Report, Washington, DC, USA, 1966.

[20] M. Babaee and A. Castel, "Water vapor sorption isotherms, pore structure, and moisture transport characteristics of alkali-activated and Portland cement-based binders," *Cement and Concrete Research*, vol. 113, pp. 99–120, 2018.

[21] A. Valori, P. J. McDonald, and K. L. Scrivener, "The morphology of C–S–H: lessons from 1 H nuclear magnetic resonance relaxometry," *Cement and Concrete Research*, vol. 49, pp. 65–81, 2013.

[22] A. C. A. Muller, K. L. Scrivener, A. M. Gajewicz, and P. J. McDonald, "Use of bench-top NMR to measure the density, composition and desorption isotherm of C-S-H in cement paste," *Microporous and Mesoporous Materials*, vol. 178, pp. 99–103, 2013.

[23] A. C. A. Muller, K. L. Scrivener, A. M. Gajewicz, and P. J. McDonald, "Densification of C–S–H measured by ^{1}H NMR relaxometry," *The Journal of Physical Chemistry C*, vol. 117, pp. 403–412, 2013.

Hindawi
Journal of Nanomaterials
Volume 2019, Article ID 4867909, 7 pages
https://doi.org/10.1155/2019/4867909

Research Article

Facile Hydrothermal Synthesis of Two-Dimensional Porous ZnO Nanosheets for Highly Sensitive Ethanol Sensor

Lai Van Duy,[1] Nguyen Hong Hanh,[1] Dang Ngoc Son,[1] Pham Tien Hung,[2] Chu Manh Hung,[1] Nguyen Van Duy,[1] Nguyen Duc Hoa,[1] and Nguyen Van Hieu[3,4]

[1]*International Training Institute for Materials Science (ITIMS), Hanoi University of Science and Technology (HUST), No. 1 Dai Co Viet, Hai Ba Trung, Hanoi, Vietnam*
[2]*Physics Faculty, Le Quy Don Technical University, No. 236 Hoang Quoc Viet street, Cau Giay District, Hanoi, Vietnam*
[3]*Faculty of Electrical and Electronic Engineering, Phenikaa Institute for Advanced Study (PIAS), Phenikaa University, Yen Nghia, Ha-Dong District, Hanoi 10000, Vietnam*
[4]*Phenikaa Research and Technology Institute (PRATI), A&A Green Phoenix Group, 167 Hoang Ngan, Hanoi 10000, Vietnam*

Correspondence should be addressed to Chu Manh Hung; mhchu@itims.edu.vn and Nguyen Duc Hoa; ndhoa@itims.edu.vn

Received 19 July 2019; Accepted 28 September 2019; Published 11 November 2019

Guest Editor: Fei Ke

Two-dimensional porous ZnO nanosheets were synthesized by a facile hydrothermal method for ethanol gas-sensing application. The morphology, composition, and structure of the synthesized materials were characterized by scanning electron microscopy, energy-dispersive X-ray spectroscopy, powder X-ray diffraction, and high-resolution transmission electron microcopy. Results showed that the synthesized ZnO materials were porous nanosheets with a smooth surface and a thickness of 100 nm and a large pore size of approximately 80 nm. The as-prepared nanosheets, which had high purity, high crystallinity, and good dispersion, were used to fabricate a gas sensor for ethanol gas detection at different operating temperatures. The porous ZnO nanosheet gas sensor exhibited a high response value of 21 toward 500 ppm ethanol at a working temperature of 400°C with a reversible and fast response to ethanol gas (12 s/231 s), indicating its potential application. We also discussed the plausible sensing mechanism of the porous ZnO nanosheets on the basis of the adopted ethanol sensor.

1. Introduction

Semiconductor metal oxide materials are drawing considerable attention for the development of sensors toward applications in numerous fields, such as air quality control, environmental monitor, and public safety from hazardous gases (e.g, NO_x, SO_x, CO_x, and H_2S) [1–6]. Substantial effort has also been devoted to the fabrication of metal oxide-based gas sensors for volatile organic compound (VOC) monitoring, such as benzene, toluene, acetone, methanol, and ethanol [7–11]. Studies have been attempting to adjust the properties of these gas-sensitive nanomaterials and to form new multifunctional nanostructures. Such nanostructures and/or quantum dots exhibit many attractive features, such as high chemical and thermal stability, large surface area, adjustable electronic state, quantum confinement, high electron mobility, and excellent catalytic properties [11, 12]. Different types of metal oxide nanostructures such as tin oxide (SnO_2), indium oxide (In_2O_3), zinc oxide (ZnO), tungsten trioxide (WO_3), cobalt oxide (Co_3O_4), nickel oxide (NiO), and titanium oxide (TiO_2) have been discovered for gas-sensing applications [4, 10, 13–17]. ZnO is a potential sensing material because of its outstanding properties; it is an environmentally friendly n-type semiconductor that has a direct and wide band gap of 3.37 eV, interenergy large exciton at room temperature (~60 meV), high thermal and chemical stability, high electronic mobility, ease of synthesis, low cost, high sensitivity to target gases, and large surface-to-volume ratio [10, 17, 18]. Extensive studies have been focused on the development of gas sensors based on ZnO nanostructures with various morphologies and composition for the detection of VOCs [19–21]. ZnO can reportedly be prepared on a large

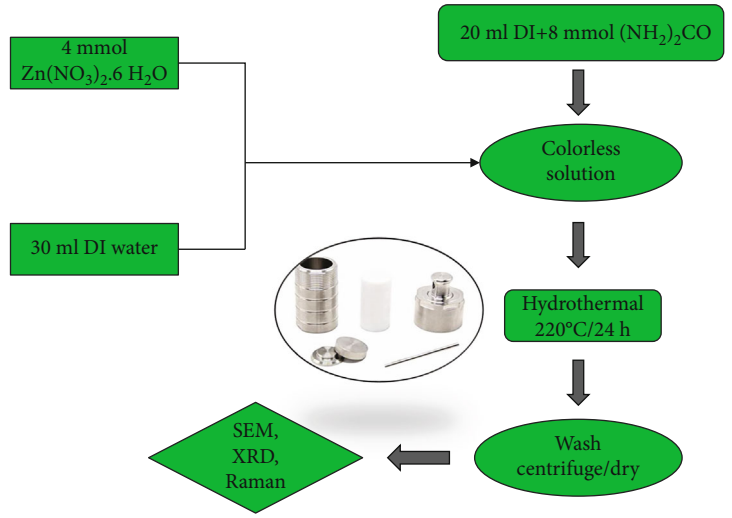

Figure 1: Hydrothermal synthesis process of porous ZnO nanosheets.

scale by using simple wet chemical glands as hydrothermal [17, 22], coprecipitation [23], sol-gel [24], electrospinning [25], thermal evaporation [26], and electrodeposition methods [27]. By utilizing the hydrothermal method, researchers can create a huge number of shapes and structures of this material [17, 22], which has a large surface-to-volume ratio, for use in different fields. However, an easy synthesis of porous ZnO nanosheets for gas sensor applications remains challenging.

In this study, we develop a simple hydrothermal method for synthesizing porous ZnO nanosheets for effective ethanol gas sensing in industry applications. Porous ZnO nanosheets possess a large specific surface area for gas adsorption because of its porous structure, thus showing superior sensitivity to ethanol.

2. Materials and Methods

Porous ZnO nanosheets were synthesized via a hydrothermal method followed by annealing at 600°C. The synthesis processes of the porous ZnO nanosheets are summarized in Figure 1, which was adapted from the literature [28, 29] with modification. In a typical synthesis, zinc nitrate hexahydrate ($Zn(NO_3)_2{\cdot}6H_2O$) (4 mmol) was dissolved in 30 mL deionized water. After this solution was stirred for 15 min, 20 mL urea (CH_4N_2O) (8 mmol) solution was added with further stirring for 15 min to adjust the pH to 5. The above turbid solution was transferred into a 100 mL Teflon-lined stainless steel autoclave for hydrothermal. The hydrothermal process was maintained at 220°C for 24 h. After being natural cooled to room temperature, the precipitate was centrifuged and washed with deionized water several times. Then, it was washed twice using an ethanol solution and collected by centrifugation at 4000 rpm. Finally, the white product was obtained and dried in an oven at 60°C for 24 h. The synthesized materials were characterized by field-emission scanning electron microscopy (SEM, JEOL 7600F), powder X-ray diffraction (XRD; Advance D8, Bruker), energy-dispersive X-ray spectroscopy (EDS), and high-resolution transmission electron microscopy (HRTEM, Tecnai G2F20S-TWIN, Philips). The synthesized porous ZnO nanosheets were then characterized sensing properties using a lab-made gas-sensing system [30].

3. Results and Discussion

Figures 2(a) and 2(b) show the SEM images of the grown material after it was calcined at 600°C for 2 h. The low-magnification SEM image (Figure 2(a)) demonstrates that the as-prepared products are composed of homogeneous nanosheets with porous structure. The high-magnification SEM image (Figure 2(b)) reveals that the synthesized nanosheets are nanosized porous architectures comprising sheet nanostructures with edge thicknesses of about 100 nm. Moreover, many small, round holes about 80 nm in diameter are evenly distributed on the surface. The large surface-to-volume ratio of nanosheets may provide large sites for gaseous-molecule adsorption, thereby enhancing the gas-sensing performance [4]. Herein, the homogenous nanosheets were obtained without using any surfactant, thus reducing the usage of chemicals. Zinc nitrate hexahydrate was used as a Zn^{2+} precursor, whereas the urea was utilized as media to control the solution pH. Urea was easily decomposed into NH_3 and HNCO during the hydrothermal process. Thus, it reacted with Zn^{2+} to form ZnO and generate the porous structure.

The crystal structure of the synthesized nanosheets was studied by XRD, and the data are shown in Figure 3(a). The main diffraction peaks are indexed to the (100), (002), (101), (102), (110), (103), (200), (112), (201), and (202) lattice planes of ZnO. All the diffraction peaks correspond to wurtzite ZnO (JCPDS card No. 36-1451) without other observable impurity characteristic peaks; therefore, high-purity ZnO can be obtained using the solvothermal method combined with calcination [10, 17]. The EDS analysis indicates the presence of Zn and O elements from the nanosheets

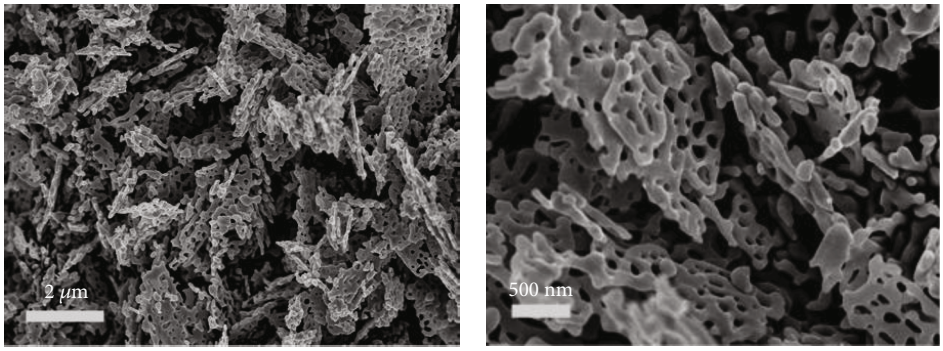

(a) (b)

Figure 2: (a) Low- and (b) high-magnification SEM images of synthesized porous ZnO nanosheets.

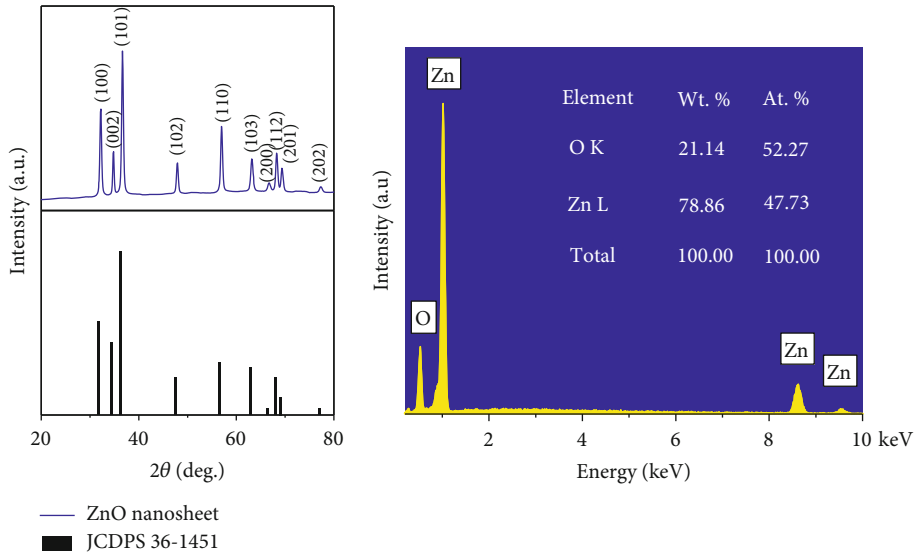

(a) (b)

Figure 3: (a) XRD pattern and (b) EDS spectrum of the synthesized ZnO nanosheets annealed at 600°C for 2 h in air.

(Figure 3(b)). The synthesized nanosheets have no impurity and are thus of high quality. The O and Zn compositions estimated from the EDX analysis are 52.27 at.% and 47.74 at.%, respectively. This composition is approximately the stoichiometry ZnO [9].

The atomic structure of the porous ZnO nanosheets was investigated by HRTEM images and the selected area electron diffraction (SAED) patterns. Figure 4(a) shows a representative low magnification TEM image of the ZnO nanosheets taken on the red square region of the inset. It exhibits a smooth surface and the porous structure of the synthesized nanosheets, which confirm the results obtained from the SEM images. Figure 4(b) reveals a representative high magnification TEM image captured on the yellow square area of Figure 4(a). The image shows a well-defined lattice fringe separation with a lattice spacing of 0.52 nm, indicating a periodic ZnO lattice growth along the (001) plane. The inset of Figure 4(b) shows the corresponding SAED pattern obtained from the lattice fringes of the ZnO nanosheets, confirming that the synthesized ZnO has the single crystalline wurtzite structure growing along the [0001] direction [31].

The transient resistance versus time upon exposure to different concentrations of C_2H_5OH measured at temperatures ranging from 250°C to 400°C is shown in Figures 5(a)–5(d). Clearly, the sensor response value initially increases and then decreases with increased operating temperature. The maximum response for ethanol is 21 at the optimum operating temperature of 400°C. The sensor response S (R_a/R_g), as a function of C_2H_5OH concentrations measured at different temperatures, is shown in Figure 5(b).

At all measured temperatures, the sensor response increases with increased C_2H_5OH concentration in the measured range. At a given concentration, the sensor response increases with increased working temperature. However, increasing the working temperature requires a

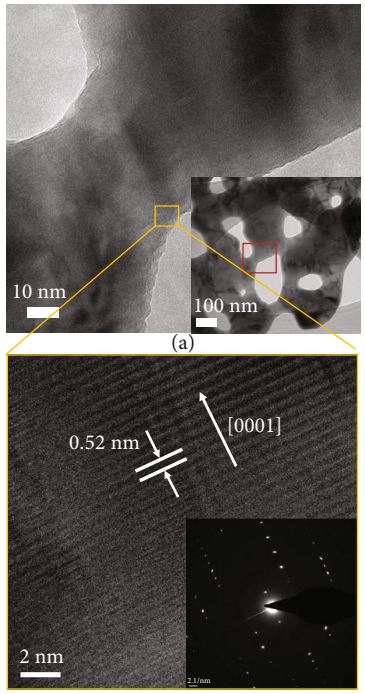

Figure 4: (a) Low and (b) high magnification TEM images of the porous ZnO nanosheet. Inset of (b) shows SAED pattern.

considerable amount of energy, which can damage microheaters. For practical applications, the power consumption of the device should be limited; thus, the sensor response at temperatures higher than 450°C did not need to be characterized.

The gas-sensing mechanism of metal oxide is based on the adsorption and desorption of gas molecules and chemical reactions on the surface of sensing materials [10, 32]. Herein, band diagrams of nanoporous ZnO nanosheet in air and in ethanol are shown in Figure 6 to explain the gas-sensing mechanism. ZnO is a well-known n-type conductor. When the sensor is exposed to air, oxygen molecules originating from the atmosphere adsorb onto the ZnO surface and then ionize to negative oxygen species via trapping free electrons from the conduction band, as shown in Equations (1)–(3).

$$O_2(\text{gas}) \longrightarrow O_2(\text{ads}) \quad (1)$$

$$O_2(\text{ads}) + e- \longrightarrow O^{2-}(\text{ads}) \quad (2)$$

$$O^{2-}(\text{ads}) + e- \longrightarrow 2O^{-}(\text{ads}) \quad (3)$$

When reductive C_2H_5OH gas vapour approaches to the sensor, it reacts with the adsorbed oxygen species on the ZnO sheets. Consequently, the captured electrons will be released to the ZnO, ultimately decreasing the surface depletion layer and the sensor resistance. The reaction process

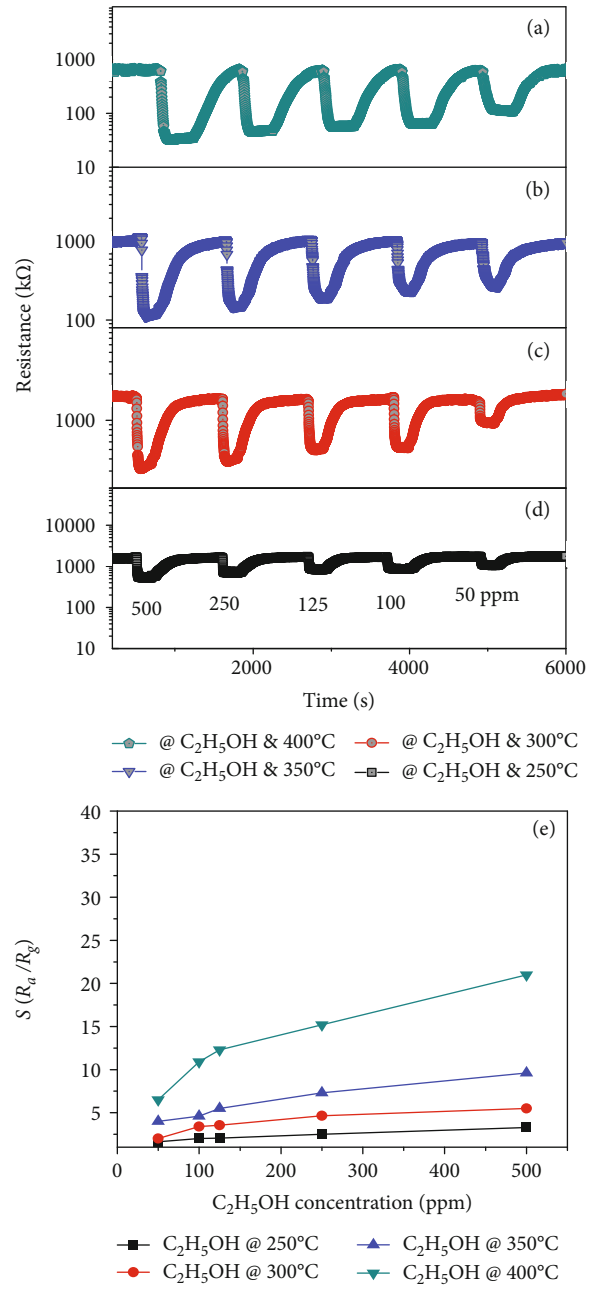

Figure 5: C_2H_5OH sensing characteristics of porous ZnO nanosheets measured at different operating temperatures: transient resistance versus time upon exposure to different C_2H_5OH concentrations at 450°C (a), 400°C (b), 350°C (c), and 250°C (d); (e) gas response as a function of C_2H_5OH concentration.

between the surface-adsorbed oxygen species and ethanol is described by Equations (4)–(6).

$$C_2H_5OH + 3O_2^{-} \longrightarrow 2CO_2 + 3H_2O + 3e^{-} \quad (4)$$

$$C_2H_5OH + 6O^{-} \longrightarrow 2CO_2 + 3H_2O + 6e^{-} \quad (5)$$

$$C_2H_5OH + 6O^{-} \longrightarrow 2CO_2 + 3H_2O + 12e^{-} \quad (6)$$

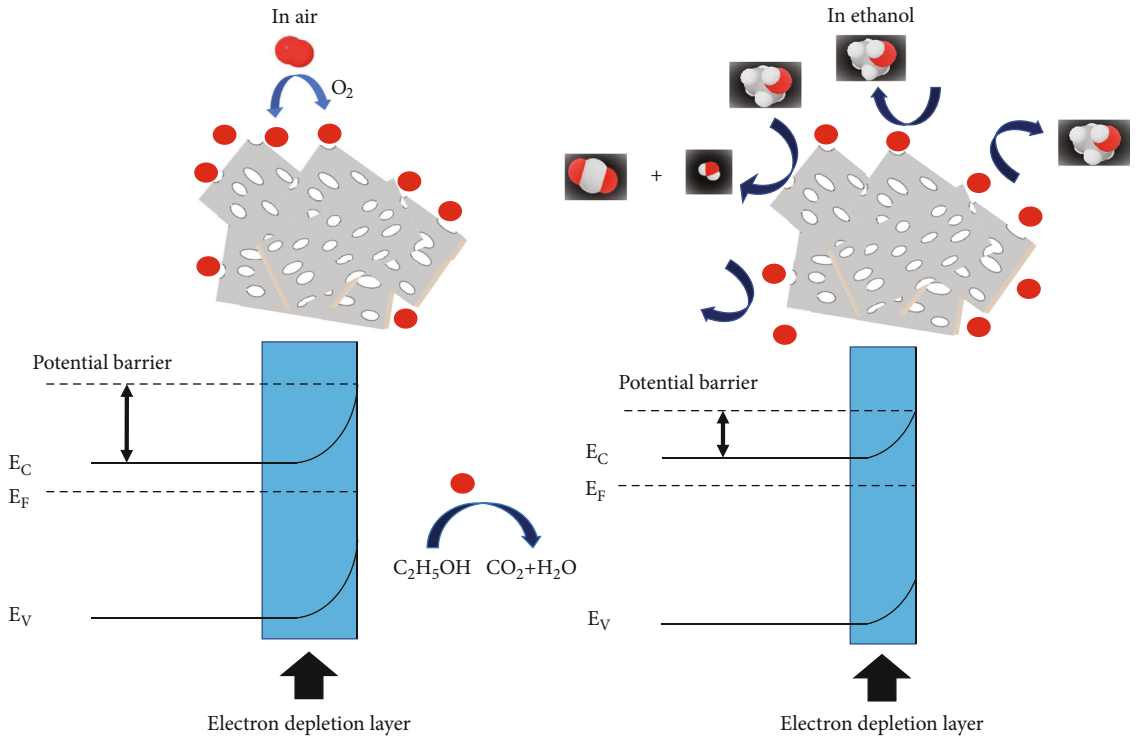

Figure 6: Schematic of the C_2H_5OH gas-sensing mechanism of the nanoporous ZnO.

Table 1: Comparison of different ZnO nanosheet-based VOC gas sensors.

Materials	Gas	C (ppm)	Response	T (°C)	Ref.
ZnO NPs	Ethanol	100	5	350	[33]
Au-ZnO NWs	Ethanol	50	7	325	[34]
ZnO NFs	Ethanol	100	6	340	[35]
ZnO NFs	Acetone	100	4	360	[35]
Sn doped ZnO NSs	Acetone	200	5.55	320	[36]
ZnO nanoplate	Chlorobenzene	100	2	400	[37]
Porous ZnO NSs	Ethanol	100	11	400	This work
Porous ZnO NSs	Ethanol	500	21	400	This work

Given the porous structure of the nanosheets, gas molecules can easily adsorb onto the total surface of the ZnO nanosheet and significantly change the depletion region, thus maximizing the sensing performance [13].

Comparative results of the fabricated sensor with those in other reports are summarized in Table 1. The porous ZnO nanosheets produced the highest response value to ethanol, followed by the Au-modified ZnO nanowires, ZnO nanofibers, and ZnO nanoparticles. The sensor also showed a higher response value for ethanol gas compared with acetone and chlorobenzene. However, the porous ZnO nanosheets operated at a relatively higher working temperature. The high working temperature and low sensitivity of the sensor limited its potential application. Therefore, the controlled synthesis of highly sensitive ethanol sensors that operate at low temperatures is mandatory for future sensor applications.

The gas selectivity of the porous ZnO nanosheet sensor was tested to various gases, namely, CH_3OH, $C_6H_5CH_3$, and NH_3, at 400°C with a gas concentration of 500 ppm, as shown in Figure 7(a). The data show that the response of the nanoporous ZnO sensor to 500 ppm C_2H_5OH is much higher than that of the sensors to other gases at the same concentration and working temperature. This finding indicates good selectivity of the porous ZnO nanosheet sensor to C_2H_5OH gas. Figure 7(b) reveals the short-term stability of the porous ZnO nanosheet sensor with 10 response/recovery cycles to 125 ppm C_2H_5OH at 400°C. The sensor can noticeably maintain its initial response amplitude with 10 continuous response/recovery cycles. These results indicate that the sensor has good selectivity, reproducibility, and short-term stability, which are important characteristics of gas sensors for practical applications.

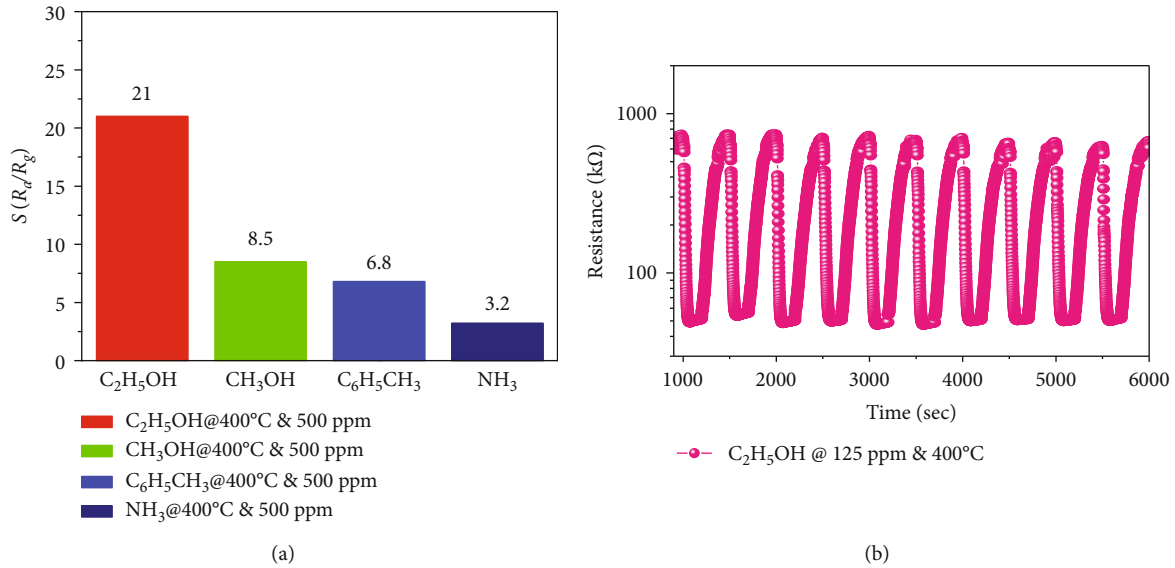

FIGURE 7: (a) Selectivity to various gases at 400°C and stability at 125 ppm C_2H_5OH gas at 400°C of the nanoporous ZnO nanosheet-based sensors.

4. Conclusions

We introduced an easy and scalable hydrothermal synthesis of nanoporous ZnO nanosheets for effective C_2H_5OH gas-sensing applications. The obtained porous nanosheets performed good crystallinity and dispersing levels. The mean thickness of the ZnO nanosheets is approximately 100 nm, and the pore size is about 80 nm. The obtained nanoporous ZnO nanosheets exhibited excellent gas-sensing properties to ethanol in terms of high and fast response and recovery times. The results show that nanoporous ZnO nanosheets can be a potential material for high-performance ethanol gas sensing.

Data Availability

The data used to support the findings of this study are included within the article.

Conflicts of Interest

The authors declare that there is no conflict of interest regarding the publication of this paper.

Acknowledgments

This research was funded by the Vietnam National Foundation for Science and Technology Development (NAFOSTED) under grant number 103.02-2017.15. We would like to thank Prof. Young-Woo Heo (Kyungpook National University) for his help with TEM measurement.

References

[1] P. Van Tong, N. D. Hoa, H. T. Nha, N. Van Duy, C. M. Hung, and N. Van Hieu, "SO_2 and H_2S sensing properties of hydrothermally synthesized CuO nanoplates," *Journal of Electronic Materials*, vol. 47, no. 12, pp. 7170–7178, 2018.

[2] C. M. Hung, D. T. T. Le, and N. Van Hieu, "On-chip growth of semiconductor metal oxide nanowires for gas sensors: a review," *Journal of Science: Advanced Materials and Devices*, vol. 2, no. 3, pp. 263–285, 2017.

[3] T. M. Ngoc, N. Van Duy, N. Duc Hoa, C. Manh Hung, H. Nguyen, and N. Van Hieu, "Effective design and fabrication of low-power-consumption self-heated SnO_2 nanowire sensors for reducing gases," *Sensors and Actuators B: Chemical*, vol. 295, pp. 144–152, 2019.

[4] N. D. Hoa, C. M. Hung, N. Van Duy, and N. Van Hieu, "Nanoporous and crystal evolution in nickel oxide nanosheets for enhanced gas- sensing performance," *Sensors and Actuators B: Chemical*, vol. 273, pp. 784–793, 2018.

[5] N. D. Hoa, N. V. Duy, S. A. el-Safty, and N. V. Hieu, "Meso-/nanoporous semiconducting metal oxides for gas sensor applications," *Journal of Nanomaterials*, vol. 2015, 14 pages, 2015.

[6] X. Li, X. Li, N. Chen et al., "CuO-In_2O_3 Core-Shell Nanowire Based Chemical Gas Sensors," *Journal of Nanomaterials*, vol. 2014, Article ID 973156, 7 pages, 2014.

[7] C. Su, L. Zhang, Y. Han et al., "Glucose-assisted synthesis of hierarchical flower-like Co_3O_4 nanostructures assembled by porous nanosheets for enhanced acetone sensing," *Sensors and Actuators B: Chemical*, vol. 288, pp. 699–706, 2019.

[8] X. Liu, K. Zhao, X. Sun, X. Duan, C. Zhang, and X. Xu, "Electrochemical sensor to environmental pollutant of acetone based on Pd- loaded on mesoporous In_2O_3 architecture," *Sensors and Actuators B: Chemical*, vol. 290, pp. 217–225, 2019.

[9] X. Wang, F. Chen, M. Yang et al., "Dispersed WO_3 nanoparticles with porous nanostructure for ultrafast toluene sensing," *Sensors and Actuators B: Chemical*, vol. 289, pp. 195–206, 2019.

[10] C. T. Quy, N. X. Thai, N. D. Hoa et al., "C_2H_5OH and NO2sensing properties of ZnO nanostructures: correlation between

crystal size, defect level and sensing performance," *RSC Advances*, vol. 8, no. 10, pp. 5629–5639, 2018.

[11] C. Su, L. Zhang, Y. Han et al., "Controllable synthesis of crescent-shaped porous NiO nanoplates for conductometric ethanol gas sensors," *Sensors and Actuators B: Chemical*, vol. 296, p. 126642, 2019.

[12] J. Zhu, F. Zhu, X. Yue et al., "Waste utilization of synthetic carbon quantum dots based on tea and peanut shell," *Journal of Nanomaterials*, vol. 2019, 7 pages, 2019.

[13] T. T. Le Dang, M. Tonezzer, and V. H. Nguyen, "Hydrothermal growth and hydrogen selective sensing of nickel oxide nanowires," *Journal of Nanomaterials*, vol. 2015, Article ID 785856, 8 pages, 2015.

[14] P. Bindra and A. Hazra, "Selective detection of organic vapors using TiO_2 nanotubes based single sensor at room temperature," *Sensors and Actuators B: Chemical*, vol. 290, pp. 684–690, 2019.

[15] D. Zhang, Y. Fan, G. Li et al., "Highly sensitive BTEX sensors based on hexagonal WO_3 nanosheets," *Sensors and Actuators B: Chemical*, vol. 293, pp. 23–30, 2019.

[16] P. Van Tong, N. D. Hoa, N. Van Duy, V. Van Quang, N. T. Lam, and N. Van Hieu, "In-situ decoration of Pd nanocrystals on crystalline mesoporous NiO nanosheets for effective hydrogen gas sensors," *International Journal of Hydrogen Energy*, vol. 38, no. 27, pp. 12090–12100, 2013.

[17] V. T. Duoc, D. T. T. Le, N. D. Hoa et al., "New design of ZnO nanorod- and nanowire-based NO_2 room-temperature sensors prepared by hydrothermal method," *Journal of Nanomaterials*, vol. 2019, Article ID 6821937, 9 pages, 2019.

[18] M. L. M. Napi, S. M. Sultan, R. Ismail, M. K. Ahmad, and G. M. T. Chai, "Optimization of a hydrothermal growth process for low resistance 1D fluorine-doped zinc oxide nanostructures," *Journal of Nanomaterials*, vol. 2019, Article ID 4574507, 10 pages, 2019.

[19] N. D. Khoang, D. D. Trung, N. Van Duy, N. D. Hoa, and N. Van Hieu, "Design of SnO_2/ZnO hierarchical nanostructures for enhanced ethanol gas-sensing performance," *Sensors and Actuators B: Chemical*, vol. 174, pp. 594–601, 2012.

[20] S.-M. Li, L.-X. Zhang, M.-Y. Zhu et al., "Acetone sensing of ZnO nanosheets synthesized using room-temperature precipitation," *Sensors and Actuators B: Chemical*, vol. 249, pp. 611–623, 2017.

[21] S. Agarwal, P. Rai, E. N. Gatell et al., "Gas sensing properties of ZnO nanostructures (flowers/rods) synthesized by hydrothermal method," *Sensors and Actuators B: Chemical*, vol. 292, pp. 24–31, 2019.

[22] G. Amin, M. H. Asif, A. Zainelabdin, S. Zaman, O. Nur, and M. Willander, "Influence of pH, precursor concentration, growth time, and temperature on the morphology of ZnO nanostructures grown by the hydrothermal method," *Journal of Nanomaterials*, vol. 2011, Article ID 269692, 9 pages, 2011.

[23] M. El-Hilo, A. A. Dakhel, and Z. J. Yacoob, "Magnetic interactions in Co^{2+} doped ZnO synthesised by co-precipitation method: efficient effect of hydrogenation on the long-range ferromagnetic order," *Journal of Magnetism and Magnetic Materials*, vol. 482, pp. 125–134, 2019.

[24] Y. Zeng, L. Qiao, Y. Bing et al., "Development of microstructure CO sensor based on hierarchically porous ZnO nanosheet thin films," *Sensors and Actuators B: Chemical*, vol. 173, pp. 897–902, 2012.

[25] J.-H. Kim, A. Mirzaei, H. W. Kim, P. Wu, and S. S. Kim, "Design of supersensitive and selective ZnO-nanofiber-based sensors for H_2 gas sensing by electron-beam irradiation," *Sensors and Actuators B: Chemical*, vol. 293, pp. 210–223, 2019.

[26] C. M. Hung, H. V. Phuong, N. Van Duy, N. D. Hoa, and N. Van Hieu, "Comparative effects of synthesis parameters on the NO_2 gas-sensing performance of on-chip grown ZnO and Zn_2SnO_4 nanowire sensors," *Journal of Alloys and Compounds*, vol. 765, pp. 1237–1242, 2018.

[27] C. Wang, Z.-G. Wang, R. Xi et al., "In situ synthesis of flower-like ZnO on GaN using electrodeposition and its application as ethanol gas sensor at room temperature," *Sensors and Actuators B: Chemical*, vol. 292, pp. 270–276, 2019.

[28] Z. Feng, Y. Ma, V. Natarajan, Q. Zhao, X. Ma, and J. Zhan, "In-situ generation of highly dispersed Au nanoparticles on porous ZnO nanoplates via ion exchange from hydrozincite for VOCs gas sensing," *Sensors and Actuators B: Chemical*, vol. 255, pp. 884–890, 2018.

[29] Y. Xiao, L. Lu, A. Zhang et al., "Highly enhanced acetone sensing performances of porous and single crystalline ZnO nanosheets: high percentage of exposed (100) facets working together with surface modification with Pd nanoparticles," *ACS Applied Materials & Interfaces*, vol. 4, no. 8, pp. 3797–3804, 2012.

[30] K. Nguyen, C. M. Hung, T. M. Ngoc et al., "Low-temperature prototype hydrogen sensors using Pd-decorated SnO_2 nanowires for exhaled breath applications," *Sensors and Actuators B: Chemical*, vol. 253, pp. 156–163, 2017.

[31] W. L. Ong, H. Huang, J. Xiao, K. Zeng, and G. W. Ho, "Tuning of multifunctional cu-doped ZnO films and nanowires for enhanced piezo/ferroelectric-like and gas/photoresponse properties," *Nanoscale*, vol. 6, no. 3, pp. 1680–1690, 2014.

[32] X. Xing, Y. Yang, Z. Yan et al., "CdO-Ag-ZnO nanocomposites with hierarchically porous structure for effective VOCs gas-sensing properties," *Ceramics International*, vol. 45, no. 4, pp. 4322–4334, 2019.

[33] L. Zhu, Y. Li, and W. Zeng, "Hydrothermal synthesis of hierarchical flower-like ZnO nanostructure and its enhanced ethanol gas-sensing properties," *Applied Surface Science*, vol. 427, pp. 281–287, 2018.

[34] N. S. Ramgir, M. Kaur, P. K. Sharma et al., "Ethanol sensing properties of pure and Au modified ZnO nanowires," *Sensors and Actuators B: Chemical*, vol. 187, pp. 313–318, 2013.

[35] L. Liu, S. Li, J. Zhuang et al., "Improved selective acetone sensing properties of Co-doped ZnO nanofibers by electrospinning," *Sensors and Actuators B: Chemical*, vol. 155, no. 2, pp. 782–788, 2011.

[36] Y. Al-Hadeethi, A. Umar, S. H. Al-Heniti et al., "2D Sn-doped ZnO ultrathin nanosheet networks for enhanced acetone gas sensing application," *Ceramics International*, vol. 43, no. 2, pp. 2418–2423, 2017.

[37] Z. Jing and J. Zhan, "Fabrication and Gas-Sensing Properties of Porous ZnO Nanoplates," *Advanced Materials*, vol. 20, no. 23, pp. 4547–4551, 2008.

Hindawi
Journal of Nanomaterials
Volume 2019, Article ID 2483060, 7 pages
https://doi.org/10.1155/2019/2483060

Research Article

Reactions of Microorganisms with Atomic Oxygen Radical Anions: Damage of Cells and Irreversible Inactivation

Longchun Li,[1] **Fan Wu**,[1] **Yu Chen**,[1] **Lei Xu**,[1] **Xiaochang Hao**,[1] **Yonghuan Chen**,[1] **Yixiang Sun**,[2] **and Guoyin Xiong**[3]

[1]*Department of Applied Chemistry, School of Science, Anhui Agricultural of University, Hefei, Anhui 230023, China*
[2]*Soil and Fertilizer Institute of Anhui Academy of Agricultural Science, Hefei, Anhui 230001, China*
[3]*Anhui JUKAI Agrochemical Co., LTD., Hefei, Anhui 230088, China*

Correspondence should be addressed to Longchun Li; llch75@163.com and Yixiang Sun; sunyixiang@126.com

Received 18 July 2019; Accepted 28 August 2019; Published 3 November 2019

Guest Editor: Yunpan Ying

Reactive oxygen species play important effects on organisms not only *in vivo* but also *in vitro*. The atomic oxygen radical anion (O^-) has shown extremely high oxidation and reactivity towards small molecules of hydrocarbons. However, the O^- effects on cells of microorganisms are scarcely investigated. This work showed the evidence that O^- could react quickly with microorganisms (*Escherichia coli*, *Bacillus subtilis*, *Staphylococcus aureus*, *Aspergillus niger*, *Saccharomyces cerevisiae*, and *Actinomycetes* (*5046*)) and damaged the cell walls seriously as well as their intrinsic structures, arising a fast and irreversible inactivation. SEM and TEM micrographs were used to reveal the structure changes of cells before and after reacting with O^- radicals. The inactivation efficiencies of the microorganisms depended on the O^- intensity, the initial population of microorganisms, the exposed area, the environment, and the microorganisms' types. Over 99% reduction of an initial 1.0×10^7 colony-forming unit (cfu), *E. coli* population only required less than 2 minutes while exposed to a 0.23 $\mu A/cm^2$ O^- flux under dry argon atmosphere (30°C, 1 atm). The observation of anionic intermediates (CO^-, CO^{2-}, H_2O^-, and anionic hydrocarbons) by time-of-flight (TOF) mass spectrometry and the neutral volatile products (CO, CO_2, and H_2O) by quadrupole mass spectrometry (Q-MS) provided an evidence of the reactions of O^- with hydrocarbon bonds of the microorganisms. The inactivation mechanism of microorganisms induced by O^- was discussed.

1. Introduction

Reactive oxygen species (ROS), such as the superoxide anion radical (O_2^-), the hydroxyl radical (OH), and the singlet oxygen ($^1O_2$), are key chemical species in the biochemical processes and exert a very important effect on organisms [1–6]. Organisms can suffer lipid peroxidation, protein denaturation, DNA injuries, and enzyme inactivation by ROS [7–13]. Due to high reactivity of ROS, all the cellar components, lipids, proteins, nucleic acids, and carbohydrates may be damaged by their reactions with ROS, giving rise to metabolic and cellular disturbances or cell death [14–17]. There are increasing evidences showing that ROS are responsible for many diseases such as inflammation, lung injury, ischaemia-reperfusion injury, cancer, and aging [18–20]. On the other hand, ROS are not always harmful to organisms. For instance, ROS may be used as the intracellular signaling species for the introduction of defense gene expression and destroying malignant cells or tissue [21, 22].

Atomic oxygen radical anion (O^-) is a monovalent anion (or monovalent negative ion) through the attachment of an electron to atomic oxygen (O). At the same time, O^- is also considered as a radical because it has an unpaired electron in its outermost orbit. It was found that atomic O^- had extremely high oxidation and reactivity towards the hydrocarbons' small molecules [23–26]. Moreover, O^- may be one of the most reactive oxygen species and therefore has various potential applications, such as a one-step synthesis of phenol from benzene [27], the reduction of NO [28], and the dissociation and oxidation of bio-oil [29, 30]. Previously, our work showed that the O^- could quickly react with the *B. subtilis* cells and seriously damage the cell walls as well as

their other contents, leading to a fast and irreversible inactivation [31].

Herein, we investigated the O^- effects on the microorganisms' inactivation (including the *B. subtilis* cells), the changes of cell structures caused by O^-, and the products formed by the reaction of the microorganisms with O^-. Our results demonstrate that O^- can quickly react with the microorganisms, including Gram-positive bacteria (*B. subtilis*, *S. aureus*), Gram-negative bacteria (*E. coli*, *B. A. niger*), and fungi (*S. cerevisiae*, *Actinomycetes* (*5046*)), and seriously damage the cell walls and their intrinsic structures, leading to a fast and irreversible inactivation. The observed intermediates and volatile products provided an important evidence of the reactions of O^- with hydrocarbon bonds of the microorganisms.

2. Experimental Section

2.1. O^- Source. A sustainable and high-purity O^- source was developed by using the microporous crystal $[Ca_{24}Al_{28}O_{64}]^{4+}\cdot 4O^-$ as an O^- emitter [32, 33]. We prepared the $[Ca_{24}Al_{28}O_{64}]^{4+}\cdot 4O^-$ crystal (C12A7-O^-) by the solid-state reaction of $CaCO_3$ and γ-Al_2O_3 (molar ratio of $CaCO_3 : \gamma - Al_2O_3 = 12 : 7$) under dry oxygen atmosphere. The powder mixtures were pressed to a pellet and sintered at 1350°C for 18 hours under flowing dried oxygen. The sintered product was cooled to 430°C slowly at a rate of ~10°C/min and then quickly quenched to room temperature. Recently, a special characteristic of C12A7-O^-, emitting high intensity and purity O^-, has been identified by our previous work [32, 33]. The emitted species from the C12A7-O^- surface were about 90% O^- and weak electron (<10%). A reflective field was used to reflect the electrons. We controlled the beam intensity of O^- (0.01-2.0 $\mu A/cm^2$) by changing the temperature of the C12A7-O^- sample and the ion extraction field.

2.2. Microorganisms' Preparation. The microorganisms investigated in our experiments were Gram-positive bacteria (*B. subtilis*, *S. aureus*), Gram-negative bacteria (*E. coli*, *B. A. niger*), and fungi (*S. cerevisiae*, *Actinomycetes* (*5046*)) which were purchased from China General Microbiological Culture Collection Center and maintained on nutrient agar slants at 5-6°C. Before the inactivation experiments, microorganisms were harvested by centrifuging (4000 rpm, 4°C) for 10 min and the microorganisms' pellets were washed three times with sterile water. After pouring upper water, *E. coli*, *B. subtilis*, *S. aureus*, *S. cerevisiae*, and *Actinomycetes* (*5046*) were inoculated to L-broth (Bacto peptone 10 g/L, Bacto yeast extract 10 g/L, NaCl 5 g/L, pH = 7.2) and then incubated at 37°C on a shaking tray for 12 hours. *A. niger* was cultured in potato dextrose broth (200 g peeled potato with a size of ~$4.0 \times 2.0 \times 2.0$ cm^3 were cooked in 1000 mL boiling distilled water for 8 min. After passing through four lay cheesecloths, the broth was collected and 20 g of dextrose was added.) and incubated at 27°C on a shaking tray for 12 hours. The density of microorganisms was controlled at 10^7~10^8 cfu/mL. Then, we transferred 0.1 mL resulted microorganisms to glass slide (20 mm × 20 mm) for exposure to O^- flux under the dry argon environment (1 atm). All petri dishes and glass microscopy slides used for holding the microorganisms were first autoclaved at 125°C for 1 h. The numbers of colonies on the slides before and after O^- exposure were determined by the spread plate method with nutrient agar grown at 37°C for 12 h.

E. coli spheroplasts were prepared by treating the intact *E.coli* cell suspension with 0.03 M Tris-HCl buffer (pH = 8.1) containing 20% sucrose with lysozyme (1 mg/mL) and EDTA (ethylenediaminetetraacetate, 0.1 M pH = 7.0) at 30°C for 60 min [34]. The treated cells were separated by centrifugation and resuspended in 0.2 M phosphate buffer (pH = 6.6) containing 0.2% $MgCl_2$ to form *E. coli* spheroplasts.

2.3. Inactivation Experiments. The experimental arrangement for measuring the inactivation efficiency and the reactions of microorganisms with O^- was made up of three major parts: an O^- radical source, a reaction chamber, and a product analysis system. The inactivation experiments were carried out in a cylindrical quartz reactor with a length of 60 cm and an inner diameter of 15 cm. The microorganism samples prepared were maintained by Petri dishes or slides, which were supported by a copper dish. The inactivation experiments can be performed under different environmental conditions by flowing different gases (such as Ar, He, N_2, H_2O, and O_2). In order to study the atomic oxygen radical anion effects, all inactivation measurements were carried out in the dry argon environment. The reaction temperature was varied by cooling or heating copper dish with a water-cycled system. The O^- flux emitted from the C12A7-O^- sample was irradiated onto the microorganisms. The absolute O^- ion flux was measured by a picoammeter and corrected by a TOF mass spectrometer. The numbers of colonies on the slides before and after O^- exposure were determined by the spread plate method with nutrient agar grown at 37°C for 12 h.

2.4. Reaction Product Analysis. For online analysis of reaction products, a time-of-flight (TOF) mass spectrometry and a quadrupole mass (Q-MS) spectrometry were connected to the reactor. A time-of-flight (TOF) mass spectrometer was used for measuring the anionic intermediates formed by the reactions of microorganisms with O^-. The neutral products were detected by a quadrupole mass (Q-MS) spectrometry.

2.5. SEM and TEM Measurements. SEM (scanning electron microscopy) and TEM (transmission electron microscopy) experiments were performed to study the structural changes of cells before and after exposure to O^-. The preparation of test samples was similar to the inactivation experiments mentioned above. After exposure to O^-, the suspensions of *E. coli* were fixed with an equal volume of 3% glutaraldehyde buffered at pH = 7.2 with phosphate for about 1 h. Then, the samples were centrifuged, and the resulting bacterial pellets were exposed overnight to additional phosphate-buffered 3% glutaraldehyde solution. The glutaraldehyde-fixed bacteria were embedded in 1% agar and washed with phosphate buffer. After that, the samples were fixed in buffered 1% osmium tetroxide in cacodylate buffer for 1 h at room temperature and then dehydrated by successive soakings in 50, 70, 90, and 100% ethanol. The dried samples were rinsed

twice with propylene oxide and infiltrated with propylene oxide-epoxy resin mixtures until the samples were in pure epoxy resin. Finally, the samples were placed in polyethylene capsules and resin polymerized at 60°C overnight [35]. Thin sections were cut using an ultracrotome and were mounted on 200 mesh copper grids and stained with uranyl acetate and lead citrate. The sections were examined with X-650 SEM (HITACHI) operating at 30 kV and H-800 TEM (HITACHI) operating at 100 kV.

3. Results and Discussion

3.1. Destruction of Cell Structures Caused by O^-. SEM and TEM micrographs were used to disclose any changes in the cell structures (the wall, the membrane, or the nucleoid) of the microorganisms induced by O^-. Figures 1(a) and 1(b) present the SEM photographs for *E. coli* cells before (Figure 1(a)) and after the O^- exposure (Figure 1(b)). The irradiated cells appeared dramatically swollen and collapsed with a large amount of fragments, which were associated with the damages to the cell walls and subsequent lysis due to the O^- irradiation. Figures 1(c) and 1(d) show the representative TEM micrographs of the initial (Figure 1(c)) and the O^--irradiated (Figure 1(d)) *E. coli* cells, respectively. The lighter part of the cell was the nuclear region containing some DNA fibrils and electron-dense ribosomes. The nucleoids after the exposure had contracted and a coarse precipitation of DNA appeared (Figure 1(d)), which indicated that O^- might be able to penetrate the cells, and reacted with proteins or numerous enzymes involved in the control of DNA conformation in the nucleoids, resulting in the precipitation of DNA. Some of the cells appeared to be disrupted, and fragments of lysed cells were observed. The TEM results reveal that the secondary structure of the DNA-binding proteins of the cells was destroyed by the exposure to O^-. These results are in good agreement with our earlier research [31].

3.2. O^- Effects on the Microorganisms' Inactivation. The correlation between the inactivation efficiency of the microorganisms and the O^- intensity was also demonstrated by measuring the survival curves under different O^- intensity. Figure 2(a) displays a series of survival diagrams under different O^- intensity for *E. coli* intact cells, which exhibits biphasic curves (fast and slow processes). The decay of the survival numbers of *E. coli* cells, both in the fast and slow phases, depends on the O^- intensity. On the other hand, the survival curves of *E. coli* spheroplasts in the fast processes are much different from those of *E. coli* intact cells (Figure 2(b)). The survival numbers of *E. coli* spheroplasts quickly decreased to the slow phases within 1 min while *E. coli* intact cells require about 5 min at the same condition. This result indicates that O^- destroy cell walls firstly, which agree with the result by the SEM measurements.

For the biphasic inactivation processes, we deduce that during the first phase; the O^- radicals react with the cell walls and form the volatile small molecules (such as CO, CO_2, and H_2O), resulting in quickly irreversible damage and lysis of the cells in the top layer (Figure 1(b)). As the microorganisms are killed in the first phase, the inactivated cells may stack and form an isolated layer. The occurrence of slow processes may be attributed to protection resulting from the contents of dead cells, which shielded the remaining survivors or aggregation during the treatment. The second phase, therefore, would mainly reflect the time required for sufficient erosion by reacting with the debris on the top layer.

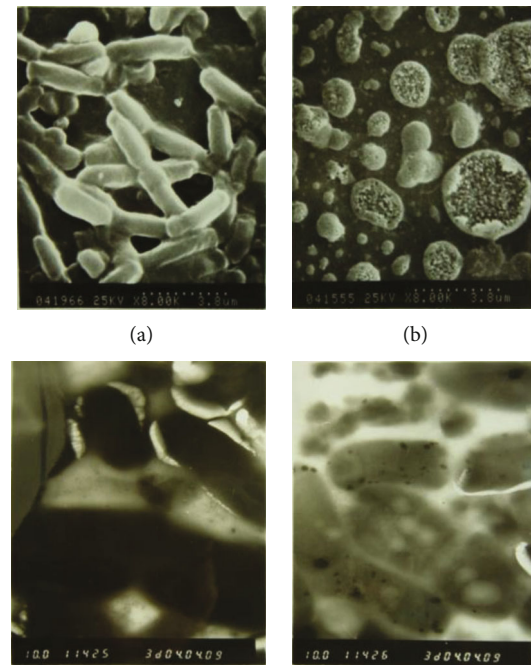

(a) (b) (c) (d)

Figure 1: (a) SEM image of the initial *E. coli* cells (image size: $13.7 \times 11.4\ cm^2$, initial number: $N_0 = 1.0 \times 10^8$ cfu/mL). (b) SEM image of the exposed *E. coli* cells (O^- flux intensity: $192\ nA/cm^2$, exposure time: 10 min, and reaction temperature: 30°C). (c) TEM image of the initial *E. coli* cells (image size: $7.4 \times 5.1\ cm^2$, $N_0 = 5 \times 10^7$ cfu/mL). (d) TEM image of the exposed *E. coli* cells (O^- flux intensity: $135\ nA/cm^2$, exposure time: 10 min, and reaction temperature: 30°C).

O^- effects on the other microorganisms' inactivation were also observed. As shown in Figure 3, the O^--induced inactivation efficiencies for *B. subtilis*, *S. aureus*, *A. niger*, *S. cerevisiae*, and *Actinomycetes (5046)* were also investigated. We found *Actinomycetes* (*5046*) were most resistant to the O^- interaction, because *Actinomycetes* (*5046*) are terrestrial prokaryotes that grow mainly in mycelia and reproduce by spore. On the other hand, fungi (*A. niger*, *S. cerevisiae)* were easiest to inactivate in the same O^- intensity. It appears that Gram-negative bacteria (*E. coli*) are more sensitive to O^- than Gram-positive bacteria (*B. subtilis*, *S. aureus*). Thus, the inactivation efficiencies depend on the microorganisms' types, because the microorganisms with different components may have different resistant ability to O^-.

Moreover, the inactivation efficiencies also depend on the reaction temperature and the exposure area. Figure 4 presents the survival curves of *E. coli* at different reaction temperature (29°C, 34°C, and 42°C). With elevatory reaction temperature, the inactivation efficiency of *E. coli* increases, which indicate that the inactivation process of *E. coli* by O^-

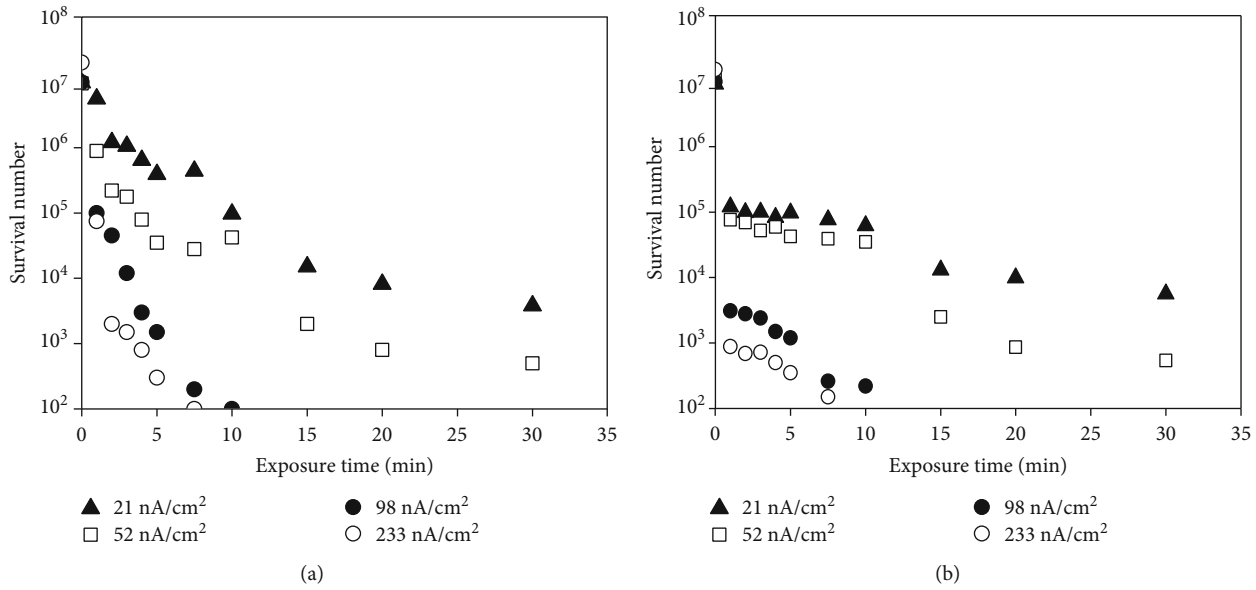

Figure 2: (a) Survival curves of *E. coli* cells ($N_0 = 1.0 \times 10^7$ cfu/mL) exposed to a series of O^- flux intensity (exposure size: 1.8 cm^2). (b) Survival curves of E. coli spheroplasts ($N_0 = 1.0 \times 10^7$ cfu/mL) exposed to a series of O^- flux intensity (exposed size: 1.8 cm^2), reaction temperature: 30°C.

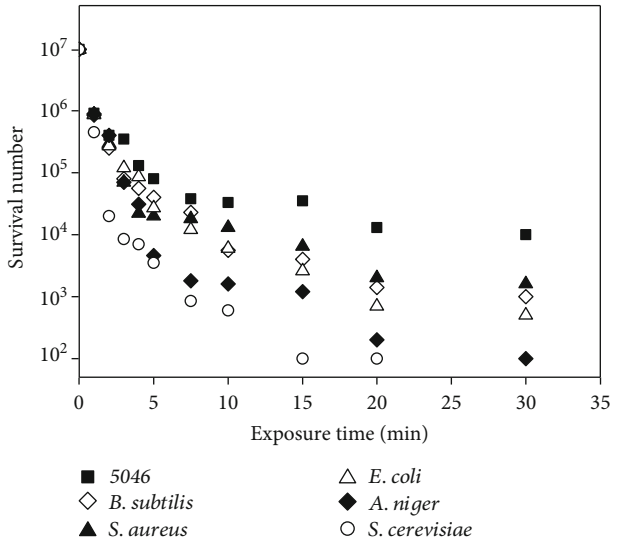

Figure 3: Survival curves of different types of microorganisms exposed to O^-: *B. subtilis*, *S. aureus*, *A. niger*, *E. coli*, *S. cerevisiae*, and *Actinomycetes (5046)*. N_0: 1.0×10^7 cfu/mL, O^- flux intensity: 52 nA/cm^2, reaction temperature: 30°C, exposed size: 1.8 cm^2.

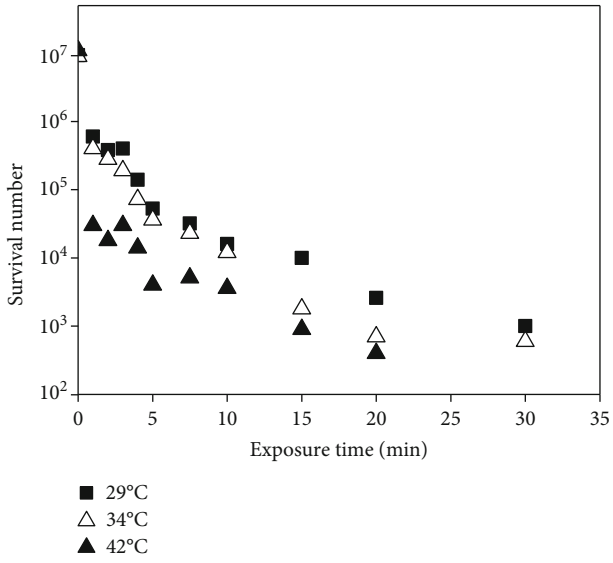

Figure 4: Reaction temperature effect on survival curves of E. coli exposed to O^-, N_0: 1.0×10^7 cfu/mL, O^- flux intensity: 52 nA/cm^2, exposure size: 1.8 cm^2.

is a thermally enhanced process. In addition, with enlarged exposure area, the inactivation efficiency also increases.

3.3. Products Formed by the Reaction of E. coli with O^-. The reaction products had been detected by the online analysis of the trail gases when O^- is exposed onto the microorganisms. The anionic intermediates and the neutral products were detected by a time-of-flight spectrometry (TOF) and a quadrupole mass (Q-MS) spectrometry, respectively. Figure 5(a) displays a typical TOF spectrum for the O^-/*E. coli* reaction system. The anionic species of H^-, OH^-, CO^-, CO_2^-, H_2O^-, and anionic hydrocarbons were clearly identified (Figure 5(a)). In addition, the neutral products of CO, CO_2, and H_2O were also observed by the Q-MS spectra (Figure 6(a)). It was also found that the peak intensities both for the anionic species and the neutral products increased with the increasing of the O^- flux intensity (Figure 5(b) and Figure 6(b)). The microorganisms, briefly, are macromolecules mainly consisted of carbon, hydrogen, oxygen, and nitrogen atoms. Among these elements, carbon atom is the only one not self-associating to make volatile molecules such as CO and

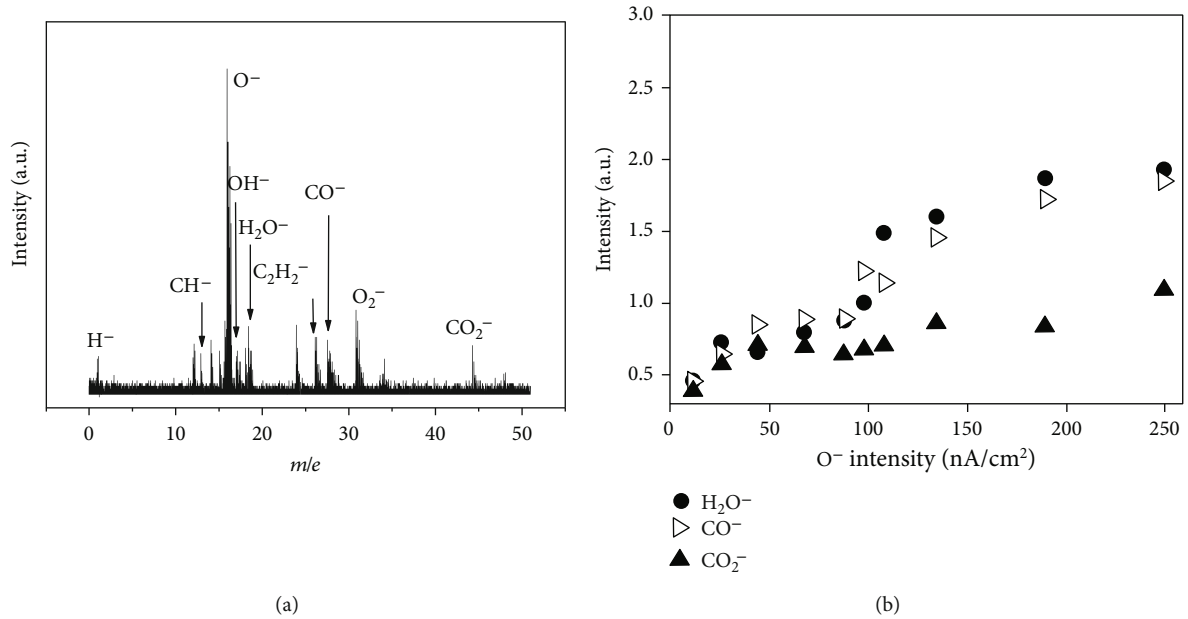

Figure 5: (a) Typical TOF spectrum shows the anionic intermediate species formed in the O^--induced inactivation processes (O^-: 250 nA/cm^2). (b) The intensity changes of H_2O^-, CO^-, and CO_2^- with different O^- intensity. Sample: *E. coli*, N_0: 1.0×10^{10} cfu/mL, exposure size: 1.8 cm^2.

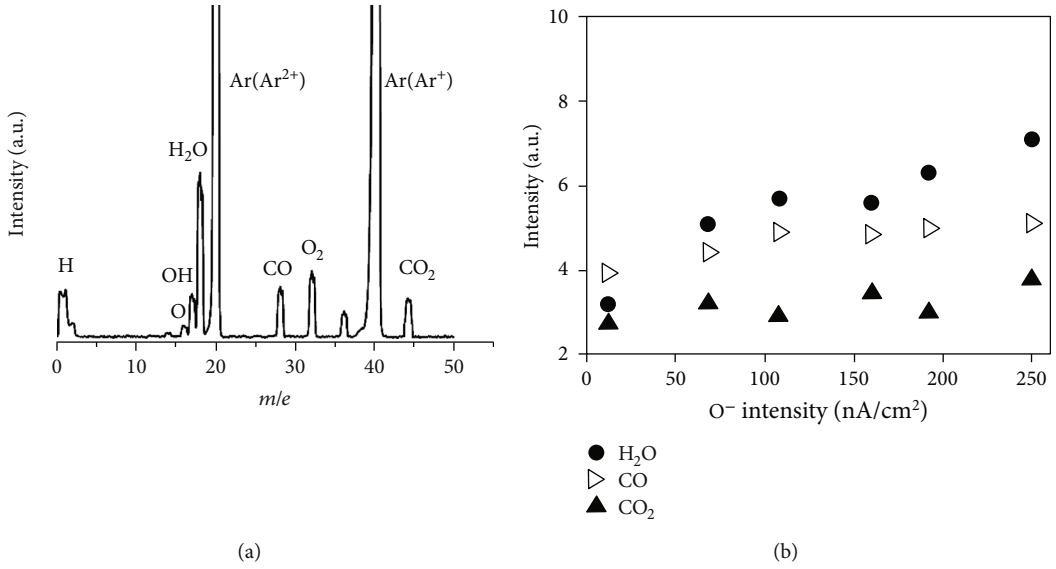

Figure 6: (a) Typical Q-MS spectrum shows that the volatile small molecules of CO, CO_2, and H_2O were formed in the O^--induced inactivation processes (O^-: 250 nA/cm^2). (b) The intensity changes of H_2O, CO, and CO_2 with different O^- intensity. Sample: *E. coli*, N_0: 1.0×10^{10} cfu/mL, exposure size: 1.8 cm^2.

CO_2, and it must therefore form volatile compounds with other atoms in order to be removed from the cell surface. The released CO and CO_2 would originate from the reactions of O^- with hydrocarbon bonds of the microorganisms' cells. Based on the observations mentioned above, the active O^- radical anions can react with the microorganisms, damage their cell structures, and finally result in a fast and irreversible inactivation. The inactivation mechanism of microorganisms induced by O^- was schematically described in Figure 7.

4. Conclusions

The active O^- radical anions possess high reactivity towards the microorganisms and damage the cell walls as well as their intrinsic structures, resulting in a fast and irreversible inactivation. The inactivation efficiencies depend on the O^- flux intensity, the initial population of microorganisms, the exposed area, environment, as well as the microorganisms' types. The observation of anionic intermediates (CO^-, CO_2^-, H_2O^-, and anionic hydrocarbons) by time-of-flight (TOF)

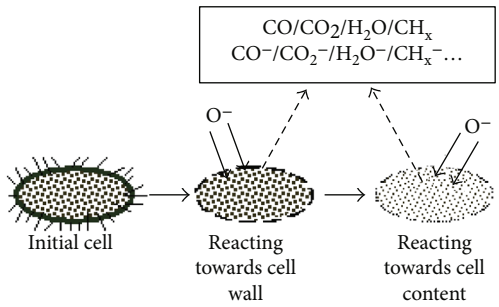

Figure 7: A schematic diagram shows the inactivation process induced by the O^- reactions with the macromolecules of the outer wall and the inner content of the microorganism cell.

mass spectrometry and the neutral volatile products (CO, CO_2, and H_2O) by quadrupole mass spectrometry (Q-MS) provided an evidence of the reactions of O^- with hydrocarbon bonds of the microorganisms. We believe that the present approach would be extended to other fields such as the O^- effects on lipid, protein, DNA, enzyme, and virus.

Data Availability

The data used to support the findings of this study are available from the corresponding authors upon request.

Conflicts of Interest

The authors declare no conflict of interest.

Acknowledgments

This study was financially supported by the Key Project of Natural Science Foundation of Universities in Anhui Province (KJ2017A137), the research fund of Anhui Agricultural University (Grant No. wd2018-03), finance support from the Project of School-Enterprise Cooperation (KJ20180142), and finance support from the Soil and Fertilizer Institute of Anhui Academy of Agricultural Sciences.

References

[1] S. Lenzen, "Chemistry and biology of reactive species with special reference to the antioxidative defence status in pancreatic β-cells," *Biochimica et Biophysica Acta-General Subjects*, vol. 1861, no. 8, pp. 1929–1942, 2017.

[2] M. S. Massima Mouele, O. O. Fatoba, O. Babajide, K. O. Badmus, and L. F. Petrik, "Review of the methods for determination of reactive oxygen species and suggestion for their application in advanced oxidation induced by dielectric barrier discharges," *Environmental Science and Pollution Research International*, vol. 25, no. 10, pp. 9265–9282, 2018.

[3] A. H. Paul, B. H. Daniel, U. S. Ingrid, G. C. Charles, K. Samuel, and V. Klaus, "Hydrogen peroxide as a potent bacteriostatic antibiotic: implications for host defense," *Free Radical Biology & Medicine*, vol. 19, no. 1, pp. 31–37, 1995.

[4] Y. Yoko, U. Naoli, R. Akemi et al., "Active oxygen species generated from photoexcited fullerene(C_{60}) as potential medicines: O_2^- versus $^1O_2$," *Journal of the American Chemical Society*, vol. 125, no. 42, pp. 12803–12809, 2003.

[5] Y. Ma, B. Wang, R. Zhang et al., "Initial simulated acid rain impacts reactive oxygen species metabolism and photosynthetic abilities in Cinnamonum camphora undergoing high temperature," *Industrial Crops and Products*, vol. 135, pp. 352–361, 2019.

[6] M. E. Orczykowski, S. M. Calderazzo, E. Shobin et al., "Cell based therapy reduces secondary damage and increases extent of microglial activation following cortical injury," *Brain Research*, vol. 1717, pp. 147–159, 2019.

[7] Q. S. Freya and R. B. Garry, "Acidic pH amplifies iron-mediated lipid peroxidation in cells," *Free Radical Biology & Medicine*, vol. 28, no. 8, pp. 1175–1181, 2000.

[8] S. Kawanishi, Y. Hiraku, and S. Oikawa, "Mechanism of guanine-specific DNA damage by oxidative stress and its role in carcinogenesis and aging," *Mutation Research/Reviews in Mutation Research*, vol. 488, no. 1, pp. 65–76, 2001.

[9] Y. S. Kim, M. J. Kang, and Y. M. Cho, "Low production of reactive oxygen species and high DNA repair: mechanism of radioresistance of prostate cancer stem cells," *Anticancer Research*, vol. 33, no. 10, pp. 4469–4474, 2013.

[10] P. Gaudu, V. Nivière, Y. Pétillot, B. Kauppi, and M. Fontecave, "The irreversible inactivation of ribonucleotide reductase from Escherichia coli by superoxide radicals," *FEBS Letters*, vol. 387, no. 2-3, pp. 137–140, 1996.

[11] J. A. Escobar, M. A. Rubio, and E. A. Lissi, "SOD and catalase inactivation by singlet oxygen and peroxyl radicals," *Free Radical Biology & Medicine*, vol. 20, no. 3, pp. 285–290, 1996.

[12] M. J. Davies, "Singlet oxygen-mediated damage to proteins and its consequences," *Biochemical Biophysical Research Communications*, vol. 305, no. 3, pp. 761–770, 2003.

[13] X. W. Yue and V. T. Andreas, "Impact of fungicides on active oxygen species and antioxidant enzymes in spring barley (*Hordeum vulgare* L.) exposed to ozone," *Environmental Pollution*, vol. 116, no. 1, pp. 37–47, 2002.

[14] V. Antonio and M. Julio, "Reactive oxygen species induce different cell death mechanisms in cultured neurons," *Free Radical Biology & Medicine*, vol. 36, no. 9, pp. 1112–1125, 2004.

[15] F. Julia, D. Vadim, H. F. B. John et al., "Reactive oxygen species produced by NADPH oxidase regulate plant cell growth," *Nature*, vol. 422, no. 6930, pp. 442–446, 2003.

[16] J. Aikens and T. A. Dix, "Perhydroxyl radical (HOO.) initiated lipid peroxidation: the role of fatty acid hydroperoxides," *The Journal of Biological Chemistry*, vol. 266, no. 23, pp. 15091–15098, 1991.

[17] E. R. Stadtman, "Protein oxidation and aging," *Science*, vol. 257, no. 5074, pp. 1220–1224, 1992.

[18] C. M. Martinez, "Oxygen free radicals and human disease," *Biochimie*, vol. 77, no. 3, pp. 147–161, 1995.

[19] J. M. McCord, "Superoxide radical: a likely link between reperfusion injury and inflammation," *Advances in Free Radical Biology & Medicine*, vol. 29, no. 2, pp. 325–345, 1986.

[20] J. L. Marx, "Oxygen free radicals linked to many diseases," *Science*, vol. 235, no. 4788, pp. 529–531, 1987.

[21] J. M. Matés and F. M. Sánchez-Jiménez, "Role of reactive oxygen species in apoptosis: implications for cancer therapy," *International Journal of Biochemistry & Cell Biology*, vol. 32, no. 2, pp. 157–170, 2000.

[22] N. Yuji, T. Tomohisa, I. Hiroshi et al., "A novel potent inhibitor of inducible nitric oxide inhibitor, ONO-1714, reduces

intestinal ischemia-reperfusion injury in rats," *Nitric Oxide*, vol. 10, no. 3, pp. 170–177, 2004.

[23] W. H. Wang, W. Feng, W. L. Wang, and P. Li, "Ab initio molecular dynamics simulation study on the stereo reactions between atomic oxygen anion and methane," *Molecules*, vol. 23, no. 10, pp. 1–13, 2018.

[24] J. Ma, B. Xu, X. J. Meng et al., "Reactivity of atomic oxygen radical anions bound to titania and zirconia nanoparticles in the gas phase: low-temperature oxidation of carbon monoxide," *Journal of the American Chemical Society*, vol. 135, no. 8, pp. 2991–2998, 2013.

[25] L. Tian, J. Meng, X. Wu et al., "Reactivity of oxygen radical anions bound to scandia nanoparticles in the gas phase: C–H bond activation," *Chemistry-A European Journal*, vol. 20, no. 4, pp. 1167–1175, 2014.

[26] J. Lee and J. J. Grabowski, "Reactions of the atomic oxygen radical anion and the synthesis of organic reactive intermediates," *Chemical Reviews*, vol. 92, no. 7, pp. 1611–1647, 1992.

[27] T. Dong, J. Li, F. Huang et al., "One-step synthesis of phenol by O^- and OH^- emission material," *Chemical Communications*, vol. 21, pp. 2724–2726, 2005.

[28] A. M. Gao, X. Zhu, H. Wang et al., "Reduction features of NO over a potassium-dope C12A7-O^- catalyst," *Journal of Physical Chemistry B*, vol. 110, no. 24, pp. 11854–11862, 2006.

[29] Z. Wang, T. Dong, L. Yuan et al., "Characteristics of bio-oil-syngas and its utilization in Fischer–Tropsch synthesis," *Energy Fuels*, vol. 21, no. 4, pp. 2421–2432, 2007.

[30] Z. Wang, Y. Pan, T. Dong et al., "Production of hydrogen from catalytic steam reforming of bio-oil using C12A7-O^--based catalysts," *Applied Catalysis A: General*, vol. 320, pp. 24–34, 2007.

[31] L. Li, L. Wang, Z. Yu, X. Lv, and Q. Li, "Inactivation of Bacillus subtilis by atomic oxygen radical anion," *Plasma Science and Technology*, vol. 9, no. 1, pp. 119–124, 2007.

[32] Q. Li, H. Hosono, M. Hirano et al., "High-intensity atomic oxygen radical anion emission mechanism from $12CaO{\cdot}7Al_2O_3$ crystal surface," *Surface Science*, vol. 527, no. 1, pp. 100–112, 2003.

[33] Q. Li, K. Hayashi, M. Nishioka et al., "Absolute emission current density of O^- from 12 $CaO{\cdot}7\ Al_2\ O_3$ crystal," *Applied Physics Letters*, vol. 80, no. 22, pp. 4259–4426, 2002.

[34] S. Kayano, W. Toshiya, and H. Kazuhito, "Studies on photokilling of bacteria on TiO_2 thin film," *Journal of Photochemistry and Photobiology A: Chemistry*, vol. 156, no. 1-3, pp. 227–233, 2003.

[35] H. Chen, S. Chan, J. C. Lee, C. Chang, M. Murugan, and R. W. Jack, "Transimission elctron microscopic observations of membrane effects of antibiotic cecropin B on *Escherichia coli*," *Microscopy Research and Technique*, vol. 62, no. 5, pp. 423–430, 2003.

Hindawi
Journal of Nanomaterials
Volume 2019, Article ID 4035075, 8 pages
https://doi.org/10.1155/2019/4035075

Research Article

An Effective Microwave-Assisted Synthesis of MOF235 with Excellent Adsorption of Acid Chrome Blue K

Jinlong Ge,[1,2] **Zhong Wu**,[1,2] **Xiaochen Huang**,[1,2] **and Ming Ding**[2,3]

[1]*School of Material and Chemistry Engineering, Bengbu University, Bengbu 233030, China*
[2]*Engineering Technology Research Center of Si-Based Material, Anhui Province, Bengbu 233030, China*
[3]*Engineering Laboratory of Si-Based Material, Anhui Province, Bengbu 233030, China*

Correspondence should be addressed to Jinlong Ge; jinlongge2005@126.com

Received 18 July 2019; Accepted 5 September 2019; Published 29 October 2019

Guest Editor: Fei Ke

An efficient, rapid, and fast kinetics of the metal-organic framework MOF235 was successfully prepared by microwave-assisted thermolysis strategy. Fourier transform infrared spectra (FTIR), X-ray diffraction (XRD), X-ray photoelectron spectroscopy (XPS), N_2 adsorption-desorption isotherm, and scanning electron microscopy (SEM) were used to characterize the samples. Experimental results revealed the suitability of MOF235 for use as an adsorbent for acid chrome blue K. The maximum adsorption capacity of acid chrome blue K onto MOF235 can reach to 591.79 mg g^{-1} at 293 K. The sorption behavior fitted to the pseudo-second-order kinetic model and the Langmuir isotherm. Adsorption of acid chrome blue K is a spontaneous and endothermic process. Therefore, the as-prepared MOF235 displays a great potential for environmental purification.

1. Introduction

Organic dyes are typical pollutants found in many important industries and receive major worldwide concern. Dyes are main organic pollutants because they are toxic or carcinogenic to mammals and other living organisms even at low concentrations [1]. Efficient removal of organic dyes from wastewater has become a severe problem due to its ecological, biological, and environmental importance [2]. Acid chrome blue K is an azo dye and has been used as a spectrophotometric and electrochemical reagent for protein assay [3].

Dye effluent is usually treated by conventional methods such as adsorption, coagulation, electrochemical degradation, and photocatalysis. Adsorption is considered as one of the simplest, highly effective, and economically beneficial methods to remove the dye [4]. Effective removal of these dyes from aqueous solution is gaining more and more interests [5].

Traditional adsorbent materials, such as clay minerals, activated carbon (AC), carbonaceous materials, ordered mesoporous carbon, carbon nanotubes, and graphene oxides (GO), have been widely applied in the adsorption of organic dyes. However, these adsorbent materials generally have several disadvantages in dye adsorption including small pore sizes or pore volumes and low adsorption capacity [6]. Therefore, the development of advanced porous materials for more effective and inexpensive adsorption is highly valuable [7].

In parallel to the conventional porous materials, much research effort has been devoted to find new adsorbent. Metal-organic frameworks (MOFs) show many interesting characteristic features such as a large specific surface area, low framework density, versatile functionality, controlled porosity, and tailorable structure [8]. These excellent properties have attracted increasing attention for adsorption [9], catalysis, storage, and electrochemistry in recent years [10].

The MOF235 is orange hexagonal single crystals. The crystal structure of the MOF235 is built up from corner sharing octahedral iron trimers. Linear terephthalic acid is connected, and each iron atom is trivalent. MOF235 synthesized by a solvothermal method has been investigated, and it performs high capacity to adsorb CH_4 due to the high pore volume and large number of open metal sites [11].

Microwave-assisted synthesis has been widely revealed distinct advantages as an alternative method for the chemical synthesis of organic and inorganic materials [12]. Microwave irradiation has attracted much attention. It has the

advantages of short reaction time, high reaction rate, and conservation energy.

It has been demonstrated that the microwave-assisted synthesis was one of the most efficient routes to carry out many reactions [13]. Microwave irradiation can accelerate the crystallization of porous materials that require several days or several hours compared with the conventional solvothermal synthesis [14]. A great diversity of MOFs has been prepared quickly and in high yield by a microwave-assisted routes, such as MOF-5, MIL-88B, MIL-53, and UiO-66. The microwave irradiation power, irradiation time, concentration of the reagents, and solvent system were deeply investigated [15]. Microwave heating have a beneficial effect on the properties and performance of materials [16].

In this work, orange octahedral crystals of MOF235 were successfully prepared by a facile and green synthetic route under microwave heating. Moreover, the adsorption capacity for acid chrome blue K with MOF-235 is about 591.9 mg g^{-1}. The textural and chemical properties of the MOF235 were reported. The adsorption kinetics and mechanism were investigated using the adsorption isotherm technique. The effectiveness of the MOF235 in the adsorption was evaluated. This work provided a fast preparation method for MOF235 and development of a highly successful and efficient adsorbent in acid chrome blue K wastewater treatment.

2. Materials and Methods

2.1. Materials. Ferric chloride hexahydrate ($FeCl_3$), terephthalic acid (Sigma-Aldrich, >99%), *N*,*N*-dimethylformamide (DMF), and absolute ethanol were purchased from Shanghai Chemical Reagent Inc. of the Chinese Medicine Group. All reagents were used as received.

2.2. Synthesis of MOF235. In a typical synthesis, a mixture of 0.3015 g terephthalic acid was dissolved in 30 mL DMF solvent and the mixture was stirred for 10 min. Then, 0.3000 g of $FeCl_3{\cdot}6H_2O$ was added into the solution and stirred for 10 min; the reactant mixture of 30 mL and 30 mL of ethanol was dispersed into the round Pyrex flask [11]. The round flask was put into ultrasonic and microwave-assisted extraction (Shanghai CW-2000) and irradiated simultaneously by microwaves under the protection of nitrogen for a specified period. After cooling down to room temperature, the orange resultant solid was collected by centrifugation, washed with DMF-ethanol (1 : 1, *v*/*v*) mixture and finally dried in a vacuum at 423 K for 12 h and the orange octahedral crystals of MOF235 were obtained.

2.3. Adsorption Test. In a typical preparation process, 10 mg of MOF235 was added to a solution with 50 mL of acid chrome blue K at initial concentration from 40 ppm to 140 ppm. The solution was shaked under mechanical conditions for different times. The residual concentration of the dyes was determined at the maximum wavelength using UV-vis spectroscopy. The adsorption capacities were calculated using the calibration curve.

2.4. Characterizations. The synthesized MOF235 were thoroughly characterized by various sophisticated analytical techniques. X-ray diffraction (XRD) experiments were conducted using an X-ray diffractometer with the Cu target (SmartLab) operating at 36 kV and 25 mA from 5 to 70°. Fourier transform infrared (FTIR) spectra of powder samples were obtained in the 400-4000 cm^{-1} range with a resolution of 4 cm^{-1} using a Nicolet Nexus 870 FTIR spectrometer. X-ray photoelectron spectroscopy (XPS) analysis was carried out in the Thermo Scientific K-Alpha spectrometer using monochromated Al Ka X-rays. Ultraviolet absorbance spectra were collected on a Shimadzu UV 3600 plus spectrophotometer over a range of 200–800 nm. Nitrogen adsorption-desorption isotherms were measured at 77 K by multipoint BET and a Barrett-Joyner-Halenda (BJH) method using a Micromeritics ASAP 3020 analyzer. The samples were heated at 150°C for 12 h prior to each test. The morphology and microstructure were observed by a field emission scanning electron microscope (SEM: Hitachi S-4800). Thermogravimetric analysis was determined from room temperature to 800°C with a heating rate of 10°C/min using a Pyris1 TGA-1.

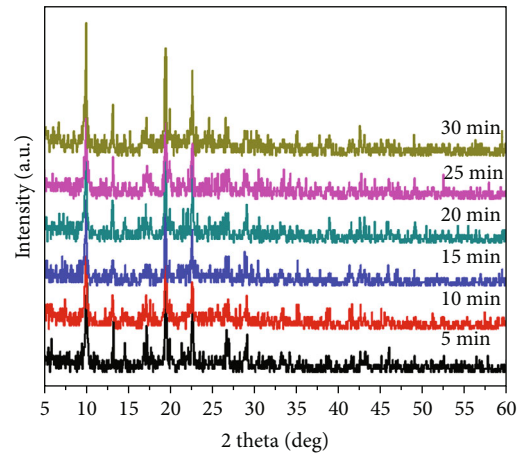

Figure 1: XRD patterns of the as-synthesized MOF235 with different microwave times.

3. Results and Discussion

3.1. Characterization of MOF235. The crystalline nanostructures and phase purities of the MOF235 samples were recorded with X-ray distraction (XRD) in Figure 1. Strong major peaks of the samples were observed at $2\theta = 9.7°$, 10.8°, 12.6°, 19.0°, 22.0°, and 26°, which are in good consistent with the previously reported literature [17]. In the XRD patterns, the minimum microwave time to obtain complete crystallinity MOF235 was required for 15 min. The sharp crystalline of the reflections derived from the MOF235 increases with the prolonged reaction time under microwave. This indicated that the well crystallinity of MOF235 in the samples is proportional to the reaction time about 20 min [18, 19]. The results described the advantages of the effective and convenient microwave-assisted method. The intensities of all crystallinity peaks which increased gradually in short periods could be attributed to the fast heating precursor and avoid thermal gradients [20, 21]. It also demonstrated that the increased irradiation time leads to high yields and

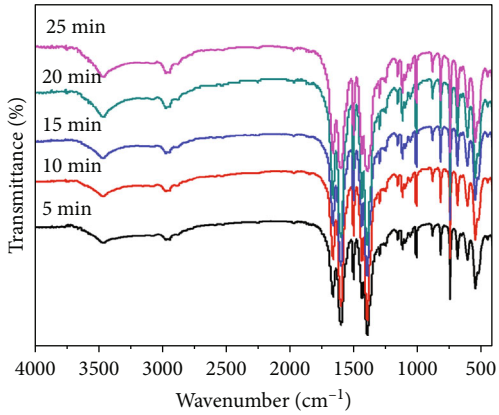

Figure 2: FTIR of the as-synthesized MOF235 with different microwave irradiation times.

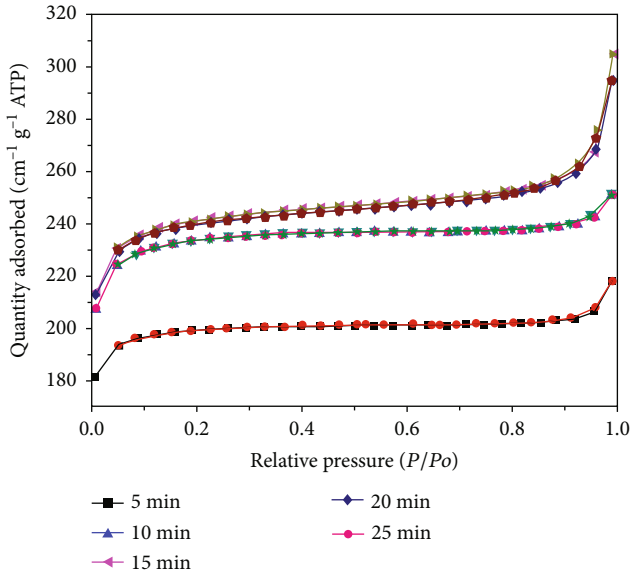

Figure 3: Nitrogen adsorption-desorption isotherms of the MOF235.

larger crystals [22]. It indicated that microwave heating was more effective than the convenient heating.

Fourier transform infrared (FTIR) spectra of the MOF235 were shown in Figure 2. All of the samples display similar spectra in general. The main spectra peaks of MOF235 were at 3440 cm^{-1}, 2931 cm^{-1}, 1597 cm^{-1}, 1398 cm^{-1}, 1016 cm^{-1}, 810 cm^{-1}, 748 cm^{-1}, respectively. The peaks observed at 1597 cm^{-1} were attributed to the asymmetric C–O bonds. The peaks at 1398 cm^{-1} were attributed to symmetric stretch vibrations in the carboxyl groups. According to the lower frequencies, the bands around 810 cm^{-1}, 748 cm^{-1}, and 710 cm^{-1} were attributed to the mixture with the C–H vibration, C=C stretch, OH bend, and O-C-O bend in H_2BDC [23].

Nitrogen adsorption isotherms of the samples prepared under different preparation conditions are shown in Figure 3. All samples confirmed a type I sorption isotherm, indicating a typical microporous structure. The results

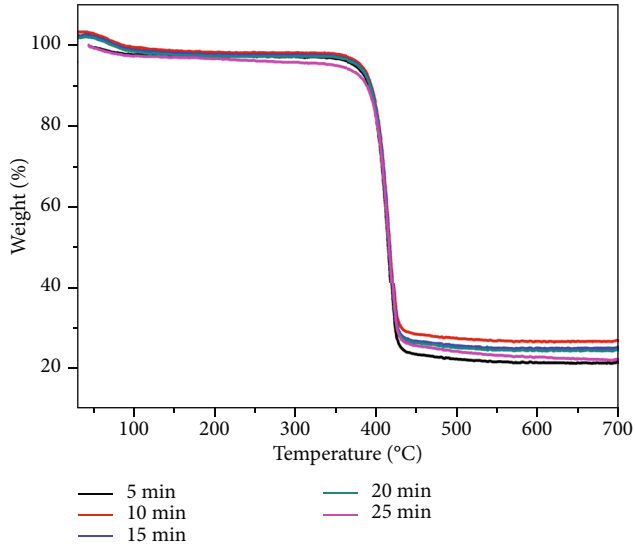

Figure 4: TG of the as-synthesized MOF235.

revealed that the BET surface area was significantly increased from 444.25, 583.20, 602.72, 620.53, and 729.21 m^2 g^{-1} of the samples by microwave heating time. It proves that the microwave-assisted preparation of MOF235 is feasible and efficient. The pore size distribution is an important influence factor of an adsorbent. It will have a great impact on the size and shape of a given dye molecules. The average pore size of MOF235 is 4.13 nm. When the adsorbent pore diameter is as large as 1.7 times that of the adsorbate, adsorption can reach to the most effective results [24]. However, the amount of micropores decreased significantly after the incorporation. The increase in the BET surface area and micropore volume of the MOF235 could be attributed to the loss of the well-ordered structure; the pore can be an efficient space for large substrates which allows the dye to go inside the pore and react with MOF235.

The thermal stability of MOF235 was carried out by TGA to investigate the material stability and the correlation between the reaction time and the structural integrity. As shown in Figure 4(a), the TGA curves of all the samples exhibit a degradation at the temperature of 400°C. The weight loss of the samples MOF235 showed similar thermal curves. The maximum structural integrity and robustness of the MOF235 were achieved with a microwave irradiation time of 25 min. Moreover, the thermal stabilities of these MOF235 were consistent with those obtained using the previously reported solvothermal approach [25]. With the extended response time from 5 to 10 min, the sample crystals were still underdeveloped and with some unreacted precursors attached in the pore. The full growth of crystals was completed after 15 min. The TGA curve results showed that the MOF235 have high thermal stability in the adsorption dye reaction [26].

X-ray photoelectron spectral (XPS) analyses were applied to analyze the elemental distribution, surface composition, and bond of the samples and their valence states [27]. It shows that the sample surface consists of carbon, nitrogen,

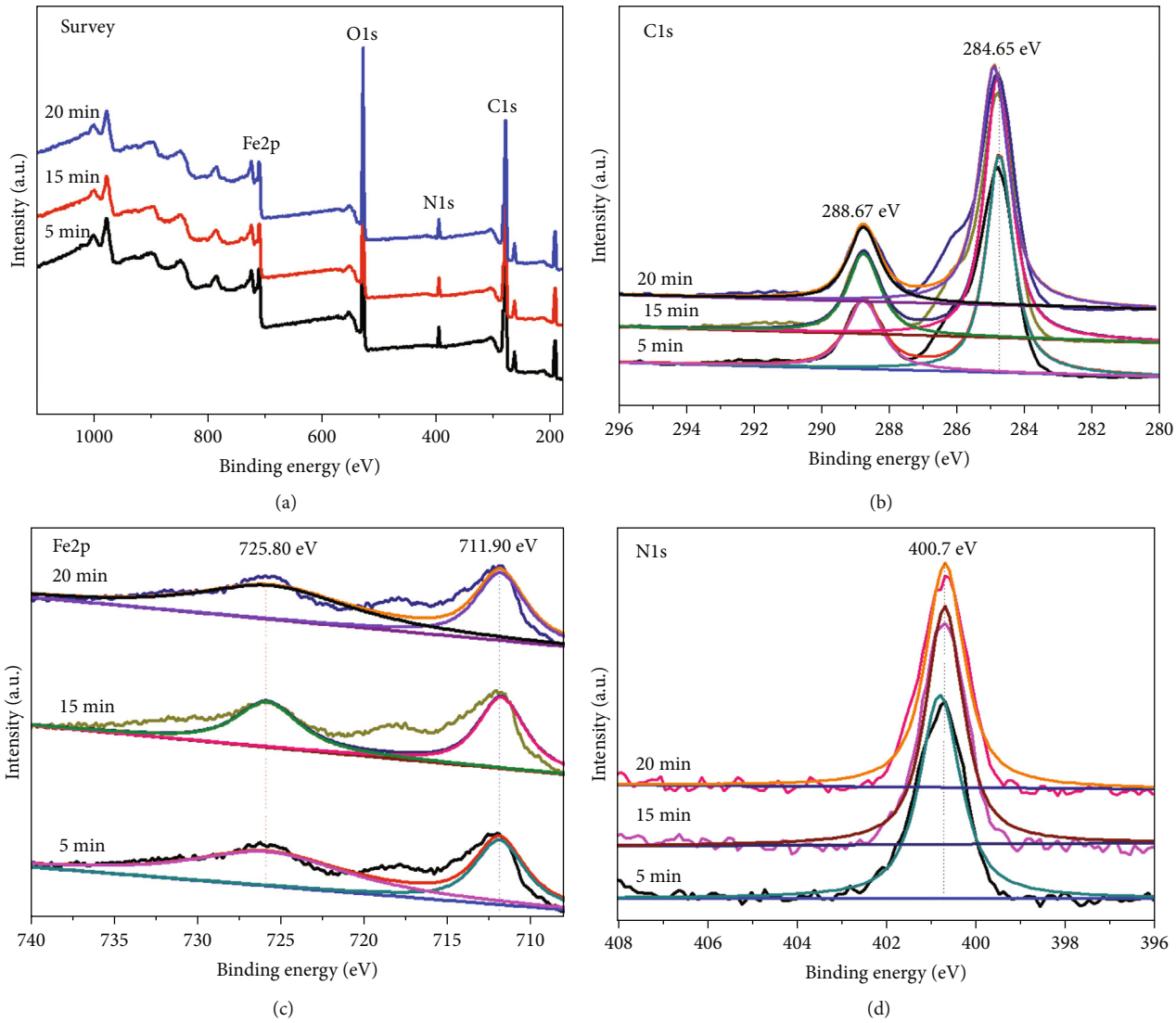

Figure 5: XPS spectra of MOF235: (a) survey, (b) C1s, (c) Fe2p, and (d) N1s.

oxygen, and iron, with binding energies of C1s, N1s, O1s, and Fe2p, respectively (Figure 5(a)). As shown in Figure 5(b), the fitting result of the C1s spectrum of MOF235 suggests the existence of two peak components of C=C and C-C (284.65 eV) and O-C=O (288.67 eV), indicated that there were two types of chemical environments for carbon in the samples [28]. The two characteristic peaks at 711.90 and 725.80 eV (Fe2p region) indicated the presence of Fe^{3+} species (Figure 5(c)). The peak centered at 400.7 eV can be assigned to graphitic N, in agreement with the N states in N/C (Figure 5(d)), indicating the change of chemical environment of nitrogen in MOF235.

The MOF235 morphology of the microwave heating method under different times was studied by SEM in Figure 6. The well-crystallized octahedral morphological materials are built up from corner-sharing octahedral iron trimers that are connected through terephthalic acid linear links. The Fe_3O plane of each trimer has Fe-(μ3-O)-Fe angles (120°) and the two adjacent Fe ion separation of 3.33 Å [17]. The octahedral crystallites have the particle size around 450 nm and a uniform size distribution. The SEM images show that the materials have an obvious advantage of a higher degree of crystallinity with the extension of microwave irradiation time.

3.2. Adsorption Properties of Acid Chrome Blue K on MOF235. Adsorption equilibrium of acid chrome blue K onto MOF235 was studied at six initial concentrations of 40, 60, 80, 100, 120, and 140 ppm. As shown in Figure 7, it was clearly shown that the adsorption quantity of acid chrome blue K increased sharply within 50 min and no marked changes are observed with further increases in contact time. It is suggested that the samples were allowed reacting for 200 min to ensure adsorption equilibrium. During the desorption process, the equilibrium adsorption amounts of acid chrome blue K were 94.81, 189.60, 259.84, 366.05, 464.84, and 591.79 mg g^{-1}, respectively. The results indicated that the adsorption amounts were improved with the increase of the initial concentrations and it could reach the

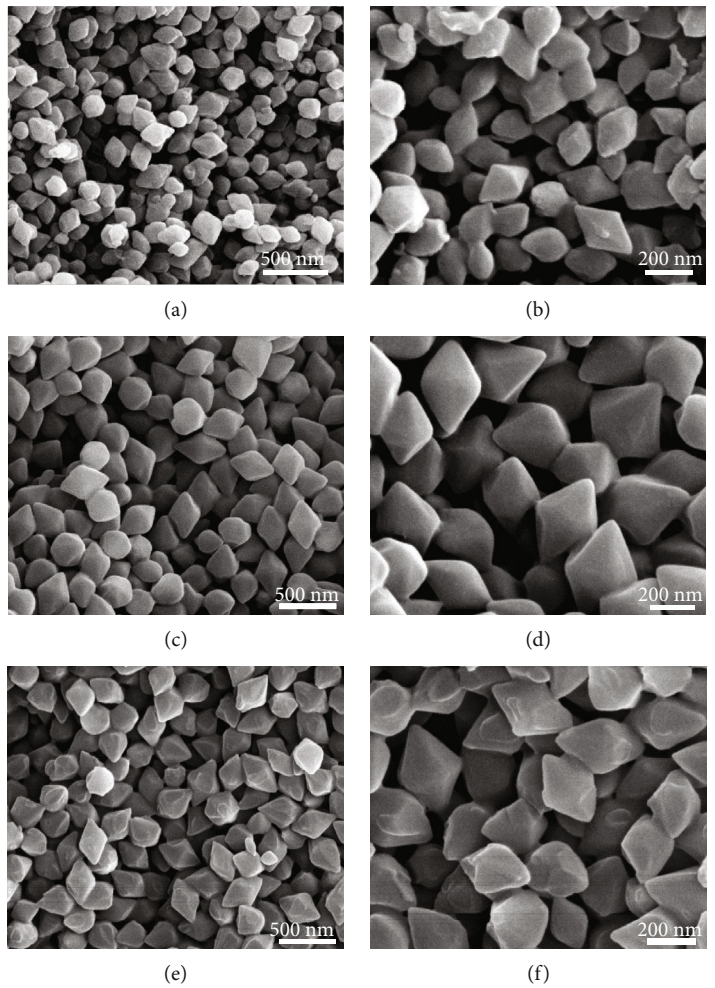

FIGURE 6: SEM micrographs of MOF235: (a) 10 min, (b) 15 min, and (c) 15 min.

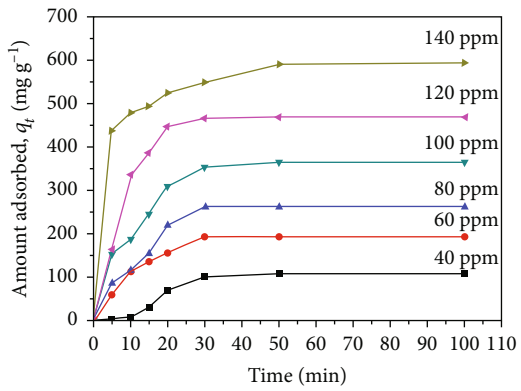

FIGURE 7: Adsorption amounts of acid chrome blue K with different initial concentrations.

maximums of 591.79 mg g^{-1} from the 140 ppm initial concentration aqueous solution [29].

Adsorption kinetics were investigated to study the mechanism of adsorption which is important for adsorption efficiency of the acid chrome blue K in aqueous solutions [30]. The pseudo-first-order and pseudo-second-order models were both usually applied to the experimental data [31]. The models are used to explore the potential rate controlling the phenomenon in the adsorption of acid chrome blue K onto MOF235 [32]. The adsorption rate is proportional to the square of the number of unoccupied adsorption sites, and the rate equation is

$$\frac{d_q}{d_t} = k_2(q_e - q)^2,$$
$$\frac{t}{q_t} = \frac{1}{q_e^2 k_2} + \frac{t}{q_e}, \quad (1)$$

where q_e and q_t (mg/g) refer to the amounts of acid chrome blue K adsorbed at equilibrium and at time t, respectively. k_2 (g mg^{-1} min^{-1}) represents the rate constants [33]. It is obvious that the experimental kinetic data fitted better with the pseudo-second-order rate model. The higher coefficients of R^2 and lower normalized standard deviation are better than those in the pseudo-first-order kinetic model [34]. As shown in Figure 8, all the coefficients of the pseudo-second-order model were higher than 0.999 for all the initial acid chrome blue K concentrations at 293 K. It implied that the

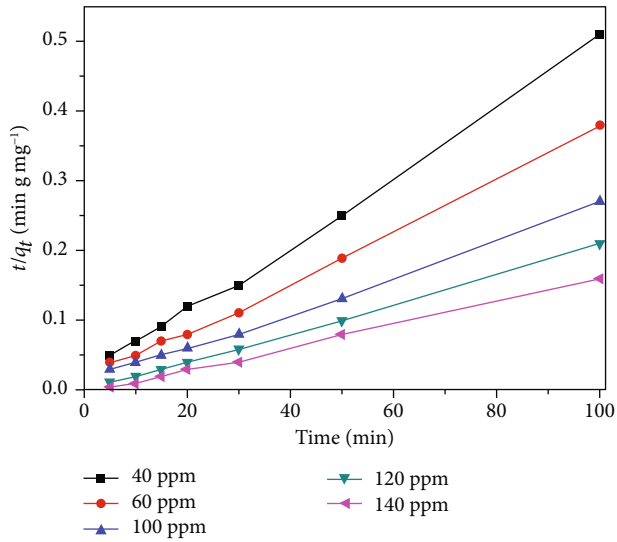

Figure 8: Langmuir plots of the isotherms.

adsorption process was a combination of physical and chemical adsorption [35].

The pseudo-first-order kinetics model is a widely used monolayer adsorption model. The equilibrium adsorption data of acid chrome blue K on MOF235 was further evaluated through Langmuir and Freundlich isotherm equations [36, 37]. The Langmuir isotherm is valid for monolayer adsorption onto a surface containing a finite number of identical adsorption sites [29]. The Freundlich isotherm is applied for multilayer adsorption of adsorbates with a heterogeneous surface and a nonuniform distribution of adsorption heat [38]. Their linear forms are as follows:

$$\frac{C_e}{q_e} = \frac{C_e}{Q_0} + \frac{1}{Q_0 b}, \tag{2}$$

where q_e is the amount of adsorbate adsorbed per unit mass of adsorbent (mg g^{-1}), C_e is the retained adsorbate concentration at equilibrium (mg L^{-1}) [39], q_0 is the maximum adsorption capacity, and b is the adsorption energy, obtained from the slope and intercept of the plot of C_e/q_e against C_e, respectively [40], and found to be 131.8 mg g^{-1} and 0.0485 L mg^{-1} with the correlation of 0.995.

4. Conclusions

In summary, the microwave-assisted thermolysis strategy is simple, rapid, and robust, thereby providing a promising route for the synthesis of MOF235. Acid chrome blue K can be efficiently removed with MOF235. The adsorption kinetics and adsorption isotherms were investigated in detail. All of the MOF235 exhibited high adsorption capacities and fast adsorption kinetics. It is indicated that MOF235 under microwave can be applied in the highly attractive adsorbent for the removal of acid chrome blue K.

Data Availability

The data used to support the findings of this study are available from the corresponding author upon request.

Conflicts of Interest

The authors declare that there is no conflict of interests regarding the publication of this paper.

Acknowledgments

This work was supported by the Major Project Natural Science Fund of Anhui Department of Education (Nos. KJ2019ZD62, KJ2018ZD055, KJ2019A0852, and KJ2019A0848) and Funding of High Research for High Talents (BBXY2018KYQD08 and BBXY2018KYQD16).

References

[1] S. Cheng, L. Zhang, H. Xia et al., "Adsorption behavior of methylene blue onto waste-derived adsorbent and exhaust gases recycling," *RSC Advances*, vol. 7, no. 44, pp. 27331–27341, 2017.

[2] Y. He, T. Xu, J. Hu et al., "Amine functionalized 3D porous organic polymer as an effective adsorbent for removing organic dyes and solvents," *RSC Advances*, vol. 7, no. 48, pp. 30500–30505, 2017.

[3] L. Mouni, L. Belkhiri, J. C. Bollinger et al., "Removal of methylene blue from aqueous solutions by adsorption on kaolin: kinetic and equilibrium studies," *Applied Clay Science*, vol. 153, pp. 38–45, 2018.

[4] C. Li, H. Xia, L. Zhang et al., "Kinetics, thermodynamics, and isotherm study on the removal of methylene blue dye by adsorption via copper modified activated carbon," *Research on Chemical Intermediates*, vol. 44, no. 4, pp. 2231–2250, 2018.

[5] D. Li, W. Dong, S. Sun, Z. Shi, and S. Feng, "Photocatalytic degradation of acid chrome blue K with porphyrin-sensitized TiO_2 under visible light," *The Journal of Physical Chemistry C*, vol. 112, no. 38, pp. 14878–14882, 2008.

[6] E. M. Dias and C. Petit, "Towards the use of metal–organic frameworks for water reuse: a review of the recent advances in the field of organic pollutants removal and degradation and the next steps in the field," *Journal of Materials Chemistry A*, vol. 3, no. 45, pp. 22484–22506, 2015.

[7] L. Wen, X. Wang, H. Shi, K. Lv, and C. Wang, "A multifunctional cadmium–organic framework comprising tricarboxytriphenyl amine: selective gas adsorption, liquid-phase separation and luminescence sensing," *RSC Advances*, vol. 6, no. 2, pp. 1388–1394, 2016.

[8] H. K. Kala, R. Mehta, K. K. Sen, R. Tandey, and V. Mandal, "Strategizing method optimization of microwave-assisted extraction of plant phenolics by developing standard working principles for universal robust optimization," *Analytical Methods*, vol. 9, no. 13, pp. 2089–2103, 2017.

[9] F. Jeremias, V. Lozan, S. K. Henninger, and C. Janiak, "Programming MOFs for water sorption: amino-functionalized MIL-125 and UiO-66 for heat transformation and heat storage applications," *Dalton Transactions*, vol. 42, no. 45, pp. 15967–15973, 2013.

[10] P. Kumar, K. H. Kim, E. E. Kwon, and J. E. Szulejko, "Metal–organic frameworks for the control and management of air quality: advances and future direction," *Journal of Materials Chemistry A*, vol. 4, no. 2, pp. 345–361, 2016.

[11] Y. Li, G. Hou, J. Yang et al., "Facile synthesis of MOF 235 and its superior photocatalytic capability under visible light irradiation," *RSC Advances*, vol. 6, no. 20, pp. 16395–16403, 2016.

[12] F. Iskandar, U. Hikmah, E. Stavila, and A. H. Aimon, "Microwave-assisted reduction method under nitrogen atmosphere for synthesis and electrical conductivity improvement of reduced graphene oxide (rGO)," *RSC Advances*, vol. 7, no. 83, pp. 52391–52397, 2017.

[13] Y. Kalinovskyy, N. J. Cooper, M. J. Main, S. J. Holder, and B. A. Blight, "Microwave-assisted activation and modulator removal in zirconium MOFs for buffer-free CWA hydrolysis," *Dalton Transactions*, vol. 46, no. 45, pp. 15704–15709, 2017.

[14] A. U. H. S. Rana, M. Kang, and H. S. Kim, "Microwave-assisted facile and ultrafast growth of ZnO nanostructures and proposition of alternative microwave-assisted methods to address growth stoppage," *Scientific Reports*, vol. 6, no. 1, article 24870, 2016.

[15] J. He, Y. Zhang, X. Zhang, and Y. Huang, "Highly efficient Fenton and enzyme-mimetic activities of NH_2-MIL-88B(Fe) metal organic framework for methylene blue degradation," *Scientific Reports*, vol. 8, no. 1, article 5159, 2018.

[16] B. Reeja-Jayan, K. L. Harrison, K. Yang, C. L. Wang, A. E. Yilmaz, and A. Manthiram, "Microwave-assisted low-temperature growth of thin films in solution," *Scientific Reports*, vol. 2, no. 1, article 1003, 2012.

[17] A. C. Sudik, A. P. Côté, and O. M. Yaghi, "Metal-organic frameworks based on trigonal prismatic building blocks and the new "acs" topology," *Inorganic Chemistry*, vol. 44, no. 9, pp. 2998–3000, 2005.

[18] C. Zhang, H. Zhang, R. Li, and Y. Xing, "Morphology and adsorption properties of chitosan sulfate salt microspheres prepared by a microwave-assisted method," *RSC Advances*, vol. 7, no. 76, pp. 48189–48198, 2017.

[19] Y. J. Heo and S. J. Park, "Facile synthesis of MgO-modified carbon adsorbents with microwave-assisted methods: effect of MgO particles and porosities on CO_2 capture," *Scientific Reports*, vol. 7, no. 1, article 5653, 2017.

[20] H. Reinsch and N. Stock, "Synthesis of MOFs: a personal view on rationalisation, application and exploration," *Dalton Transactions*, vol. 46, no. 26, pp. 8339–8349, 2017.

[21] H. Liu, T. Liu, M. Takafuji, H. Qiu, and H. Ihara, "Monodisperse core shell melamine formaldehyde polymer-modified silica microspheres prepared using a facile microwave-assisted method," *New Journal of Chemistry*, vol. 41, no. 20, pp. 11517–11520, 2017.

[22] F. H. Wei, D. Chen, Z. Liang, S. Q. Zhao, and Y. Luo, "Synthesis and characterization of metal–organic frameworks fabricated by microwave-assisted ball milling for adsorptive removal of Congo red from aqueous solutions," *RSC Advances*, vol. 7, no. 73, pp. 46520–46528, 2017.

[23] Y. Han, M. Liu, K. Li et al., "Facile synthesis of morphology and size-controlled zirconium metal–organic framework UiO-66: the role of hydrofluoric acid in crystallization," *CrystEngComm*, vol. 17, no. 33, pp. 6434–6440, 2015.

[24] M. V. B. Krishna, G. Venkateswarlu, and D. Karunasagar, "Development of a simple and robust microwave assisted decomposition method for the determination of rare earth elements in coal fly ash by ICP-OES," *Analytical Methods*, vol. 9, no. 13, pp. 2031–2040, 2017.

[25] Y. H. Huang, W. S. Lo, Y. W. Kuo, W. J. Chen, C. H. Lin, and F. K. Shieh, "Green and rapid synthesis of zirconium metal–organic frameworks *via* mechanochemistry: uio-66 analog nanocrystals obtained in one hundred seconds," *Chemical Communications*, vol. 53, no. 43, pp. 5818–5821, 2017.

[26] R. Babu, R. Roshan, A. C. Kathalikkattil, D. W. Kim, and D. W. Park, "Rapid, microwave-assisted synthesis of cubic, three-dimensional, highly porous MOF-205 for room temperature CO_2 fixation via cyclic carbonate synthesis," *ACS Applied Materials & Interfaces*, vol. 8, no. 49, pp. 33723–33731, 2016.

[27] M. Anbia, V. Hoseini, and S. Sheykhi, "Sorption of methane, hydrogen and carbon dioxide on metal-organic framework, iron terephthalate (MOF-235)," *Journal of Industrial and Engineering Chemistry*, vol. 18, no. 3, pp. 1149–1152, 2012.

[28] C. A. Bizzi, M. F. Pedrotti, J. S. Silva, J. S. Barin, J. A. Nóbrega, and E. M. M. Flores, "Microwave-assisted digestion methods: towards greener approaches for plasma-based analytical techniques," *Journal of Analytical Atomic Spectrometry*, vol. 32, no. 8, pp. 1448–1466, 2017.

[29] E. Haque, J. W. Jun, and S. H. Jhung, "Adsorptive removal of methyl orange and methylene blue from aqueous solution with a metal-organic framework material, iron terephthalate (MOF-235)," *Journal of Hazardous Materials*, vol. 185, no. 1, pp. 507–511, 2011.

[30] C. Du, Y. Xue, Z. Wu, and Z. Wu, "Microwave-assisted one-step preparation of macadamia nut shell-based activated carbon for efficient adsorption of reactive blue," *New Journal of Chemistry*, vol. 41, no. 24, pp. 15373–15383, 2017.

[31] J. Klinowski, F. A. Almeida Paz, P. Silva, and J. Rocha, "Microwave-assisted synthesis of metal–organic frameworks," *Dalton Transactions*, vol. 40, no. 2, pp. 321–330, 2011.

[32] Y. He, M. Pei, N. Xue, L. Wang, and W. Guo, "Synthesis of sodium polyacrylate–bentonite using *in situ* polymerization for Pb^{2+} removal from aqueous solutions," *RSC Advances*, vol. 6, no. 53, pp. 48145–48154, 2016.

[33] M. Taddei, P. V. Dau, S. M. Cohen et al., "Efficient microwave assisted synthesis of metal–organic framework UiO-66: optimization and scale up," *Dalton Transactions*, vol. 44, no. 31, pp. 14019–14026, 2015.

[34] B. Saha, S. Das, J. Saikia, and G. Das, "Preferential and enhanced adsorption of different dyes on iron oxide nanoparticles: a comparative study," *The Journal of Physical Chemistry C*, vol. 115, no. 16, pp. 8024–8033, 2011.

[35] S. Deng, G. Zhang, Y. Li, Y. Dou, and P. Wang, "Facile preparation of amidoxime-functionalized fiber by microwave-assisted method for the enhanced adsorption of chromium(VI) from aqueous solution," *RSC Advances*, vol. 6, no. 69, pp. 64665–64675, 2016.

[36] L. Xu, Y. S. Ding, C. H. Chen et al., "3D flowerlike α-nickel hydroxide with enhanced electrochemical activity synthesized by microwave-assisted hydrothermal method," *Chemistry of Materials*, vol. 20, no. 1, pp. 308–316, 2008.

[37] V. Bon, I. Senkovska, J. D. Evans, M. Wöllner, M. Hölzel, and S. Kaskel, "Insights into the water adsorption mechanism in the chemically stable zirconium-based MOF DUT-67 – a prospective material for adsorption-driven heat transformations," *Journal of Materials Chemistry A*, vol. 7, no. 20, pp. 12681–12690, 2019.

[38] H. Guo, F. Lin, J. Chen, F. Li, and W. Weng, "Metal-organic framework MIL-125(Ti) for efficient adsorptive removal of rhodamine B from aqueous solution," *Applied Organometallic Chemistry*, vol. 29, no. 1, pp. 12–19, 2015.

[39] J. M. Yang, R. J. Ying, C. X. Han et al., "Adsorptive removal of organic dyes from aqueous solution by a Zr-based metal organic framework effects of Ce(III) doping," *Dalton Transactions*, vol. 47, no. 11, pp. 3913–3920, 2018.

[40] P. Yang, W. Wei, and L. Yang, "Simultaneous voltammetric determination of dihydroxybenzene isomers using a poly(acid chrome blue K)/carbon nanotube composite electrode," *Microchimica Acta*, vol. 157, no. 3-4, pp. 229–235, 2007.

Hindawi
Journal of Nanomaterials
Volume 2019, Article ID 1454358, 11 pages
https://doi.org/10.1155/2019/1454358

Review Article

Magnetic Nanoparticles@Metal-Organic Framework Composites as Sustainable Environment Adsorbents

Gege Zhao,[1] Nianqiao Qin,[1] An Pan,[1,2] Xiaoyan Wu,[1] Chuanyi Peng,[1,2] Fei Ke,[1] Mudassar Iqbal,[3] Karna Ramachandraiah,[4] and Jing Zhu[1]

[1]*Department of Applied Chemistry and State Key Laboratory of Tea Plant Biology and Utilization, Anhui Agricultural University, Hefei 230036, China*
[2]*School of Tea and Food Science & Technology, Anhui Agricultural University, Hefei 230036, China*
[3]*Department of Agricultural Chemistry, The University of Agriculture Peshawar, Pakistan*
[4]*School of Life Sciences, Department of Food Science and Biotechnology, Sejong University, Seoul 05006, Republic of Korea*

Correspondence should be addressed to Fei Ke; kefei@ahau.edu.cn and Jing Zhu; zhujing@ahau.edu.cn

Received 16 July 2019; Revised 31 August 2019; Accepted 18 September 2019; Published 27 October 2019

Academic Editor: Ilaria Fratoddi

Metal-organic frameworks (MOFs) are an intriguing class of porous inorganic-organic hybrid networks synthesized from metal ions with multidentate organic ligands. MOFs have uniform and tunable cavities and tailorable chemistry, making them promising materials for hazardous component removal from the environment. Controllable integration of magnetic nanoparticles (NPs) and MOFs is leading to the creation of many novel multifunctional MOF-based composites, which exhibit advanced performance that is superior to both of the individual units. This review summarizes the recent significant advances in the development of MOF-based magnetic heterostructure materials for the removal of hazardous contaminants from the environment. The successful methods reported till date for the magnetic MOF synthesis are also provided. In the final section, we provide our views on the future development of the magnetic MOF heterostructure materials for the pollution management.

1. Introduction

In recent years, environmental pollution is increasing and posing serious threat to the ecosystem and human health [1]. Inorganic pollutants such as heavy metal ions in water have drawn much attention due to their long half-life and nonbiodegradability. For these reasons, numerous technologies have been developed for water purification, such as ion exchange [2], biological treatment [3], chemical precipitation [4], and reverse osmosis [5]. Although these technologies are effective, their practical applications are usually hampered by the high cost and poor selectivity. On the other hand, dyes are considered as serious organic pollutants, which are produced by various industrial wastewater such as textile, leather, printing, plastics, cosmetics, pharmaceutical, and food wastewater [6, 7]. The presence of dyes not only gives rise to high visibility but also can reduce the solubility of gas in water and even more has a strong toxicity and carcinogenicity to the human body. Therefore, the removal of inorganic and organic pollutants from wastewater is very necessary for water safety and human health protection. Compared with these methods, adsorption is considered as an ideal pollution treatment method due to its low cost, strong universality, and simple operation [8]. Traditional adsorbents, such as zeolite, metal oxide, and activated carbon, cannot show satisfactory adsorption capacity or require long contact time [9, 10]. Hence, the development of a novel high efficiency adsorbent with large capacity will be an important challenge.

Metal-organic frameworks (MOFs) are constructed by ditopic or polytopic organic ligands and transition metal ions or clusters [11]. Owning to their diverse structures, adjustable aperture, large surface area, and coordinated unsaturated metal sites, MOFs have been widely used in social and industrial fields, such as gas storage [12], separation [13], catalysis [14], sensing [15], and drug delivery [16]. In particular,

adsorption is one of the most potential applications for MOFs during the past 20 years. Compared with traditional adsorbents, MOFs have huge porosity and tunable pore sizes, endowing highly selective adsorption of hazardous contaminants from the environment [17]. However, these novel MOF-based adsorbents are difficult to be recycled from the mixture solution. To overcome this problem, combining MOFs with magnetic nanoparticles (NPs) has been made due to their high adsorption capacity, easy functionality, and easy isolation with an external magnetic field. The methods of preparing magnetic MOF composites include the hydrothermal method [18] and layer-by-layer assembly method [19]. These composite materials have the magnetic response on the basis of magnetic particles, which facilitates product recovery and lower operational cost in MOF separation. Moreover, the components of MOF-based magnetic composites can be easily engineered [20–22]. Hence, compared to conventional adsorbents used in the environmental pollution treatment, the MOF-based magnetic adsorbents are more suitable for industrial applications. Although magnetic composites at the industrial scale are still facing great challenges, numerous magnetic particles are commercially available, making the magnetic MOFs compatible with commercial applications in the near future [23].

In this review, we summarize the recent significant progress in the development of MOF-based magnetic nanocomposites for hazardous contaminant removal from the environment (Figure 1). The structures, properties, and the methods for the synthesis of the magnetic nanocomposites are discussed briefly. Particular challenges of MOF-based magnetic NPs for further development toward adsorption applications are critically discussed.

2. Design and Synthesis of Magnetic NP@MOF Structure

Magnetic metal-organic framework nanocomposites are new functional materials that have emerged in recent years [24]. They are composed of porous MOFs and magnetic NPs. It not only retains the structure and performance of the MOF material but also increases the magnetic properties of the granular material. It can be separated and recovered from the mix aqueous solution or soil by using a magnet and has the advantages of high selectivity, good dispersion, and multiple reuse [25]. It can be recycled again and is in line with the green concept. The synthesis of magnetic NP@MOFs generally can be seen as the following four methods.

2.1. Presynthesized Magnetic NP Template Method. In this method, the presynthesized magnetic NPs are used as seeds to grow MOFs. Firstly, the presynthesized magnetic NPs should be functionalized by capping agents or surfactants. For instance, Li et al. reported MOF-5@SiO_2@Fe_3O_4 core-shell magnetic catalysts, which were prepared through coating the typical MOF-5 on the surface of SiO_2@Fe_3O_4 NPs [26]. The results displayed that the as-synthesized magnetic core-shell nanocomposites can be easily separated from the mixture reaction system by a magnet. Zhao et al. also reported the synthesis of magnetic Fe_3O_4@MOF and demonstrated as an immobilization vector for enzymes [27]. Fe_3O_4 NPs were functionalized by the polydopamine (PDA) layer, and then $Cu_3(btc)_2$ was synthesized on the surface of Fe_3O_4@PDA by introducing Fe_3O_4@PDA into an ethanol solution containing copper acetate and 1,3,5-benzenetricarboxylic acid (Figure 2). The MOF shell has a large surface area to ensure high load carrying capacity. Due to the strong affinity for the enzyme, the Fe_3O_4@PDA@[$Cu_3(btc)_2$]-enzyme composites achieved excellent digestion efficiency, good reusability, durability, and reproducibility.

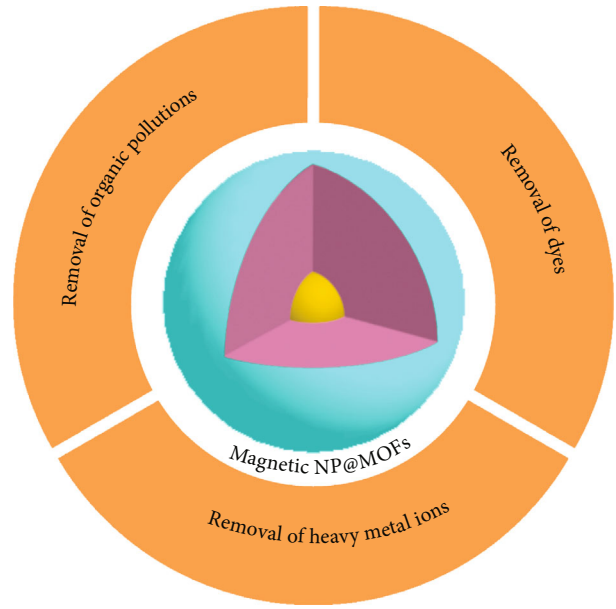

Figure 1: Schematic illustration of magnetic NP@MOF heterostructure for hazardous contaminant removal from the environment.

2.2. Step-by-Step Method. Our group fabricated a series of Fe_3O_4@MOFs (e.g., Fe_3O_4@$Cu_3(btc)_2$, Fe_3O_4@MIL-100(Fe), and Au-Fe_3O_4@MIL-100(Fe)) core-shell nanocomposites with a controllable MOF shell thickness by the versatile step-by-step strategy (Figure 3) [28–30]. Functionalization of magnetic Fe_3O_4 core with the mercaptoacetic acid (MAA) before the coating process was vitally important during the initial stage of the step-by-step assembly, because no core-shell structures could be obtained using the unfunctionalized magnetic Fe_3O_4 core [28]. The growth of MOF shell on the MAA-functionalized Fe_3O_4 core can be initiated by first the metal ions binding to the MAA on the Fe_3O_4 surface, to which then the organic ligands from the solution bind. The thickness of the MOF shell can be facile controlled by tuning the number of step-by-step assembly cycles. Zhang et al. also prepared the novel porous Fe_3O_4@MIL-100(Fe) core-shell nanospheres by this method to achieve large enrichment capacity and high size exclusion selectivity for phosphopeptides [31].

2.3. Self-Template Method. In the self-template method, the magnetic metal or metal oxide composites will provide metal ions by sacrificing themselves and then coordinate to organic ligand. For example, Fe_3O_4@SiO_2@HKUST-1 magnetic core-

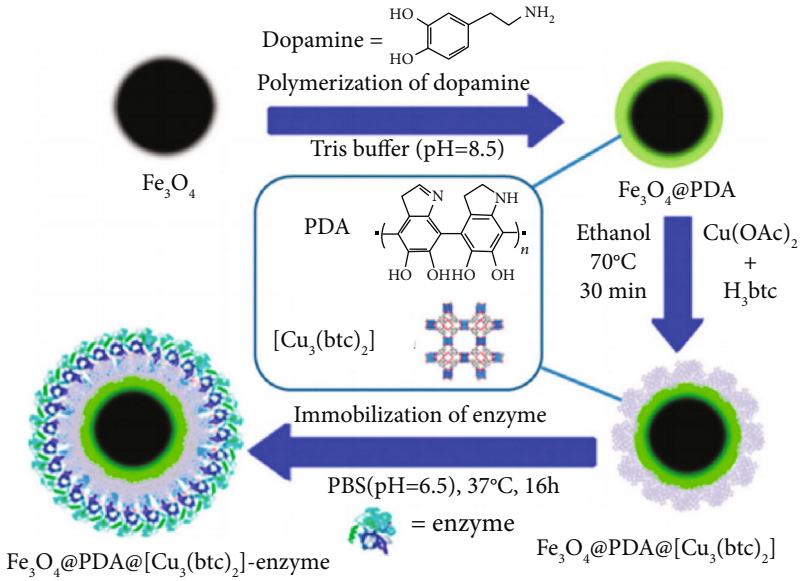

Figure 2: Schematic illustration of Fe_3O_4@PDA@$[Cu_3(btc)_2]$ microspheres and the procedure for enzyme immobilization. Reprinted from Ref. [27] with permission of the Royal Society of Chemistry.

shell composite has been obtained by the self-template strategy in which magnetic Fe_3O_4@SiO_2 were first coated with $Cu(OH)_2$ shell as the sacrificial template and then HKUST-1 grew around the core [32]. Here, $Cu(OH)_2$ shell not only was the sacrificial template but also provides copper ion sources for the formation of HKUST-1 [32]. Compared to other template strategies, this approach shows decisive economy advantage and does not require additional surface modification. Moreover, the Bi-I-functionalized Fe_3O_4@SiO_2@HKUST-1 magnetic composite exhibited excellent adsorption for Hg^{2+} from water (Figure 4). By using this method, Cai and coworkers also reported the novel magnetic Prussian blue (PB) composite using the self-template method [33]. PB cube was used both as the sacrificial template and as the iron source of Fe_3O_4 for the formation of PB-Fe_3O_4 composite.

2.4. Dry Gel Conversion Method. Tan et al. demonstrated a dry gel conversion (DGC) method to fabricate HKUST-1/Fe_3O_4 composites for desulfurization and denitrogenation applications [34]. In this method, the solvent is first separated from the mixed Fe_3O_4 and MOF precursors, and then solvent vapor is generated into the mixture to induce MOF formation around magnetic NPs. With this simple method, HKUST-1/Fe_3O_4 composites have been successfully constructed without blockage of the MOF pores (Figure 5). Significantly, the obtained magnetic porous adsorbents not only can undergo efficient adsorption of various aromatic sulfur and nitrogen compounds from model fuels but also can be easily separated from mixture by an external magnetic field.

3. Applications of Magnetic NP@MOF Composites in the Environment

MOF-based magnetic nanostructures have been widely used for many applications due to their outstanding physicochemical performance [24]. In this review, we are particularly interested in applying these magnetic composites as sustainable environment adsorbents. Environmental pollution has become one of the major problems worldwide at present. Due to the decline of water quality, water bodies continue to deteriorate, leading to the suspension of relevant factories and agricultural production. The adverse social impact and economic loss caused threaten the sustainable development of society and the healthy development of mankind. There are a large number of organic, inorganic, and biological pollutants in water and soil, such as herbicides [35] and dyes [36]. The advantages of magnetic NP@MOF composites for the adsorption of hazardous materials from the environment will be discussed in later sections. Further, we will also point out the state-of-the-art progress in magnetic NP@MOF composite adsorption applications categorized by the hazardous compound type.

3.1. Adsorption of Organic Contaminants. Magnetic NP@MOF composites are promising porous adsorbents for the adsorption of organic contaminants from the environment due to their magnetic core for easy magnetic separation along with porous MOF shell for highly selective removal of contaminants. For example, Zhou et al. developed a novel magnetic Fe_3O_4@MIL-100(Fe) NPs for mechanochemical magnetic solid phase extraction (MCMSPE) of organochlorine pesticides from tea leaves [37]. Fe_3O_4@MIL-100(Fe) magnetic NPs were synthesized by the step-by-step method and further successfully used for the separation of organochlorine pesticides from tea. Moreover, Fe_3O_4@MIL-100(Fe) magnetic NPs can be reused with no significant changes in the organochlorine pesticide recovery after five adsorption cycles. The results indicated that such magnetic NPs are ideal recyclable adsorbents for removal of organochlorine pesticides from plant samples. In the same time, Fe_3O_4@SiO_2@Zr-MOF magnetic composites were also reported for

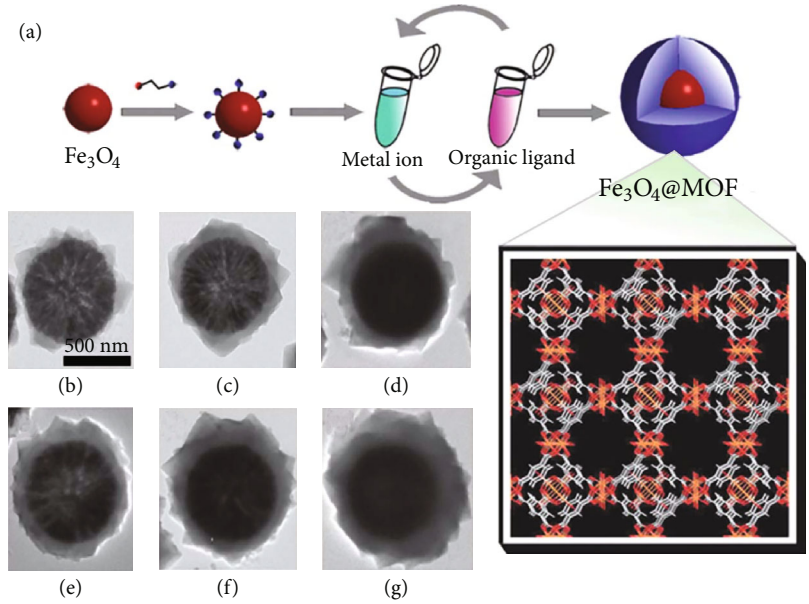

FIGURE 3: Schematic representation of the step-by-step assembly strategy (a) and TEM images of Fe_3O_4@$[Cu_3(btc)_2]$ core-shell magnetic microspheres after (b) 10, (c) 20, (d) 25, (e) 30, (f) 40, and (g) 50 assembly cycles at 25°C. Reprinted from Ref. [28] with permission of the Royal Society of Chemistry.

the effective removal of pharmaceutical compounds from water [38]. The obtained Fe_3O_4@SiO_2@UiO-66-NH_2 displayed a high adsorption capacity and rapid separation rate for the adsorption of salicylic acid (SA) and acetylsalicylic acid (ASA) due to the magnetic NPs in combination with porous Zr-MOF (Figure 6). The saturated magnetization value of Fe_3O_4@SiO_2@UiO-66-NH_2 was measured to be 25.4 emu g^{-1}. The easy separation, high capacities, and reusability of the magnetic Zr-based MOF make it as superior adsorbents for removal of pharmaceutical contaminants.

Based on a similar process, four other magnetic composites, magG@SiO_2@ZIF-8 [39], Fe_3O_4@SiO_2@MOF/TiO_2 [40], Fe@SiO_2@MOF-5 [41], and Fe_3O_4@m-SiO_2/PSA@Zr-MOF [42], were successfully synthesized based on the magnetic NPs coated with a layer of SiO_2. The magnetic NPs@SiO_2 cores help adsorption of metal ions and organic linkers for the growth of outer shell of MOF layers. The magG@SiO_2@ZIF-8 composites displayed high extraction efficiency and reusability for adsorption of phthalate esters with the linear range of 50-8000 ng mL^{-1} and up to 92% recoveries [39]. Fe_3O_4@SiO_2@MOF/TiO_2 [40] and Fe@SiO_2@MOF-5 [41] core-shell nanocomposites were used as efficient adsorbents for MSPE of five triazole fungicides as well as N- and S-containing polycyclic aromatic hydrocarbons from contaminated water. Here, TiO_2 immobilized on the surface of Fe_3O_4@SiO_2@MOF could enhance the adsorption properties of magnetic MOF with the detection and quantification limits of 0.19-1.20 ng L^{-1} and 0.61-3.62 ng L^{-1}, respectively [40]. The Fe@SiO_2@MOF-5 exhibited a good adsorption for N- and S-containing polycyclic aromatic hydrocarbons with LODs in the range of 0.025-0.033 μg L^{-1} [41]. In addition to these, Xu and coworkers developed a novel Fe_3O_4@m-SiO_2/PSA@Zr-MOF magnetic nanocomposite for bifenthrin determination from water [42]. Considering the outstanding performance and limitless of MOFs, it is expected that such MOF-based magnetic core-shell nanocomposites will open a new doorway in the field of adsorption of organic contaminants from the environment.

3.2. Adsorption of Dyes from Wastewater. Dye has become an important industrial hazardous contaminant in water. In recent years, with the development of the dye industry, it has a great adverse impact on the environment and human health. Therefore, it is crucial to devise a strategy for the treatment and removal of these dyes from polluted water. Wang et al. reported the use of magnetic Fe_3O_4/MIL-101(Cr) composite for effective adsorption of two dyes, acid red 1 (AR1) and orange G (OG) [6]. They fabricated Fe_3O_4/-MIL-101(Cr) magnetic composites by a reduction-precipitation method with large surface areas, strong magnetism, and excellent dispersion effect. The adsorption capacities of AR1 and OG with Fe_3O_4/MIL-101(Cr) were 142.9 and 200.0 mg g^{-1}, respectively [6]. The authors suggested that the adsorption of AR1 and OG was spontaneous, exothermic, and randomness decreased with monolayer adsorption during this process. Very recently, perfect $MgFe_2O_4$@MOF [43] and Fe_3O_4@SiO_2@Zn-TDPAT [44] core-shell magnetic materials were reported by the presynthesized magnetic NP template method. The $MgFe_2O_4$@MOF magnetic composites were fabricated by a mercaptoacetic acid- (MAA-) functionalized $MgFe_2O_4$ NPs as the template method [43]. The obtained $MgFe_2O_4$@MOF hybrid nanomaterials displayed excellent removal of Rhodamine B (RB, 219.78 mg g^{-1}) and Rhodamine 6G (Rh6G, 306.75 mg g^{-1}) from wastewater. Moreover, these magnetic hybrid nanomaterials showed good reusability even after 10 times reused. The as-synthesized Fe_3O_4@SiO_2@Zn-TDPAT core-shell magnetic material also displayed a high performance activity in adsorption of polluted dyes [44]. The adsorption efficiencies can reach 100 and 99% for Congo red (CR) and methylene blue (MB) by this

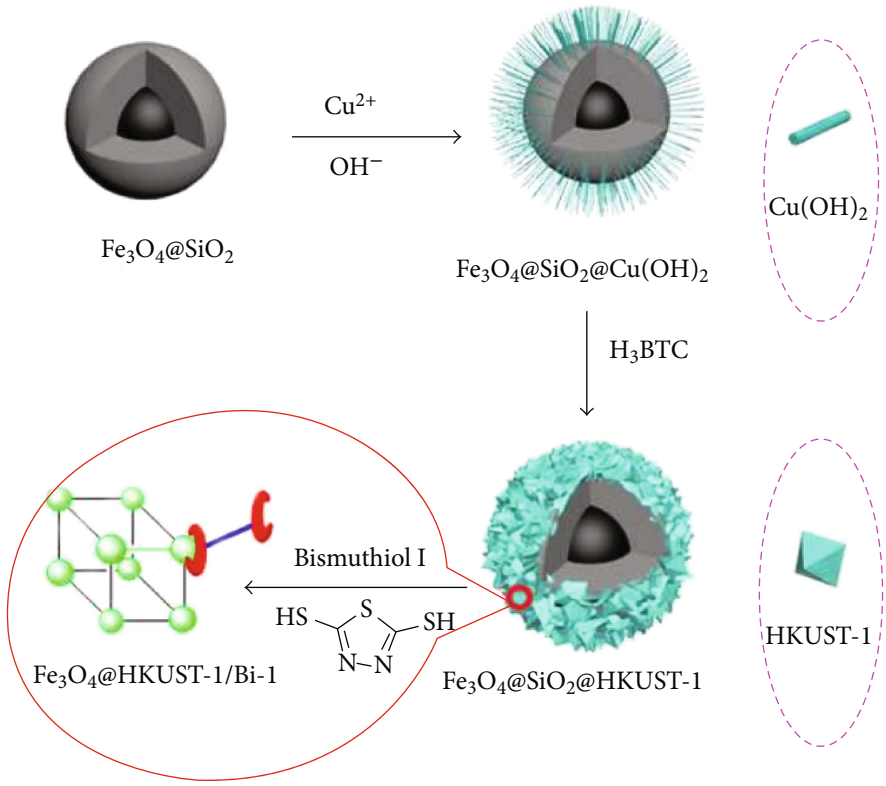

Figure 4: Scheme of the preparation of Bi-I functionalized Fe_3O_4@SiO_2@HKUST-1 composites. Reprinted from Ref. [32] with permission of the Royal Society of Chemistry.

magnetic material, respectively. Significantly, such Fe_3O_4@SiO_2@Zn-TDPAT core-shell magnetic material can be stable under different acid-alkaline conditions. The results suggested that MOF-based magnetic core-shell materials are promising adsorbents for dye removal from wastewater.

These MOF-based magnetic composites have high capacity toward a certain dye; the application of selective removal of specific dye from a mixture of multiple dye-polluted water needs more development. In 2018, Yang et al. reported a novel Fe_3O_4-PSS@ZIF-67 magnetic core-shell composite for selective adsorption of methyl orange (MO) from MO and methylene blue (MB) mixed solution (Figure 7) [45]. The results demonstrated that the adsorption capacity of the magnetic composites for MO was measured to be 738 mg g^{-1} with the separation rate of up to 92%. The selective adsorption mechanism can be attributed to charge-selectivity between the dye molecule and the MOF. The sizes of the MO and MB molecules are $1.54 \times 0.48 \times 0.28$ nm^3 and $1.38 \times 0.64 \times 0.21$ nm^3, while ZIF-67 has pore cage of 1 nm. Therefore, MO and MB molecules can be adsorbed in the pore cage of Fe_3O_4-PSS@ZIF-67. Furthermore, the negatively charged MO can be adsorbed with the Lewis base of Co^{2+} centrals because of the electrostatic attraction while the positively charged MB is hard to be adsorbed because of the electrostatic repulsion.

3.3. Adsorption of Heavy Metal Ions. Recently, MOF-based magnetic composites have been also used as porous adsorbents for the removal of heavy metal ions from the environment. MOF-based magnetic composites are promising adsorbents for the removal of heavy metal ions because of their easy modification and isolation. Karimi et al. reported a chemical bond between the $NHSO_3H$-functionalized Fe_3O_4 and the HKUST-1 method for the synthesis of magnetic Fe_3O_4-$NHSO_3H$@HKUST-1 nanocomposites for the adsorption of lead ions (Pb^{2+}) from wastewater [46]. According to this work, the maximum adsorption capacity of Pb^{2+} with Fe_3O_4-$NHSO_3H$@HKUST-1 was 384.6 mg g^{-1}, which corresponds to 46.3% of the magnetic adsorbent occupied sites. After the adsorbent is separated by the magnet and washed with 0.1 M of HCl and distilled water, it can be used for another adsorption experiment. As a result, Fe_3O_4-$NHSO_3H$@HKUST-1 could be reused four times without significant loss of adsorption activity (>90%). Huang et al. reported two amino-modified Zr-based magnetic MOF composites (Fe_3O_4@SiO_2@UiO-66-NH_2 and Fe_3O_4@SiO_2@UiO-66-Urea) for the extraction of heavy metal ions [47]. Fe_3O_4@SiO_2@UiO-66-NH_2 and Fe_3O_4@SiO_2@UiO-66-Urea were prepared by a simple one-pot strategy with different precursors. The obtained amine-decorated magnetic composites exhibited high adsorption for heavy metal ions compared to pure magnetic composites. In particular, Fe_3O_4@SiO_2@UiO-66-NH_2 showed the highest adsorption capacity for Pb^{2+} (102 mg g^{-1}). The authors concluded that the improvement in the removal of Pb^{2+} by the amine-decorated magnetic composites compared with Fe_3O_4@SiO_2@UiO-66 is due to

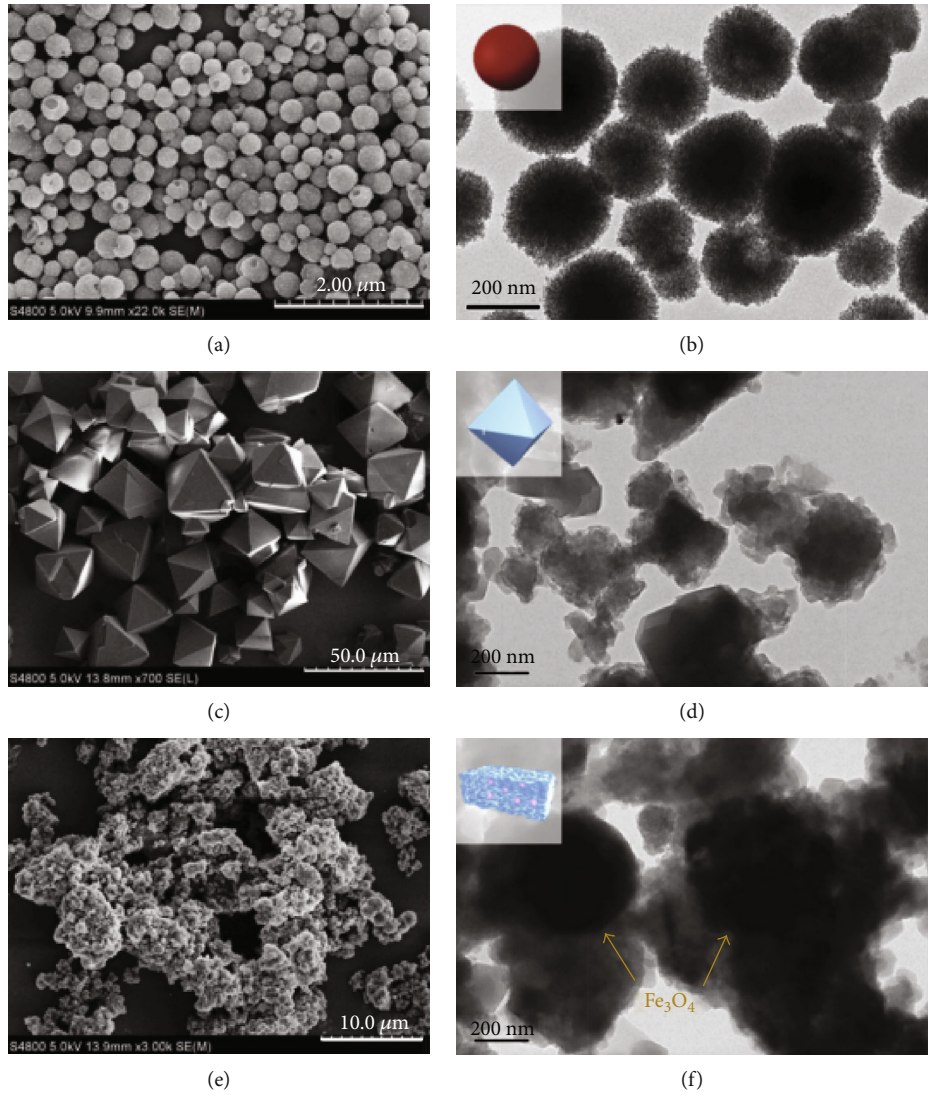

Figure 5: SEM and TEM images of (a, b) Fe_3O_4, (c, d) HKUST-1, and (e, f) the HKUST-1/Fe_3O_4 composites. Reprinted from Ref. [34] with permission of Elsevier.

the fact that the $-NH_2$ groups on the magnetic composites provide more binding sites for the adsorption of Pb^{2+} by chelating. Further, hierarchically HPU-13@Fe_3O_4 (HPU-13 = $\{[Cu_3(L)_2]\cdot OH\cdot 2CH_3CH_2OH\cdot 10H_2O\}n$; HL = 2-(5-pyridin-4-yl-2H-[1,2,4]triazol-3-yl)pyrimidine) magnetic hybrid composites were synthesized for high removal and excellent reuse of Cr(VI) ions from water [48]. HPU-13@Fe_3O_4 showed high adsorption capacities for $Cr_2O_7^{2-}$ (398.41 mg g^{-1}) and CrO_4^{2-} (471.69 mg g^{-1}). The results proved that oxidation of Cu(I) to Cu(II) on the magnetic adsorbents occurred during the adsorption process and partial reduction of Cr(VI) to Cr(III) in the solution at the same time. Finally, the authors revealed that the high adsorption of Cr(VI) under these conditions is due to the synergistic reaction of Cr(VI) reduction and adsorption [48].

The radioactive elements are also a major issue to the environment such as U(VI) and Th(IV). These radioactive metal ions can create numerous diseases including liver and lung cancers. In this case, the adsorption of these metal ions from the environment is a challenge and critical issue for the environmental remediation. Alqadami et al. prepared an Al-based magnetic MOF nanocomposite (Fe_3O_4@AMCA-MIL53(Al)) for the adsorption of U(VI) and Th(IV) from wastewater [49]. The adsorption capacities for U(VI) and Th(IV) were measured to be 227.3 and 285.7 mg g^{-1}, respectively. The adsorption equilibrium time of Fe_3O_4@AMCA-MIL53(Al) for both radioactive metal ions was demonstrated within 90 min. The results suggested the adsorption mechanism for U(VI) and Th(IV) over Fe_3O_4@AMCA-MIL53(Al) through the electrostatic interactions between the organic part of the magnetic nanocomposite and the radioactive metal ions and coordinate interactions between the metal ions and nitrogen in the framework. Min et al. reported a novel Fe_3O_4@ZIF-8 magnetic nanocomposite for selective removal of UO_2^{2+} from water, which showed a high adsorption capacity of 523.5 mg U g^{-1} [50]. Furthermore,

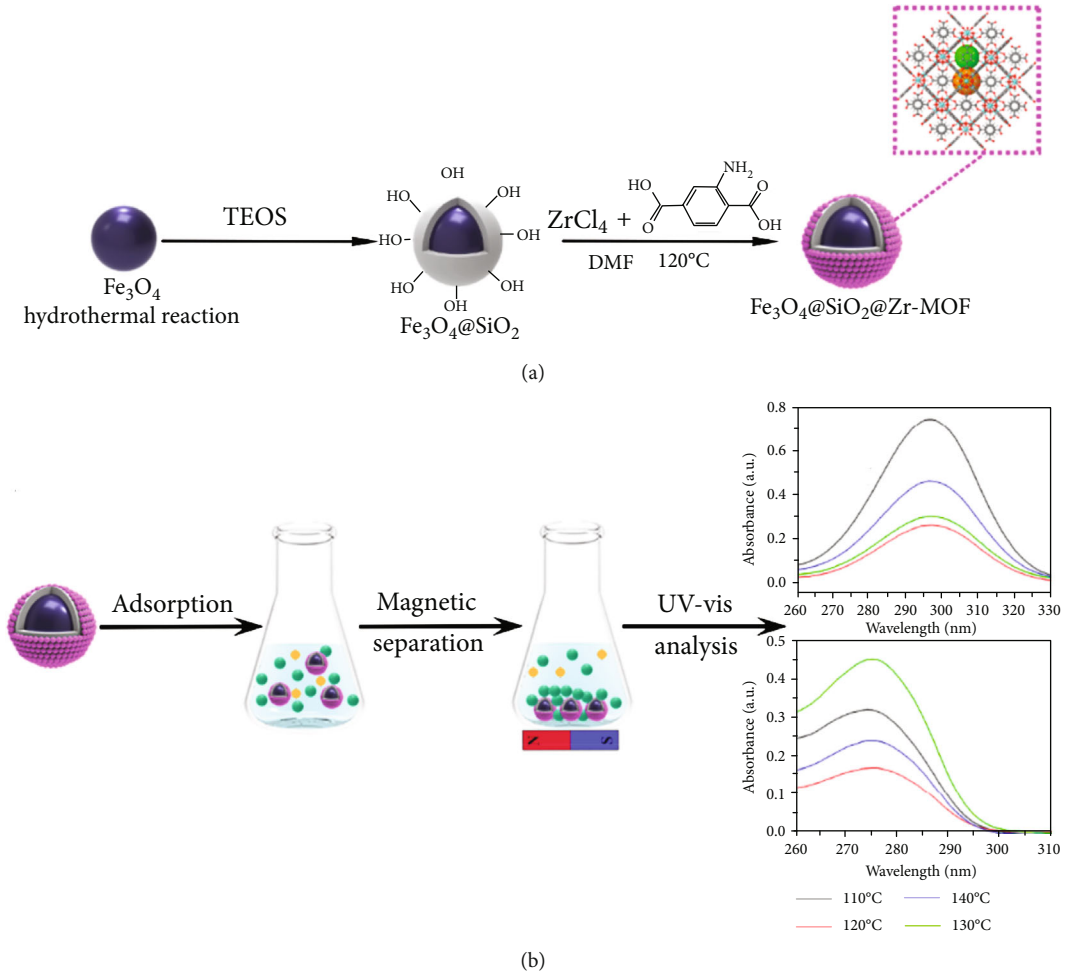

FIGURE 6: Scheme of (a) the preparation of $Fe_3O_4@SiO_2@Zr$-MOF composites and (b) the adsorption of SA and ASA. Reprinted from Ref. [38] with permission of the American Chemical Society.

the selective separation of the UO_2^{2+} from lanthanide results indicated that the obtained $Fe_3O_4@ZIF$-8 displayed remarkable selectivity performance for UO_2^{2+} in the presence of lanthanides at pH 3.

Selectivity is one of the most primary issues of a good adsorbent in the practical application. In order to solve this problem, magnetic adsorbents can be modified by various functional groups for the removal of target metal ions. The functional groups can be easily introduced into the MOF-based magnetic composites by a facile postsynthetic modification (PSM) method. Very recently, we prepared thiol-functionalized $Fe_3O_4@Cu_3(btc)_2$ core-shell magnetic microspheres and investigated their application in selective adsorption of heavy metal ions in the presence of other background ions from water [51]. $Fe_3O_4@Cu_3(btc)_2$ core-shell magnetic microspheres were synthesized by a step-by-step assembly fashion. Further, $Cu_3(btc)_2$ shell of the magnetic microspheres was modified by thiol groups of dithioglycol using such PSM method (Figure 8). Significantly, the thiol-functionalized $Fe_3O_4@Cu_3(btc)_2$ showed high selective adsorption for Pb^{2+} ($K_d = 1.23 \times 10^4$ mL g^{-1}) and Hg^{2+} ($K_d = 5.98 \times 10^4$ mL g^{-1}) in the presence of background ions of Ni^{2+}, Na^+, Mg^{2+}, Ca^{2+}, Zn^{2+}, and Cd^{2+} [51].

4. Adsorption Mechanism

The adsorption method is widely accepted for the removal of hazardous pollutants from the environment [52]. Magnetic MOF composites are superior to the traditional porous materials, due to their rational design, tunable porosity, controllable dimensions, large internal surface area, and easy isolation. Particularly, the pore shape and size of the magnetic MOFs can be controlled to selective adsorption of targeted hazardous molecules [53]. The mechanism for the removal of hazardous pollutants can be summarized as the four major types [17, 53]: (I) The hazardous molecules can be bound to the coordinatively unsaturated metal centers of magnetic MOFs. (II) The hazardous molecules can be adsorbed by π-π stacking interactions between the organic part of the MOFs and the hazardous molecules. (III) There are electrostatic interactions between the hazardous molecules and the magnetic MOFs. (IV) There is molecule bonding between the decorate functional groups on ligands of magnetic MOFs and the hazardous molecules. With the rapid new multifunctional MOF development, the mechanisms for the adsorption of pollutants over the magnetic MOFs become increasingly clear.

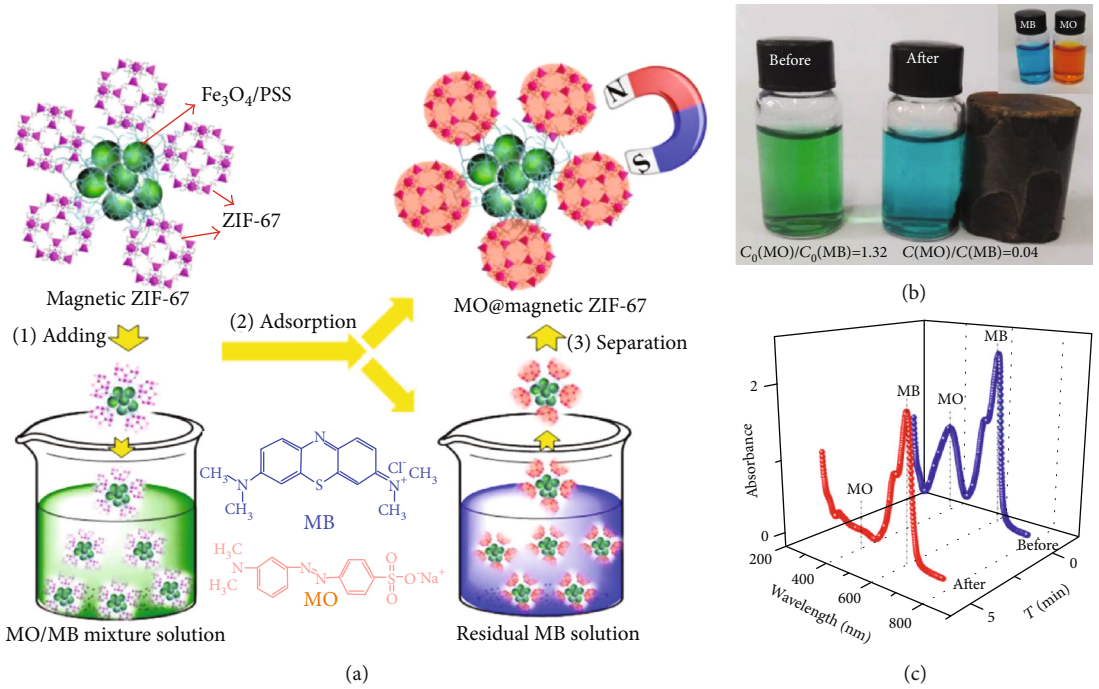

FIGURE 7: (a) Scheme of selective adsorption of MO from the mixed MO/MB solution by Fe_3O_4-PSS@ZIF-67 magnetic composites; photographs (b) and UV-vis spectra (c) of the mixed MO/MB solution before and after magnetic separation. Reprinted from Ref. [45] with permission of Elsevier.

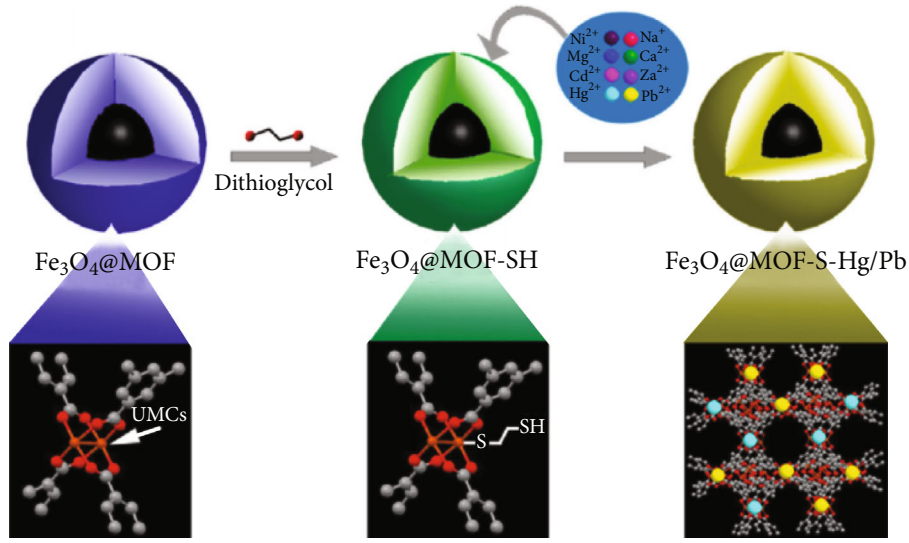

FIGURE 8: Scheme of the preparation of thiol-functionalized Fe_3O_4@$Cu_3(btc)_2$ and its use for selective removal of Pb^{2+} and Hg^{2+} from the mixed heavy metal ion solution. Reprinted from Ref. [51] with permission of Elsevier.

5. Conclusion and Outlook

Here, we summarize a review of recent developments in the MOF-based magnetic nanocomposites for the removal of hazardous contaminants from the environment. The design and synthesis of the magnetic core-shell MOF composites are promising methods to achieve synergies of magnetic particle core and porous MOF shell. Compared with traditional adsorption materials, magnetic MOF adsorbents have a larger specific surface area and more surface active sites and can be quickly and easily recovered by an external magnetic field, which is in line with the modern green concept. Because of these excellent properties, magnetic MOF adsorbents have great application prospects in the removal of hazardous materials from the environment. The magnetic MOF composites with highly selective adsorption of target toxic compounds can be constructed by chemical modification, which will further improve the removal efficiency. This review has demonstrated several synthetic methods for the MOF-based magnetic core-shell composites. However, the

current challenge is that most of the reported magnetic MOFs are still in the small-scale application stage and the far distance from large-scale industrial production and application to safeguard the environment. In addition, the incorporated magnetic particle shape and size are highly desirable, which are key issues for the application in adsorption with high capacity and selectivity. Meanwhile, the understanding of the electronic structure and interactions present between the magnetic core and MOF shell remains a challenge. Furthermore, the exact mechanism of enhanced adsorption activity by the magnetic MOF composites is still unclear. Although challenges still exist, it is expected that with the in-depth development and discussion of the magnetic MOF composites at home and abroad, it will show a broad prospect in the future practical application.

Conflicts of Interest

The authors declare that they have no conflicts of interest.

Authors' Contributions

Gege Zhao and Nianqiao Qin contributed equally to this work.

Acknowledgments

This work was supported by the National Natural Science Foundation of China (NSFC, 21501003), Science and Technology Major Projects of Anhui Province (18030801104), Natural Science Foundation of Anhui Province (1608085QB27), National Undergraduate Training Programs for Innovation and Entrepreneurship of Anhui Agriculture University (201910364013), and Provincial Undergraduate Training Programs for Innovation and Entrepreneurship of Anhui Agriculture University (201810364080).

References

[1] T. Wen, J. Wang, S. Yu, Z. Chen, T. Hayat, and X. Wang, "Magnetic porous carbonaceous material produced from tea waste for efficient removal of As(V), Cr(VI), humic acid, and dyes," *ACS Sustainable Chemistry & Engineering*, vol. 5, no. 5, pp. 4371–4380, 2017.

[2] H. M. Baker, A. M. Massadeh, and H. A. Younes, "Natural Jordanian zeolite: removal of heavy metal ions from water samples using column and batch methods," *Environmental Monitoring and Assessment*, vol. 157, no. 1-4, pp. 319–330, 2009.

[3] A. V. Desai, B. Manna, A. Karmakar, A. Sahu, and S. K. Ghosh, "A water-stable cationic metal–organic framework as a dual adsorbent of oxoanion pollutants," *Angewandte Chemie International Edition*, vol. 55, no. 27, pp. 7811–7815, 2016.

[4] P. Mondal, C. B. Majumder, and B. Mohanty, "Laboratory based approaches for arsenic remediation from contaminated water: recent developments," *Journal of Hazardous Materials*, vol. 137, no. 1, pp. 464–479, 2006.

[5] M. G. Khedr, "Nanofiltration of oil field-produced water for reinjection and optimum protection of oil formation," *Desalination and Water Treatment*, vol. 55, no. 12, pp. 3460–3468, 2015.

[6] T. Wan, P. Zhao, N. Lu, H. Chen, C. Zhang, and X. Hou, "Facile fabrication of Fe_3O_4/MIL-101(Cr) for effective removal of acid red 1 and orange G from aqueous solution," *Chemical Engineering Journal*, vol. 295, pp. 403–413, 2016.

[7] F. P. Almeida, M. B. S. Botelho, C. Doerenkamp et al., "Mesoporous aluminosilicate glasses: potential materials for dye removal from wastewater effluents," *Journal of Solid State Chemistry*, vol. 253, pp. 406–413, 2017.

[8] F. Ke, C. Peng, T. Zhang et al., "Fumarate-based metal-organic frameworks as a new platform for highly selective removal of fluoride from brick tea," *Scientific Reports*, vol. 8, no. 1, p. 939, 2018.

[9] J.-L. Gong, B. Wang, G.-M. Zeng et al., "Removal of cationic dyes from aqueous solution using magnetic multi-wall carbon nanotube nanocomposite as adsorbent," *Journal of Hazardous Materials*, vol. 164, no. 2-3, pp. 1517–1522, 2009.

[10] S. Liu, Y. Ding, P. Li et al., "Adsorption of the anionic dye Congo red from aqueous solution onto natural zeolites modifified with N,N-dimethyl dehydroabietylamine oxide," *Chemical Engineering Journal*, vol. 248, pp. 135–144, 2014.

[11] Q.-L. Zhu and Q. Xu, "Metal–organic framework composites," *Chemical Society Reviews*, vol. 43, no. 16, pp. 5468–5512, 2014.

[12] B. Boukoussa, F. Abidallah, Z. Abid et al., "Synthesis of polypyrrole/Fe-kanemite nanocomposite through in situ polymerization: effect of iron exchange, acid treatment, and CO_2 adsorption properties," *Journal of Materials Science*, vol. 52, no. 5, pp. 2460–2472, 2017.

[13] X. Kuang, Y. Ma, H. Su, J. Zhang, Y.-B. Dong, and B. Tang, "High-performance liquid chromatographic enantioseparation of racemic drugs based on homochiral metal–organic framework," *Analytical Chemistry*, vol. 86, no. 2, pp. 1277–1281, 2014.

[14] R. Kaur, K. Vellingiri, K.-H. Kim, A. K. Paul, and A. Deep, "Efficient photocatalytic degradation of rhodamine 6G with a quantum dot-metal organic framework nanocomposite," *Chemosphere*, vol. 154, pp. 620–627, 2016.

[15] Q. Meng, X. Xin, L. Zhang, F. Dai, R. Wang, and D. Sun, "A multifunctional Eu MOF as a fluorescent pH sensor and exhibiting highly solvent-dependent adsorption and degradation of rhodamine B," *Journal of Materials Chemistry A*, vol. 3, no. 47, pp. 24016–24021, 2015.

[16] R. Ma, P. Yang, Y. Ma, and F. Bian, "Facile synthesis of magnetic hierarchical core–shell structured Fe3O4@PDA-Pd@MOF nanocomposites: highly integrated multifunctional catalysts," *ChemCatChem*, vol. 10, no. 6, pp. 1446–1454, 2018.

[17] N. A. Khan, Z. Hasan, and S. H. Jhung, "Adsorptive removal of hazardous materials using metal-organic frameworks (MOFs): a review," *Journal of Hazardous Materials*, vol. 244-245, pp. 444–456, 2013.

[18] S. Bao, K. Li, P. Ning, J. Peng, X. Jin, and L. Tang, "Synthesis of amino-functionalization magnetic multi-metal organic framework (Fe_3O_4/MIL-101($Al_{0.9}Fe_{0.1}$)/NH_2) for efficient removal of methyl orange from aqueous solution," *Journal of the Taiwan Institute of Chemical Engineers*, vol. 87, pp. 64–72, 2018.

[19] Z. Miao, X. Shu, and D. Ramella, "Synthesis of a Fe_3O_4@P4VP@metal–organic framework core–shell structure and studies of its aerobic oxidation reactivity," *RSC Advances*, vol. 7, no. 5, pp. 2773–2779, 2017.

[20] N. Wang, X.-K. Ouyang, L.-Y. Yang, and A. M. Omer, "Fabrication of a magnetic cellulose nanocrystal/metal–organic framework composite for removal of Pb(II) from water,"

ACS Sustainable Chemistry & Engineering, vol. 5, no. 11, pp. 10447–10458, 2017.

[21] S. K. Elsaidi, M. A. Sinwell, A. Devaraj et al., "Extraction of rare earth elements using magnetite@MOF composites," *Journal of Materials Chemistry A*, vol. 6, no. 38, pp. 18438–18443, 2018.

[22] E. Wu, Y. Li, Q. Huang, Z. Yang, A. Wei, and Q. Hu, "Laccase immobilization on amino-functionalized magnetic metal organic framework for phenolic compound removal," *Chemosphere*, vol. 233, pp. 327–335, 2019.

[23] R. Ricco, L. Malfatti, M. Takahashi, A. J. Hill, and P. Falcaro, "Applications of magnetic metal–organic framework composites," *Journal of Materials Chemistry A*, vol. 1, no. 42, pp. 13033–13045, 2013.

[24] M.-X. Wu, J. Gao, F. Wang et al., "Multistimuli responsive core–shell nanoplatform constructed from Fe_3O_4@MOF equipped with pillar[6]arene nanovalves," *Small*, vol. 14, no. 17, article 1704440, 2018.

[25] H. Zhang, S. Qi, X. Niu et al., "Metallic nanoparticles immobilized in magnetic metal–organic frameworks: preparation and application as highly active, magnetically isolable and reusable catalysts," *Catalysis Science & Technology*, vol. 4, no. 9, pp. 3013–3024, 2014.

[26] Q. Li, S. Jiang, S. Ji, D. Shi, and H. Li, "Synthesis of magnetically recyclable MOF-5@SiO_2@Fe_3O_4 catalysts and their catalytic performance of Friedel–Crafts alkylation," *Journal of Porous Materials*, vol. 22, no. 5, pp. 1205–1214, 2015.

[27] M. Zhao, X. Zhang, and C. Deng, "Rational synthesis of novel recyclable Fe_3O_4@MOF nanocomposites for enzymatic digestion," *Chemical Communications*, vol. 51, no. 38, pp. 8116–8119, 2015.

[28] F. Ke, L.-G. Qiu, Y.-P. Yuan, X. Jiang, and J.-F. Zhu, "Fe_3O_4@-MOF core-shell magnetic microspheres with a designable metal-organic framework shell," *Journal of Materials Chemistry*, vol. 22, no. 19, pp. 9497–9500, 2012.

[29] F. Ke, L.-G. Qiu, and J. Zhu, "Fe_3O_4@MOF core-shell magnetic microspheres as excellent catalysts for the Claisen-Schmidt condensation reaction," *Nanoscale*, vol. 6, no. 3, pp. 1596–1601, 2014.

[30] F. Ke, L. Wang, and J. Zhu, "Multifunctional Au-Fe_3O_4@MOF core-shell nanocomposite catalysts with controllable reactivity and magnetic recyclability," *Nanoscale*, vol. 7, no. 3, pp. 1201–1208, 2015.

[31] Y. Chen, Z. Xiong, L. Peng et al., "Facile preparation of core–shell magnetic metal–organic framework nanoparticles for the selective capture of phosphopeptides," *ACS Applied Materials & Interfaces*, vol. 7, no. 30, pp. 16338–16347, 2015.

[32] L. Huang, M. He, B. Chen, and B. Hu, "A designable magnetic MOF composite and facile coordination-based post-synthetic strategy for the enhanced removal of Hg^{2+} from water," *Journal of Materials Chemistry A*, vol. 3, no. 21, pp. 11587–11595, 2015.

[33] W. Cai, S. Wu, Y. Liu, and D. Li, "A novel Prussian blue-magnetite composite synthesized by self-template method and its application in reduction of hydrogen peroxide," *Applied Organometallic Chemistry*, vol. 32, no. 1, article e3909, 2018.

[34] P. Tan, X.-Y. Xie, X.-Q. Liu et al., "Fabrication of magnetically responsive HKUST-1/Fe_3O_4 composites by dry gel conversion for deep desulfurization and denitrogenation," *Journal of Hazardous Materials*, vol. 321, pp. 344–352, 2017.

[35] R. Zhao, Y. Wang, X. Li et al., "Surface activated hydrothermal carbon-coated electrospun PAN fiber membrane with enhanced adsorption properties for herbicide," *ACS Sustainable Chemistry & Engineering*, vol. 4, no. 5, pp. 2584–2592, 2016.

[36] K. R. Reddy, K. Nakata, T. Ochiai, T. Murakami, D. A. Tryk, and A. Fujishima, "Facile fabrication and photocatalytic application of Ag nanoparticles-TiO_2 nanofiber composites," *Journal of Nanoscience and Nanotechnology*, vol. 11, no. 4, pp. 3692–3695, 2011.

[37] Y. Zhou, J. Zhu, J. Yang et al., "Magnetic nanoparticles speed up mechanochemical solid phase extraction with enhanced enrichment capability for organochlorines in plants," *Analytica Chimica Acta*, vol. 1066, pp. 49–57, 2019.

[38] R. Zhang, Z. Wang, Z. Zhou et al., "Highly effective removal of pharmaceutical compounds from aqueous solution by magnetic Zr-based MOFs composites," *Industrial & Engineering Chemistry Research*, vol. 58, no. 9, pp. 3876–3884, 2019.

[39] Y. Lu, B. Wang, Y. Yan, H. Liang, and D. Wu, "Silica protection–sacrifice functionalization of magnetic graphene with a metal–organic framework (ZIF-8) to provide a solid-phase extraction composite for recognization of phthalate easers from human plasma samples," *Chromatographia*, vol. 82, no. 2, pp. 625–634, 2019.

[40] H. Su, Y. Lin, Z. Wang, Y.-L. E. Wong, X. Chen, and T.-W. D. Chan, "Magnetic metal-organic framework-titanium dioxide nanocomposite as adsorbent in the magnetic solid-phase extraction of fungicides from environmental water samples," *Journal of Chromatography A*, vol. 1466, pp. 21–28, 2016.

[41] Q. Zhou, M. Lei, J. Li, Y. Liu, K. Zhao, and D. Zhao, "Magnetic solid phase extraction of N- and S-containing polycyclic aromatic hydrocarbons at ppb levels by using a zerovalent iron nanoscale material modified with a metal organic framework of type Fe@MOF-5, and their determination by HPLC," *Microchimica Acta*, vol. 184, no. 4, pp. 1029–1036, 2017.

[42] M. Xu, K. Chen, C. Luo, G. Song, Y. Hu, and H. Cheng, "Synthesis of Fe_3O_4@m-SiO_2/PSA@Zr-MOF nanocomposites for bifenthrin determination in water samples," *Chromatographia*, vol. 80, no. 3, pp. 463–471, 2017.

[43] H. Tian, J. Peng, T. Lv, C. Sun, and H. He, "Preparation and performance study of $MgFe_2O_4$/metal-organic framework composite for rapid removal of organic dyes from water," *Journal of Solid State Chemistry*, vol. 257, pp. 40–48, 2018.

[44] R. Wo, Q.-L. Li, C. Zhu et al., "Preparation and characterization of functionalized metal–organic frameworks with core/-shell magnetic particles (Fe_3O_4@SiO_2@MOFs) for removal of Congo red and methylene blue from water solution," *Journal of Chemical & Engineering Data*, vol. 64, no. 6, pp. 2455–2463, 2019.

[45] Q. Yang, S. Ren, Q. Zhao et al., "Selective separation of methyl orange from water using magnetic ZIF-67 composites," *Chemical Engineering Journal*, vol. 333, pp. 49–57, 2018.

[46] M. A. Karimi, H. Masrouri, H. Karami, S. Andishgar, M. A. Mirbagheri, and T. Pourshamsi, "Highly efficient removal of toxic lead ions from aqueous solutions using a new magnetic metal-organic framework nanocomposite," *Journal of the Chinese Chemical Society*, vol. 66, no. 10, pp. 1327–1335, 2019.

[47] L. Huang, M. He, B. Chen, and B. Hu, "Magnetic Zr-MOFs nanocomposites for rapid removal of heavy metal ions and dyes from water," *Chemosphere*, vol. 199, pp. 435–444, 2018.

[48] H. Li, Q. Li, X. He et al., "The magnetic hybrid Cu(I)-MOF@-Fe_3O_4 with hierarchically engineered micropores for highly efficient removal of Cr(VI) from aqueous solution," *Crystal Growth & Design*, vol. 18, no. 10, pp. 6248–6256, 2018.

[49] A. A. Alqadami, M. Naushad, Z. A. Alothman, and A. A. Ghfar, "Novel metal–organic framework (MOF) based composite material for the sequestration of U(VI) and Th(IV) metal ions from aqueous environment," *ACS Applied Materials & Interfaces*, vol. 9, no. 41, pp. 36026–36037, 2017.

[50] X. Min, W. Yang, Y.-F. Hui, C.-Y. Gao, S. Dang, and Z.-M. Sun, "Fe_3O_4@ZIF-8: a magnetic nanocomposite for highly efficient UO_2^{2+} adsorption and selective UO_2^{2+}/Ln^{3+} separation," *Chemical Communications*, vol. 53, no. 30, pp. 4199–4202, 2017.

[51] F. Ke, J. Jiang, Y. Li, J. Liang, X. Wan, and S. Ko, "Highly selective removal of Hg^{2+} and Pb^{2+} by thiol-functionalized Fe_3O_4@metal-organic framework core-shell magnetic microspheres," *Applied Surface Science*, vol. 413, pp. 266–274, 2017.

[52] F. Rouhani and A. Morsali, "Goal-directed design of metal–organic frameworks for HgII and PbII adsorption from aqueous solutions," *Chemistry*, vol. 24, no. 65, pp. 17170–17179, 2018.

[53] S.-W. Lv, J.-M. Liu, C.-Y. Li et al., "Fabrication of Fe_3O_4@UiO-66-SO_3H core–shell functional adsorbents for highly selective and efficient removal of organic dyes," *New Journal of Chemistry*, vol. 43, no. 20, pp. 7770–7777, 2019.

Hindawi
Journal of Nanomaterials
Volume 2019, Article ID 8175803, 8 pages
https://doi.org/10.1155/2019/8175803

Research Article

Preparation of Ag-Coated SiO_2@TiO_2 Core-Shell Nanocomposites and Their Photocatalytic Applications towards Phenol and Methylene Blue Degradation

Ning Fu,[1,2] **Xue-chang Ren**,[1] **and Jian-xin Wan**[1]

[1]*School of Environmental & Municipal Engineering, Lanzhou Jiaotong University, Lanzhou 730070, China*
[2]*Gansu Environmental Monitoring Center, Lanzhou 730020, China*

Correspondence should be addressed to Xue-chang Ren; rxchang1698@hotmail.com

Received 2 July 2019; Accepted 24 August 2019; Published 15 October 2019

Guest Editor: Fei Ke

Ag-coated SiO_2@TiO_2 (Ag-SiO_2@TiO_2) core-shell nanocomposites were synthesized by a two-step method, which combined hydrothermal process and photodeposition. The morphology, structure, composition, and optical properties of the Ag-coated SiO_2@TiO_2 nanocomposites were extensively characterized by field-emission scanning microscopy (FE-SEM), transmission electron microscopy (TEM), energy-dispersive X-ray spectroscopy (EDS), X-ray diffraction (XRD), X-ray photoelectron spectroscopy (XPS), and Fourier-transform infrared spectra (FT-IR spectra). The anatase TiO_2 nanoparticles (5-10 nm) with high surface area were loaded on SiO_2 spheres (200-300 nm) in the form of SiO_2@TiO_2 core-shell nanoparticle with a porous shell of controlled thickness (10–30 nm). Ag nanoparticles of different mass concentrations were photodeposited on SiO_2@TiO_2 core-shell structure with particle sizes of about 10-20 nm. The results showed that Ag nanoparticles increased the photocatalytic activity of SiO_2@TiO_2 core-shell nanoparticle improved the degradation of phenol and methylene blue under UV irradiation. The experimental results showed that Ag nanoparticles with mass concentrations of 6% had the highest photocatalytic activity on SiO_2@TiO_2 core-shell nanoparticles.

1. Introduction

Titanium dioxide (TiO_2), because of its high chemical stability, easy availability, and nontoxicity, is one of the most important semiconductor photocatalysts [1–3]. Using of high surface area TiO_2 as a photocatalyst for the degradation of contaminants has attracted intense attention and has been widely used [4–6]. However, the degradation efficiency of TiO_2 is restricted by the large bandgap (3.2 eV) and the high recombination rate of photogenerated electron-hole pairs tend to reduce the full use of UV and solar energy [7–9]. Besides, it is difficult to recycle the TiO_2 particles from solution after photodegradation. In order to eliminate these obstacles, larger SiO_2 particles were chosen as the carrier for the dispersion of TiO_2 nanoparticles due to its thermal stability, high chemical inertia, large specific surface area, and high adsorption, which are beneficial to the interfacial reaction of the composite material [10–12]. Compared with TiO_2 catalyst, SiO_2@TiO_2 core-shell nanoparticles have good photocatalytic activity as photocatalyst [13, 14].

Noble metals such as Ag, Au, and Pt were deposited on the surface of TiO_2 nanoparticles, thereby suppressing the recombination of electron-hole pairs, prolonging the lifetime of the electron-hole pairs and improving its degradation efficiency [15–19]. Among noble metals, Ag has been proved as an effective doping metal on the surface of TiO_2 nanoparticles to improve photocatalytic efficiency due to its high work function and its ability to generated surface plasmons at desired wavelengths [20]. In addition, Ag is not only easy to attach to the surface of SiO_2@TiO_2 spheres but also stable and easily available [21–25].

Previous studies on Ag-TiO_2-SiO_2 photocatalysts mostly deposited Ag nanoparticles on agglomerated SiO_2/TiO_2 nanocomposites with irregular shape and size [26–28], ignoring Ag-TiO_2-SiO_2 nanoparticles with uniform shape and size [29–31]. Besides, few studies focused on the degradation

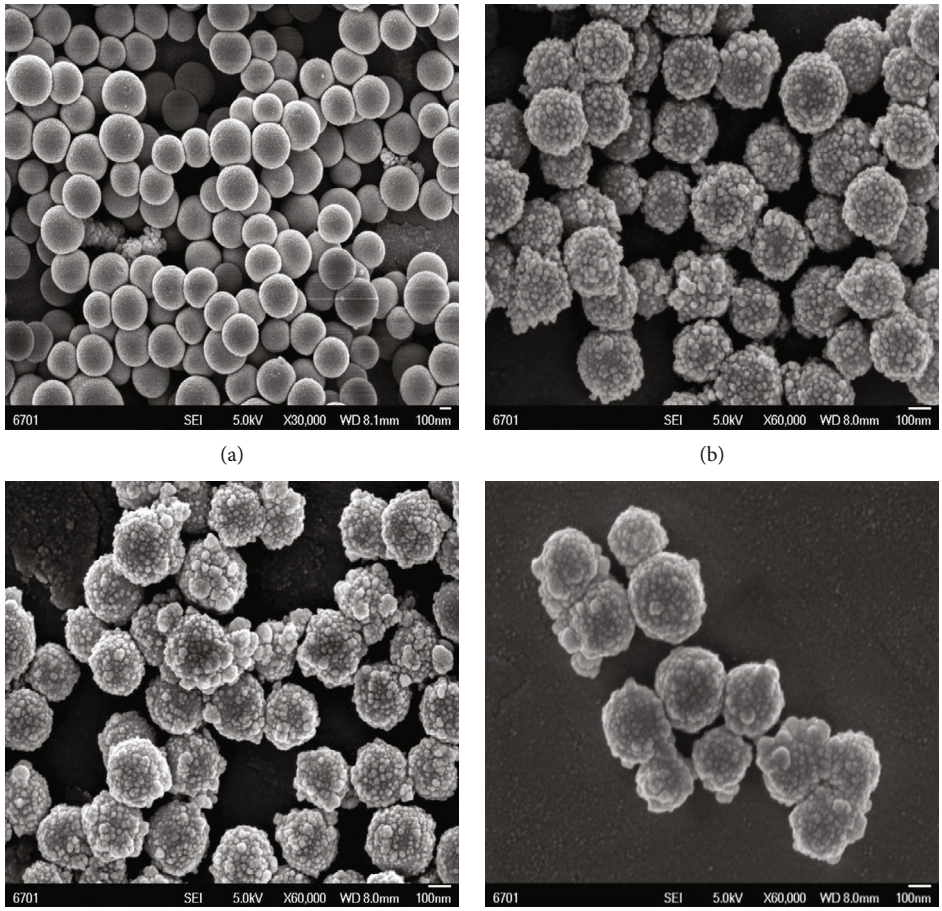

Figure 1: SEM images of (a) SiO_2, (b) SiO_2@TiO_2 core-shell particles, and (c, d) 6 wt.% Ag-coated SiO_2@TiO_2.

substrates towards both colorless organic matters (such as phenol) and colored organic dyes (such as methylene blue) with higher photocatalytic efficiency.

Here, the TiO_2 nanoparticles were coated on the SiO_2 spheres by hydrothermal method using SiO_2 as core to increase the surface area. Further, Ag-coated SiO_2@TiO_2 nanocomposites were synthesized by photodeposited Ag nanoparticles on the SiO_2@TiO_2 composite spheres with uniformity in size and shape. The surface morphology of the Ag-coated SiO_2@TiO_2 nanocomposite was investigated by transmission electron microscopy (TEM) and scanning electron microscopy (SEM). The photocatalytic activity toward the degradation of phenol and methylene blue under UV light was tested.

2. Experimental

2.1. Chemicals. In this study, analytical-grade chemicals were used without further purification. Tetraethyl orthosilicate (TEOS; 99.9%) was purchased from XiYa Reagent company, titanium (IV) isopropoxide (TTIP; 95%) was obtained from Sigma-Aldrich, silver nitrate ($AgNO_3 \cdot 6H_2O$; 99%), isopropanol, ethanol, NH_4OH (25%), sodium bromide, phenol, and methylene blue (MB) were manufactured by Sinopharm Chemical Reagent company.

2.2. Synthesis of SiO_2 Spheres. The SiO_2 spheres were prepared according to the literature [30]. Typically, 15 mL H_2O and 4 mL NH_4OH (25%) were added to 100 mL ethanol in a Teflon reactor and left under magnetic stirring for 30 min. Then, 3.0 mL of TEOS was quickly added to the above mixture and stirred at room temperature ($25 \pm 2^{\circ}C$) for 3 h. Then, the mixture was neutralized with 5 mol L^{-1} HCl and centrifuged at 4000 rpm for 10 min. The SiO_2 spheres were separated by centrifugation and washed four times with ethanol and distilled water. The resulting precipitate was dried at 70°C for at least 20 h to obtain SiO_2 spheres.

2.3. Synthesis of SiO_2@TiO_2 Core-Shell Nanoparticles. The SiO_2@TiO_2 core-shell nanoparticles were also fabricated according to the literatures with minor modifications [30]. The synthesis process is as follows: 1.0 g SiO_2 powder was dried at 110°C for 1 h and then sonicated in 80 mL isopropanol for 1 h. Then, 1.0 mL titanium isopropoxide (TTIP) was quickly added and kept under magnetic stirring for 24 h. Subsequently, 15 mL water–alcohol mixture (5 mL H_2O : 10 mL isopropanol) was slowly added (2 mL min^{-1}) and magnetically stirred for 3 h. The resulting precipitate was washed once with isopropanol and subsequently twice with deionized water at 8000 rpm. The amorphous TiO_2 shell was crystallized by hydrothermal treatment. The resulting

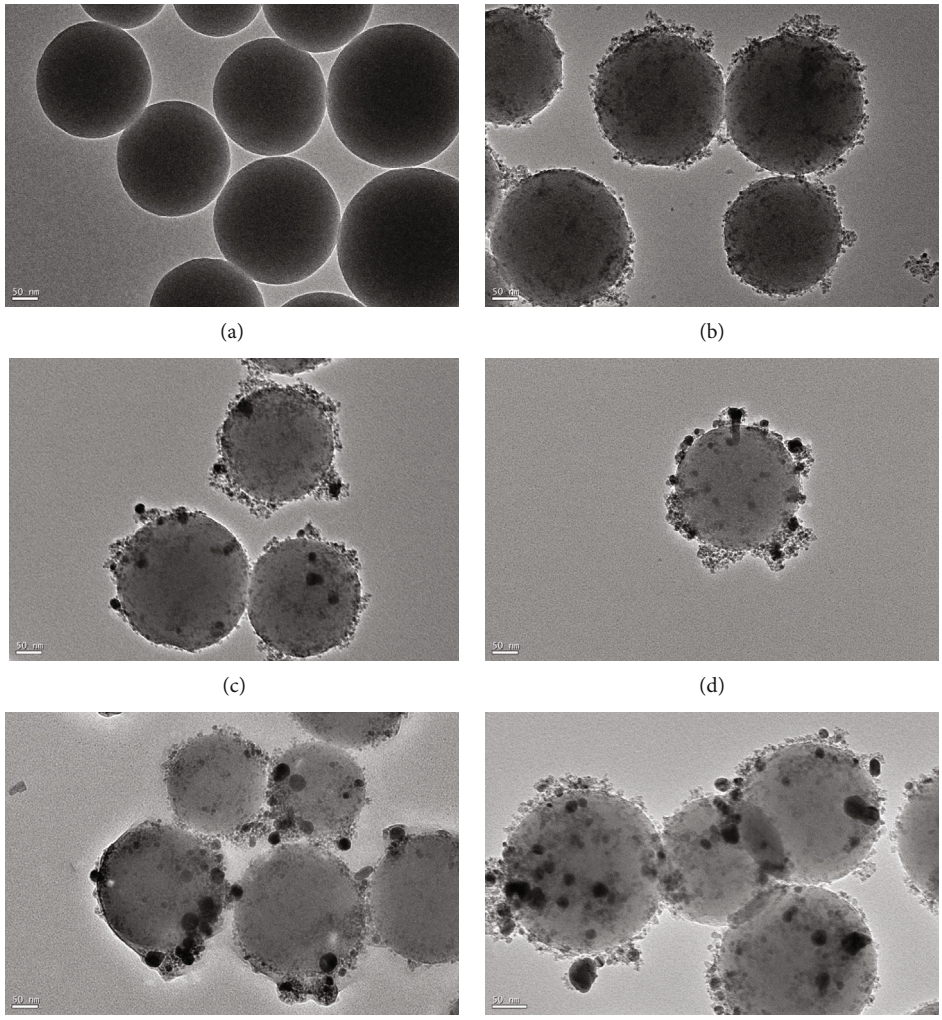

Figure 2: TEM images of (a) SiO_2, (b) SiO_2@TiO_2 core-shell particles, (c) 1 wt.% Ag-coated SiO_2@TiO_2 photocatalysts, (d) 3 wt.% Ag-coated SiO_2@TiO_2 photocatalysts, (e) 6 wt.% Ag-coated SiO_2@TiO_2 photocatalysts, and (f) 9 wt.% Ag-coated SiO_2@TiO_2 photocatalysts.

amorphous SiO_2@TiO_2 core-shell nanoparticles were suspended in 50 mL H_2O, treated at 105°C for 24 h, and then centrifuged again at 8000 rpm for 10 min. The obtained precipitate was dried at 70°C for 20 h, and finally calcined at 450°C for 2 h. The unsupported TiO_2 was also prepared using 3 mL of TTIP by the same procedure used for the preparation of SiO_2@TiO_2 core-shell nanoparticles but in the absence of SiO_2 in the reaction mixture.

2.4. Synthesis Ag-Coated SiO_2@TiO_2 Core-Shell Nanoparticles. Different concentrations of Ag particles were deposited on SiO_2@TiO_2 core-shell nanoparticles by photodeposition. 0.2 g SiO_2@TiO_2 composite spheres were dispersed by ultrasonication in 80 mL ethanol for 1 h. 0.340 g silver nitrate was dissolved in 50 mL deionized water with the concentration of 2 mM. The various amounts of silver nitrate were then added into the suspension of SiO_2@TiO_2 core-shell nanoparticles such that the Ag^+ concentration was maintained at 1, 3, 6, and 9 wt.% relative to the SiO_2@TiO_2. The above solution mixtures were then placed under a high-pressure Hg UV lamp for 60 min to deposit Ag^+ light on the SiO_2@TiO_2 composite spheres. The precipitate was obtained by centrifugation, and then sodium bromide was added to the supernatant to detect the presence of silver bromide to determine whether or not free "Ag" ions were present. The results confirmed that silver ions were deposited on the surface of SiO_2@TiO_2 core-shell nanoparticles. Finally, the resulting precipitate was washed with ethanol and dried at 70°C for 24 h.

2.5. Materials Characterization. The crystal phase of the as-prepared samples was determined by X-ray diffraction (XRD) using Cu-Kα radiation ($\lambda = 1.5418$°A). Fourier-transform infrared (FT-IR) spectra of the samples were evaluated by an IR Prestige-21 FT-IR spectrometer (Shimadzu, Japan) using the conventional KBr pellet method. A PHI-5702 multifunctional X-ray photoelectron spectroscope (XPS) was used to analyze the chemical state of Ag on the TiO_2 surface, using Mg Ka radiation as the excitation source and the binding energy of contaminated carbon (C1s: 285 eV) as the reference. The surface morphology was examined by SEM (JSM-6701F, Japan) and TEM (Tecnai G^2,

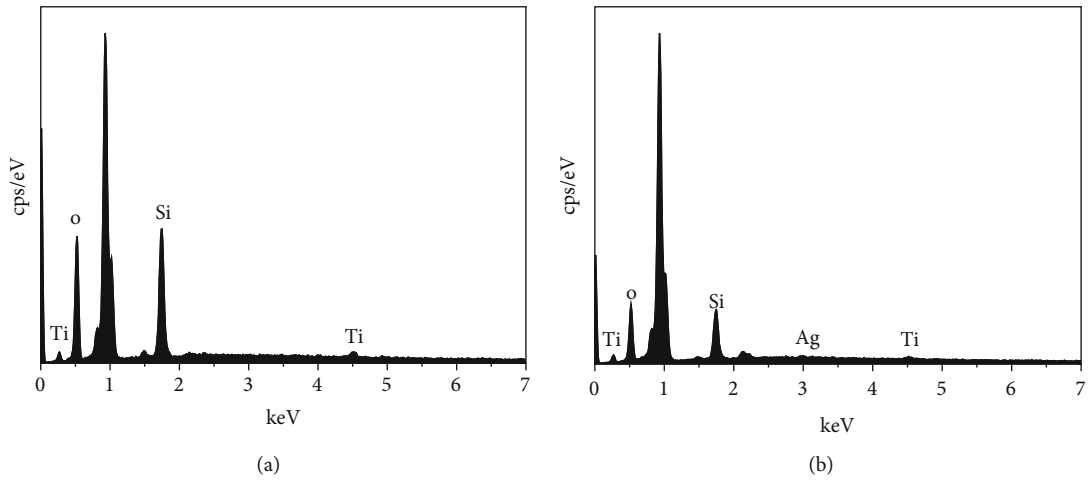

Figure 3: EDS spectrum of (a) SiO_2@TiO_2 core-shell particles and (b) 6 wt.% Ag-SiO_2@TiO_2 nanocomposite spheres.

American). The degradation of phenol and MB was monitored by a 3100 UV spectrophotometer.

2.6. Photodegradation Experiments. The photocatalytic activity of the samples were evaluated by the photodegradation of phenol and MB in a reactor using a 500 W high-pressure mercury lamp. In each experiment, 75 mg of prepared photocatalysts and 300 mL of an aqueous solution of phenol or MB having an initial concentration of 20 mg/L were dispersed in the substrate solution. In order to ensure the adsorption and desorption equilibrium between the photocatalyst and substrates, the reaction solutions were carried out under UV light after stirring for 30 minutes in the dark. 4 mL of the suspension was collected from the reactor at different irradiation time intervals and centrifuged to remove the photocatalyst completely. The concentration changes of MB were analyzed by recording the maximum absorbance of MB at 664 nm, and the phenol was analyzed by colorimetric method of 4-aminoantipyrine at 510 nm.

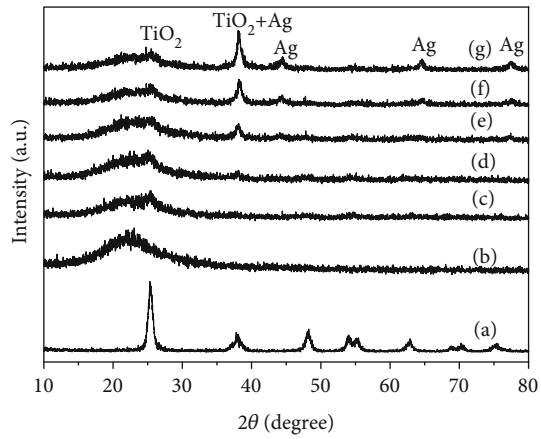

Figure 4: XRD patterns of (a) TiO_2, (b) SiO_2, (c) SiO_2@TiO_2 core-shell particles, (d) 1 wt.% Ag-coated SiO_2@TiO_2 photocatalysts, (e) 3 wt.% Ag-coated SiO_2@TiO_2 photocatalysts, (f) 6 wt.% Ag-coated SiO_2@TiO_2 photocatalysts, and (g) 9 wt.% Ag-coated SiO_2@TiO_2 photocatalysts.

3. Results and Discussion

3.1. Synthesis and Morphological Characterization. The morphology and structure of Ag-coated SiO_2@TiO_2 photocatalysts were characterized by SEM and TEM. As shown in Figure 1(a), the SiO_2 core was a smooth spherical particle of about 200-300 nm. As shown in Figure 1(b), the SiO_2@TiO_2 core-shell particles still kept spherical structure compared with SiO_2 spheres, but the surface appears rough and textured due to the amount of TiO_2 nanoparticles deposited on the SiO_2 spheres. The average SiO_2@TiO_2 core-shell particles size was 210-330 nm, and the coating small TiO_2 particles with the size of about 5~10 nm aggregated on the surface of SiO_2 spheres after annealing at 450°C for 2 h. Figures 1(c) and 1(d) show the SEM images of 6 wt.% Ag-coated SiO_2@TiO_2 photocatalysts; it was difficult to distinguish the photodeposited Ag nanoparticles on SiO_2@TiO_2 composite spheres for aggregating together with TiO_2 nanoparticles.

The TEM images of SiO_2 core spheres and SiO_2@TiO_2 core-shell particles in Figures 2(a) and 2(b) showed the same morphology and structure with the SEM images. Figures 2(c)–2(f) show TEM images of the 1, 3, 6, and 9 wt.% (initial concentration) Ag nanoparticles photodeposited on SiO_2@TiO_2 composite spheres and also show the morphology of photodeposited Ag nanoparticles. The size and density of the Ag nanoparticles increased as the initial concentration of $AgNO_3$ increased.

The EDS spectrum of the SiO_2@TiO_2 composite spheres and the 6 wt.% Ag-coated SiO_2@TiO_2 nanocomposites are shown in Figures 3(a) and 3(b). At the same time, the EDS analysis also confirmed that Si and Ti and O peaks were present in the SiO_2@TiO_2 composite spheres (Figure 3(a)). The presence of Ag nanoparticles was confirmed by EDS in Ag-coated SiO_2@TiO_2 photocatalysts as shown in Figure 3(b).

3.2. XRD Analysis. The XRD patterns of the synthesized TiO_2, SiO_2, SiO_2@TiO_2, and Ag-coated SiO_2@TiO_2 photocatalysts are shown in Figure 4. As shown in Figure 4(a), the

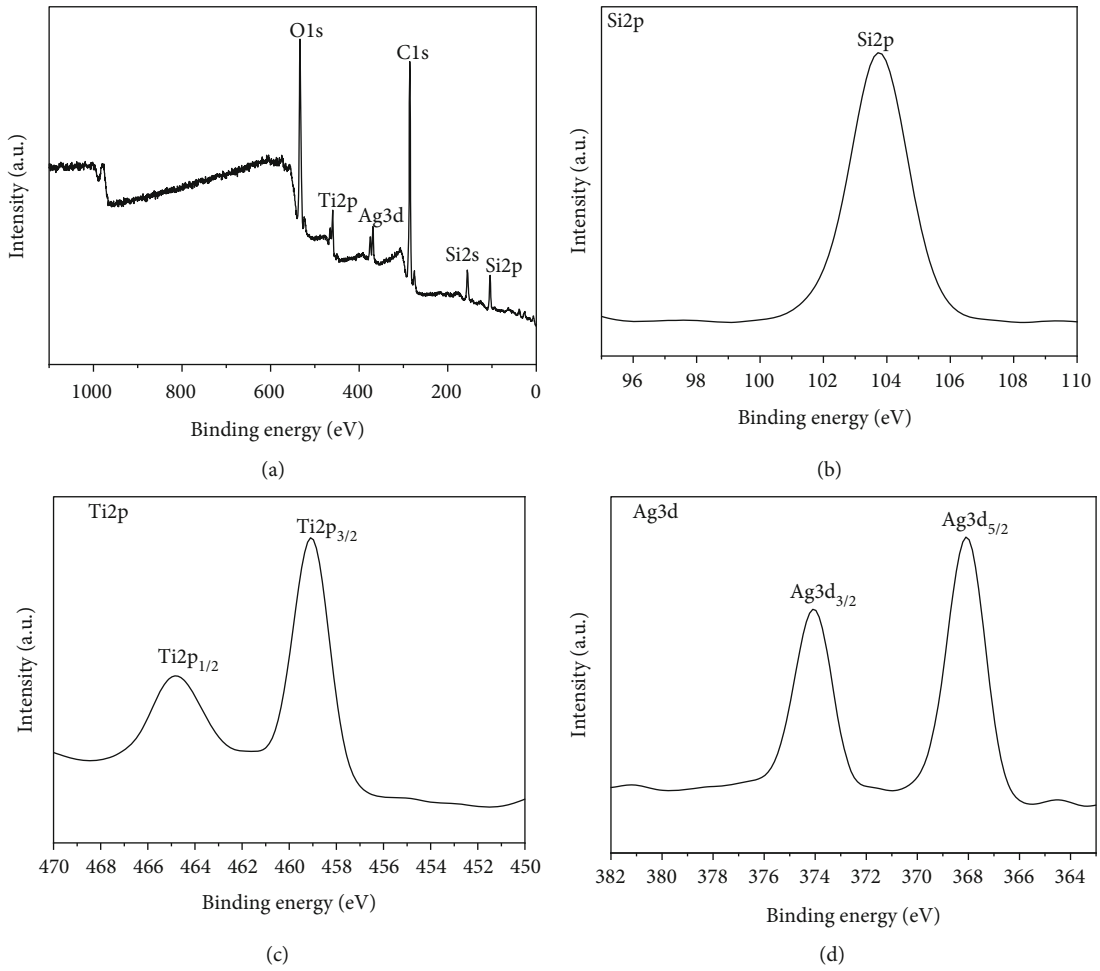

Figure 5: XPS spectra of 6 wt.% Ag-coated SiO_2@TiO_2 photocatalysts: survey (a), high-resolution Si 2p (b), Ti 2p (c), and Ag 3d (d).

obvious diffraction peaks at $2\theta = 25.3^\circ$, 37.8°, 48.2°, 54°, and 62.9° corresponded to (101), (004), (200), (211), and (204) crystal planes of anatase TiO_2, respectively [27]. The wide diffraction peak at $2\theta = 23^\circ$ was ascribed to the amorphous SiO_2 in Figure 4(b). No characteristic anatase TiO_2 diffraction peaks occurred in the SiO_2@TiO_2 precursor spheres after the deposition of TiO_2 because of more SiO_2 amorphous structure in Figure 4(c). After photodeposition of Ag on SiO_2@TiO_2, new peaks appeared at 38°, 44.1°, 64.6°, and 77° that corresponded to the (111), (200), (220), and (311) diffraction planes of face-centered cubic Ag crystal (PDF#65-2871), respectively [32]. Meanwhile, the peak intensity of Ag significantly enhanced because the Ag weight increased as shown in Figures 4(d)–4(g).

3.3. XPS Analysis. X-ray photoelectron spectroscopy (XPS) was used to analyze the surface compositions and chemical states of the Si, Ti, and Ag elements in the 6 wt.% Ag-coated SiO_2@TiO_2 nanocomposites as shown in Figure 5. As shown in Figure 5(a), four elements of Ag, O, Si, and Ti appeared in the measured spectrum, indicating that Ag successfully adhered to the surface of SiO_2@TiO_2. The binding energy peaks of Si, Ti, and Ag are shown in Figures 5(b)–5(d), respectively. The binding energy of Si 2p XPS spectrum

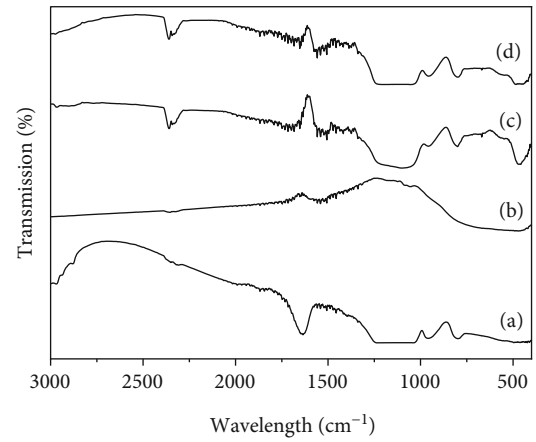

Figure 6: FT-IR spectra of (a) SiO_2, (b) TiO_2, (c) SiO_2@TiO_2, and (d) 6 wt.% Ag-coated SiO_2@TiO_2.

(Figure 5(b)) at 103.7 eV indicated the formation of a Si-O-Si bond. The binding energy of Ti 2p XPS spectrum (Figure 5(c)) showed at 464.7 and 459.0 eV corresponds to Ti $2p_{1/2}$ and Ti $2p_{3/2}$, respectively. This result confirmed the formation of pure anatase TiO_2. The binding energy of Ag 3d appeared at 368.1 eV and 374.1 eV which corresponded

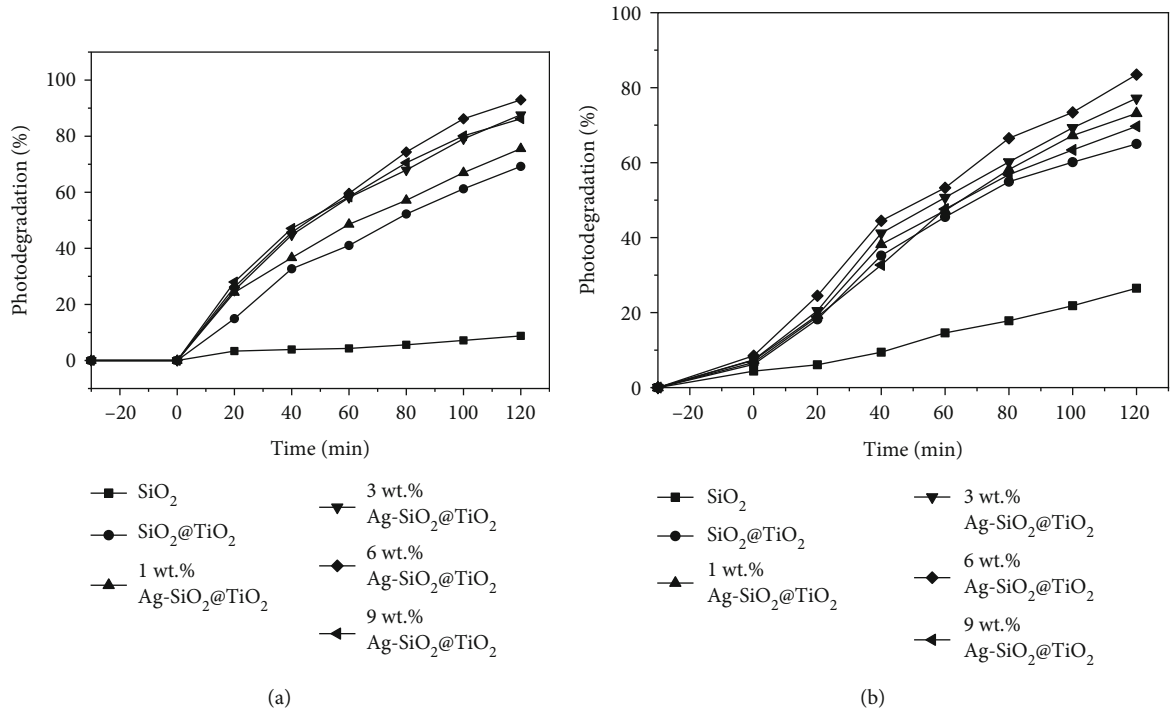

Figure 7: Photodegradation of phenol (a) and methylene blue (b) under UV light: SiO_2, SiO_2@TiO_2, and Ag-coated SiO_2@TiO_2.

to the Ag $3d_{5/2}$ and Ag $3d_{3/2}$ orbits, respectively, as shown in Figure 2(b), and the splitting of the 3d doublet was 6.0 eV. The results indicated that Ag presented in the composites in the form of metallic Ag. This result was in good agreement as well with standard binding energy value of metallic silver (Ag^0) present in the SiO_2@TiO_2 composite spheres [32–34]. According to the results of XRD patterns, it can be concluded that Ag particles were not oxidized in the process of preparation under UV irradiation.

3.4. FT-IR Spectra Analysis. FT-IR spectra were performed to analyze the composition of SiO_2, TiO_2, SiO_2@TiO_2, and 6 wt.% Ag-coated SiO_2@TiO_2. As shown in Figure 6, the bands at 800 cm^{-1} were ascribed to the symmetric stretching vibration of Si-O-Si (Figure 6(a)) [35]; the peaks around 470 cm^{-1} were attributed to the Ti-O-Ti vibration in TiO_2 (Figure 6(b)). For SiO_2@TiO_2 and Ag-coated SiO_2@TiO_2, the peaks at 955 cm^{-1} and 1053 cm^{-1} were assigned to the asymmetric vibration of Ti-O-Si (Figures 6(a)–6(d)) [36].

3.5. Photocatalytic Activity. Figure 7 shows the photocatalytic activity of phenol (Figure 7(a)) and MB (Figure 7(b)) in the presence of SiO_2, SiO_2@TiO_2, and Ag-coated SiO_2@TiO_2, respectively. As shown in Figure 7(a), SiO_2 had only 8.78% photocatalytic efficiency after 120 min photodegration of phenol which was attributed to the adsorption of SiO_2. It can be clearly seen that the photocatalytic efficiency of Ag-coated SiO_2@TiO_2 showed more excellent activity than SiO_2@TiO_2 microspheres. The results indicated that among the different weights of Ag-coated SiO_2@TiO_2 photocatalysts, 6 wt.% Ag-coated SiO_2@TiO_2 photocatalysts showed the highest photocatalytic efficiency of 92.9%. From Figure 7(b), the photocatalytic efficiency of SiO_2, SiO_2@TiO_2, and Ag-coated SiO_2@TiO_2 towards MB at the wavelength of 664 nm showed the same photocatalytic regulation of photodegration of phenol under UV irradiation. SiO_2 showed more photocatalytic efficiency of 26.5% after 120 min photodegration of MB than the photodegration of phenol which indicated that SiO_2 had more adsorption efficiency towards colored dye than colorless organic matters on the surface or inside of the SiO_2 spheres. The results also showed that Ag-coated SiO_2@TiO_2 exhibited higher photocatalytic efficiency than SiO_2 and SiO_2@TiO_2, and 6 wt.% Ag-coated SiO_2@TiO_2 photocatalysts presented the highest photocatalytic efficiency of 83.5%. The more excellent photocatalytic activity of Ag-coated SiO_2@TiO_2 may be caused by the smaller particle size and the higher concentration of catalytically active centers of the anatase nanocrystals in the calcined TiO_2 shell than in the calcined solid TiO_2 sphere [37, 38]. Besides, the Ag nanoparticles helped suppress the regeneration of the electron-hole recombination of the semiconductor (TiO_2). Obviously, in the Ag-coated SiO_2@TiO_2 photocatalytic system, SiO_2 acted as the adsorbent, while TiO_2 acted as the photoactive center, and Ag acted as an electron trapping agent [37].

4. Conclusions

Ag-coated SiO_2@TiO_2 core-shell nanocomposites were synthesized by a two-step hydrothermal and photodeposition method. The samples were characterized by TEM and other methods. The results showed that Ag nanoparticles were deposited on the SiO_2@TiO_2 composite spheres with good dispersibility and no aggregation. The XRD profiles showed the presence of anatase phase in TiO_2 and the XPS results indicated that Ag existed in the form of metallic Ag in the Ag-coated SiO_2@TiO_2 composite sphere. FT-IR spectra

results showed that the asymmetric vibration of Ti-O-Si presented in the Ag-coated SiO_2@TiO_2 composite sphere. Compared with the SiO_2@TiO_2 composite spherical photocatalyst, the Ag-coated SiO_2@TiO_2 composite sphere had better catalytic activity for the degradation of phenol and MB under UV light irradiation.

Data Availability

The data used to support the findings of this study are available from the corresponding author upon request.

Conflicts of Interest

The authors declare that there is no conflict of interests regarding the publication of this paper.

Acknowledgments

The authors would like to thank the financial support from the National Natural Science Foundation of China (NSFC no. 51268026).

References

[1] A. Fujishima and K. Honda, "Electrochemical photolysis of water at a semiconductor electrode," *Nature*, vol. 238, no. 7, pp. 37-38, 1972.

[2] N. S. Waldmann and Y. Paz, "Away from TiO_2: a critical mini-review on the developing of new photocatalysts for degradation of contaminants in water," *Materials Science in Semiconductor Processing*, vol. 42, no. 6, pp. 72–80, 2016.

[3] H. Zangeneh, A. A. L. Zinatizadeh, M. Habibi, M. Akia, and M. H. Isa, "Photocatalytic oxidation of organic dyes and pollutants in wastewater using different modified titanium dioxides: a comparative review," *Journal of Industrial and Engineering Chemistry*, vol. 26, no. 10, pp. 1–36, 2015.

[4] E. B. Moushoul, Y. Mansourpanah, K. Farhadi, and M. Tabatabaei, "TiO_2 nanocomposite based polymeric membranes: a review on performance improvement for various applications in chemical engineering processes," *Chemical Engineering Journal*, vol. 283, no. 124, pp. 29–46, 2016.

[5] B. Szczepanik, "Photocatalytic degradation of organic contaminants over clay-TiO_2 nanocomposites: a review," *Applied Clay Science*, vol. 141, no. 29, pp. 227–239, 2017.

[6] E. Grabowska, J. Reszczyńska, and A. Zaleska, "RETRACTED:Mechanism of phenol photodegradation in the presence of pure and modified-TiO_2: a review," *Water Research*, vol. 46, no. 17, pp. 5453–5471, 2012.

[7] A. L. Linsebigler, G. Lu, and J. T. Yates Jr., "Photocatalysis on TiO2 surfaces: principles, mechanisms, and selected results," *Chemical Reviews*, vol. 95, no. 3, pp. 735–758, 2012.

[8] H. Xu, S. X. Ouyang, L. Q. Liu, P. Reunchan, N. Umezawa, and J. Ye, "Recent advances in TiO_2-based photocatalysis," *Journal of Materials Chemistry A*, vol. 2, no. 32, pp. 12642–12661, 2014.

[9] G. Liu, L. C. Yin, J. Wang et al., "A red anatase TiO_2 photocatalyst for solar energy conversion," *Energy & Environmental Science*, vol. 5, no. 11, pp. 9603–9610, 2014.

[10] I. Kitsou, P. Panagopoulos, T. Maggos, M. Arkas, and A. Tsetsekou, "Development of SiO_2@TiO_2 core-shell nanospheres for catalytic applications," *Applied Surface Science*, vol. 441, no. 5, pp. 223–231, 2018.

[11] L. H. Wu, Y. F. Zhou, W. Y. Nie, L. Song, and P. Chen, "Synthesis of highly monodispersed teardrop-shaped core-shell SiO_2/TiO_2 nanoparticles and their photocatalytic activities," *Applied Surface Science*, vol. 351, no. 5, pp. 320–326, 2015.

[12] W. Li, J. P. Yang, Z. X. Wu et al., "A versatile kinetics-controlled coating method to construct uniform porous TiO_2 shells for multifunctional core–shell structures," *Journal of the American Chemical Society*, vol. 134, no. 29, pp. 11864–11867, 2012.

[13] J. W. Lee, M. R. Othman, Y. Eomc, T. G. Lee, W. S. Kim, and J. Kim, "The effects of sonification and TiO_2 deposition on the micro-characteristics of the thermally treated SiO_2/TiO_2 spherical core–shell particles for photo-catalysis of methyl orange," *Microporous and Mesoporous Materials*, vol. 116, no. 1-3, pp. 561–568, 2008.

[14] C. Anderson and A. J. Bard, "An improved photocatalyst of TiO2/SiO2 prepared by a Sol-gel synthesis," *The Journal of Chemical Physics*, vol. 99, no. 24, pp. 9882–9885, 1995.

[15] T. Okuno, G. Kawamuran, H. Muto, and A. Matsuda, "Photocatalytic properties of Au-deposited mesoporous SiO_2–TiO_2 photocatalyst under simultaneous irradiation of UV and visible light," *Journal of Solid State Chemistry*, vol. 235, no. 12, pp. 132–138, 2016.

[16] L. X. Zhang, C. H. Ni, H. F. Jiu, C. Xie, J. Yan, and G. Qi, "One-pot synthesis of Ag-TiO_2/reduced graphene oxide nanocomposite for high performance of adsorption and photocatalysis," *Ceramics International*, vol. 43, no. 7, pp. 5450–5456, 2017.

[17] R. Kaur and B. Pal, "Size and shape dependent attachments of Au nanostructures to TiO_2 for optimum reactivity of Au–TiO_2 photocatalysis," *Journal of Molecular Catalysis A: Chemical*, vol. 355, no. 11, pp. 39–43, 2012.

[18] Z. Zheng, B. Huang, X. Qin, X. Zhang, Y. Dai, and M.-H. Whangbo, "Facile *in situ* synthesis of visible-light plasmonic photocatalysts M@TiO_2 (M = Au, Pt, Ag) and evaluation of their photocatalytic oxidation of benzene to phenol," *Journal of Materials Chemistry*, vol. 21, no. 11, pp. 9079–9087, 2011.

[19] D. Y. Zhou, Y. M. Liu, W. G. Zhang, W. Liang, and F. Yang, "Au-TiO_2 nanofilms for enhanced photocatalytic activity," *Thin Solid Films*, vol. 636, no. 11, pp. 490–498, 2017.

[20] H. Eskandarloo, A. Badiei, M. A. Behnajady, and M. Afshar, "Enhanced photocatalytic removal of phenazopyridine by using silver-impregnated SiO_2–TiO_2 nanoparticles: optimization of synthesis variables," *Research on Chemical Intermediates*, vol. 41, no. 12, pp. 9929–9949, 2015.

[21] H. M. S. Suh, J. R. Choi, H. J. Hah, S. M. Koo, and Y. C. Bae, "Comparison of Ag deposition effects on the photocatalytic activity of nanoparticulate TiO_2 under visible and UV light irradiation," *Journal of Photochemistry and Photobiology A: Chemistry*, vol. 163, no. 1-3, pp. 37–44, 2004.

[22] J. X. Li, J. H. Xu, W. L. Dai, and K. Fan, "Dependence of Ag deposition methods on the photocatalytic activity and surface state of TiO_2 with twistlike helix structure," *Journal of Physical Chemistry C*, vol. 113, no. 19, pp. 8343–83449, 2009.

[23] R. M. Mohamed and I. A. Mkhalid, "Characterization and catalytic properties of nano-sized Ag metal catalyst on TiO_2–SiO_2 synthesized by photo-assisted deposition and impregnation methods," *Journal of Alloys and Compounds*, vol. 501, no. 2, pp. 301–306, 2010.

[24] B. Braconnier, C. A. Páez, S. Lambert et al., "Ag- and SiO_2-doped porous TiO_2 with enhanced thermal stability," *Microporous and Mesoporous Materials*, vol. 122, no. 1-3, pp. 247–254, 2009.

[25] S. C. Chan and M. A. Barteau, "Preparation of highly uniform Ag/TiO_2 and Au/TiO_2 supported nanoparticle catalysts by photodeposition," *Langmuir*, vol. 21, no. 12, pp. 5588–5595, 2005.

[26] K. P. O. Mahesh, D. H. Kuo, and B. R. Huang, "Facile synthesis of heterostructured Ag-deposited SiO2@TiO2 composite spheres with enhanced catalytic activity towards the photodegradation of AB 1 dye," *Journal of Molecular Catalysis A: Chemical*, vol. 396, no. 10, pp. 290–296, 2015.

[27] X. Zhang, Y. Zhu, X. Yang et al., "Enhanced visible light photocatalytic activity of interlayer-isolated triplex $Ag@SiO_2@TiO_2$ core–shell nanoparticles," *Nanoscale*, vol. 5, no. 8, pp. 3359–3366, 2013.

[28] W. Zhao, L. Feng, R. Yang, J. Zheng, and X. Li, "Synthesis, characterization, and photocatalytic properties of Ag modified hollow SiO_2/TiO_2 hybrid microspheres," *Applied Catalysis B: Environmental*, vol. 103, no. 1-2, pp. 181–189, 2011.

[29] J. Zhou, F. Ren, S. Zhang et al., "SiO_2–Ag–SiO_2–TiO_2 multi-shell structures: plasmon enhanced photocatalysts with wide-spectral-response," *Journal of Materials Chemistry A*, vol. 1, no. 42, pp. 13128–13138, 2013.

[30] S. Ullah, E. P. F. Neto, A. A. Pasa et al., "Enhanced photocatalytic properties of core@shell $SiO_2@TiO_2$ nanoparticles," *Applied Catalysis B: Environmental*, vol. 179, no. 5, pp. 333–343, 2015.

[31] J. Ma, X. Guo, H. Ge, G. Tian, and Q. Zhang, "Seed-mediated photodeposition route to Ag-decorated $SiO_2@TiO_2$ microspheres with ideal core-shell structure and enhanced photocatalytic activity," *Applied Surface Science*, vol. 434, no. 5, pp. 1007–1014, 2018.

[32] W. Q. Li, X. H. Xiao, A. L. Stepanov et al., "The ion implantation-induced properties of one-dimensional nanomaterials," *Nanoscale Research Letters*, vol. 8, no. 1, article 175, 2013.

[33] M. Diak, E. Grabowska, and A. Zalesk, "Synthesis, characterization and photocatalytic activity of noble metal-modified TiO_2 nanosheets with exposed {0 0 1} facets," *Applied Surface Science*, vol. 347, pp. 275–285, 2015.

[34] C. Liu, D. Yang, Y. Wang, J. Shi, and Z. Jiang, "Fabrication of antimicrobial bacterial cellulose–Ag/AgCl nanocomposite using bacteria as versatile biofactory," *Journal of Nanoparticle Research*, vol. 14, no. 8, article 1084, pp. 1-2, 2012.

[35] C. Liu, D. Yang, Y. Jiao, Y. Tian, Y. Wang, and Z. Jiang, "Biomimetic synthesis of TiO_2–SiO_2–Ag nanocomposites with enhanced visible-light photocatalytic activity," *ACS Applied Materials & Interfaces*, vol. 5, no. 9, pp. 3824–3832, 2013.

[36] B. Subash, B. Krishnakumar, M. Swaminathan, and M. Shanthi, "Highly efficient, solar active, and reusable photocatalyst: Zr-loaded Ag–ZnO for reactive red 120 dye degradation with synergistic effect and dye-sensitized mechanism," *Langmuir*, vol. 29, no. 3, pp. 939–949, 2013.

[37] Q. Zhang, I. Lee, J. I. B. Joo, F. Zaera, and Y. Yin, "Core–shell nanostructured catalysts," *Accounts of Chemical Research*, vol. 46, no. 8, pp. 1816–1824, 2013.

[38] W. Li and D. Zhao, "Extension of the Stöber method to construct mesoporous SiO_2 and TiO_2 shells for uniform multifunctional core–shell structures," *Advanced Materials*, vol. 25, no. 1, pp. 142–149, 2013.

Hindawi
Journal of Nanomaterials
Volume 2019, Article ID 9082132, 10 pages
https://doi.org/10.1155/2019/9082132

Research Article

Carbon-Coated SnO_2/Ti_3C_2 Composites with Enhanced Lithium Storage Performance

Zijing Wang, Fen Wang, Kaiyu Liu, Jianfeng Zhu, and Abdul Waras

School of Material Science and Engineering, Shaanxi Key Laboratory of Green Preparation and Functionalization for Inorganic Materials, Shaanxi University of Science and Technology, Xi'an 710021, China

Correspondence should be addressed to Fen Wang; wangf@sust.edu.cn

Received 11 April 2019; Revised 14 June 2019; Accepted 31 August 2019; Published 7 October 2019

Guest Editor: Fei Ke

Tin-based anode materials including oxides, composites oxides, and tin-based alloys are identified as promising candidates for energy storage attributed to the highest theoretical specific capacity. We introduce Ti_3C_2-MXene as structural skeletons and amorphous carbon as conductive networks for tin oxide in this work. Herein, carbon-coated kernel-like SnO_2 coupling with two-dimensional (2D) layered structure Ti_3C_2-MXene ($C@SnO_2/Ti_3C_2$) composites were prepared by a hydrothermal reaction and a further calcination process. The fabricated $C@SnO_2/Ti_3C_2$ nanocomposites exhibit smaller charge transfer resistance, larger Li^+ diffusion coefficient, and better cycling stability than SnO_2/Ti_3C_2 and pure Ti_3C_2. Most of all, $C@SnO_2/Ti_3C_2$ nanocomposites display excellent initial capacity of 1531.5 mAh g^{-1} at current density of 100 mA g^{-1} and show outstanding rate performance of 540 mAh g^{-1}even after 200 cycles. In our work, we will provide a new research idea for the composite materials of metal oxides and two-dimensional layered materials in the field of electrode materials for batteries.

1. Introduction

Lithium-ion batteries (LIBs) are widely used because of their excellent specific capacity, superior cycle performance, and good safety performance. In recent years, it has become more and more widely used in mobile phones, electric vehicles, and laptops as well [1–4]. However, the current cycle stability and specific capacity of LIBs have not been able to meet the needs of the people, so it is necessary to develop LIBs with better capacity and higher cycle performance. As a new 2D transition metal carbide, MXene has a better electrochemical performance than any other carbon material in the electrode material of LIBs [5–19].

$Ti_3C_2T_x$ (T = O, OH, and F) is the most popular MXene. The 2D structure $Ti_3C_2T_x$ can be obtained by corroding the Al layer in the Ti_3AlC_2 with a ceramic structure by HF. Furthermore, Ti_3C_2-MXenes have the following excellent properties, such as lower Li^+ diffusion barrier and advanced Li storage capacity, electronic conductivity, and low operating voltage, combined with good surface hydrophilicity and excellent chemical stability and structural stability [12]. According to Sun et al.'s research, the capacity of Ti_3C_2 reaches 123.6 mAh g^{-1} at 1 C rate and a coulombic efficiency of 47% [15]. Due to these advantages and disadvantages of Ti_3C_2, it is necessary to chemically modify Ti_3C_2 with high surface area to meet the capacity requirements of the battery.

Throughout the development of lithium-ion batteries, tin-based materials are one of the most commonly used anode materials for LIBs because of their nontoxicity and excellent theoretical capacity (782 mAh g^{-1}) [20–23]. Zhu et al. used a hydrothermal method to combine SnO_2 and graphene to obtain SnO_2/G nanomaterials. SnO_2/G shows excellent electrochemical performance of 860 mAh g^{-1} after 50 cycles at 200 mA g^{-1} [24]. In Wu et al.'s work, a SnO_2/graphene nanocomposite was proposed as an anode material for LIBs by a facile method, which shows a good specific capacity of 540 mAh g^{-1} after 90 cycles [25]. According to the previous work, SnO_2-based materials have specific capacities but their capacity decays fast and the electrochemical stability needs to be improved. Therefore, it needs to be

chemically modified with B having excellent chemical stability to improve its electrochemical performance.

In our research, we have adopted a novel method to enhance the cycle stability and specific capacity of multilayer $Ti_3C_2T_x$ (T = F, OH) particles by loading SnO_2 nanoparticles (NPs) between $Ti_3C_2T_x$ layers followed by coating amorphous carbon on its surface. In previous reports, there were many methods for preparing the nanocomposite, such as Wang et al.'s preparation of the SnO_2-Ti_3C_2 nanocomposite by a hydrothermal method and using it as the anode material of the lithium-ion battery [26]. Chen and Lou used the calcination method to prepare the SnO_2 nanorods to test their electrochemical performance [27]; Zheng et al. prepared SnO_2/Ti_3C_2 nanocomposites by microwave irradiation and tested their electrochemical properties [28]. Compared with the above methods, our method has the advantages of low temperature, simple and easy operation, and low requirements on equipment; in addition, it can make SnO_2 load all the more consistently on the layers of $Ti_3C_2T_x$, improving the consistency of the SnO_2, and, in the meantime, coat the amorphous carbon all the more effectively in the calcination stage, which is an increasingly productive and advantageous approach to synthesize $C@SnO_2/Ti_3C_2$ nanocomposites. Amorphous carbon connects isolated MXene particles, and it remarkably improves the electric transportation and decreases their contact resistance by coating these voids/gaps, which makes an inordinate contribution to the electrochemical properties of the as-prepared $C@SnO_2/Ti_3C_2$ composite.

2. Materials and Methods

2.1. Synthesis Procedure. Ti_3C_2-MXene was synthesized by a solid phase calcination method as reported previously [26]. All chemicals are purchased directly and do not require further processing. $C@SnO_2/Ti_3C_2$ nanocomposites were synthesized by a hydrothermal reaction and synthesized further by the calcination process. To obtain the Ti_3C_2 solution, mix 100 mg of as-prepared Ti_3C_2 and 100 mL of ultrapure water (UPW) and then sonicate for 2 h. Then, 3.0 g polyvinyl alcohol (PVA) was added to 100 mL UPW and stirred for 30 minutes to obtain PVA solution. After this, add 12.5 g $SnCl_4{\cdot}5H_2O$ to 60 mL UPW and then add 1 mL of HCl (36.0~38.0 wt.%), mix the solution with appropriate stirring, add Ti_3C_2 solution and PVA solution to it, and then adjust the pH value to 9~10 by injecting $NH_3{\cdot}H_2O$ (25.0~38.0 wt.%). Then, the mixed solution was quickly stirred in a water bath at 85°C for 1 h and then dried at 100°C for 24 hours. Finally, under argon protection, the target product is obtained by sintering 500°C in a tube furnace and marking it as $C@SnO_2/Ti_3C_2$. As a comparative sample, SnO_2/Ti_3C_2 is prepared in the same manner as above except that there is no addition of PVA.

Figure 1 demonstrates the preparation process of $C@SnO_2/Ti_3C_2$, when solutions of polyvinyl acetate (PVA) and $SnCl_4{\cdot}5H_2O$ are thoroughly mixed. The Sn^{4+} produced by the dissolved $SnCl_4{\cdot}5H_2O$ can be combined with -OH in the uniformly distributed PVA chain, and Sn^{4+} can be uniformly distributed in the solution, so PVA is an excellent surfactant, and the $Ti_3C_2T_x$ (T = OH, F) is added. It allows the PVA chains to be oriented on the surface of the $Ti_3C_2T_x$ layers by the mutual attraction between the functional groups. After calcination process, we can obtain $C@SnO_2$-Ti_3C_2 with different structure and morphology.

2.2. Material Characterization. The characterization of the morphology and structure for the as-prepared $C@SnO_2$-Ti_3C_2 nanocomposites will be carried out in the following instruments. Morphological characterization is carried out by field-emission scanning electron microscopy (FE-SEM, S4800) and transmission electron microscopy (TEM JEM2100F) equipped with an energy dispersive X-ray analyzer (EDX). Beyond that, the composition and structure of $C@SnO_2/Ti_3C_2$ nanocomposites are characterized in X-ray diffraction (XRD, D/MAX-2500).

2.3. Electrochemical Measurements. The assemblage of lithium-ion batteries is necessary to test the electrochemical performance of as-prepared $C@SnO_2/Ti_3C_2$ nanocomposites. Right off the bat, the dynamic materials, poly(vinylidene) fluoride (PVDF), and acetylene black are completely mixed in an agate mortar at a weight proportion of 80 : 10 : 10, then N-methyl l-2-pyrrolidinone (NMP) is added dropwise, grinding is continued until the mixture was uniformly glue like, and the mixture was connected to the surface of the Cu foil by a coater, dried in a vacuum at 120°C for 12 h, and cut into small wafers. At the same time, lithium foil is used as the counter electrode, and the LIBs with the CR2032 coin type are assembled in the vacuum glove box. The electrochemical performance of the assembled battery is tested on an Ametek PARSTAT 4000 electrochemistry workstation, including cyclic voltammograms (CV) and electrochemical impedance spectroscopy (EIS). The charge and discharge performance of the gathered battery is estimated on a Land CT2001A cycler.

3. Results and Discussion

3.1. Characterization of $C@SnO_2$-Ti_3C_2. XRD patterns of as-prepared SnO_2, Ti_3C_2, and $C@SnO_2/Ti_3C_2$ nanocomposites appear in Figure 2. As shown in Figure 2(a), the Ti_3C_2, SnO_2 have a standard XRD design as detailed in the literature [5, 20]. The peaks distinguished at (002), (006), (008), and (0010) were allotted as the diffraction peaks of Ti_3C_2 [16]. The diffraction peaks of $C@SnO_2/Ti_3C_2$ nanocomposites were indexed to the (110), (101), (200), and (211) planes of tetragonal SnO_2 (JCPDS No. 41-1445). In addition, there is a small peak at about 20° demonstrating the presence of the amorphous carbon. Figure 2(b) shows partial magnification of XRD designs for these examples; the peaks at 9.28° indexed to the (002) plane move 0.43° towards 8.85°; the result shows the cross-section steady changes and the between-planar separating increments. According to the Bragg equation,

$$2d \sin\theta = n\lambda. \quad (1)$$

It can be calculated that when the (002) plane is at 9.28°, $d_1 = 9.5228$ nm is obtained; when the (002) plane is offset by

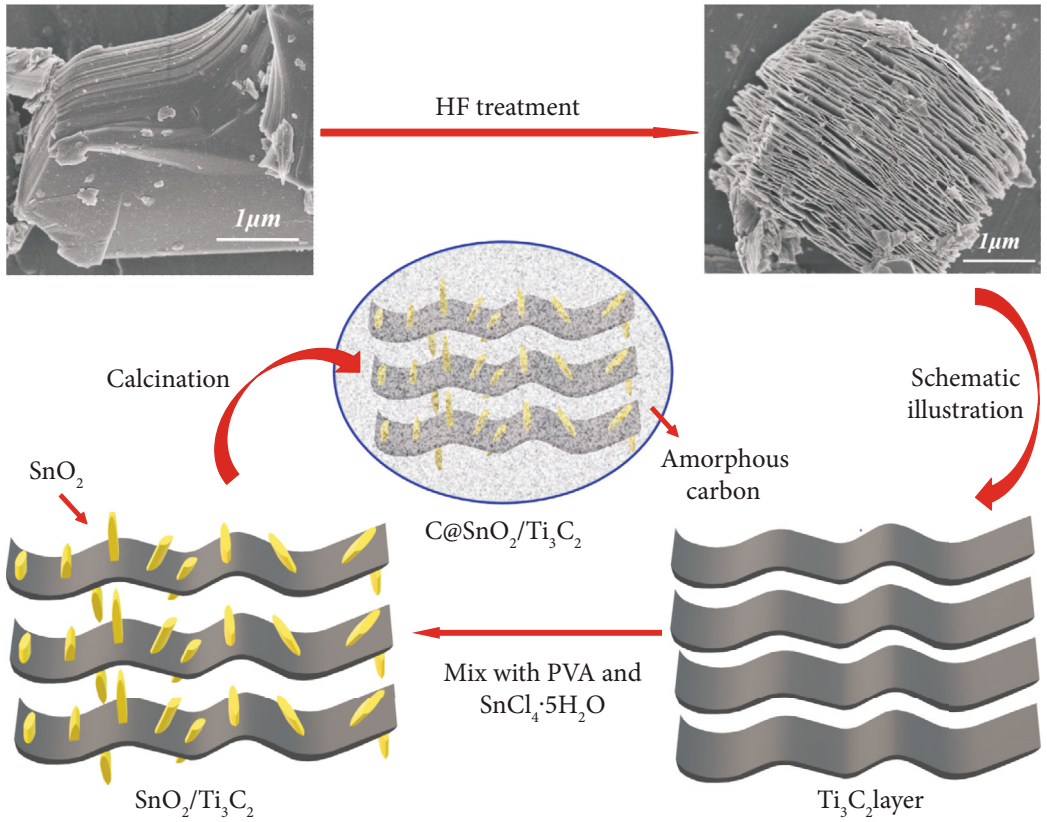

Figure 1: Synthesis schematic of $C@SnO_2/Ti_3C_2$ nanocomposites.

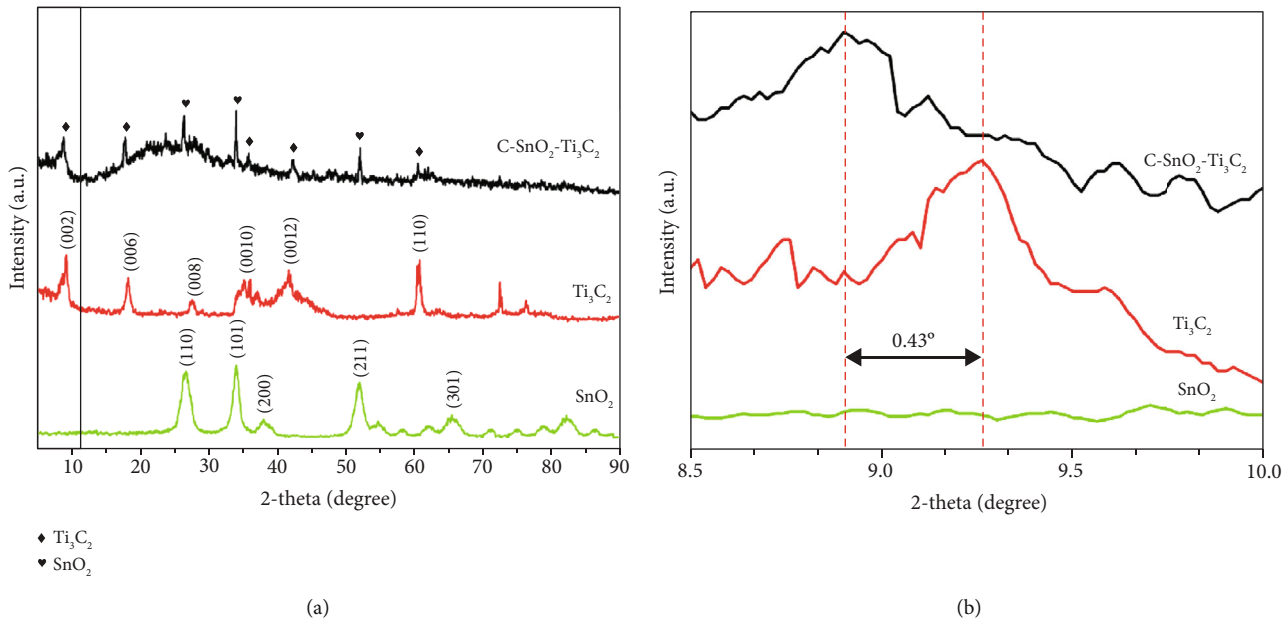

(a) (b)

Figure 2: (a) XRD patterns of the three different samples SnO_2, Ti_3C_2, and $C@SnO_2/Ti_3C_2$; (b) partial enlargement of XRD patterns in (a).

0.43° to 8.85°, $d_2 = 9.9844$ nm is obtained, so it can be concluded that the layer spacing is increased that $\Delta d = 0.4616$ nm. This outcome demonstrates that both Ti_3C_2 and SnO_2 have been effectively prepared in $C@SnO_2/Ti_3C_2$ nanocomposites and there is no impurity.

The morphologies of the extraordinary 2D structure of Ti_3C_2, single-deck Ti_3C_2, SnO_2-Ti_3C_2, and $C@SnO_2/Ti_3C_2$ nanocomposites are seen by TEM, as shown in Figure 3. The morphologies of Ti_3C_2, single-deck Ti_3C_2, and SnO_2-Ti_3C_2 appear in Figures 3(a), 3(b), and 3(d) to compare with

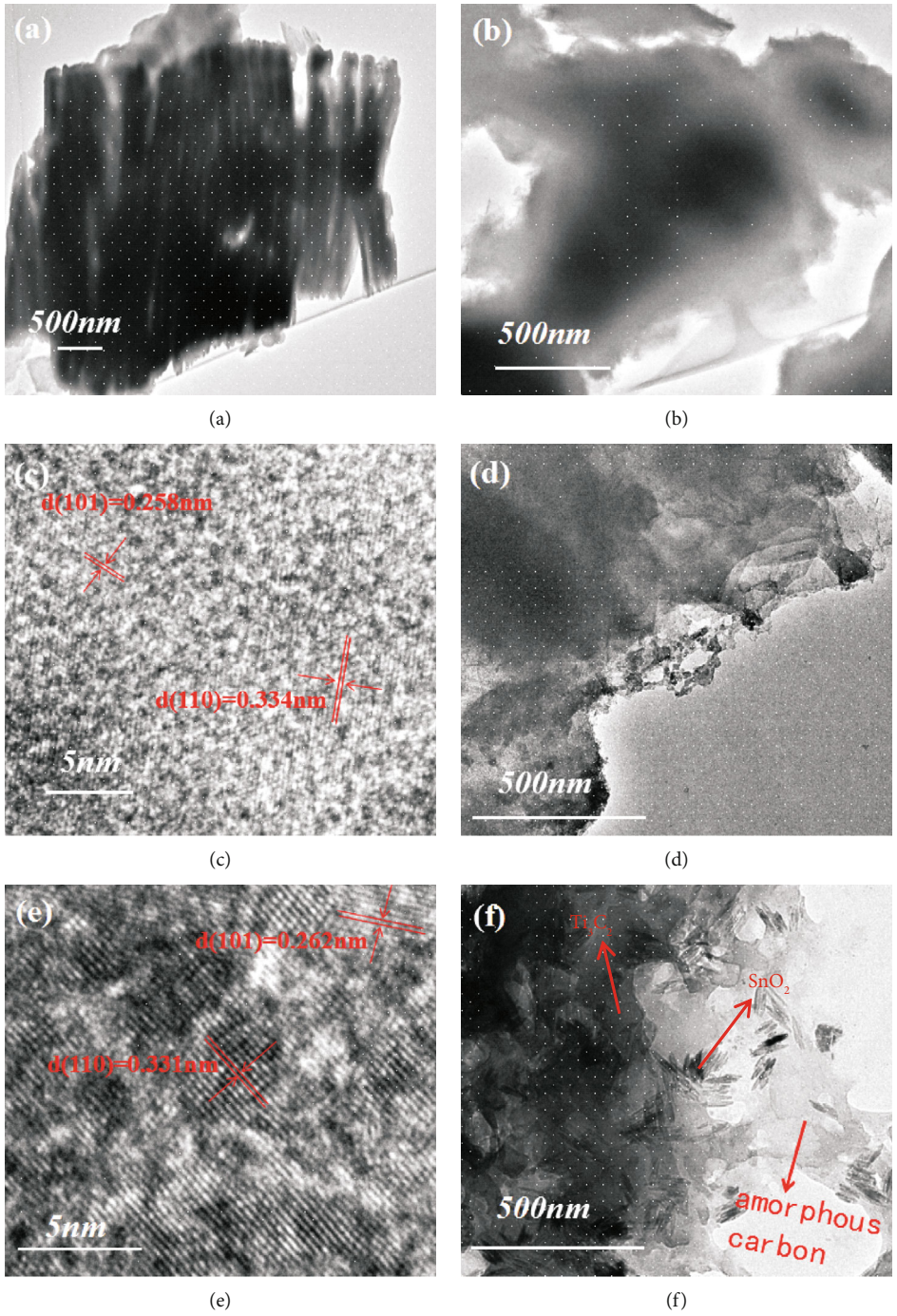

FIGURE 3: TEM images of $Ti_3C_2T_x$ (a) and single-deck $Ti_3C_2T_x$ nanoparticles (b); HRTEM image (c) and TEM image (d) of the SnO_2-Ti_3C_2 nanoparticles; HRTEM image (e) and TEM image (f) of the C@SnO_2/Ti_3C_2 nanoparticles.

the C@SnO_2/Ti_3C_2 composites. As can be seen from Figure 3(f), countless kernel-like SnO_2 NPs are scattered on the surface of layered $Ti_3C_2T_x$, which are about nm in size; in addition to that, it can be clearly seen that the surface of the $Ti_3C_2T_x$ sheet is covered with a large amount of amorphous carbon like a tissue. At the same time, the individual components have been marked with arrows in Figure 3(f). Corrugated amorphous carbon emerged on the surface of $Ti_3C_2T_x$ and it ensures that calcination improves the conjugated level of PVA, which can increase conductivity of C@SnO_2/Ti_3C_2 composites. Moreover, due to calcination in argon gas, the SnO_2 NPs in C@SnO_2/Ti_3C_2 with a uniform size of about 150 nm are clearly observed in Figure 3(f). From the HRTEM pictures in Figures 3(c) and 3(e), the interplanar distances of 0.331 nm and 0.262 nm may be distinguished as d (110) and d (101) of SnO_2 NPs, individually.

Figure 4 demonstrates the SEM pictures of samples. As shown in Figure 4(a), the SEM image of $Ti_3C_2T_x$ which is

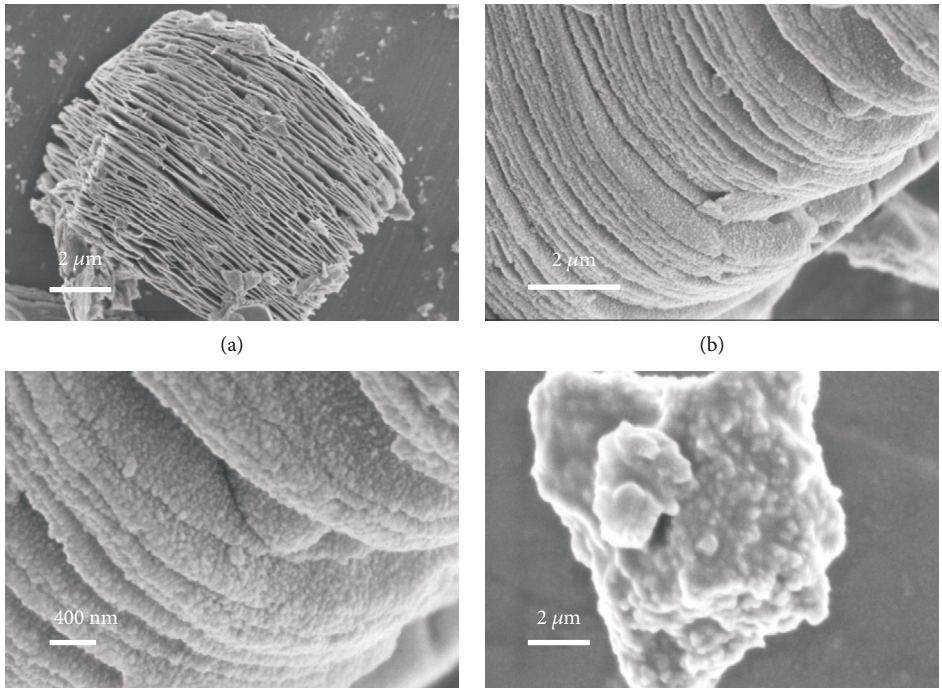

Figure 4: SEM images of $Ti_3C_2T_x$ (a), SnO_2-Ti_3C_2 nanocomposites (b, c), and C@SnO_2/Ti_3C_2 nanoparticles.

the product obtained by treating Ti_3AlC_2 with HF solution environment [5]. As can be seen from Figure 4(a), $Ti_3C_2T_x$ is an exceptionally uniform and remarkable 2D-layered structure. As observed from the SEM image of SnO_2-Ti_3C_2 (Figure 4(b)), SnO_2 nanoparticle with a particle size of around 30 nm (Figure 4(c)) is consistently upheld on the surface of $Ti_3C_2T_x$. Figure 4(d) is the SEM image of C@SnO_2/-Ti_3C_2 composites. It very well may be seen from the image that the surface of the C@SnO_2/Ti_3C_2 composite is wrapped by a layer of gauze-like amorphous carbon and the clearly visible small protrusion is SnO_2 NPs.

Elemental mapping images of C@SnO_2/Ti_3C_2 composites are shown in Figure 5. The inset in Figure 5(b) is the EDS quantitative analysis of C@SnO_2/Ti_3C_2 nanocomposites, which has the mass percentage and atomic percentage of each element. We know that the active material used in the negative electrode material of a LIB with the CR2032 coin type is about 3.76 mg, calculated from the mass percentage, and has a carbon content of about 0.7246 mg and a Ti content of about 1.9394 mg. Carbon is mainly supplied by $Ti_3C_2T_x$ and amorphous carbon. The mass of $Ti_3C_2T_x$ can be calculated according to the Ti content, and the remaining carbon is the mass of amorphous carbon. The calculated carbon content is about 0.3963 mg. The bright regions correspond to the elements tin, titanium, oxygen, and carbon. Sn, Ti, O, and C are distributed uniformly throughout the composite material, which further confirms the structure of the C@SnO_2/Ti_3C_2 composites.

3.2. Performance of C@SnO_2-Ti_3C_2 as Anodes. The electrochemical performance was assessed by utilizing the nanocomposites ($Ti_3C_2T_x$, SnO_2-Ti_3C_2, and C@SnO_2/Ti_3C_2) as working electrodes and lithium foil as the counter electrode in half-cell batteries. The thickness of the electrode and the accurate mass of active material are 300 μm and 3.76 mg, respectively. Figure 6(a) presents the CV curves of C@SnO_2/-Ti_3C_2 at a scan rate of 0.1 mV s^{-1} in the voltage range of 0.01~3.00 V (vs. Li/Li^+). As can been seen, the characteristic reduction peak was found nearly 0.69 V in the first lithiation process for the C@SnO_2/Ti_3C_2 electrode. The reduction peak of 0.69 V might be generated by the formation of a solid electrolyte interphase (SEI) layer on the surface of the active material and the formation of Li_2O while SnO_2 chemically reacts to form Sn. Nonetheless, it vanished in the following cycles, indicating that the irreversible reaction happened [9, 29]. It is important that the $Ti_3C_2T_x$ after HF corrosion has functional groups, for example, hydroxyl groups and fluorine groups. During the lithiation process, lithium ions enter the $Ti_3C_2T_x$ layer and interact with these functional groups, resulting in the irreversibility of the first cycle [15, 30]. The obvious peak near 0.02 V which compares to the lithiation of carbon rises in the active materials. In the first delithiation process, there are two distinct anodic peaks situated at 0.58 V and 1.25 V, ascribing to the dealloying process for Li_xSn and the Li ions from MXene sheets [9, 31]. The peak at 0.21 V indicates that Li ions enter the interlayer of $Ti_3C_2T_x$ to increase the capacity of lithium. C@SnO_2/Ti_3C_2 shows a couple of excellent redox peaks, suggesting C@SnO_2/Ti_3C_2 has outstanding reversible performance during charging and discharging.

EIS of $Ti_3C_2T_x$, SnO_2-Ti_3C_2, and C@SnO_2/Ti_3C_2 are shown in Figure 6(b). Nyquist plots of $Ti_3C_2T_x$, SnO_2-

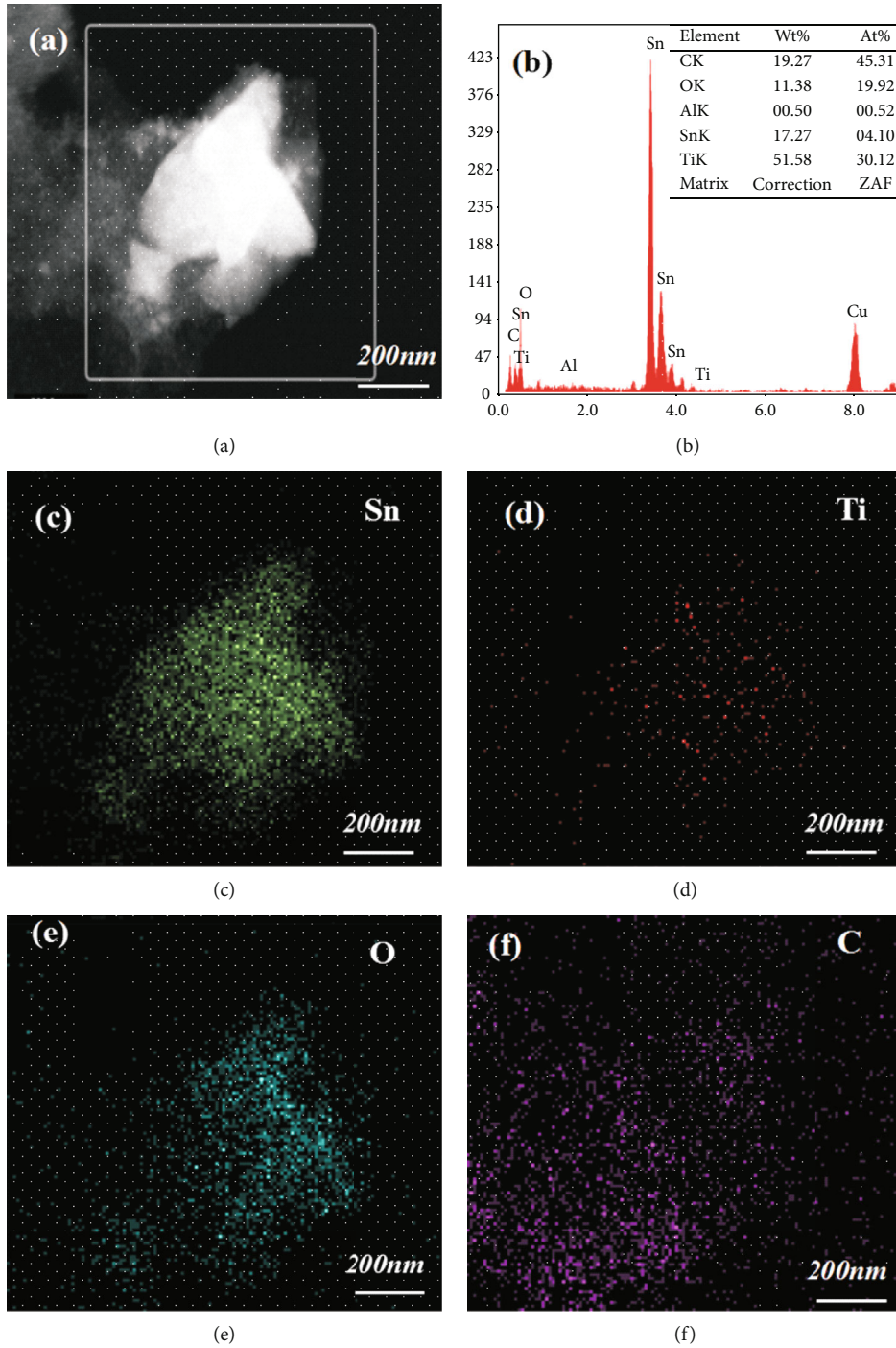

FIGURE 5: Elemental mapping images of C@SnO_2/Ti_3C_2 nanoparticles: (a) TEM image; (b) electron dispersive spectroscopy (EDS) pattern of (c) tin, (d) titanium, (e) oxygen, and (f) carbon distribution in the selected area.

Ti_3C_2, and C@SnO_2/Ti_3C_2 comprise a straight line at low frequencies and a semicircle at high frequencies. As can be seen from the figure, the semicircle of C@SnO_2/Ti_3C_2 is the smallest among all samples and the slope of the line of C@SnO_2/-Ti_3C_2 is the largest. Therefore, it can be concluded that the minimum impedance of C@SnO_2/Ti_3C_2 means that it has excellent conductivity, which is credited to the uniform dispersion of SnO_2 NPs and the presence of large amounts of amorphous carbon. At the same time, the increase of conductivity is beneficial to the improvement of electrochemical performance of C@SnO_2/Ti_3C_2.

With the galvanostatic charge/discharge profiles of $Ti_3C_2T_x$, SnO_2-Ti_3C_2, and C@SnO_2/Ti_3C_2 anodes at a current density of 100 mA g^{-1}, all the samples are tested over the voltage range of 0.01~3.00 V as presented in Figure 6(c). The first-cycle discharge and charge capacities of as-prepared C@SnO_2/Ti_3C_2 anodes are 811.4 and 1531.5 mAh g^{-1}, respectively, which are just about 3 times as much as that of

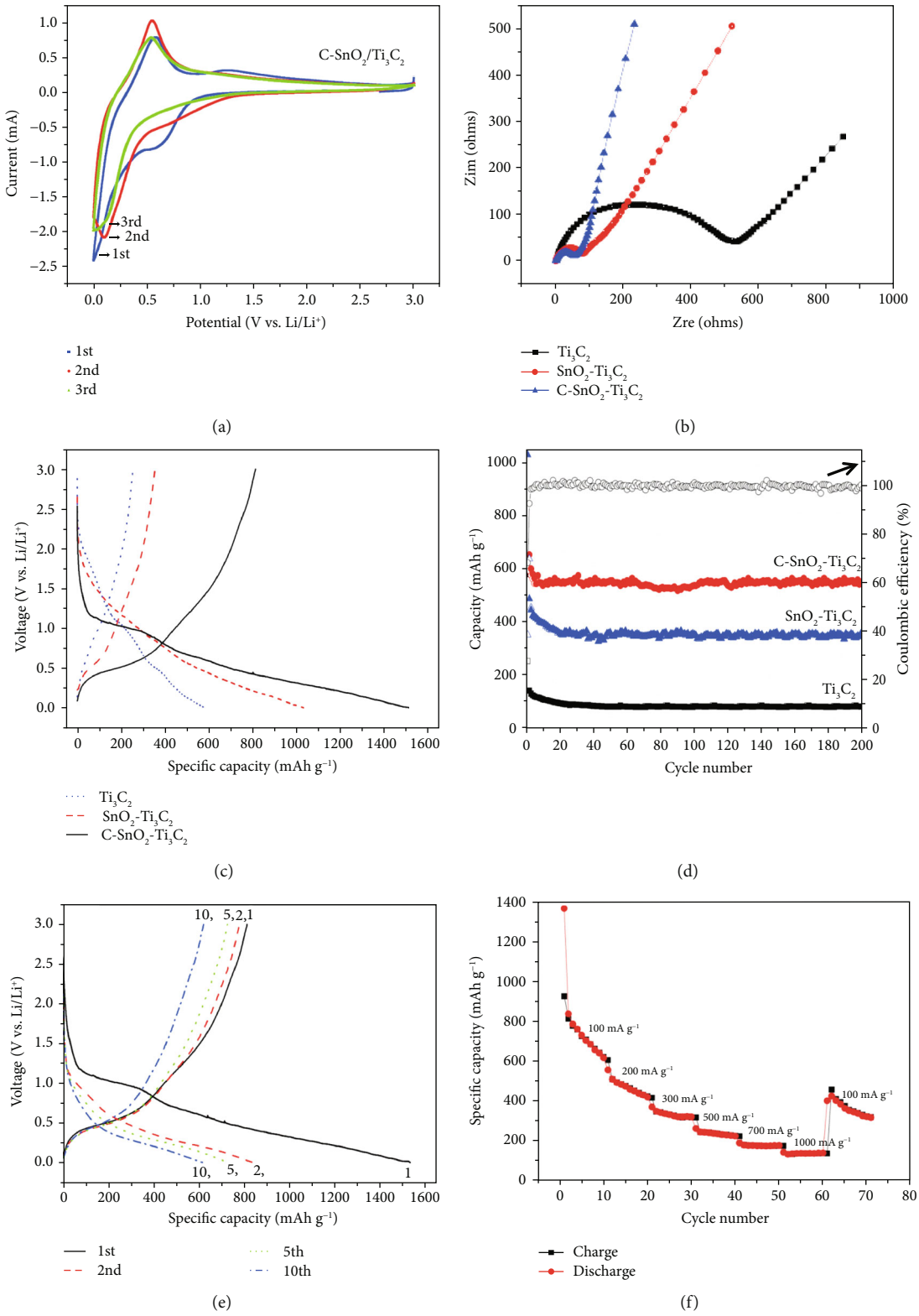

FIGURE 6: (a) CV curves of C@SnO_2/Ti_3C_2 from 3.0 V to 0.01 V vs. Li/Li^+ at a scan rate of 0.1 mV s^{-1}; (b) EIS for $Ti_3C_2T_x$, SnO_2-Ti_3C_2, and C@SnO_2/Ti_3C_2; (c) charge/discharge profiles of $Ti_3C_2T_x$, SnO_2-Ti_3C_2, and C@SnO_2/Ti_3C_2 at 100 mA g^{-1}; (d) cycling performance of $Ti_3C_2T_x$, SnO_2-Ti_3C_2, and C@SnO_2/Ti_3C_2 at 100 mA $g^{-1}$and the coulombic efficiency of C@SnO_2/Ti_3C_2; (e) charge/discharge profiles of C@SnO_2/Ti_3C_2 at 100 mA g^{-1}; (f) rate performance of the C@SnO_2/Ti_3C_2 nanocomposite electrode.

unadulterated $Ti_3C_2T_x$ (580.5 mAh g^{-1}) and higher than SnO_2-Ti_3C_2 nanocomposites (1030.1 mAh g^{-1}). The initial capacity loss is about 53% for C@SnO_2/Ti_3C_2. The voltage plateau and slope of the discharge/charge profiles correspond to the CV curves recently reported in our work. The enormous capacity decay is due to the arrangement of the SEI layer and the functional groups, including fluorine and hydroxyls, on the surface of the active material. These outcomes affirm that an exceedingly conjugated carbonaceous polymer improves conductivity and the introduction of SnO_2 NPs amplifies the d-spacing of $Ti_3C_2T_x$ layers, which expands the Li storage capacity significantly.

As shown in Figure 6(d), the first discharge capacities for the pure $Ti_3C_2T_x$ and SnO_2/Ti_3C_2 nanocomposites are 581.1 mAh g^{-1} and 1031.1 mAh g^{-1}, respectively. However, C@SnO_2/Ti_3C_2 demonstrates extraordinarily the first capacity of 1531.5 mAh g^{-1} at 100 mA g^{-1}; the first charge and discharge capacity can stay at around 540 mAh g^{-1} even after 200 cycles and the relevant coulombic efficiency of C@SnO_2/Ti_3C_2 remains at around 98% (Figure 6(d)). The outstanding electrochemical reversibility of C@SnO_2/Ti_3C_2 is attributed to the carbon coating layers. In addition to improving conductivity, the amorphous carbon can also alleviate the volume expansion of SnO_2 NPs. For a comparison, pure $Ti_3C_2T_x$ begins to decay rapidly after the third charge and discharge cycles and remains at around 82.3 mAh g^{-1} at 200 cycles. However, SnO_2-Ti_3C_2 shows lower reversible capacities than C@SnO_2/Ti_3C_2. In addition, from Figure 6(d) we can also see that the coulomb efficiency of C@SnO_2/Ti_3C_2 can still be maintained between 98% and 99% and with no significant attenuation after the tenth cycles. Moreover, C@SnO_2/Ti_3C_2 likewise has great rate capacity as appears in Figure 6(f). As the current density recovers from 1000 to 100, the capacity of C@SnO_2/Ti_3C_2 also recuperates to 454.3 mAh g^{-1}, indicating a good capacity reversibility of C@SnO_2/Ti_3C_2. It can be seen from Figure 7 that at the current density of 300 mA g^{-1}, the reversible specific capacity of C@SnO_2/Ti_3C_2 still remains at around 480 mAh g^{-1} even after 200 cycles.

Table 1 shows the electrochemical properties of different MXene-based nanomaterials as anode materials for LIBs. As can be seen from the table, the electrochemical performance of C@SnO_2/Ti_3C_2 is significantly better than other MXene-based nanomaterials. Meanwhile, the electrochemical properties of the previously reported MXene-based nanomaterials are inadmissible, especially in terms of capacity and cycle stability. In their work, storing Li^+ relies on MXene having larger lattice parameters, while larger lattice parameters imply larger layer spacing, which is beneficial for Li^+ storage [15].

However, in this paper, we rely on metal oxides (SnO_2 NPs) with high theoretical capacity to increase the Li^+ storage capacity of C@SnO_2/Ti_3C_2. At the same time, the presence of SnO_2 NPs can increase the interlayer spacing of C@SnO_2/Ti_3C_2, thereby increasing the lithium storage of the C@SnO_2/Ti_3C_2 capacity. In addition, SnO_2 NPs improve the conductivity by the transportation of Sn^{4+}, which promotes the release and insertion speed of Li^+ in the electrode material. In this way, the combination of metal oxide and MXene provides a promising research strategy for LIB anode materials.

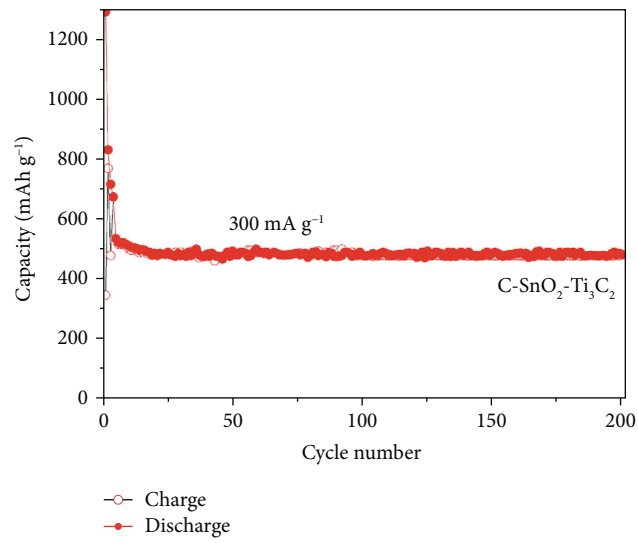

Figure 7: Cycling performance of C@SnO_2/Ti_3C_2 nanocomposite at a current density of 300 mA g^{-1}.

Table 1: Comparison of the performances of the various MXene-based materials for LIBs.

Electrode material	Current density	Initial capacity	Steady capacity/cycle number
$Ti_3C_2T_x$ [15]	260 mA g^{-1}	123.6 mAh g^{-1}	69 mAh g^{-1}/100
Ti_2CT_x [14]	260 mA g^{-1}	480 mAh g^{-1}	110 mAh g^{-1}/80
Ti_3C_2/CNF [32]	320 mA g^{-1}	848 mAh g^{-1}	320 mAh g^{-1}/80
C@SnO_2/Ti_3C_2	300 mA g^{-1}	1531.5 mAh g^{-1}	540 mAh g^{-1}/200

4. Conclusions

In this work, C@SnO_2/Ti_3C_2 nanocomposites with amazing electrochemical performance as anode material for LIBs are synthesized via hydrothermal strategy pursued by a simple calcination. Due to $Ti_3C_2T_x$ providing C@SnO_2/-Ti_3C_2 with a decent skeleton structure, amorphous carbon gives C@SnO_2/Ti_3C_2 with fantastic electrical conductivity; C@SnO_2/Ti_3C_2 nanocomposites display excellent initial capacity of 1531.5 mAh g^{-1} at current density of 100 mA g^{-1} and show outstanding rate performance of 540 mAh g^{-1} even after 200 cycles. The exceptional electrochemical performance credits the uniform dispersion of SnO_2 NPs, high conductivity of amorphous carbon, and chemical stability of $Ti_3C_2T_x$. Another reason is that SnO_2 NPs improve the conductivity by the transportation of Sn^{4+} and Li^+ insertion/extraction into the anode. These outstanding properties show that amorphous carbon and metal oxide composites in 2D-layered material MXene have comprehensive application prospects in energy storage.

Data Availability

The data used to support the findings of this study are available from the corresponding authors upon request.

Conflicts of Interest

There is no conflict of interest.

Acknowledgments

This work was supported by the National Natural Science Foundation of China (51472153, 51572158) and the Graduate Innovation Fund of Shaanxi University of Science & Technology.

References

[1] M. Armand and J.-M. Tarascon, "Building better batteries," *Nature*, vol. 451, no. 7179, pp. 652–657, 2008.

[2] Y. Li, K. Yan, H. W. Lee, Z. Lu, N. Liu, and Y. Cui, "Growth of conformal graphene cages on micrometre-sized silicon particles as stable battery anodes," *Nature Energy*, vol. 1, no. 2, article 15029, 2016.

[3] Y. H. Huang, Q. Bao, B. H. Chen, and J. G. Duh, "Nano-to-microdesign of Marimo-like carbon nanotubes supported frameworks via in-spaced polymerization for high performance silicon lithium ion battery anodes," *Small*, vol. 11, no. 19, pp. 2314–2322, 2015.

[4] C. Fang, Y. Deng, Y. Xie, J. Su, and G. Chen, "Improving the electrochemical performance of Si nanoparticle anode material by synergistic strategies of polydopamine and graphene oxide coatings," *The Journal of Physical Chemistry C*, vol. 119, no. 4, pp. 1720–1728, 2015.

[5] M. Naguib, M. Kurtoglu, V. Presser et al., "Two-dimensional nanocrystals produced by exfoliation of Ti_3AlC_2," *Advanced Materials*, vol. 23, no. 37, pp. 4248–4253, 2011.

[6] M. Naguib, O. Mashtalir, J. Carle et al., "Two-dimensional transition metal carbides," *ACS Nano*, vol. 6, no. 2, pp. 1322–1331, 2012.

[7] M. Naguib, J. Halim, J. Lu et al., "New two-dimensional niobium and vanadium carbides as promising materials for Li-ion batteries," *Journal of the American Chemical Society*, vol. 135, no. 43, pp. 15966–15969, 2013.

[8] M. Naguib, V. N. Mochalin, M. W. Barsoum, and Y. Gogotsi, "25th anniversary article: MXenes: a new family of two-dimensional materials," *Advanced Materials*, vol. 26, no. 7, pp. 992–1005, 2014.

[9] M. Naguib, J. Come, B. Dyatkin et al., "MXene: a promising transition metal carbide anode for lithium-ion batteries," *Electrochemistry Communications*, vol. 16, no. 1, pp. 61–64, 2012.

[10] O. Mashtalir, M. Naguib, V. N. Mochalin et al., "Intercalation and delamination of layered carbides and carbonitrides," *Nature Communications*, vol. 4, no. 1, article 1716, 2013.

[11] J. Hu, B. Xu, C. Ouyang, S. A. Yang, and Y. Yao, "Investigations on V_2C and V_2CX_2 (X = F, OH) monolayer as a promising anode material for Li ion batteries from first-principles calculations," *Journal of Physical Chemistry C*, vol. 118, no. 42, pp. 24274–24281, 2014.

[12] Q. Tang, Z. Zhou, and P. Shen, "Are MXenes promising anode materials for Li ion batteries? Computational studies on electronic properties and Li storage capability of Ti_3C_2 and $Ti_3C_2X_2$ (X = F, OH) monolayer," *Journal of the American Chemical Society*, vol. 134, no. 40, pp. 16909–16916, 2012.

[13] Y. Xie, M. Naguib, V. N. Mochalin et al., "Role of surface structure on Li-ion energy storage capacity of two-dimensional transition-metal carbides," *Journal of the American Chemical Society*, vol. 136, no. 17, pp. 6385–6394, 2014.

[14] S. Zhao, W. Kang, and J. Xue, "Role of strain and concentration on the Li adsorption and diffusion properties on Ti_2C layer," *Journal of Physical Chemistry C*, vol. 118, no. 27, pp. 14983–14990, 2014.

[15] D. Sun, M. Wang, Z. Li, G. Fan, L. Z. Fan, and A. Zhou, "Two-dimensional Ti_3C_2 as anode material for Li-ion batteries," *Electrochemistry Communications*, vol. 47, pp. 80–83, 2014.

[16] M. R. Lukatskaya, O. Mashtalir, C. E. Ren et al., "Cation intercalation and high volumetric capacitance of two-dimensional titanium carbide," *Science*, vol. 341, no. 6153, pp. 1502–1505, 2013.

[17] M. Ghidiu, M. R. Lukatskaya, M. Q. Zhao, Y. Gogotsi, and M. W. Barsoum, "Conductive two-dimensional titanium carbide 'clay' with high volumetric capacitance," *Nature*, vol. 516, no. 7529, pp. 78–81, 2014.

[18] Y. Dall'Agnese, M. R. Lukatskaya, K. M. Cook, P. L. Taberna, Y. Gogotsi, and P. Simon, "High capacitance of surface-modified 2D titanium carbide in acidic electrolyte," *Electrochemistry Communications*, vol. 48, pp. 118–122, 2014.

[19] M. D. Levi, M. R. Lukatskaya, S. Sigalov et al., "Solving the capacitive paradox of 2D MXene using electrochemical quartz-crystal admittance and in situ electronic conductance measurements," *Advanced Energy Materials*, vol. 5, no. 1, article 1400815, 2015.

[20] Y. Chen, B. Song, R. Chen, L. Lu, and J. Xue, "A study of the superior electrochemical performance of 3 nm SnO_2 nanoparticles supported by graphene," *Journal of Materials Chemistry A*, vol. 2, no. 16, pp. 5688–5695, 2014.

[21] Y. Idota, T. Kubota, A. Matsufuji, Y. Maekawa, and T. Miyasaka, "Tin-based amorphous oxide: a high-capacity lithium-ion-storage material," *Science*, vol. 276, no. 5317, pp. 1395–1397, 1997.

[22] M. V. Reddy, G. V. Subba Rao, and B. V. R. Chowdari, "Metal oxides and oxysalts as anode materials for Li ion batteries," *Chemical Reviews*, vol. 113, no. 7, pp. 5364–5457, 2013.

[23] J. Liang, W. Wei, D. Zhong, Q. Yang, L. Li, and L. Guo, "One-step in situ synthesis of SnO_2/graphene nanocomposites and its application as an anode material for Li-ion batteries," *ACS Applied Materials & Interfaces*, vol. 4, no. 1, pp. 454–459, 2012.

[24] Y. G. Zhu, Y. Wang, J. Xie et al., "Effects of graphene oxide function groups on SnO_2/graphene nanocomposites for lithium storage application," *Electrochimica Acta*, vol. 154, pp. 338–344, 2015.

[25] G. Wu, M. Wu, D. Wang et al., "A facile method for in-situ synthesis of SnO_2/graphene as a high performance anode material for lithium-ion batteries," *Applied Surface Science*, vol. 315, no. 1, pp. 400–406, 2014.

[26] F. Wang, Z. Wang, J. Zhu et al., "Facile synthesis SnO_2 nanoparticle-modified Ti_3C_2 MXene nanocomposites for enhanced lithium storage application," *Journal of Materials Science*, vol. 52, no. 7, pp. 3556–3565, 2017.

[27] J. S. Chen and X. W. D. Lou, "SnO_2-based nanomaterials: synthesis and application in lithium-ion batteries," *Small*, vol. 9, no. 11, pp. 1877–1893, 2013.

[28] W. Zheng, P. G. Zhang, W. B. Tian et al., "Microwave-assisted synthesis of SnO_2-Ti_3C_2 nanocomposite for enhanced supercapacitive performance," *Materials Letters*, vol. 209, pp. 122–125, 2017.

[29] X. Li, X. Wang, L. Zhang, S. Lee, and H. Dai, "Chemically derived, ultra smooth graphene nanoribbon semiconductors," *Science*, vol. 319, no. 5867, pp. 1229–1232, 2008.

[30] M. A. Hope, A. C. Forse, K. J. Griffith et al., "NMR reveals the surface functionalisation of Ti_3C_2 MXene," *Physical Chemistry Chemical Physics*, vol. 18, no. 7, pp. 5099–5102, 2016.

[31] J. Luo, W. Zhang, H. Yuan et al., "Pillared structure design of MXene with ultralarge interlayer spacing for high-performance lithium-ion capacitors," *ACS Nano*, vol. 11, no. 3, pp. 2459–2469, 2017.

[32] Z. Lin, D. Sun, Q. Huang, J. Yang, M. W. Barsoum, and X. Yan, "Carbon nanofiber bridged two-dimensional titanium carbide as a superior anode for lithium-ion batteries," *Journal of Materials Chemistry A*, vol. 3, no. 27, pp. 14096–14100, 2015.

Hindawi
Journal of Nanomaterials
Volume 2019, Article ID 8346251, 7 pages
https://doi.org/10.1155/2019/8346251

Research Article

Controlled Synthesis of Porous Co_3O_4 Nanostructures for Efficient Electrochemical Sensing of Glucose

Jiankang Luo,[1] Jun Wu,[1] Zheng Liu,[2] Zenghe Li,[1] and Li Deng[1,3]

[1]*College of Life Science and Technology, Beijing University of Chemical Technology, Beijing 100029, China*
[2]*Chinese Research Academy of Environmental Sciences, Beijing 100012, China*
[3]*Amoy-BUCT Industrial Bio-Technovation Institute, Beijing University of Chemical Technology, Amoy 361022, China*

Correspondence should be addressed to Zenghe Li; lizh@mail.buct.edu.cn and Li Deng; dengli@mail.buct.edu.cn

Received 20 May 2019; Accepted 10 August 2019; Published 16 September 2019

Guest Editor: Fei Ke

A shape-controlled strategy was developed to synthesize porous Co_3O_4 nanoparticles, and the delicate morphology including nanourchins, nanowires, nanoflowers, and nanoplates could be well adjusted by adopting different anion precursors. The Co_3O_4 nanomaterials were further applied as the electrocatalysts for glucose detection, and the effect of nanostructure on the electrochemical performance was investigated. Results show that Co_3O_4 nanourchins illustrate the highest glucose sensitivity of 565 mA mM^{-1} cm^{-2} and a good linear detection ranging from 20 μM to 0.25 mM. The improved performance of obtained products was originally from the large surface area and high pore volume, which leads to a significantly increased accessibility of reactant and decreased Faradic electron transfer resistance, making it a promising candidate for glucose sensing.

1. Introduction

In recent years, great efforts have been devoted to the development of highly sensitive and selective, cost-effective detectors for glucose in pharmaceuticals, food, and clinical diagnostics [1], due to their risk of increasing cholesterol content, food allergies, and diabetes. Among various methods, using an electrochemical sensor is recognized as one of the most promising techniques compared to its counterparts including optical [2], thermometric [3], and fluorescent [4] sensors, owing to its high sensitivity, reliability, and affordable cost. However, using conventional natural enzymes as a biological sensor suffers from several disadvantages for electrochemical glucose detection, such as high cost [5], storage difficulties, easy denaturation by environmental changes (e.g., temperature, humidity, and pH), and digestion by proteases [6]. Consequently, a series of nonenzymatic sensors have been proposed as the glucose probe in the past few decades, and these catalysts are mainly of noble metals (e.g., Au, Pt, and Pd), noble metal alloys (e.g., Pt–Pd, Pt–Cu, and Pt–Au), and transition metal oxides (e.g., Fe_3O_4, Co_3O_4, and CoO) [7]. However, the scarcity and high cost of these noble metal sensors make an obstacle for their applications, and it is still highly desired to develop alternative earth-abundant sensor materials with high efficiency [8].

Compared to noble metal-based glucose sensing catalysts, transition metal compounds are of low cost and abundant. Recent studies also show that shape-controlled synthesis of nanoparticles is capable of offering excellent performances in various applications [9–11]. Co_3O_4 is regarded as one of the most promising electrocatalysts for glucose detection. However, the inherently high electronic resistance and low surface area of Co_3O_4 retard its practical application [12]. Generally, the electrocatalytic properties of materials are strongly dependent on their morphology and microstructures, which creates substantial differences in the surface area, particle size, pore structure, mass transport, and electron transfer efficiency, which in turn influence their electrochemical sensing performance [13]. Therefore, the morphology and nanostructure control of Co_3O_4 are of vital importance to improve the electrochemical reactivity [6]. To this end, various Co_3O_4 nanoarchitectures such as nanospheres, nanocubes, and nanofibers have been synthesized by conventional precipitation, a hydrothermal process, and a

microwave-assisted approach [14]. Although there has been an extensive effort in the development of shape-controlled synthesis, the facile and mild approaches are still rare. Furthermore, few studies are focusing on the effect of morphologies and microstructures on the electrochemical activity of glucose detection [15].

Herein, a shaped-controlled synthesis route was developed to prepare Co_3O_4 nanostructures with tunable morphology by simply adopting different anions. The obtained Co_3O_4 nanourchins, nanowires, nanoflowers, and nanoplates are further used as the sensing materials for glucose detection, and the results reveal that Co_3O_4 nanourchins exhibit the highest glucose sensitivity of 565 mA mM^{-1} cm^{-2} and good stability due to the large surface area and low carrier transfer resistance [16].

2. Experiment

2.1. Synthesis of Co_3O_4 Nanomaterials. All chemicals were of analytical grade and used as received without further purification.

The porous Co_3O_4 nanostructures, including nanourchins, nanowires, nanoflowers, and nanoplates, were synthesized by a surfactant-assisted hydrothermal method using different cobalt precursors. Typically, 5 mM of $CoSO_4{\cdot}7H_2O$ or ($CoCl_2{\cdot}6H_2O$, $Co(NO_3)_2{\cdot}6H_2O$, and $Co(Ac)_2{\cdot}4H_2O$) was dissolved in water (40 mL) under stirring, followed by adding 1.5 g of $CO(NH_2)_2$ and 0.05 g of CTAB. After stirring for 30 min, the resulted transparent solution was transferred into a 50 mL autoclave, sealed, and maintained at 120°C for 12 h. After cooling to room temperature, the precipitate was collected by centrifugation, rinsed with water and ethanol, and dried at 80°C for 24 h. Finally, the obtained product was calcined at 500°C for 2 h in air.

2.2. Structural and Electrochemical Characterization of Co_3O_4 Nanomaterials. The composition and phase of the Co_3O_4 nanostructures were obtained by using the X-ray diffraction (XRD) profile on a Rigaku D/Max 2500 PC diffractometer with Cu Kα radiation ($\lambda = 1.54056$ Å) as the X-ray source. The morphology was examined by JEOL 6701F scanning electron microscopy (SEM). The N_2 adsorption-desorption analysis was measured on a Micromeritics Tristar 3020II instrument. Cyclic voltammetry (CV) and amperometry measurements were performed using a CHI660E electrochemical station (Chenhua, China) equipped with a standard three-electrode cell. The Co_3O_4 nanostructure-modified glassy carbon electrode (GCE) was used as the working electrode, while platinum wire and saturated calomel electrodes (SCE) served as the counter and reference electrodes, respectively. In preparing the working electrode, 5 mg of Co_3O_4 and 50 μL of Nafion (5 wt.%, DuPont) were ultrasonically dispersed in 1.0 mL ethanol for 0.5 h. Then, 6 μL of the homogeneous slurry was transferred onto the GCE (0.071 cm^2) and evaporated in an ambient atmosphere. The electrolyte was diluted with glucose in 0.1 M NaOH. Electrochemical impedance spectroscopy (EIS) measurements were performed at open-circuit potential with the frequency range of 0.1-100 kHz and an ac perturbation of 5.0 mV.

3. Results and Discussion

In our work, the porous Co_3O_4 nanostructures were synthesized using different cobalt precursors (see the experimental section in supporting information), and the morphology of the obtained products was firstly investigated and is shown in Figure 1. As observed, the featured morphologies of nanourchins, nanowires, nanoflowers, and nanoplates were realized by choosing distinct anion precursors. The self-assembly nanourchin Co_3O_4, which is obtained by using sulphate precursors, appears with an external diameter of about 3 μm, and the thorns grown on the surface are in the diameter of 23 nm with a length of 200 nm. Each urchin is estimated to have hundreds of thorns on the surface, which creates a significant roughness and offers a large surface area. Also, with all the thorns vertical to the surface, the transport would be facilitated if there were any reactions catalyzed over the nanostructure [17]. The chloridion-controlled Co_3O_4 synthesis, however, shows a significantly different structure of nanowires [18]. Each wire has a length of several micrometers and a diameter of 40 nm. The wire tends to aggregate with another or two, forming several combos, which reduces the surface area. With a careful examination, it can be seen that each wire is fabricated with about twenty nanorods end to end. This suggests that there has been a self-assembly process in the synthesis. The Co_3O_4 nanoflowers were prepared with the existence of nitrate ions. The flower has an apparent diameter of 15 μm and consists of dozens of twisted plates in the width of 0.6 μm and thickness of 0.1 μm. This self-assembled structure forms voids among the plates which is favorable to enlarge the surface area. However, compared to the nanourchin structure, the voids are confined between the plates, resulting in a poor interconnection [19]. The Co_3O_4 nanoplates were obtained with the presence of acetate. The plates are not that well-defined as those in the nanoflowers [20]. There are several random fragments and aggregates. The relatively large plates are in a width of 3 μm, and the thickness is about 0.1 μm.

The XRD patterns of the prepared Co_3O_4 nanomaterials are all indexed to a cubic Co_3O_4 phase, without any signal from other phases of cobalt oxides being detected, as shown in Figure 2. The higher intensity of the (311) plane as compared to the other planes could be observed from the patterns. In addition, the obvious broader peaks for Co_3O_4 nanourchins as compared to other nanostructures shown in Figure 2 (b–d) were observed, which is attributed to the suppression of crystal size by the sulphate anions. The grain sizes of the nanomaterials were estimated to be 16.9, 33.8, 22.5, and 28.1 nm for the Co_3O_4 nanourchins, nanowires, nanoflowers, and nanoplates, respectively, according to the Scherrer equation [21]. The variety in the grain size is believed to be caused by the tuned nucleation and grow process when different anions are present [22].

The surface area and pore structure of the Co_3O_4 nanomaterials were examined by the N_2 adsorption-desorption measurement. As shown in Fig. S1, each sample displays a type IV plot with a hysteresis loop. This suggests the presence of mesopores, which is confirmed by the Barrett-Joyner-Halenda (BJH) pore size distribution. The specific surface

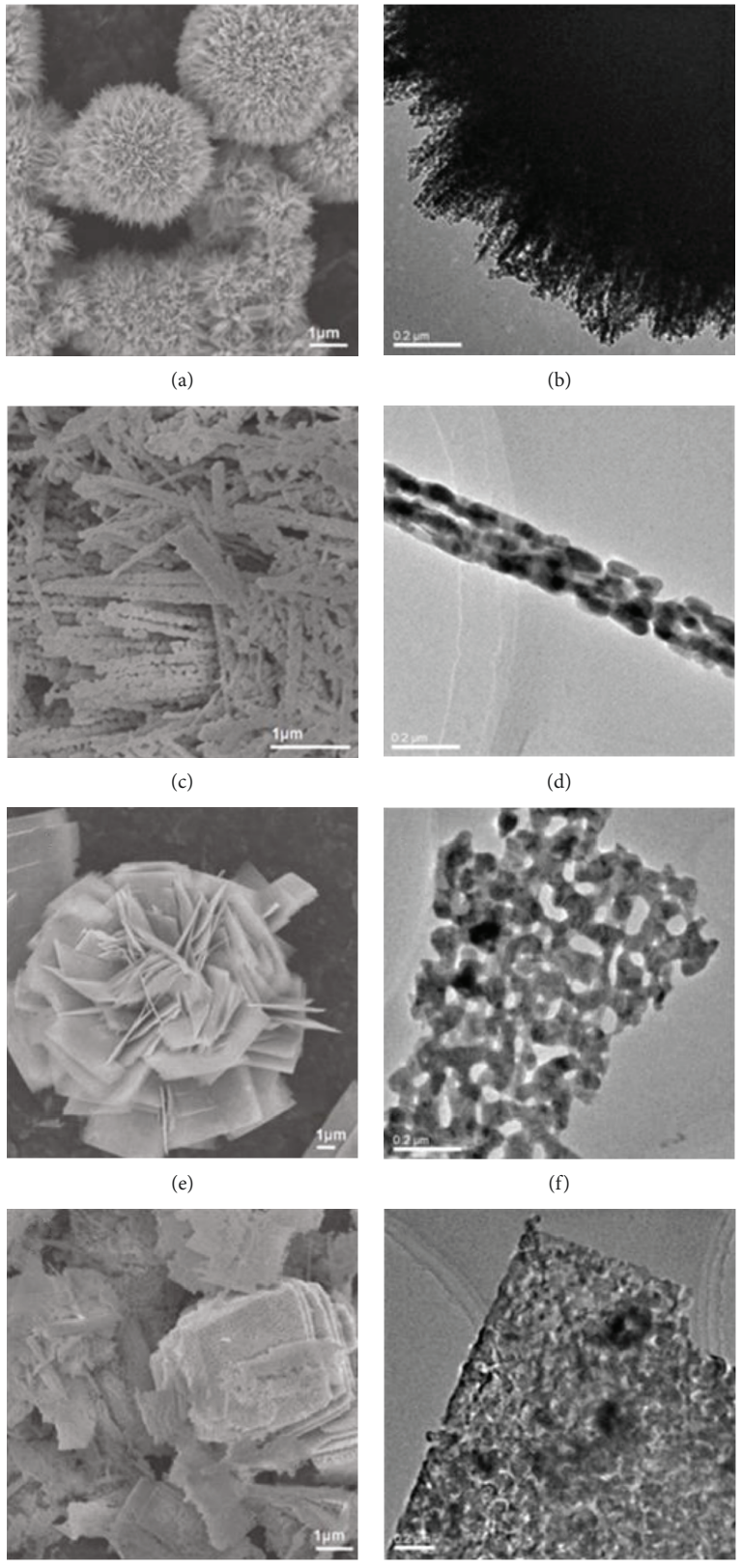

Figure 1: SEM and corresponding TEM images of Co_3O_4 synthesized with different anion precursors: (a, b) cobalt sulphate, (c, d) cobalt chloride, (e, f) cobalt nitrate, and (g, h) cobalt acetate.

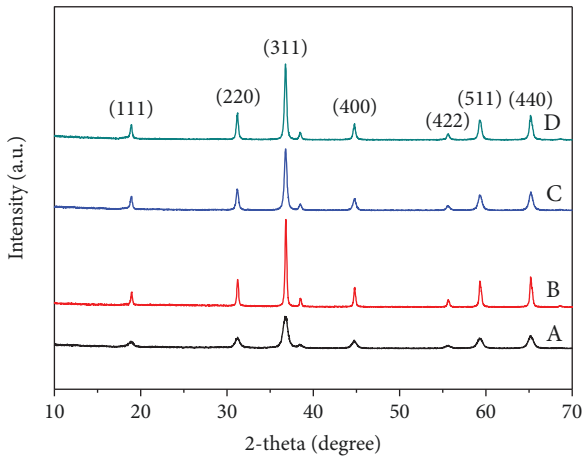

FIGURE 2: XRD patterns of the obtained Co_3O_4 nanoparticles after annealing treatment: (a) nanourchins, (b) nanowires, (c) nanoflowers, and (d) nanoplates.

area, pore volume, and average pore size of the Co_3O_4 nanomaterials are summarized in Table S1. The Co_3O_4 nanourchins have a specific surface area of 70.76 m^2 g^{-1}, which is significantly higher than that of the nanowires (11.75 m^2 g^{-1}), nanoflowers (9.93 m^2 g^{-1}), and nanoplates (13.06 m^2 g^{-1}). This feature is attributed to the abundant thorns with a small diameter of 23 nm grown on the surface of nanourchins. The average pore sizes of the Co_3O_4 nanourchins, nanowires, nanoflowers, and nanoplates are 10.81, 18.56, 36.22, and 36.27 nm, respectively, showing that the nanourchins have the smallest pores [23].

Further phase characterization of the Co_3O_4 nanomaterials before calcination was carried out to investigate the formation mechanism of the porous structure. As shown in Fig. S2, the uncalcined precursors have different phases. The peaks of the Co_3O_4 nanourchin precursor are composed of $CoCO_3$ (JCPDS: 11-0692) and $Co(OH)_2$ (JCPDS: 30-0443) [24]. While for a Co_3O_4 nanowire precursor, a pattern of $Co(CO_3)_{0.35}(Cl)_{0.20}(OH)_{1.10}{\cdot}1.74H_2O$ is discovered, the Co_3O_4 nanoflower precursor, however, is found to have the $Co(CO_3)_{0.5}(OH){\cdot}0.11H_2O$ (JCPDS: 48-0083) phase. As for the Co_3O_4 nanoplate precursor, a phase of $CoCO_3$ (JCPDS: 11-0692) is detected. These results suggest that the anions have a significant influence on the precursor formation due to the unique space-structure effect [25]. During heat treatment, the precursors decompose to oxide and release gas, which results in the formation of porous nanostructures [26].

The electrochemical activity towards glucose oxidation was determined by cyclic voltammetry (CV) and chronoamperometry. As shown in Figure 3, two pairs of redox peaks are observed for the Co_3O_4 nanomaterials in 0.1 M NaOH. The redox pair located between 0.1 and 0.4 V is attributed to the transformation of Co_3O_4/CoOOH, with the cathodic response which is not that obvious. The other redox pair of CoOOH/CoO_2 emerges between 0.5 and 0.6 V, as shown in

$$Co_3O_4 + OH^- + H_2O \rightarrow 3CoOOH + e^- \quad (1)$$

$$CoOOH + OH^- \rightarrow CoO_2 + H_2O + e^- \quad (2)$$

After the addition of 1 mM glucose, the peak currents of all the Co_3O_4 nanomaterials significantly increase due to the glucose oxidation. This electrochemical-chemical (EC) process is promoted by the Co_3O_4 intermediates, dominated by the CoO_2 species [27]. The glucose was oxidized by CoO_2 during the anodic scan and generated CoOOH. The formed CoOOH further contributes to the oxidation current, resulting in the increased anodic signal. The glucose detection by the Co_3O_4 nanomaterials is illustrated as follows [15].

$$CoOOH + OH^- \rightarrow CoO_2 + H_2O + e^- \quad (3)$$

$$CoO_2 + \text{glucose} \rightarrow CoOOH + \text{gluconolactone} \quad (4)$$

Therefore, the glucose oxidation activity of Co_3O_4 nanomaterials can be indicated by the increment in the anodic current density. With the addition of glucose, the current increase in Co_3O_4 nanourchins is 26.2 μA, which is higher than that with the Co_3O_4 nanowires (4.6 μA), nanoflowers (5.7 μA), and nanoplates (7.3 μA). The highest activity of Co_3O_4 nanourchins is attributed to the large surface area and facile accessibility of the active sites.

The Co_3O_4 nanomaterials were coated on the GCE and applied as the electrochemical sensor for glucose detection. As shown in Figure 4(a), the current increases when the glucose is added, suggesting the high electrochemical activity of Co_3O_4 nanomaterials [23, 28–30]. Figure 4(b) shows the linear relationship between the response current and the glucose concentration, and the sensitivity was calculated from the slope of the calibration curve [31]. It is observed that Co_3O_4 nanourchins have the highest electrochemical sensing performance, which is in agreement with the CV results. The detection limit is calculated to be 1.5 μM at a signal-to-noise ratio of 3 (S/N = 3) with a high sensitivity of 565 mA mM^{-1} cm^{-2} and a good linear detection ranging from 20 μM to 0.25 mM. The comparison between the previous reported glucose sensor and Co_3O_4 nanourchin-modified GCE is listed in Table S2. As can be seen, the Co_3O_4 nanourchin-modified GCE shows good performance towards the detection of glucose, offering a potential candidate for glucose detection application. Fig. S3 shows the EIS plots of Co_3O_4 nanomaterials at open-circuit potential in 0.1 M NaOH solution [28]. The plots consist of a well-defined semicircle in high frequency and a sloping line in low frequency [32]. The data was fitted to an equivalent circuit as shown in Fig. S3A, where Rs represents the inner resistance, Rct represents the Faradic electron transfer resistance, W is the Warburg impedance, Q_1 is the double-layer capacitance, and Q_2 is the pseudocapacitance [30]. The Faradic electron transfer resistance for the GCE modified by Co_3O_4 nanourchins, nanowires, nanoflowers, and nanoplates is 120, 421, 193, and 185 Ω, respectively. Notably, the Co_3O_4 nanourchin-modified GCE has the lowest Faradic electron transfer resistance, further confirming the highest electrochemical reactivity [15].

It is known that the possible coexisting species such as UA and AA may disturb the electrochemical detection of

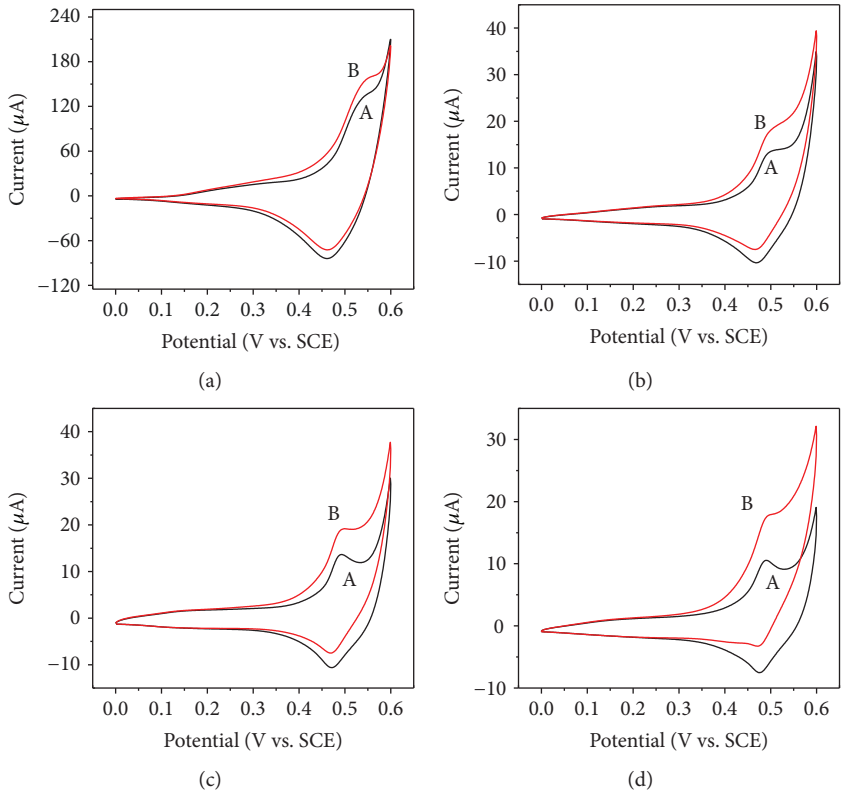

FIGURE 3: CV of Co_3O_4 (a) nanourchins, (b) nanowires, (c) nanoflowers, and (d) nanoplates (A) without and (B) with 1 mM glucose in 0.1 M NaOH.

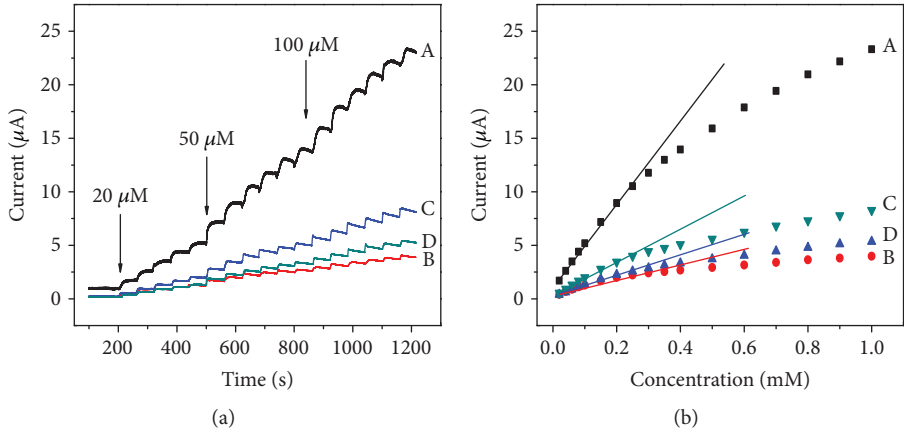

FIGURE 4: (a) Amperometric responses of Co_3O_4 (A) nanourchins, (B) nanowires, (C) nanoflowers, and (D) nanoplates. (b) Linear relationship between the response current and glucose concentration.

glucose. Fig. S4 shows the glucose selectivity of the Co_3O_4 nanourchin-modified GCE when adding UA and AA. The response current increases remarkably with the addition of glucose, but it remained almost unchanged when the UA or AA was dropped in [33]. Therefore, the Co_3O_4 nanourchin-modified electrode has a good selectivity towards glucose.

As for the reproducibility and stability, five individual tests were measured using the Co_3O_4 nanourchin-modified electrode [29]. Results show that the relative standard deviation (RSD) was only 2.9% when detecting 50 μM glucose. When the electrode was stored at 4°C for two weeks, the amperometric current only declined by 2.4%. Therefore, the Co_3O_4 nanourchin-modified electrode is stable with excellent reproducibility, which is very favorable for practical application [34–36].

4. Conclusions

In summary, a facile hydrothermal strategy was applied to synthesize porous Co_3O_4 with various morphologies. The effect of morphology and microstructures on the electrochemical performance was investigated, and the results show

that the Co_3O_4 nanourchins are self-assembled by hundreds of thorns with a three-dimensional porous network, which offer a higher surface area of 70.76 m^2 g^{-1} compared with that of Co_3O_4 nanowires, nanoflowers, and nanoplates. Electrochemical measurements reveal that the glucose sensor based on a Co_3O_4 nanourchin electrode demonstrates the significantly highest sensing performance with a high sensitivity of 565 $\mu A\,mM^{-1}$ cm^{-2} and a linear detection range of 20-250 μM as well as a low detection limit of 1.5 μM. The superior sensing performance is attributed to the higher specific surface area with a three-dimensional porous network and the lower Faradic electron transfer resistance of the urchin-like Co_3O_4. Therefore, this unique urchin-like Co_3O_4 is a promising candidate as a glucose sensor.

Data Availability

The data used to support the findings of this study are included within the article.

Conflicts of Interest

The authors declare that there is no conflict of interests regarding the publication of this paper.

Acknowledgments

This work was supported by the National Key Research Development Program (Grant No. 2016YFD0400601).

Supplementary Materials

Figure S1: nitrogen adsorption/desorption isotherms and corresponding BJH pore size distribution (inset) of Co_3O_4 (a) nanourchins, (b) nanowires, (c) nanoflowers, and (d) nanoplates. Table S1: the surface area, pore volume, and average pore size of Co_3O_4 nanomaterials. Figure S2: the XRD patterns of obtained Co3O4 nanoparticles before annealing treatment: (a) nanourchins, (b) nanowires, (c) nanoflowers, and (d) nanoplates. Table S2: performances of typical electrochemical sensing materials for glucose detection. Figure S3: impedance Nyquist plots of Co_3O_4 (a) nanourchins, (b) nanowires, (c) nanoflowers, and (d) nanoplates at open-circuit potential in 0.1 M NaOH solution. Figure S4: the amperometric response to the addition of glucose with interfering species. *(Supplementary Materials)*

References

[1] J.-L. Ma, B.-C. Yin, X. Wu, and B.-C. Ye, "Simple and cost-effective glucose detection based on carbon nanodots supported on silver nanoparticles," *Analytical Chemistry*, vol. 89, no. 2, pp. 1323–1328, 2016.

[2] J. He, X. Lu, J. Yu, L. Wang, and Y. Song, "Hierarchical $Co(OH)_2$ nanostructures/glassy carbon electrode derived from Co(BTC) metal–organic frameworks for glucose sensing," *Journal of Nanoparticle Research*, vol. 18, no. 7, pp. 184–195, 2016.

[3] X. Y. Yu, Z. G. Liu, and X. J. Huang, "Nanostructured metal oxides/hydroxides-based electrochemical sensor for monitoring environmental micropollutants," *Trends in Environmental Analytical Chemistry*, vol. 3-4, pp. 28–35, 2014.

[4] G. Rajeshkhanna, E. Umeshbabu, and G. Ranga Rao, "Charge storage, electrocatalytic and sensing activities of nest-like nanostructured Co_3O_4," *Journal of Colloid and Interface Science*, vol. 487, pp. 20–30, 2017.

[5] P. Sivasakthi, G. N. K. Ramesh Bapu, and M. Chandrasekaran, "Pulse electrodeposited nickel-indium tin oxide nanocomposite as an electrocatalyst for non-enzymatic glucose sensing," *Materials Science and Engineering: C*, vol. 58, pp. 782–789, 2016.

[6] S. Park, H. Boo, and T. D. Chung, "Electrochemical non-enzymatic glucose sensors," *Analytica Chimica Acta*, vol. 556, no. 1, pp. 46–57, 2006.

[7] Y. Li, C. Zhong, J. Liu et al., "Atomically thin mesoporous Co_3O_4 layers strongly coupled with N-rGO nanosheets as high-performance bifunctional catalysts for 1D knittable zinc–air batteries," *Advanced Materials*, vol. 30, no. 4, article 1703657, 2018.

[8] Z. Cai, Y. Bi, E. Hu et al., "Single-crystalline ultrathin Co_3O_4 nanosheets with massive vacancy defects for enhanced electrocatalysis," *Advanced Energy Materials*, vol. 8, no. 3, pp. 1–8, 2018.

[9] P. Hu, Z. Jia, H. Che et al., "Engineering hybrid $CoMoS_4/Ni_3S_2$ nanostructures as efficient bifunctional electrocatalyst for overall water splitting," *Journal of Power Sources*, vol. 416, pp. 95–103, 2019.

[10] X. Yan, Z. Jia, H. Che et al., "A selective ion replacement strategy for the synthesis of copper doped carbon nitride nanotubes with improved photocatalytic hydrogen evolution," *Applied Catalysis B: Environmental*, vol. 234, pp. 19–25, 2018.

[11] H. B. Che, X. X. Yan, Z. Y. Jia, P. Hu, and J. S. Wang, "Phosphorus doped carbon nitride nanotubes by sequential cation-exchanging reaction with enhanced photocatalytic hydrogen evolution," *Journal of Nano Research*, vol. 53, pp. 76–85, 2018.

[12] Z. Wang, H. Liu, R. Ge et al., "Phosphorus-doped Co_3O_4 nanowire array: a highly efficient bifunctional electrocatalyst for overall water splitting," *ACS Catalysis*, vol. 8, no. 3, pp. 2236–2241, 2018.

[13] W. Li, D. Liu, X. Feng, Z. Zhang, X. Jin, and Y. Zhang, "High-performance ultrathin Co_3O_4 nanosheet supported PdO/CeO_2 catalysts for methane combustion," *Advanced Energy Materials*, vol. 9, no. 18, article 1803583, 2019.

[14] J. Xu, F. Li, D. Wang et al., "Co_3O_4 nanostructures on flexible carbon cloth for crystal plane effect of nonenzymatic electrocatalysis for glucose," *Biosensors and Bioelectronics*, vol. 123, pp. 25–29, 2019.

[15] L. Tian, G. He, Y. Cai et al., "Co_3O_4 based non-enzymatic glucose sensor with high sensitivity and reliable stability derived from hollow hierarchical architecture," *Nanotechnology*, vol. 29, no. 7, pp. 75502–75506, 2018.

[16] M. H. Yang, J.-M. Jeong, K. G. Lee, D. H. Kim, S. J. Lee, and B. G. Choi, "Hierarchical porous microspheres of the Co_3O_4@ graphene with enhanced electrocatalytic performance for electrochemical biosensors," *Biosensors and Bioelectronics*, vol. 89, Part 1, pp. 612–619, 2017.

[17] P. Hu, C. K. Ngaw, Y. Yuan, P. S. Bassi, S. C. Joachim Loo, and T. T. Yang Tan, "Bandgap engineering of ternary sulfide nanocrystals by solution proton alloying for efficient photocatalytic H_2 evolution," *Nano Energy*, vol. 26, pp. 577–585, 2016.

[18] T. Liu, L. Zhang, W. You, and J. Yu, "Core–shell nitrogen-doped carbon hollow spheres/Co_3O_4 nanosheets as advanced electrode for high-performance supercapacitor," *Small*, vol. 14, no. 12, pp. 1–6, 2018.

[19] P. Tan, B. Chen, H. Xu, W. Cai, W. He, and M. Ni, "Porous Co_3O_4 nanoplates as the active material for rechargeable Zn-air batteries with high energy efficiency and cycling stability," *Energy*, vol. 166, pp. 1241–1248, 2019.

[20] P. Tan, Z. Wu, B. Chen, H. Xu, W. Cai, and M. Ni, "Exploring oxygen electrocatalytic activity and pseudocapacitive behavior of Co_3O_4 nanoplates in alkaline solutions," *Electrochimica Acta*, vol. 310, pp. 86–95, 2019.

[21] K. Fukui and Y. Suzuki, "Well-facetted spinel-type Co_3O_4 microcrystal assembly prepared by hydrothermal synthesis and post-thermal decomposition," *Ceramics International*, vol. 45, no. 7, pp. 9288–9292, 2019.

[22] G. Anandhababu and G. Ravi, "Facile synthesis of quantum sized Co_3O_4 nanostructures and their magnetic properties," *Nano-Structures & Nano-Objects*, vol. 15, pp. 1–9, 2018.

[23] Y. Jiang, X. Yan, P. Mei, Y. Zhang, W. Xiao, and H. Tang, "Electrochemical reconstruction induced high electrochemical performance of Co_3O_4/reduced graphene oxide for lithium ion batteries," *Journal of Alloys and Compounds*, vol. 764, pp. 80–87, 2018.

[24] Z. Huang, Y. Zhao, H. Xu, and J. Zhao, "Surfactant-free synthesis, photocatalytic and electrochemical property study of Co_3O_4 nanoparticles," *Materials Research Bulletin*, vol. 100, pp. 83–90, 2018.

[25] M. Y. Nassar, "Size-controlled synthesis of $CoCO_3$ and Co_3O_4 nanoparticles by free-surfactant hydrothermal method," *Materials Letters*, vol. 94, pp. 112–115, 2013.

[26] Z. Ding, B. Yao, J. Feng, and J. Zhang, "Enhanced rate performance and cycling stability of a $CoCO_3$–polypyrrole composite for lithium ion battery anodes," *Journal of Materials Chemistry A*, vol. 1, no. 37, pp. 11200–11209, 2013.

[27] X. Peng, H. X. Li, H. J. Shao et al., "Involvement of calcium-sensing receptors in hypoxia-induced vascular remodeling and pulmonary hypertension by promoting phenotypic modulation of small pulmonary arteries," *Molecular and Cellular Biochemistry*, vol. 396, no. 1-2, pp. 87–98, 2014.

[28] X. Xiao, X. Liu, H. Zhao et al., "Facile shape control of Co_3O_4 and the effect of the crystal plane on electrochemical performance," *Advanced Materials*, vol. 24, no. 42, pp. 5762–5766, 2012.

[29] Y. Liang, Y. Li, H. Wang et al., "Co_3O_4 nanocrystals on graphene as a synergistic catalyst for oxygen reduction reaction," *Nature Materials*, vol. 10, no. 10, pp. 780–786, 2011.

[30] Y. P. Zhu, T. Y. Ma, M. Jaroniec, and S. Z. Qiao, "Self-templating synthesis of hollow Co_3O_4 microtube arrays for highly efficient water electrolysis," *Angewandte Chemie International Edition*, vol. 56, no. 5, pp. 1324–1328, 2017.

[31] J. Mu, L. Zhang, M. Zhao, and Y. Wang, "Catalase mimic property of Co_3O_4 nanomaterials with different morphology and its application as a calcium sensor," *ACS Applied Materials & Interfaces*, vol. 6, no. 10, pp. 7090–7098, 2014.

[32] J. E. Kessler, A. Aliaga, N. Rosales Espitia, C. Rugge, and N. Myung, "Controlled synthesis of electrocatalytic Co_3O_4 nanofibers via electrospinning," vol. 8, pp. 324–328, 2016.

[33] T. Zhai, L. Wan, S. Sun et al., "Phosphate ion functionalized Co_3O_4 ultrathin nanosheets with greatly improved surface reactivity for high performance pseudocapacitors," *Advanced Materials*, vol. 29, no. 7, pp. 160–167, 2017.

[34] J. Ma, S. Zhang, W. Liu, and Y. Zhao, "Facile preparation of Co_3O_4 nanocrystals via a solvothermal process directly from common Co_2O_3 powder," *Journal of Alloys and Compounds*, vol. 490, no. 1-2, pp. 647–651, 2010.

[35] K. Tian, K. Baskaran, and A. Tiwari, "Nonenzymatic glucose sensing using metal oxides–comparison of CuO, Co_3O_4, and NiO," *Vacuum*, vol. 155, pp. 696–701, 2018.

[36] E. Zhang, Y. Xie, S. Ci, J. Jia, and Z. Wen, "Porous Co_3O_4 hollow nanododecahedra for nonenzymatic glucose biosensor and biofuel cell," *Biosensors and Bioelectronics*, vol. 81, pp. 46–53, 2016.

Hindawi
Journal of Nanomaterials
Volume 2019, Article ID 7414039, 17 pages
https://doi.org/10.1155/2019/7414039

Research Article

Effect of Soil Solution pH during the Tetracycline Intercalation on the Structural Properties of a Dioctahedral Smectite: Microstructural Analysis

Walid Oueslati

Université de Carthage, Faculté des Sciences de Bizerte, UR13ES46 Physique des Matériaux Lamellaires et Nano-Matériaux Hybrides (PMLNMH), 7021 Zarzouna, Tunisia

Correspondence should be addressed to Walid Oueslati; walidoueslati@ymail.com

Received 17 May 2019; Revised 19 July 2019; Accepted 25 July 2019; Published 12 September 2019

Guest Editor: Yunpan Ying

The aim of this work is to quantitatively characterize the structural response to a chemical disruption of saturated montmorillonite crystallites by organic molecules (tetracycline (TC)), derived from pharmaceutical waste. The chemical disturbance is performed by varying the surrounding soil solution pH. To show the effect of this chemical perturbation on the interlamellar space (IS) configuration and the hydration properties, an "in situ" XRD analysis, based on the modeling of the 00l reflections, is carried out. The "in situ" XRD analysis is performed by varying the relative humidity conditions (%RH). FTIR SEM and BET-(Brunauer-Emmett-Teller-) BJH (Barrett-Joyner-Halenda) analyses are used as complementary techniques to confirm the structural changes accompanying the intercalation process. Results showed a dependence between solution acid character and the TC adsorption mechanism. From pH values close to 7, the deprotonation of the TC molecule within IS is accelerated by an increasing %RH rate. IR spectroscopy shows that the structure is preserved versus pH value and only a shift of the water deformation bands ascribed to interlamellar water molecule abundance and TC conformation is observed. The surface morphology studied by SEM shows the increase in the surface porosity by increasing the pH value. BET-specific surface area and BJH pore size distribution (PSD) analyses confirm the SEM observations.

1. Introduction

The risks associated with the presence of industrial and household waste in the soil and the environment are multiplied with the great demand for everyday consumer products. Essentially, pharmaceutical industry waste releases which include organic molecules (antibiotics and others), heavy metals, and even radioactive substances represent a serious environmental problem.

To date, various conventional and modern technologies are used for reducing the organic pollutant effect on the human health (fauna and flora). Among these technologies, we can mention the ion exchange process which is in relation to the main properties of clay mineral and chemical precipitation and adsorption [1–4]. All these methods have been developed to separate, to confine, to trap, to isolate, to eliminate, and to protect human life from contaminated effluents.

Recent studies investigated the adsorption/desorption of various organic matters on/from soil particles. These include, for example, the adsorption of antibodies, surfactants, fire-retarding organics, and herbicides [5–8]. The use of these techniques is thwarted by the high cost of materials used for these purposes.

Clay, which is a material that is abundant in nature, can play an important role in the future as a geological barrier for the confinement and removal of organic pollutants in surface, ground, and wastewaters [9, 10]. Forming part of dioctahedral phyllosilicates 2 : 1, smectites can be considered a solution for this environmental problem. Montmorillonite is a natural nanomineral (layer thickness ~1.0 nm) belonging to the smectite group. The intrinsic montmorillonite properties such as low permeability, high surface area, and cation exchange capacity (CEC) [11] promote its application in such context.

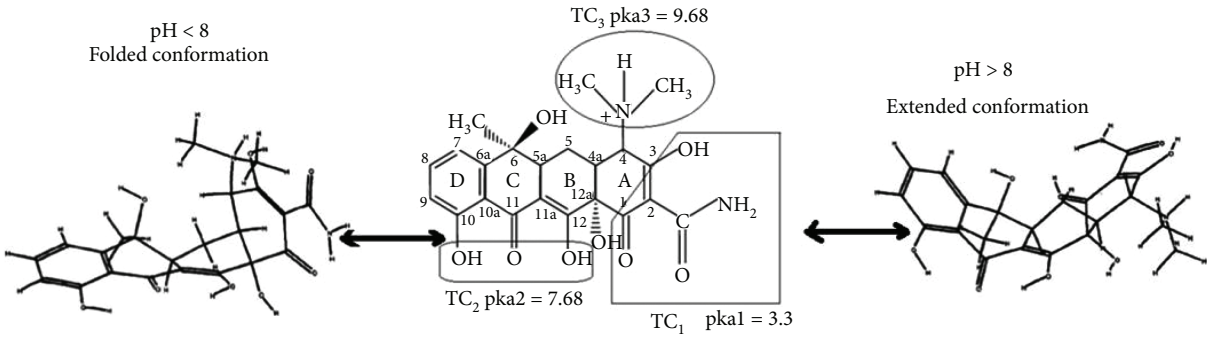

Figure 1: Scheme of the fully protonated tetracycline: folded conformation for pH < 8 and extended conformation for pH > 8.

The main montmorillonite structure is characterized by the isomorphic substitution presence which generates a permanent negative layer's charge. To compensate this charge deficit, exchangeable cation or organic molecules can be intercalated in the IS [12]. The montmorillonite layer structure can expand and contract its structures without crystallographic change. These expansions depend on the IS content (water/polar molecule) and the surrounding environment (relative humidity rate) [13–17].

Several studies, in relation to the use of montmorillonite in the pharmaceutical-sediment interaction context, have been, recently, realized [18–27].

Among the basic substances of antibiotics is the TC molecule. Recently, the interaction of TC, as an organic molecule, with montmorillonite has been studied, from the point of view of adsorption and intercalation, by several authors [28–34]. TCs comprise a group of natural and semisynthetic products that inhibit the synthesis of bacterial proteins. The TC chemical properties have been widely studied [35]. The protonation properties of the amine group on TC allow its cation exchange with exchanged cations of montmorillonite.

The presence of a TC molecule in IS generates (after the intercalation process) several structural ambiguities. Indeed, during the intercalation and/or adsorption process, several parameters such as chemical composition, solid/liquid ratio, pH dependence, soil solution composition, and environmental and atmospheric conditions come into play [36–38]. In addition, once the molecule (in our case TC) is interposed, the configuration and distribution of chemical species in IS will be disturbed and a new equilibrium (electrical, chemical, ionic, etc.) will be established. For that, a structural investigation must be directed to understanding the link between, respectively, environmental conditions, intercalation process, and structural changes.

In this regard, [37] used XRD analysis and spectroscopic methods to demonstrate that the adsorption decreases as the pH is increased and eventually becomes negligible at pH = 11 . In addition, [38] investigated TC intercalation onto a rectorite sample and highlighted the rectorite d-spacing increase during the intercalation process. Also, [38] demonstrate that the maximum interlayer expansion, obtained at a high pH value, is accompanied by an extended TC molecule conformation. Alternatively, [29] employed both simulated and experimental XRD to characterize structures, following the interlayer adsorption of OTC within Na-montmorillonite as a function of pH. They demonstrate that the intercalation of the antibiotic species within the smectite layers at low acidic pH induces a random layer stacking mode. This structural behavior turns into segregation trends by increasing the pH value.

This work focuses on the effect of soil pH variation, during the TC intercalation process, on the structural properties of Na-montmorillonite. At a fixed pH value, "in situ" XRD analysis is performed by varying %RH conditions. The contents of the interlamellar space along the c^* axis are fully identified through an XRD modeling approach. The correlation of the results obtained by XRD, IR, SEM, and BET allows a quantitative description of the montmorillonite structural changes within the intercalation process.

2. Materials and Methods

2.1. Baseline Sample. A reference montmorillonite sample (Swy-2) (from the Source Clays Repository of the Clay Minerals Society) is used in this work [39, 40]. The half-cell structural formula is given by [41]

$$\left(Si_{3,923}\, Al_{0,077}\right)\left(Al_{1,459}\, Ti^{4+}_{0,018}\, Fe^{3+}_{0,039}\, Fe^{2+}_{0,045}\, Mg^{2+}_{0,382}\right)O_{10} \cdot (OH)_2\left(Ca^{2+}_{0,177}\, Na^{+}_{0,027}\right) \quad (1)$$

Before application, a pretreatment of the natural specimen is required to guarantee a maximum dispersion. The Na-rich montmorillonite suspension is prepared according to a classical protocol detailed by [42, 43].

2.2. Tetracycline (TC). Tetracycline hydrochloride was delivered by PARAFARM. Depending on the solution pH, a TC molecule undergoes protonation-deprotonation reactions which engender (03) groups and generate the formation of (04) species. The TC stock solutions are prepared just before use to avoid degradation instigated by oxygen and light. NaOH and HCl are used for pH adjustment. The molecular conformation change is attributed to the protonation equilibrium of the TC molecule. Indeed, for pH < 8 (from acidic to neutral solution), a twisted conformation is adopted. This situation, usually referred to as folded conformation, is explained by the release of the steric crowding between the protonated nitrogen on the dimethylamino group, NH_4, and OH_{12}. The extended conformation is displayed for pH values > 8 (Figure 1) [44–46].

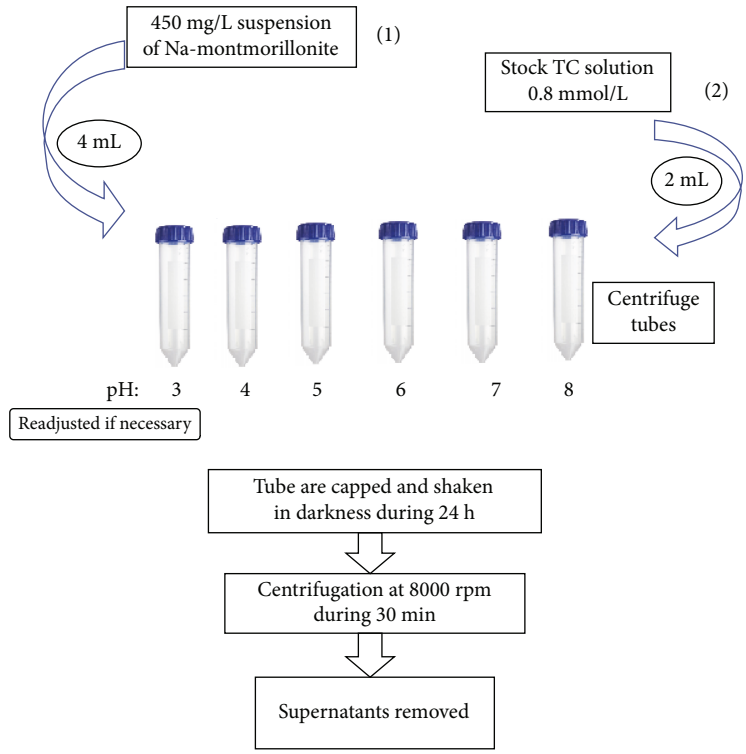

Figure 2: Experimental TC intercalation process under variable solution pH.

Table 1: The Z atomic coordinates within the 2 : 1 layer framework along the c^* axis [43].

Atom type	O_1	O_2	O_3	O_4	O_5	O_6	OH_1	OH_2	Si	Si	Al
Number	2	1	2	2	1	2	1	1	2	2	2
Zn (Å)	0	0.20	2.25	4.31	6.26	6.59	1.98	4.28	0.59	6.04	3.43

2.3. Experimental Intercalation Process. The intercalation process is performed at constant TC concentration under a variable solution pH value. Six different pH values varying from acidic to neutral solution are fixed (i.e., 3, 4, 5, 6, 7, and 8). The experimental protocol is summarized in Figure 2.

2.4. In Situ X-Ray Diffraction Measurements. All experimental XRD patterns were recorded from the oriented preparations of the air-dried sample (SWy-2-TC) using a Brucker D8 Advance X-ray diffractometer at 40 kV and 20 mA ($CuK\alpha\ monochromatic\ radiation = 0.15406\ nm$) equipped with an Ansyco_rh-plus 2250 humidity control device coupled to an Anton Paar TTK450 chamber. For each pH value, an in situ variation of the environmental RH, which extends from 20% to 80% (i.e., the almost saturated conditions), is carried out. The usual scanning parameters were $0.04^\circ 2\theta$ as step size and 6 s as counting time per step over the angular range $2–40^\circ 2\theta$. Samples were kept at 23°C in the CHC^+ chamber during the whole data collection. To maintain the desired RH rates, samples were equilibrated with their environment by a constant flow of mixed dry/saturated air.

2.5. Modeling (00l) Reflection Profiles. The XRD modeling method is used to quantify smectite hydration and ionic exchange properties as a function of a surrounding RH% rate [47–50]. Theoretical XRD models are based on the algorithm developed initially by Drits and Tchoubar [51]. The Z atomic coordinates within the 2 : 1 layer framework (tetrahedral and octahedral sheet) in the case of this study are reported in Table 1. The Z coordinates of the IS content (exchangeable cation, molecules, etc.) are optimized, during the modeling process, to improve the agreement quality. This later is controlled using the unweighted Rp parameter [52].

The diffracted intensity along the 00l rod belonging to the reciprocal space is given by [51]

$$I_{00}(2\theta) = L_p Spur\left(\mathrm{Re}\,[\phi][W]\left\{[I] + 2\sum_{n}^{M-1}\left[\frac{(M-n)}{M}\right][Q]^n\right\}\right). \quad (2)$$

The matrix formalism behind the diffracted theoretical intensity and the fitting strategy are detailed by [47, 52]. The average position of the TC molecule within the IS is fixed at 15.40 Å. Regardless of the hydration state type, the Na exchangeable cations (per half unit cell) are positioned at the center of the IS along the c^* axis. This configuration respects the provided literature data [53].

2.6. FTIR Spectroscopy. The understanding of the proposed structural models from quantitative XRD analysis requires confirmation by a complementary analysis technique. FTIR spectroscopy is used to detect the presence of groups of characteristic units in the IS [54, 55]. These units include hydroxyl groups, dimethylamino group, silicate and aluminate anions, octahedral metal cations, and interlayer cations. FTIR spectra are recorded with 400–4000 cm^{-1} spectra based on a PerkinElmer Paragon 1000 PC spectrometer. The experiments are implemented by dispersing the material in KBr discs.

2.7. Scanning Electron Microscopy (SEM). All scanning electron micrographs are obtained from a JEOL model JSM-5400 (ETAP, Tunisia) scanning electron microscope using a beam with an acceleration of 20 keV. All samples are conducted under vacuum by the FINE COATmodel JFC_1100E installation. The studied samples are, respectively, the starting SWy-2 and the intercalated TC samples with a variable solution pH value.

2.8. BET and BJH Pore Size Distribution Analysis. Nitrogen sorption (both adsorption and desorption) at the clean surface of dry solid powders is used to determine the surface area (SA) and the pore size distribution (PSD) of porous materials such as montmorillonite. In this case, powders are obtained after drying each sample. Physical gas adsorption is often the technique of choice for examining the pore characteristics of materials [56]. The technique determines the amount of gas adsorbed; this is a direct indication of the porous properties and, therefore, the overall structure of the material [57, 58]. A BET-specific surface area and PSD of the studied sample, under each pH value, were determined using a Quantachrome NOVA 2000e series volumetric gas adsorption instrument, which is a USA automated gas adsorption system using nitrogen as the adsorptive. Adsorption isotherms were performed at 77 K and at the relative pressure up to P/P_0 ~0.95. Adsorbed nitrogen and oxygen were removed under reduced (vacuum) pressure at 100°C for 8 h before measuring SA and PSD.

The PSD was determined by the BJH method [59] to the desorption section of the isotherms of nitrogen at 77 K, assuming the pores to be cylindrical in shape [60, 61].

3. Results

3.1. Qualitative XRD Analysis. The experimental XRD patterns showing the correlation between the %RH and the pH of the surrounding soil solution are reported in Figure 3. The d_{001} basal spacing value shifts from 18.25 Å to 19.85 Å, by increasing pH from 3 to 6, which indicates probably a complete TC adsorption process. For the high pH value, the obtained d_{001} value indicates two-water layer (2W) hydration states which is attributed probably to a partial adsorption process of TC. The semiquantitative analysis is based on the reflection peak geometry interpretation and the investigation of the evolution of the FWHM parameter (Table 2). Indeed, the high FWHM value is obtained at 80%RH for pH = 5 and at 60%RH for pH = 6. This value indicates an interstratified character confirmed by the asymmetric 00l geometry peaks. All studied samples are characterized by an interstratified character due to the interlayer configuration and the external constraint imposed along the adsorption and analysis process (pH and %RH).

Away high acidity degrees (pH = 7) and at 60%RH, the XRD patterns are characterized by d_{001} indicating a 2W hydration state (Table 2) and the sample seems to be unaffected by the TC adsorption process. Also, this value can be interpreted by a monocationic exchange process (Na^+) [40]. But, by exploiting the effect of the %RH variation, a partial TC adsorption is confirmed for the 20%RH, where d_{001} = 18.54 Å characteristic of high interlayer swelling which accompanied the TC adsorption.

At pH = 8 and for low 2θ angles, a minor reflection which can be attributed to the 4W (four-water) hydration state with d_{001} = 22.07 Å (Figure 3) appears. This value can be interpreted by the effect of the protonation-deprotonation reactions on the TC molecules which depends essentially on the pH value.

3.2. Quantitative XRD Analysis. Qualitative XRD analysis remains insufficient for a more precise description of the interlayer configuration. For that, a quantitative XRD analysis is performed to determine the structural parameter involved on the TC adsorption process. The best agreements between theoretical and experimental patterns are reported in Figure 3. The main structural parameters used to obtain a good fit are summarized in Table 3. For each model, several layer types with variable stacking mode are used in order to improve the obtained agreement between calculated and experimental patterns. This mixed-layer structure (MLS) is composed of a four-layer thickness type depending on the hydration state (i.e., 1W (12.40 Å), 2W (15.40 Å), 3W (18.20 Å), and 4W (21.40 Å)). The proposed MLS are obtained by weighted layer type populations which are supposed to have, respectively, identical chemical composition, identical layer thickness, and identical Z coordinates of the atoms. The cation exchange capacity (CEC) of the starting materials is saturated by Na^+ and TC molecules. The XRD pattern modeling is based on the fitting strategy described by [47].

The XRD patterns obtained at pH = 3 reflect a random layer type stacking mode (R0), whereas a partial segregation (R1) is obtained for pH varying from 4 to 8. Accordingly, for pH 3 and pH 4, a major presence of a 1W layer hydration state is noted (Table 3). The 4W hydration state is omnipresent along all the pH ranges. The clear contribution of this highly hydrated state is illustrated, respectively, at pH 5, 6, 7, and 8. The presence of the TC molecule on the interlayer space affects the 001 reflection geometry, and the appearance of broadening peaks at a low angle confirms this result. The 001 reflection is very sensitive to the content of the interlamellar space and the surrounding humidity as was observed at a high %RH value. By increasing pH from 3 to 7, there is a doublet at ~12 Å and ~18 Å, which is characteristic of crystals or domains containing essentially either a Na or TC interlayer, respectively, both types of interlayers being mutually exclusive. By increasing

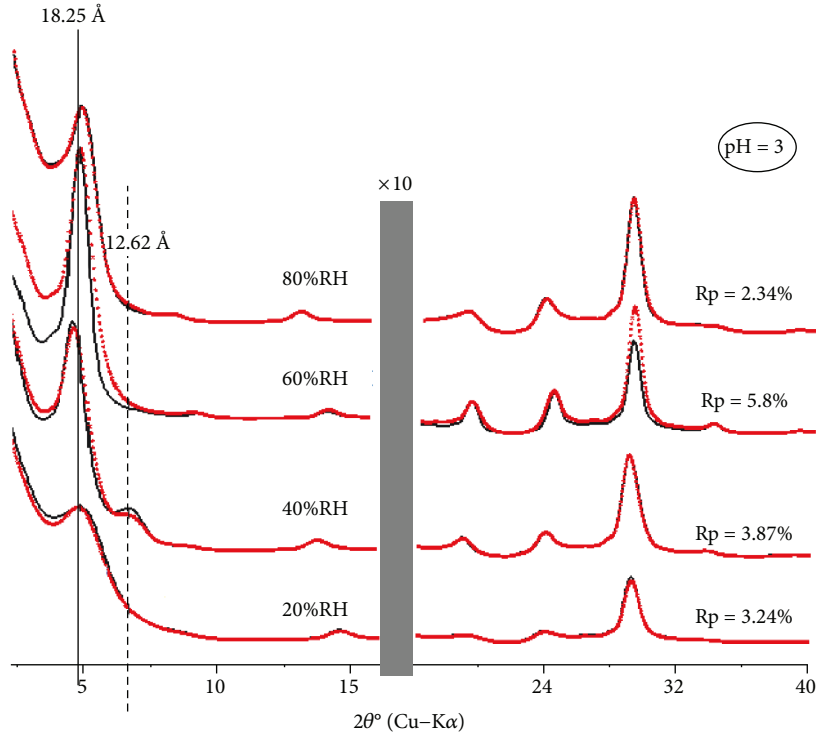

(a)

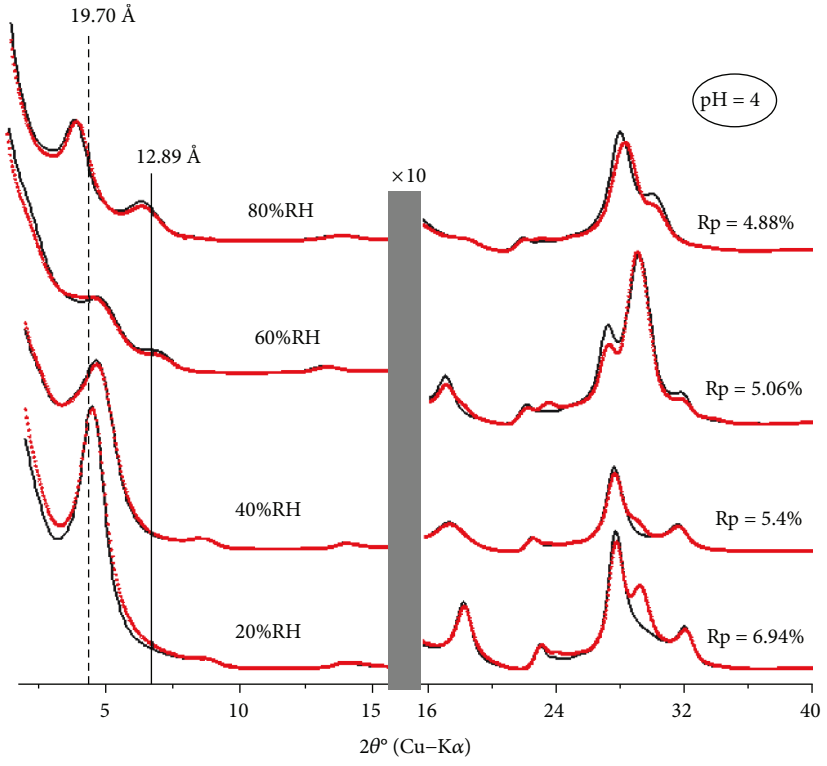

(b)

Figure 3: Continued.

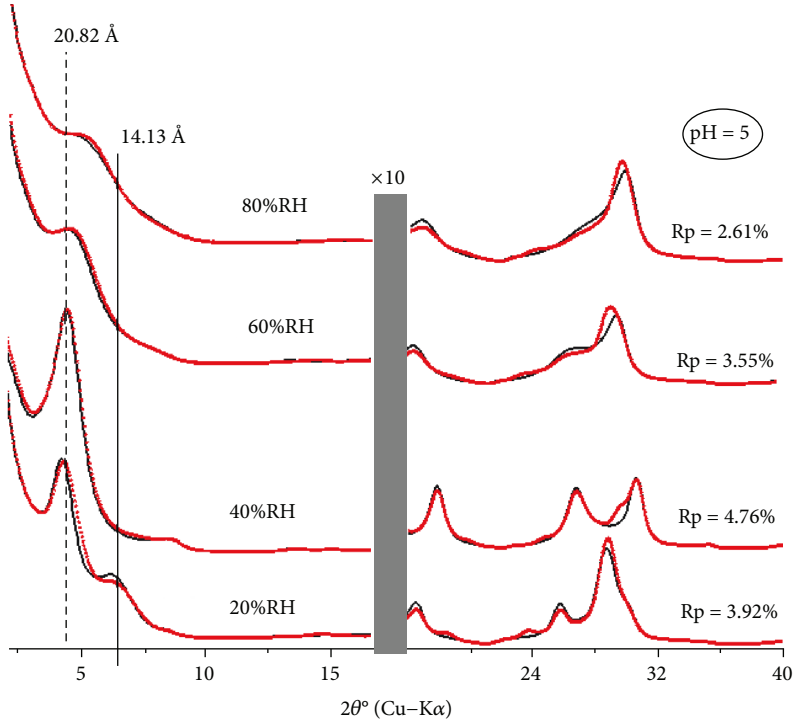

(c)

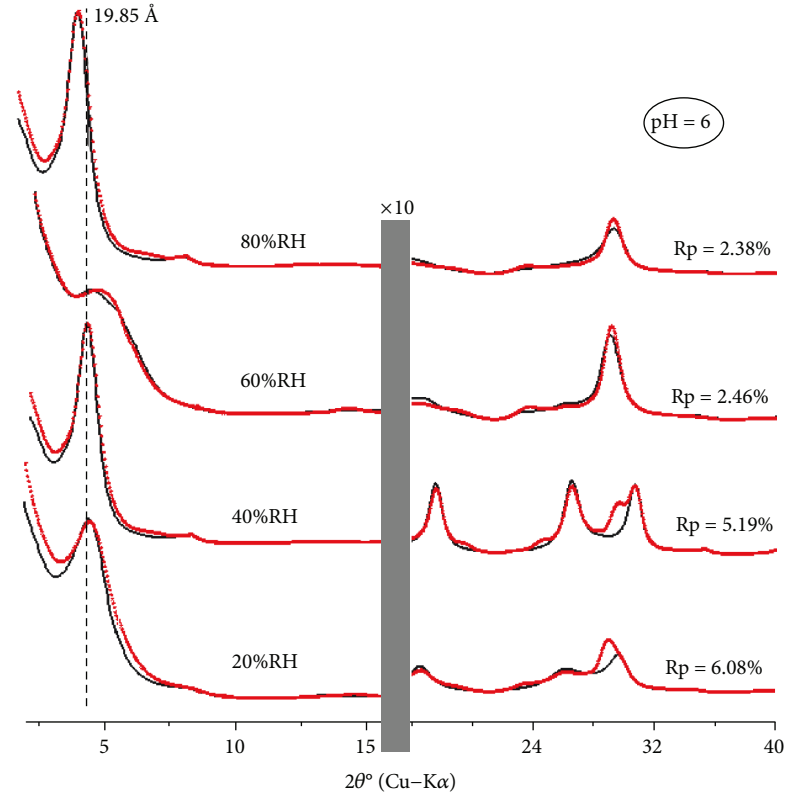

(d)

Figure 3: Continued.

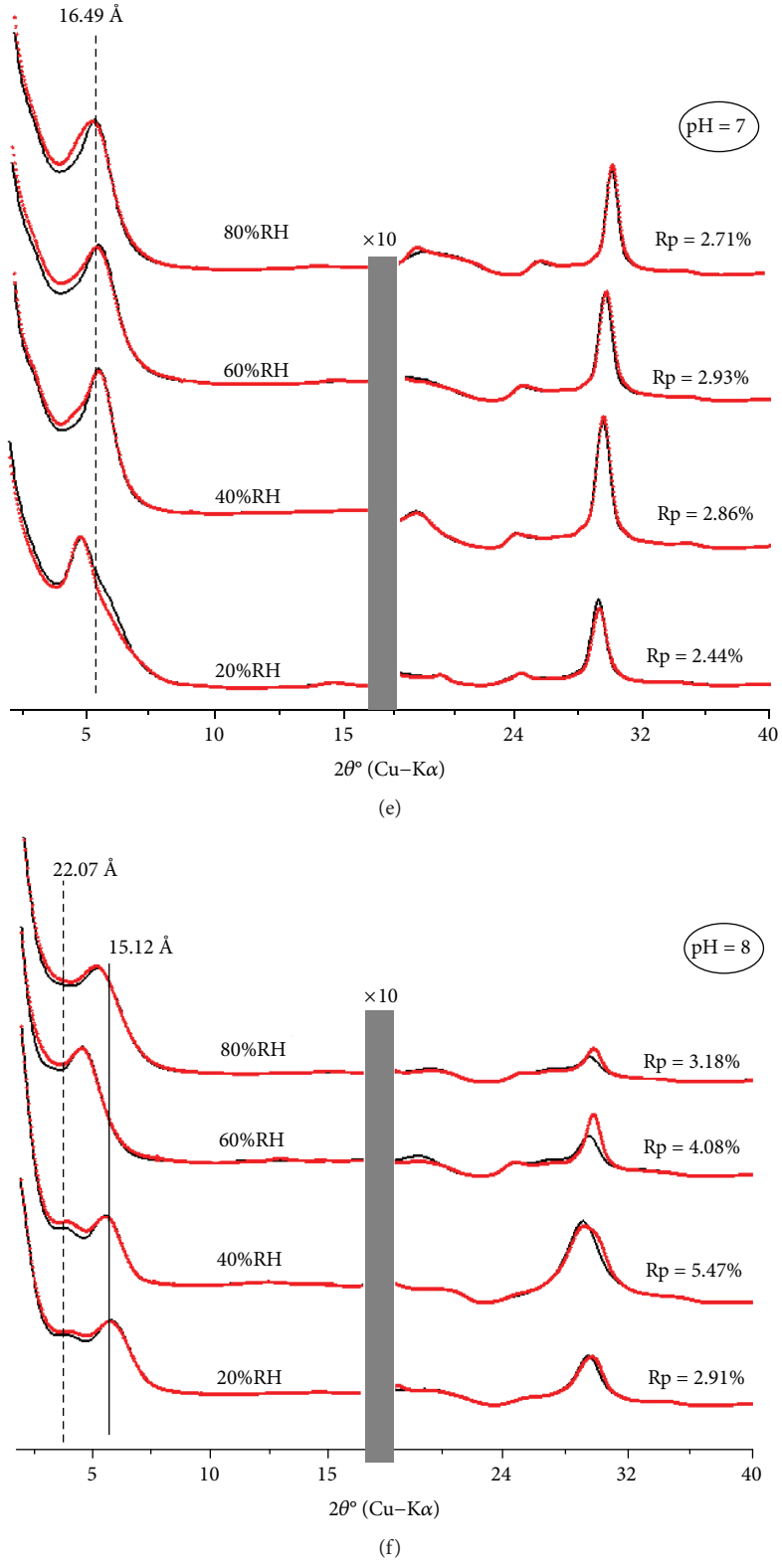

FIGURE 3: (a–f) The best agreement between theoretical (red line) and experimental (black line) XRD patterns obtained by varying %RH rates under different pH values (3-8).

%RH, a modification of the relative intensities of the two peaks occurs, as indicated by a steady increase in the ~18 Å peak at the expense of that at ~12 Å.

At pH 8, this "law" is not respected since the 18-22 Å phase (characteristic of the TC adsorption process) is reduced in favor of the 12-15 Å phase (characteristic of

Table 2: Qualitative XRD investigations for different studied samples versus pH and %RH variation.

pH	%RH	d_{001} (Å)	FWHM (°2θ)	Character
3	20	18.25	2.813	I
	40	18.87	1.412	I
	60	18.71	1.231	QH
	80	17.66	1.761	I
4	20	19.70	1.403	QH
	40	19.02	2.123	I
	60	19.53	2.910	I
	80	20.06	3.501	I
5	20	20.82	1.651	I
	40	20.25	1.767	QH
	60	20.06	2.624	I
	80	19.36	3.810	I
6	20	19.85	1.903	I
	40	20.06	1.400	QH
	60	18.25	3.810	I
	80	20.43	3.010	I
7	20	18.54	2.120	I
	40	15.65	1.560	QH
	60	16.47	1.684	QH
	80	16.49	1.708	I
8	20	15.12	2.189	I
	40	14.15	2.204	I
	60	17.51	1.904	I
	80	17.38	2.706	I

I: interstratified character; QH: quasihomogeneous character.

Na-exchanged montmorillonite), which can be interpreted by the deprotonation of the TC molecule. This result is confirmed by the decrease in the 4W layer type abundance from 60%RH.

3.3. FTIR Analysis. The FTIR spectra corresponding, respectively, to TC, SWy-2-Na, and adsorbed TC under variable solution pH are shown in Figure 4. By comparing the characteristic vibration bands of the starting sample with those obtained after the TC adsorption process, no apparent change is observed which indicates that the adsorbed specimen does not alter the structure of the host material. This result is in concordance with XRD analysis which demonstrates that the structure is preserved and only a layer thickness variation is observed and ascribed to interlamellar water molecule abundance. All FTIR band positions (cm^{-1}) for SWy-2-Na without and with TC sorption are reported in Table 4.

A small difference which lies in the effect of evolution as a function of the solution pH is observed. Indeed, the characteristic bands attributed to the OH stretching and located between 3400 and 3600 cm^{-1} are conserved for all the studied pH values with a small decrease in the peak intensity probably due to the effect of the surrounding environment acidity. The Si-O stretching vibration bands located between 950 and 1100 cm^{-1}, characteristic of the lattice vibration of the starting sample, remain present for intercalated TC samples with enlargement and decrease in the peak intensity. A small characteristic bands around 685 cm^{-1} are assigned to the symmetric stretching vibration T-O-T (i.e., where T = Si, Al) which confirms the preserved structure despite the chemical perturbation [54, 55]. A characteristic band around 1600 cm^{-1}, attributed to the vibrations of the functional groups of the OH- type related to the deformation of water, is observed regardless of the pH value. The width and intensity of this characteristic band decrease for pH values close to 7. This is consistent with the results of XRD which show a transition from 3W to 2W hydration states. The most characteristic vibration band of TC compounds is located between 1150 and 1650 cm^{-1} (Table 4) and characterized by a weak intensity and width.

3.4. Scanning Electron Microscopy. The scanning electron microscope images of the natural sample (SWy-2-Na) and the intercalated TC samples as a function of the solution pH value are shown in Figure 5. The presence of TC molecules affects the structural morphology of the starting sample. In fact, the particle aggregation of the starting sample changes in the presence of the intercalated molecules, which induces a variable porosity as a function of the fixed solution pH. Maximum surface porosity is observed for pH values close to 7.

For pH values ranging from 3 to 5, the presence of TC strengthens the morphological tissue of the sample which probably indicates in terms of abundance a high intercalation level. From pH 6, the sample has a less collapsed structure with an increase in the pore volume. This result may be related to the effect of the low acidity of the surrounding solution or to a conformational change of the TC molecule.

3.5. BET-Specific Surface Area and PSD Analyses. The impenetrability of the nitrogen to the IS makes the BET an appropriate method to show the chemical transformation occurring on the external surface of the clay layer [62]. The structure of pores and the developed external surface area are measured using the BET method. The BET equation (both single-point and multipoint BET methods were considered) is used to calculate the surface area from nitrogen isotherms. The BJH method is used to determine the mean pore diameter. Table 5 shows the BET surface area and the average nanopore diameter for all the studied samples. The calculated external surface area increases by increasing the pH value from 13.8124 m^2/g to 18.9829 m^2/g (multipoint BET).

The SA measurement by the BET method (Figure 6) showed that all the studied samples had a pore distribution categorized under type II adsorption isotherm in the classification of Brunauer, Deming, Deming, and Teller (BDDT) [63] which is due probably to the mesoporous texture with large pores (in addition to the nanopores). This result is due to the TC intercalation/adsorption

Table 3: Structural parameters used to reproduce experimental XRD patterns as a function of soil solution pH and %RH.

pH	%RH	%MLS	1W/2W/3W/4W†	$P_{ii}//W_i$	Physical mixture	Z_{Na} 1W/2W/3W/4W	M
3	20	13	00/00/89/11	0.30//0.30	R0	09.70/11.10/12.60/14.10	4
		38	60/35/05/00	0.28//0.28	R0		
		49	18/00/82/00	0.50//0.50	R0		
	40	15	70/00/30/00	0.31//0.31	R0	09.70/11.10/12.60/14.10	4
		25	14/06/80/00	0.41//0.41	R0		
		60	20/00/75/05	0.37//0.37	R0		
	60	45	00/16/84/00	0.87//0.87	R0	09.70/11.10/12.60/14.10	5
		55	11/00/85/04	0.54//0.54	R0		
	80	41	00/09/91/00	0.38//0.38	R0	09.70/11.10/12.60/–	4
		59	04/06/90/00	0.27//0.27	R0		
4	20	17	00/00/88/12	0.50//0.30	R1	09.70/11.10/12.60/14.10	5
		33	00/04/79/17	0.55//0.29	R1		
		50	10/15/75/00	0.64//0.34	R1		
	40	13	00/00/90/10	0.47//0.21	R1	09.70/11.10/12.60/14.10	6
		22	00/00/100/00	—	—		
		65	18/04/78/00	0.81//0.34	R1		
	60	16	40/12/48/00	0.64//0.29	R1	09.70/11.10/12.60/–	5
		42	33/16/51/00	0.67//0.35	R1		
		42	40/00/60/00	0.52//0.31	R1		
	80	26	00/00/77/23	0.81//0.20	R1	09.70/11.10/12.60/14.10	4
		29	40/35/15/10	0.80//0.30	R1		
		45	38/12/42/08	0.72//0.38	R1		
5	20	35	00/33/55/12	0.55//0.35	R1	–/11.10/12.60/14.10	4
		28	00/45/50/05	0.81//0.54	R1		
		37	00/32/39/29	0.64//0.35	R1		
	40	26	00/05/60/35	0.78//0.27	R1	–/11.10/12.60/14.10	5
		14	00/00/38/62	0.78//0.34	R1		
		60	00/09/50/41	0.56//0.24	R1		
	60	12	00/19/72/09	0.49//0.18	R1	–/11.10/12.60/14.10	4
		27	00/50/25/25	0.35//0.12	R1		
		40	00/24/38/38	0.48//0.28	R1		
	80	21	00/00/50/50	0.51//0.37	R1	–/11.10/12.60/14.10	4
		30	00/20/80/00	0.71//0.54	R1		
		19	00/10/60/30	0.77//0.48	R1		
		51	00/10/55/35	0.64//0.23	R1		
6	20	22	00/17/83/00	0.81//0.35	R1	–/11.10/12.60/14.10	4
		78	00/05/85/10	0.79//0.25	R1		
	40	27	00/00/80/20	0.55//0.30	R1	–/11.10/12.60/14.10	4
		73	00/09/60/31	0.74//0.35	R1		
	60	15	00/15/45/40	0.78//0.23	R1	–/11.10/12.60/14.10	5
		25	00/10/90/00	0.65//0.38	R1		
		60	00/08/87/05	0.84//0.40	R1		
	80	45	00/00/35/65	0.72//0.30	R1	–/11.10/12.60/14.10	4
		55	00/20/50/30	0.60//0.30	R1		

Table 3: Continued.

pH	%RH	%MLS	1W/2W/3W/4W†	$P_{ii}//W_i$	Physical mixture	Z_{Na} 1W/2W/3W/4W	M
7	20	20	00/44/52/04	0.55//0.30	R1	–/11.10/12.60/14.10	4
		70	00/45/55/00	0.50//0.34	R1		
		10	00/45/45/10	0.77//0.41	R1		
	40	28	00/55/45/00	0.80//0.20	R1	–/11.10/12.60/14.10	3
		72	00/35/57/08	0.76//0.25	R1		
	60	35	00/48/48/04	0.55//0.22	R1	–/11.10/12.60/14.10	5
		65	00/68/32/00	0.50//0.38	R1		
	80	38	00/50/50/00	0.55//0.18	R1	–/11.10/12.60/14.10	4
		62	00/65/30/05	0.80//0.26	R1		
8	20	25	00/55/45/00	0.71//0.21	R1	–/11.10/12.60/14.10	6
		35	00/40/10/50	0.64//0.28	R1		
		40	00/48/12/40	0.55//0.24	R1		
	40	35	00/42/18/40	0.49//0.30	R1	–/11.10/12.60/14.10	5
		35	00/50/00/50	0.62//0.15	R1		
		30	00/55/00/45	0.81//0.30	R1		
		25	00/49/40/11	0.50//0.30	R1		
	60	28	00/55/45/00	0.54//0.33	R1	–/11.10/12.60/14.10	4
		47	00/45/43/12	0.64//0.18	R1		
		42	00/40/60/00	0.66//0.30	R1		
	80	20	00/46/50/04	0.50//0.27	R1	–/11.10/12.60/14.10	4
		38	00/55/45/00	0.55//0.16	R1		

Note: 4W, 3W, 2W, and 1W are attributed to the layer hydration state. R0 and R1 describe mixed-layer structures with random interstratifications or with partial segregation, respectively. ∗ indicates homogenous structure. P_{ij} is the junction probability of layer type j to follow layer type i, and W_i abundances of layer type i. In this case, i is Na and j is TC, wherein four equations are used: $W_{Na} + W_{TC} = 1$ (1), $P_{Na\text{-}Na} + P_{Na\text{-}TC} = 1$ (2), $P_{TC\text{-}TC} + P_{TC\text{-}Na} = 1$ (3), and $W_{Na} P_{Na\text{-}TC} = W_{TC} P_{TC\text{-}Na}$ (4). Z_{Na}: position of exchangeable cations per half unit cell calculated along the c^* axis. Z_{TC}: average position of the adsorbed TC molecule is fixed at 15.40 Å. M: average layer number per stacking.

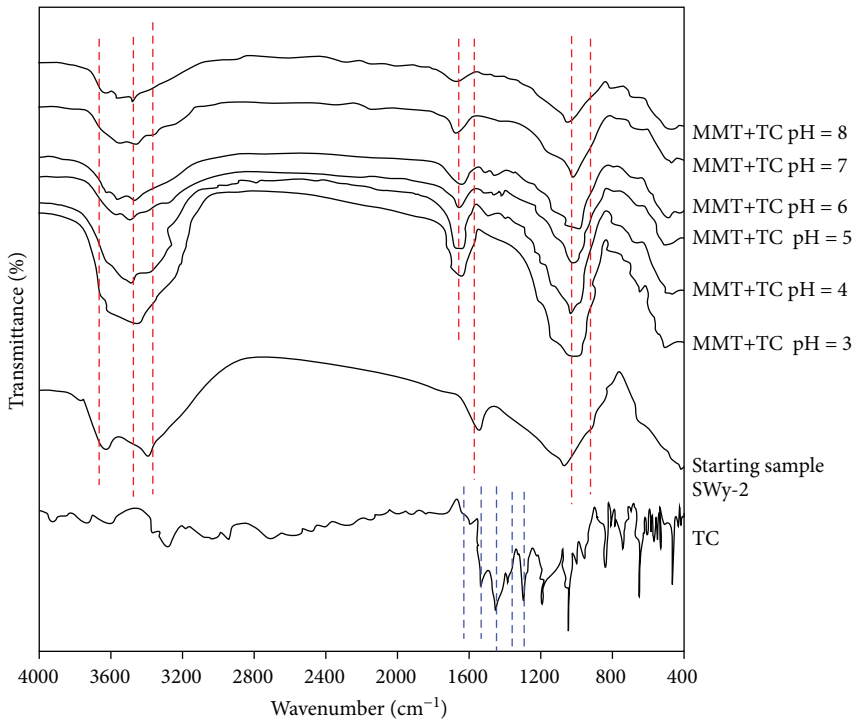

Figure 4: Transmittance IR spectra obtained, respectively, for TC, SWy-2-Na, and TC intercalated sample under a variable solution pH value.

Table 4: FTIR band position (cm^{-1}), respectively, for TC, Na-montmorillonite (SWy-2-Na), and TC sorption versus pH.

Sample	FTIR band position	Possible band assignment [38]
TC	1627	ν(CO1), ν(amid-NH), ν(CO3), ν(C2C3), δ(OH10,12)
	1572	δ(amid-NH), δ(amine-NH), ν(amid-CO), ν(C2C3), ν(CO3)
	1446	δ(OH10,12), δ(CH7,8,9), ν(D), ν(CO10,CO11), ν(C11C11a, C11aC12), δ(OH12a), δ(CH36)
	1350	ν(amid-C,C2), ν(C3,C4), δ(CH4a,5), δ(CH36), δ(OH12a), δ(amid-NH), ν(amid-CN), δ(OH10), ν(C6aC10a, C6aC7)
	1310	δ(OH10,12), δ(CH4,4a,5,5a), ν(C5aC11a), ν(C1C2), ν(C9C10, C10C10a, C10aC11), ν(CO11,12), ν(CO3), δ(CH7,8,9)
Na-montmorillonite (SWy-2-Na)	3620	OH stretching of structural hydroxyl groups
	3542	OH stretching of water coordinated to Al and Mg
	3415	OH stretching of adsorbed water
	1656	OH deformation of water
	1035	Si-O stretching
	980	Si-O stretching
MMT+TC For pH: 3 ➔ 8	3621	OH stretching of structural hydroxyl groups
	3542	OH stretching of water coordinated to Al and Mg
	3417	OH stretching of adsorbed water
	1638	OH deformation of water
	1048	Si-O stretching
	980	Si-O stretching

process. Also, because of the ability of nitrogen to cover only the outer primary surface area but not the IS, an asymptotic approach to limiting quantity is observed in nitrogen isotherms. Indeed, it is necessary to differentiate between external, internal, and interlamellar surface areas for clays.

The surface area concept does not give a complete textural description in the case of clay specimen; for that, a pore size (PS) and a pore size distribution (PSD) are necessary. The PSD in the mesopore region was determined by the BJH method assuming

(i) the shape of the pores with radius (r) approximatively half of its width is cylindrical [61]

(ii) the radii (r) of mesopores assumed to be cylindrical corresponding to V values were calculated from the corrected Kelvin equation by the use of P/P_0 values [64]

(iii) the specific micropore, mesopore, and macropore volumes (namely, V_{Mi}, V_{Me}, and V_{Ma} all in mL/g, respectively) are defined as the volumes of micropores, mesopores, and macropores including nanopores in one gram solid

(iv) the presence of macropores has a low effect on the adsorptive properties of a solid [65]

(v) the adsorption capacity as liquid nitrogen volumes which were estimated from desorption data at the relative equilibrium pressure (P/P_0) less than 0.96 is taken as the specific micro-mesopore volumes ($V = V_{Mi} + V_{Me}$)

(vi) P_0 and P are the vapor pressure of the bulk liquid nitrogen and equilibrium pressure of desorption at the liquid nitrogen temperature (~77 K)

The V-r (cumulative pore volume vs. pore radius) plots are called mesopore PSD and given in Figure 7.

The estimated V_{Mi} and V_{Me} can be obtained by the intercepts of the extrapolations of each PSD curve related to each sample [66]. The V_{Me} increase from 0.027 to 0.036 mL/g by increasing soil solution pH during the intercalation/adsorption process.

The radius derivative of the V-r curve for all samples is given in Figure 8 where the maximum mesopore volume (0.000948 mL/g) is obtained from pH 7 and the mesopore radii varied between 1.5 and 16 nm. The increase in the average pore diameter from a micropore with a width smaller than 2 nm is attributed to the reduction of microporous distribution in favor of mesoporous distribution. The porosity investigation using the BET-BJH method confirms observations obtained by SEM indicating changes on the morphological properties versus increasing pH rate. This transformation can be interpreted by a possible TC molecule conformation change.

4. Discussion

The TC intercalation on the montmorillonite interlayer is confirmed by the layer thickness variation. This result is demonstrated by several works [19–21, 37]. The layer thickness evolution is ascribed to the interlamellar space organization between interlayer species, essentially water molecules, exchangeable sodium, and TC molecules.

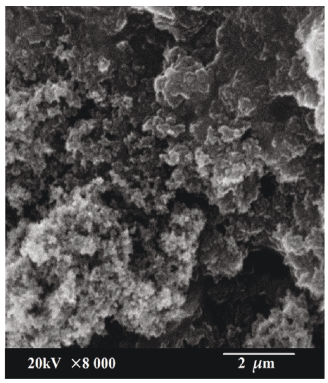

(a) Starting Na-montmorillonite (MMT)

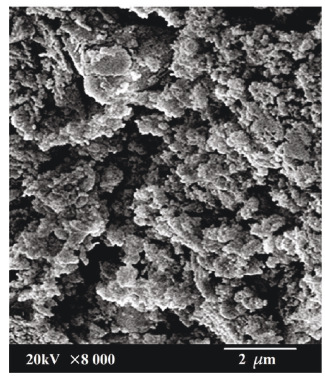

(b) MMT+TC pH = 3

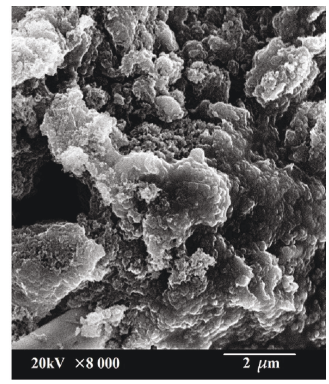

(c) MMT+TC pH = 4

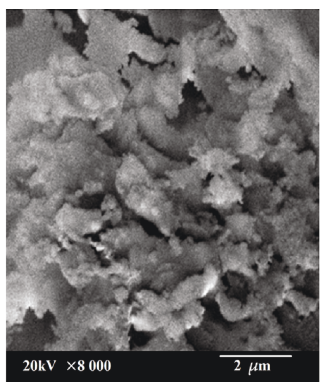

(d) MMT+TC pH = 5

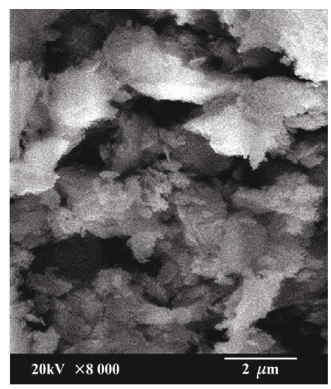

(e) MMT+TC pH = 6

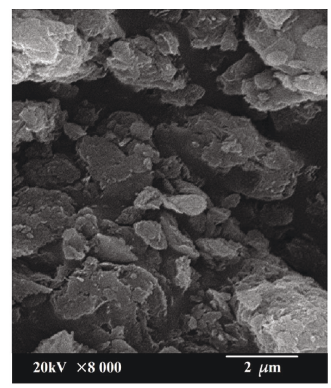

(f) MMT+TC pH = 7

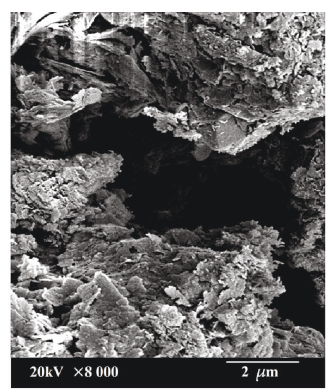

(g) MMT+TC pH = 8

Figure 5: SEM analysis in the case of the starting sample and the intercalated sample under variable solution pH.

Table 5: SA_{BET} (single-point and multipoint BET) and BJH method average pore diameter.

Sample	SA_{BET} (m^2/g) Single-point BET	SA_{BET} (m^2/g) Multi-point BET	Average nanopore diameter (nm) BJH method
MMT+TC_pH3	13.7856	13.8124	3.7102
MMT+TC_pH4	13.9145	13.9735	3.6905
MMT+TC_pH5	14.0864	14.3147	3.7289
MMT+TC_pH6	15.8261	15.9432	3.7305
MMT+TC_pH7	17.9425	18.1287	3.7646
MMT+TC_pH8	18.9461	18.9829	3.7724

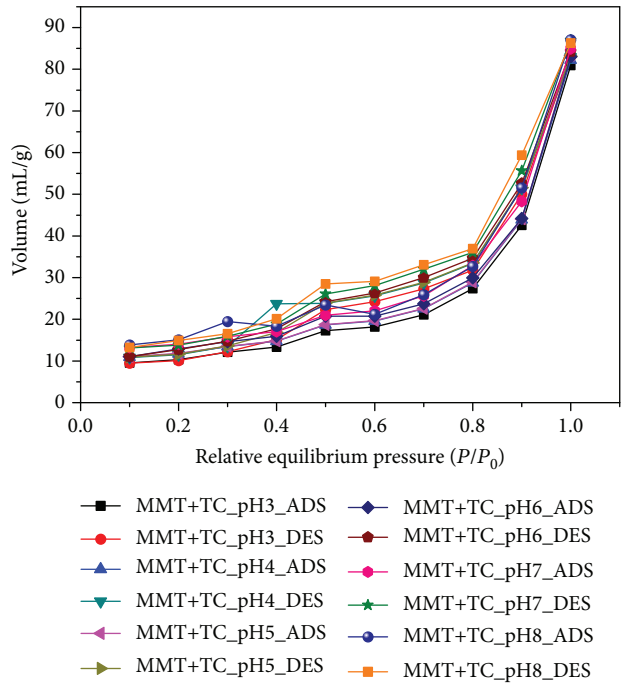

Figure 6: Nitrogen adsorption-desorption isotherms of montmorillonite-exchanged TC under varying soil solution pH. MMT: montmorillonite; TC: tetracycline; ADS: adsorption; DES: desorption.

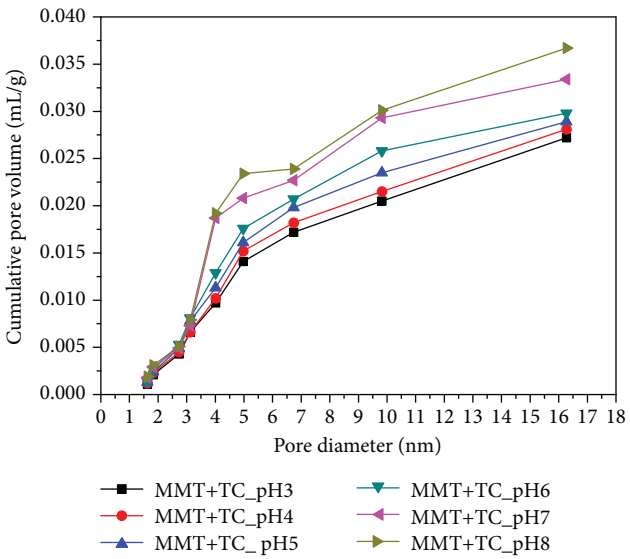

Figure 7: The pore size distribution curve in the case of montmorillonite-exchanged TC under varying soil solution pH.

Based on the theoretical XRD analysis, it is shown that this variation is mainly affected by the nature and/or the amount of the intercalated water. [29] use the XRD modeling approach in order to characterize the pH-dependent intercalation of TC within montmorillonite, and they demonstrate that pH, when increased, is responsible of the reduction of the intercalated TC amounts. Also, they reveal that the pH-

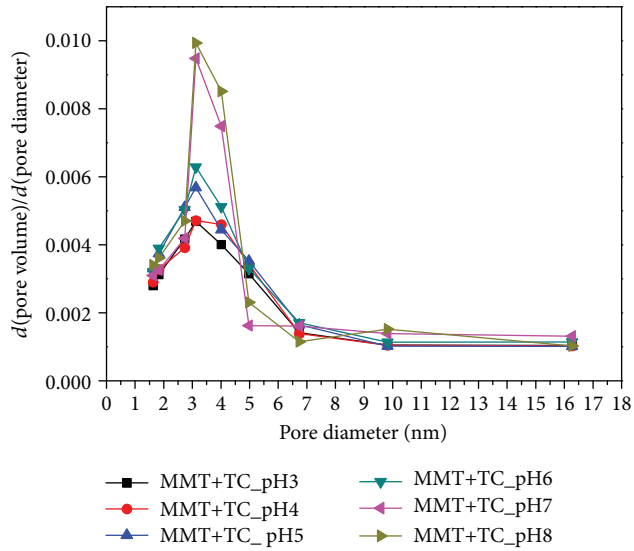

Figure 8: The derivative pore size distribution curve in the case of montmorillonite-exchanged TC under varying soil solution pH.

dependent change in the access of TC to the clay interlayers is not positively correlated with TC speciation, thus corroborating a possible correlation with changes in the clay surface chemistry as pH increases. In this work, another point of view is addressed, the correlation between the environment of the material and the soil solution pH in order to quantify the water levels present in the interlamellar space.

The investigation of the water molecule evolution versus the soil solution pH (Figure 9) shows quasiabsence of the 4W hydration state at pH = 3 and pH = 7, despite the high moisture contents at RH = 80%. For the same pH range, the 3W hydration state dominates the structure indicating probably a great abundance, within the "clay particle" of the sheets presenting a complete intercalation of TC molecules. This result is confirmed by the presence of the highly hydrated state (i.e., 3W) even for the lowest humidity rate which is the case for all investigated pH values except pH = 8. A notable effect of the pH variation is shown for the 1W hydration state which disappears from pH = 4. This may be due to a new interlayer organization where a layer "population" with partial or total CEC saturation with the TC molecule is noted. For pH = 7 and 8, a major 2W layer abundance manifests which is attributed to the TC conformation change demonstrated by the work of [29, 44, 46]. The proposition is confirmed by XRD analysis at pH = 8 where a declared 4W hydration state, characterized by d_{001} = 22.07 Å, is observed. This result agrees with those obtained by [21]. Indeed, they demonstrate that TC located in the interlayer spacing increase the d_{001} basal spacing from nearly 13.7 Å to nearly 22.0 Å. Physically, this result may have a logical explanation due to the increase in the TC molecule freedom degree within the interlayer space. This increase is attributed to the presence of 4W layers (at minimum) and a probable decrease in the concentration of exchanged TC molecules which is in concordance with earlier works.

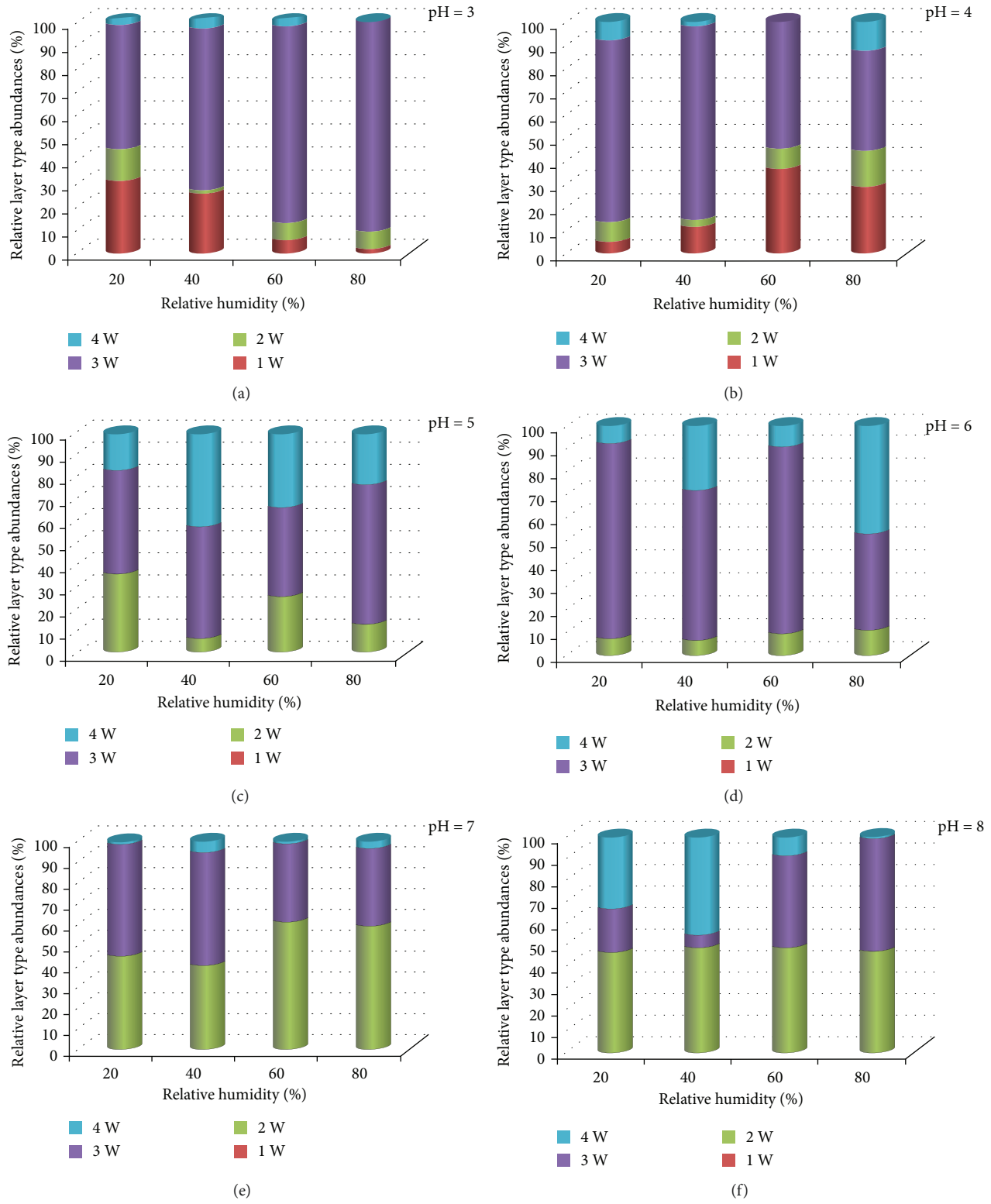

Figure 9: (a–f) Relative layer type abundances versus %RH for pH varying from 3 to 8.

5. Conclusions

The qualitative investigation of the 00l reflection obtained from XRD patterns has implied pH-dependent intercalation of TC within Na-exchanged montmorillonite but remains without real contribution to the understanding of the resulting interstratified structures. In this work, a correlation between results obtained from the XRD modeling

approach, FTIR, SEM, and BET-BJH method is employed to exceed insufficient results obtained by the simple qualitative XRD analysis.

Obtained results demonstrate the following:

(i) For a low pH value (pH = 3), clay "particle" is characterized by a random MLS distribution

(ii) By increasing the pH value, a segregated MLS distribution trend appears indicating the TC molecule intercalation process

(iii) The quasihomogeneous 2W phases (obtained, respectively, at pH 7 and pH 8), attributed to unexfoliated smectite layers, are fully described using "in situ" XRD analysis

(iv) The 4W hydration state (at pH = 4) is accompanied by a probable TC molecule conformation change

(v) The IR spectroscopy shows that the pH variation did not really affect the structure except for pH values close to 7 which confirms the obtained XRD results

(vi) The SEM images show clear surface homogeneity changes as a function of the pH value, and for pH close to 7, the porosity increases probably

(vii) SEM observations are confirmed by BET-BJH adsorption measurements which confirm a possible TC molecule conformation change from pH 7

Data Availability

No data were used to support this study.

Conflicts of Interest

The author declares no conflict of interest.

Acknowledgments

The editorial assistance of the guest editor is acknowledged.

References

[1] A. C. Q. Ladeira and C. A. Morais, "Effect of ammonium, carbonate and fluoride concentration on the uranium recovery by resins," *Radiochimica Acta*, vol. 93, no. 4, pp. 207–209, 2005.

[2] S. Kulkarni, A. Ballal, and S. K. Apte, "Bioprecipitation of uranium from alkaline waste solutions using recombinant Deinococcus radiodurans," *Journal of hazardous materials*, vol. 262, pp. 853–861, 2013.

[3] P. Gu, S. Zhang, X. Li et al., "Recent advances in layered double hydroxide-based nanomaterials for the removal of radionuclides from aqueous solution," *Environmental Pollution*, vol. 240, pp. 493–505, 2018.

[4] W. Liu, R. Yin, X. Xu, L. Zhang, W. Shi, and X. Cao, "Structural engineering of low-dimensional metal–organic frameworks: synthesis, properties, and applications," *Advancement of Science*, vol. 6, no. 12, p. 1802373, 2019.

[5] D. Fernández-Calviño, A. Bermúdez-Couso, M. Arias-Estévez et al., "Competitive adsorption/desorption of tetracycline, oxytetracycline and chlortetracycline on two acid soils: stirred flow chamber experiments," *Chemosphere*, vol. 134, pp. 361–366, 2015.

[6] B. Oliver-Rodríguez, A. Zafra-Gómez, M. S. Reis et al., "Wide-range and accurate modeling of linear alkylbenzene sulfonate (LAS) adsorption/desorption on agricultural soil," *Chemosphere*, vol. 138, pp. 148–155, 2015.

[7] Y. Keren, M. Borisover, and N. Bukhanovsky, "Sorption interactions of organic compounds with soils affected by agricultural olive mill wastewater," *Chemosphere*, vol. 138, no. 10, pp. 462–468, 2015.

[8] F. Tong, X. Gu, C. Gu, R. Ji, Y. Tan, and J. Xie, "Insights into tetrabromobisphenol A adsorption onto soils: Effects of soil components and environmental factors," *Science of the Total Environment*, vol. 536, pp. 582–588, 2015.

[9] P. Sellin and O. X. Leupin, "The use of clay as an engineered barrier in radioactive-waste management - a review," *Clays and Clay Minerals*, vol. 61, no. 6, pp. 477–498, 2013.

[10] T. Missana, U. Alonso, and M. García-Gutiérrez, "Experimental study and modelling of selenite sorption onto illite and smectite clays," *Journal of Colloid and Interface Science*, vol. 334, no. 2, pp. 132–138, 2009.

[11] E. Castellini, D. Malferrari, F. Bernini et al., "Baseline studies of the Clay Minerals Society source clay montmorillonite stx-1b," *Clays and Clay Minerals*, vol. 65, no. 4, pp. 220–233, 2017.

[12] R. Chalghaf, W. Oueslati, M. Ammar, H. B. Rhaiem, and A. B. H. Amara, "Effect of temperature and pH value on cation exchange performance of a natural clay for selective (Cu^{2+}, Co^{2+}) removal: equilibrium, sorption and kinetics," *Progress in Natural Science*, vol. 23, no. 1, pp. 23–35, 2013.

[13] P. Komadel, J. Madejová, and J. Bujdák, "Preparation and properties of reduced-charge smectites - a review," *Clays and Clay Minerals*, vol. 53, no. 4, pp. 313–334, 2005.

[14] K. F. Yan, X. S. Li, C. G. Xu, Q. N. Lv, and X. K. Ruan, "Molecular dynamics simulation of the intercalation behaviors of methane hydrate in montmorillonite," *Journal of Molecular Modeling*, vol. 20, no. 6, 2014.

[15] F. Claret, A. Bauer, T. Schäfer, L. Griffault, and B. Lanson, "Experimental investigation of the interaction of clays with high-pH solutions: a case study from the Callovo-Oxfordian formation, Meuse-Haute Marne underground laboratory (France)," *Clays and Clay Minerals*, vol. 50, no. 5, pp. 633–646, 2002.

[16] S. Dultz and J. Bors, "Organophilic bentonites as adsorbents for radionuclides: II. Chemical and mineralogical properties of HDPy-montmorillonite," *Applied Clay Science*, vol. 16, no. 1-2, pp. 15–29, 2000.

[17] S. Dultz, B. Riebe, and C. Bunnenberg, "Temperature effects on iodine adsorption on organo-clay minerals," *Applied Clay Science*, vol. 28, no. 1-4, pp. 17–30, 2005.

[18] P. Kulshrestha, R. F. Giese, and D. S. Aga, "Investigating the molecular interactions of oxytetracycline in clay and organic matter: insights on factors affecting its mobility in soil," *Environmental Science & Technology*, vol. 38, no. 15, pp. 4097–4105, 2004.

[19] R. A. Figueroa and A. A. Mackay, "Sorption of oxytetracycline to iron oxides and iron oxide-rich soils," *Environmental Science & Technology*, vol. 39, no. 17, pp. 6664–6671, 2005.

[20] J. R. V. Pils and D. A. Laird, "Sorption of tetracycline and chlortetracycline on K- and Ca-saturated soil clays, humic substances, and clay-humic complexes," *Environmental Science & Technology*, vol. 41, no. 6, pp. 1928–1933, 2007.

[21] M. E. Parolo, M. J. Avena, M. C. Savini, M. T. Baschini, and V. Nicotra, "Adsorption and circular dichroism of tetracycline on sodium and calcium-montmorillonites," *Colloids and Surfaces A: Physicochemical and Engineering Aspects*, vol. 417, pp. 57–64, 2013.

[22] Y. Zhao, X. Gu, S. Li, R. Han, and G. Wang, "Insights into tetracycline adsorption onto kaolinite and montmorillonite: experiments and modeling," *Environmental Science and Pollution Research*, vol. 22, no. 21, pp. 17031–17040, 2015.

[23] H. Wu, H. Xie, G. He, Y. Guan, and Y. Zhang, "Effects of the pH and anions on the adsorption of tetracycline on iron-montmorillonite," *Applied Clay Science*, vol. 119, pp. 161–169, 2016.

[24] L. Aristilde, B. Lanson, J. Miéhé-Brendlé, C. Marichal, and L. Charlet, "Enhanced interlayer trapping of a tetracycline antibiotic within montmorillonite layers in the presence of Ca and Mg," *Journal of Colloid and Interface Science*, vol. 464, pp. 153–159, 2016.

[25] M. Karpov, B. Seiwert, V. Mordehay, T. Reemtsma, T. Polubesova, and B. Chefetz, "Transformation of oxytetracycline by redox-active Fe(III)- and Mn(IV)-containing minerals: processes and mechanisms," *Water Research*, vol. 145, pp. 136–145, 2018.

[26] M. E. R. Jalil, F. Toschi, M. Baschini, and K. Sapag, "Silica pillared montmorillonites as possible adsorbents of antibiotics from water media," *Applied Sciences*, vol. 8, no. 8, p. 1403, 2018.

[27] L. Xu, H. Li, W. A. Mitch, S. Tao, and D. Zhu, "Enhanced phototransformation of tetracycline at smectite clay surfaces under simulated sunlight via a Lewis-base catalyzed alkalization mechanism," *Environmental Science & Technology*, vol. 53, no. 2, pp. 710–718, 2018.

[28] C. Aguzzi, C. Viseras, P. Cerezo et al., "Influence of dispersion conditions of two pharmaceutical grade clays on their interaction with some tetracyclines," *Applied Clay Science*, vol. 30, no. 2, pp. 79–86, 2005.

[29] L. Aristilde, B. Lanson, and L. Charlet, "Interstratification patterns from the pH-dependent intercalation of a tetracycline antibiotic within montmorillonite layers," *Langmuir*, vol. 29, no. 14, pp. 4492–4501, 2013.

[30] S. Pirillo, C. R. Luna, I. López-Corral, A. Juan, and M. J. Avena, "Geometrical and electronic properties of hydrated sodium montmorillonite and tetracycline montmorillonite from DFT calculations," *Journal of Physical Chemistry C*, vol. 119, no. 28, pp. 16082–16088, 2015.

[31] H. Zhu, X. Xiao, Z. Guo et al., "Adsorption of vanadium (V) on natural kaolinite and montmorillonite: characteristics and mechanism," *Applied Clay Science*, vol. 161, pp. 310–316, 2018.

[32] J. Ma, Y. Lei, M. A. Khan et al., "Adsorption properties, kinetics & thermodynamics of tetracycline on carboxymethylchitosan reformed montmorillonite," *International Journal of Biological Macromolecules*, vol. 124, pp. 557–567, 2019.

[33] K. S. D. Premarathna, A. U. Rajapaksha, N. Adassoriya et al., "Clay-biochar composites for sorptive removal of tetracycline antibiotic in aqueous media," *Journal of Environmental Management*, vol. 238, pp. 315–322, 2019.

[34] G. Lv, Z. Li, L. Elliott, M. J. Schmidt, M. P. MacWilliams, and B. Zhang, "Impact of tetracycline-clay interactions on bacterial growth," *Journal of Hazardous Materials*, vol. 370, pp. 91–97, 2019.

[35] R. Prewo and J. J. Stezowski, "Chemical-structural properties of tetracycline derivatives. 3. The integrity of the conformation of the nonionized free base," *American Chemical Society*, vol. 99, no. 4, pp. 1117–1121, 1977.

[36] J. Tolls, "Sorption of veterinary pharmaceuticals in soils: a review," *Environmental Science & Technology*, vol. 35, no. 17, pp. 3397–3406, 2001.

[37] M. E. Parolo, M. C. Savini, J. M. Valles, M. T. Baschini, and M. J. Avena, "Tetracycline adsorption on montmorillonite: pH and ionic strength effects," *Applied Clay Science*, vol. 40, no. 1-4, pp. 179–186, 2008.

[38] P.-H. Chang, Z. Li, W.-T. Jiang, and J.-S. Jean, "Adsorption and intercalation of tetracycline by swelling clay minerals," *Applied Clay Science*, vol. 46, no. 1, pp. 27–36, 2009.

[39] W. Oueslati, H. Ben Rhaiem, M. S. Karmous, S. Naaman, and A. B. H. Amara, "Study of the structural evolution and selectivity of Wyoming montmorillonite in relation with the concentration of Cu2+ and Ni2+," *Zeitschrift für Kristallographie*, vol. 2006, suppl_23_2006, pp. 425–429, 2006.

[40] W. Oueslati, H. Ben Rhaiem, and A. Ben Haj Amara, "Effect of relative humidity constraint on the metal exchanged montmorillonite performance: an XRD profile modeling approach," *Applied Surface Science*, vol. 261, pp. 396–404, 2012.

[41] W. F. Moll, "Baseline studies of the Clay Minerals Society source clays: geological origin," *Clays and Clay Minerals*, vol. 49, no. 5, pp. 374–380, 2001.

[42] D. Borden and R. F. Giese, "Baseline studies of the Clay Minerals Society source clays: cation exchange capacity measurements by the ammonia-electrode method," *Clays and Clay Minerals*, vol. 49, no. 5, pp. 444-445, 2001.

[43] M. Ammar, W. Oueslati, N. Chorfi, and A. B. H. Amara, "The water retention mechanism of a Cs+ and Na+ exchanged montmorillonite: effect of relative humidity and ionic radius on the interlayer," *Powder Diffraction*, vol. 30, no. S1, pp. S70–S75, 2015.

[44] L. Lambs, B. Decock-Le Reverend, H. Kozlowski, and G. Berthon, "Metal ion-tetracycline interactions in biological fluids. 9. Circular dichroism spectra of calcium and magnesium complexes with tetracycline, oxytetracycline, doxycycline, and chlortetracycline and discussion of their binding modes," *Inorganic Chemistry*, vol. 27, no. 17, pp. 3001–3012, 1988.

[45] Z. Qiang and C. Adams, "Potentiometric determination of acid dissociation constants (pKa) for human and veterinary antibiotics," *Water Research*, vol. 38, no. 12, pp. 2874–2890, 2004.

[46] G. Caminati and M. Puggelli, "Europium in phospholipid nanoscaffolds for the photophysical detection of antibiotic traces in solution," in *Europium: compounds, production and applications*, pp. 203–228, Nova Science Publishers Inc., New York, 2011.

[47] W. Oueslati, H. B. Rhaiem, and A. B. H. Amara, "XRD investigations of hydrated homoionic montmorillonite saturated by several heavy metal cations," *Desalination*, vol. 271, no. 1-3, pp. 139–149, 2011.

[48] W. Oueslati, M. Ammar, and N. Chorfi, "Quantitative XRD analysis of the structural changes of Ba-exchanged

montmorillonite: effect of an in situ hydrous perturbation," *Minerals*, vol. 5, no. 3, pp. 507–526, 2015.

[49] E. Ferrage, B. Lanson, L. J. Michot, and J. L. Robert, "Hydration properties and interlayer organization of water and ions in synthetic Na-smectite with tetrahedral layer charge. Part 1. Results from X-ray diffraction profile modeling," *The Journal of Physical Chemistry C*, vol. 114, no. 10, pp. 4515–4526, 2010.

[50] M. Ammar, W. Oueslati, H. Ben Rhaiem, and A. Ben Haj Amara, "XRD profile modeling approach tools to investigate the effect of charge location on hydration behavior in the case of metal exchanged smectite," *Powder Diffraction*, vol. 28, no. S2, pp. S284–S300, 2013.

[51] V. A. Drits and C. Tchoubar, "X-ray diffraction by disordered lamellar structures: feory and applications to microdivided silicates and carbons," Springer, Berlin, 1990.

[52] B. Lanson, "Modelling of X-ray diffraction profiles: investigation of defective lamellar structure crystal chemistry," *EMU Notes in Mineralogy*, vol. 11, pp. 151–202, 2011.

[53] W. Oueslati and M. Meftah, "Discretization of the water uptake process of Na-montmorillonite undergoing atmospheric stress: XRD modeling approach," *Advances in Materials Science and Engineering*, vol. 2018, 17 pages, 2018.

[54] J. Madejová and P. Komadel, "Baseline studies of the Clay Minerals Society source clays: infrared methods," *Clays and Clay Minerals*, vol. 49, no. 5, pp. 410–432, 2001.

[55] C. F. Leypold, M. Reiher, G. Brehm et al., "Tetracycline and derivatives—assignment of IR and Raman spectra via DFT calculations," *Physical Chemistry Chemical Physics*, vol. 5, no. 6, pp. 1149–1157, 2003.

[56] M. Benzina and A. Bellagi, "Détermination des propriétés du réseau poreux de matériau argileux par les techniques d'adsorption d'azote et de porosimétrie au mercure en vue de leur utilisation pour la récupération des gaz," *Annals of Chemistry Science Materials*, vol. 15, pp. 315–335, 1990.

[57] S. Gregg and K. Sing, *Adsorption, Surface Area and Porosity*, Academic Press, London, second ed. edition, 1982.

[58] J. C. Groen, L. A. A. Peffer, and J. Pérez-Ramírez, "Pore size determination in modified micro- and mesoporous materials. Pitfalls and limitations in gas adsorption data analysis," *Microporous and Mesoporous Materials*, vol. 60, no. 1-3, pp. 1–17, 2003.

[59] E. P. Barrett, L. G. Joyner, and P. P. Halenda, "The determination of pore volume and area distributions in porous substances. I. Computations from nitrogen isotherms," *Journal of the American Chemical Society*, vol. 73, no. 1, pp. 373–380, 1951.

[60] T. Jesionowski, "Characterization of silicas precipitated from solution of sodium metasilicate and hydrochloric acid in emulsion medium," *Powder Technology*, vol. 127, no. 1, pp. 56–65, 2002.

[61] N. Yildiz, Z. Aktas, and A. Calimli, "Sulphuric acid activation of a calcium bentonite," *Particulate Science and Technology*, vol. 22, no. 1, pp. 21–33, 2004.

[62] K. Song and G. Sandi, "Characterization of montmorillonite surfaces after organosilane modification," *Clays and Clay Minerals*, vol. 49, no. 2, pp. 119–125, 2001.

[63] W. Wang, P. Liu, M. Zhang, J. Hu, and F. Xing, "The pore structure of phosphoaluminate cement," *Open Journal of Composite Materials*, vol. 02, no. 03, pp. 104–112, 2012.

[64] F. Rouqueral, J. Rouqueral, and K. Sing, *Adsorption by Powder and Porous Solids*, Academic Press, London, 1999.

[65] M. Önal and Y. Sarıkaya, "Preparation and characterization of acid-activated bentonite powders," *Powder Technology*, vol. 172, no. 1, pp. 14–18, 2007.

[66] H. Noyan, M. Önal, and Y. Sarikaya, "The effect of sulphuric acid activation on the crystallinity, surface area, porosity, surface acidity, and bleaching power of a bentonite," *Food Chemistry*, vol. 105, no. 1, pp. 156–163, 2007.

Hindawi
Journal of Nanomaterials
Volume 2019, Article ID 3108742, 5 pages
https://doi.org/10.1155/2019/3108742

Research Article

Facile Synthesis of Fe_2O_3 Nanomaterials from MIL-101(Fe) Template and Its Application in Lithium Ion Batteries

Chunyan Zhang,[1] Nianqiao Qin,[1] Jing Li,[2] Yan Tian,[1] and Hui Zhang[2]

[1]*Department of Applied Chemistry, Anhui Agricultural University, Hefei 230036, China*
[2]*School of Forestry & Landscape Architecture, Anhui Agricultural University, Hefei 230036, China*

Correspondence should be addressed to Hui Zhang; zhanghuiahau@163.com

Received 1 July 2019; Accepted 14 August 2019; Published 8 September 2019

Guest Editor: Yunpan Ying

Sponge-like porous Fe_2O_3 nanomaterials were obtained through the calcination process of the iron-based metal organic framework (MIL-101). As anode materials for lithium-ion batteries, thus, obtained products show a good electrochemical performance with a high specific capacity (1358 mA h g^{-1} at 100 mA g^{-1} in the initial cycle) and a relatively stable cycle performance (750 mA h g^{-1} after 80 charge/discharge cycles). The superior cycling performance may be attributed to their special structure, which facilitates charge transfer and Li^+ diffusion.

1. Introduction

The concept of promoting environmental protection and energy conservation becomes a hot topic, and renewable clean energy has attained global attentions. Lithium-ion batteries (LIBs), as one of the prominent energy storage systems, have been extensively studied and broadly utilized in many electronic devices owing to their high energy density and long cycling life [1, 2]. The low cost, chemically stable, and highly conductive graphite carbon is recognized as the leading electrode material for the anodes of commercial LIBs. However, the low capability of charge storage (theoretical capacity is only 372 mA h g^{-1}) limits further applications of graphite carbon in LIBs [3]. In order to meet the demands of ever-growing performance, developing new alternative anode materials has become an urgent task in building next-generation LIBs. Transition metal oxides (M_xO_y, M = Fe, Co, Zn, Mn, Mo, etc.) have been extensively investigated in a diverse range of applications in energy, environment, catalysis, and electronics fields [4]. Among the available alternative anode materials, iron oxides have attracted people's attention because of nontoxicity, high corrosion resistance, and higher capacity as well as low processing cost [5–9]. However, high intrinsic resistance and the slow kinetics for ionic diffusion and charge transfer induce performance decay especially at high current densities, which seriously limited the application of Fe_2O_3 in Li-ion batteries. It has shown that Fe_2O_3 with nanostructures not only promotes ion diffusion and electron transfer but also effectively accommodates the large changes in volume that occurs during lithiation and delithiation to prevent the electrode disintegration. So far, a lot of attempts have been made to resolve the above issues by fabricating iron oxide nanostructure materials with optimized particle shapes, sizes, and component compositions [10–12]. MOF (metal-organic framework) as a novel class of organic-inorganic porous materials formed by strong bonds between organic ligands and metal ions has been used as precursors or templates for the synthesis of metal oxides by simple thermal decomposition. The MOF-derived nanomaterials exhibit relatively porous or hollow structures [13–15]. A rational design of MOF precursors with novel structures is highly desirable for the synthesis of high-performance electrode materials. For instance, Prussian blue (PB) microcubes were used as templates to prepare hollow Fe_2O_3 microboxes, which exhibited excellent cycling performance [16, 17].

Here, we present a simple and general MOF-assisted method for the fabrication of sponge-like Fe_2O_3 as anodes for LIBs. Firstly, MIL-101(Fe) nanopolyhedrons were formed by a one-pot hydrothermal method. Then,

these nanopolyhedrons could be further converted to porous sponge-like nanoparticles through a subsequent annealing treatment in air. These nanoparticles exhibit good electrochemical performance when used as anodes for LIBs. The remarkable electrochemical properties may attribute to the porous structure which not only facilitate electron transport but also efficiently relieve the volume change caused by insertion/extraction of Li^+. Therefore, the present study provides a simple way for the preparation of high-performance electrode materials for LIBs. And the method for the synthesis of Fe_2O_3 nanomaterials can be extended to the preparation of various MOF-derived functional nanocomposites for various energy-related applications.

2. Experimental Section

2.1. Preparation of the Electrode Materials. Dimethylformamide (DMF), ferric chloride ($FeCl_3{\cdot}6H_2O$), terephthalic acid (TPA), and ethyl alcohol (EtOH) were obtained from Shanghai Chemical Reagent Co. Ltd. (P. R. China) and used without further treatment. Doubly distilled water was used for preparing solutions.

2.1.1. Synthesis of MIL-101(Fe). MIL-101(Fe) nanopolyhedrons were prepared by a hydrothermal method based on the reported procedure with some modifications [18]. Specifically, 0.675 g of $FeCl_3{\cdot}6H_2O$ (2.5 mmol) and 0.21 g TPA (1.25 mmol) were mixed in 20 mL DMF, and the mixture was ultrasonicated for 20 min to make the solid full suspension. Next, the reaction mixture was loaded into a 50 mL Teflon-lined stainless steel autoclave and placed under static conditions at 110°C in an oven for 24 h. After naturally cooling down to room temperature, orange mud was obtained. Then, it was separated by centrifugation and washing with absolute DMF and EtOH to remove the raw materials. The product was vacuum-dried at 80°C for 120 min.

2.1.2. Synthesis of Fe_2O_3 Nanoparticles. The as-formed composite was placed in a ceramic boat and heated to 380°C in the muffle furnace for about 1 h under an ambient atmosphere at a ramp rate of $10^\circ C\,min^{-1}$. Upon naturally cooling down, red-brown powders of Fe_2O_3 were collected.

2.2. Characterization and Electrochemical Test of the Synthesized Materials. Characterization of these synthesized products by X-ray diffraction (XRD) using a DX-2700 X-ray diffractometer was equipped with a Cu Kα-sealed tube ($\lambda = 1.5406$ Å) and scanned in a range between 10° and 80°. Scanning electron microscopy (SEM) images were obtained by using a Hitachi S4800 scanning electron microscope operated at 10 kV. The transmission electron microscopy (TEM) images were carried out on JEM model 100SX electron microscopes (Japan Electron Co., Ltd.). Nitrogen adsorption-desorption isotherms were carried out with a Micromeritics TriStar II 3020 adsorption analyzer at 77 K. The electrochemical analysis was obtained with CR2016 coin-type half cells that were assembled in an Ar-filled glove box. The working electrode was fabricated in N-methyl-2-pyrrolidinone (NMP) by medley active materials, acetylene black, and polyvinylidene fluoride (PVDF) in a ratio of 8 : 1 : 1 ($w/w/w$). Copper foil, metallic lithium, and polyethylene film (Celgard, 2400) were employed as the collector, counter electrode, and separator, respectively. $LiPF_6$ (1 M) in the mixed solution of ethylene carbonate (EC) and dimethyl carbonate (DMC) (1 : 1 in volume ratio) was used as the electrolyte. The galvanostatic charge and discharge were performed on a battery testing system (CT-3008 W-5 V 10 mA, Neware Technology Co., Ltd., P. R. China) at various current densities between 0.01 and 3.0 V (vs. Li^+/Li).

3. Results and Discussion

3.1. Morphologies and Structures of the Samples. As seen in the XRD patterns (Figure 1(a)), the MIL-101(Fe) composites exhibit the diffraction peaks located at $2\theta = 2.7^\circ$, 5.0°, 8.9°, 9.5°, 10.6°, and 16.3° were observed, which was resembled with the existing researches [19]. This indicated that the synthesized powder is high-purity crystal. Figure 2(b) displays the XRD pattern of the calcined product; all the dominated diffraction peaks could be assigned to the hematite Fe_2O_3 (JCPDS No. 33-0664); besides, some weak diffraction peaks are indexed to Fe_3O_4 (JCPDS No. 65-3107) [10, 20].

As shown in the SEM and TEM images in Figure 2(a), MIL-101(Fe) exhibited a regular octahedron shape with a rough surface, and the average size is about 600 nm. After being annealed under an ambient atmosphere, sponge-like porous Fe_2O_3 nanomaterials with a diameter of~ 600 nm were obtained, shown in Figure 2(b).

The porosities of the nanocomposites were further calculated by N_2 adsorption-desorption isotherms at 77 K shown in Figure 3. The sample shows a type IV isotherm, suggesting microporous material with mesoporous formed by close-packed nanoparticles. The Brunauer–Emmett–Teller (BET) pore volume and surface area of the product were calculated to be $0.288\,cm^3\,g^{-1}$ and $99.8\,m^2\,g^{-1}$, respectively. Furthermore, the pore size is around 8 nm by using the Barrett-Joyner-Halenda (BJH) method.

3.2. Electrochemical Performance. Subsequently, we evaluated the lithium storage properties of the prepared samples as anode materials in LIBs (Figure 4). The electrode exhibits good performance, giving capacities of $1358\,mA\,h\,g^{-1}$ in the first cycle at a current density of $100\,mA\,g^{-1}$, and shows very stable capacity retention of $750\,mA\,h\,g^{-1}$ for over 80 cycles. What is more, from the second cycle onwards, the coulombic efficiency remains nearly 100%, which indicates an excellent reversible capacity of this electrode material. The good cycling stability may be attributed to the nanosized structure and presence of the porous architecture, which lead to an increase in the electrode/electrolyte contact area and help to accommodate the strain of Li^+ insertion/extraction [21].

4. Conclusions

In summary, porous sponge-like Fe_2O_3 nanomaterials have been successfully fabricated by a facile method. The as-

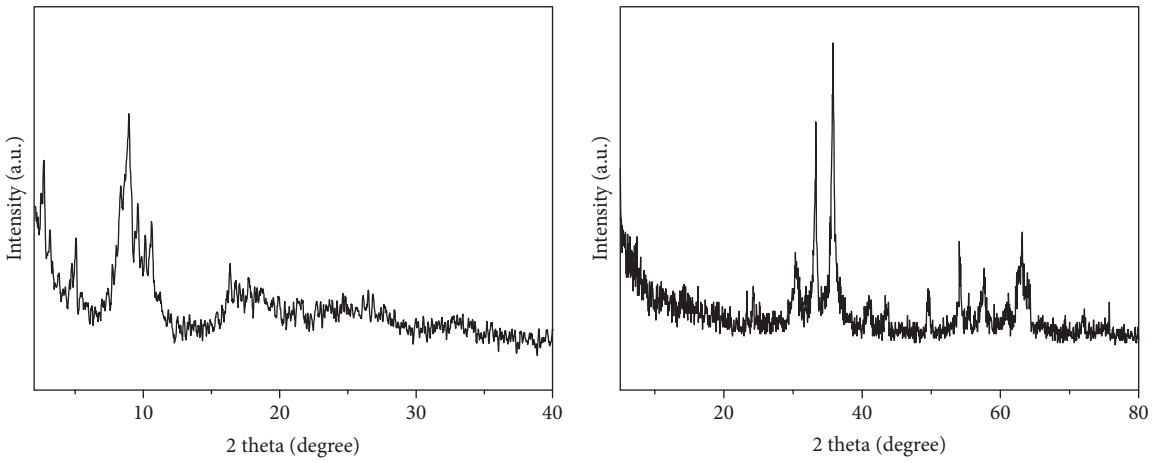

Figure 1: XRD patterns for (a) as-prepared MIL-101(Fe) and (b) the calcined product.

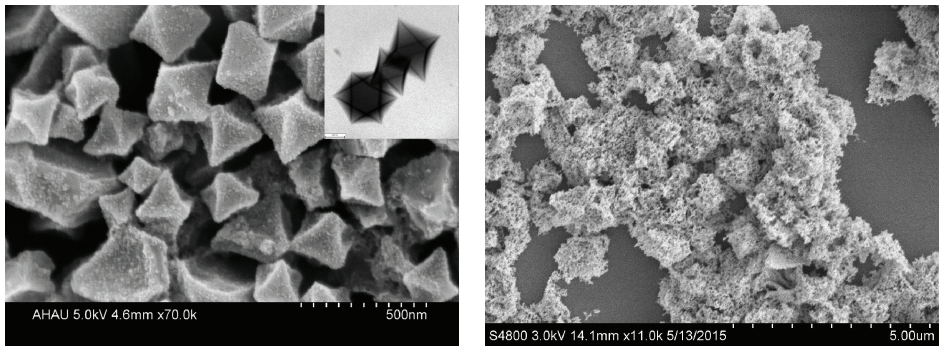

(a) (b)

Figure 2: (a) SEM and TEM image of MIL-101(Fe). (b) SEM image of the calcined product.

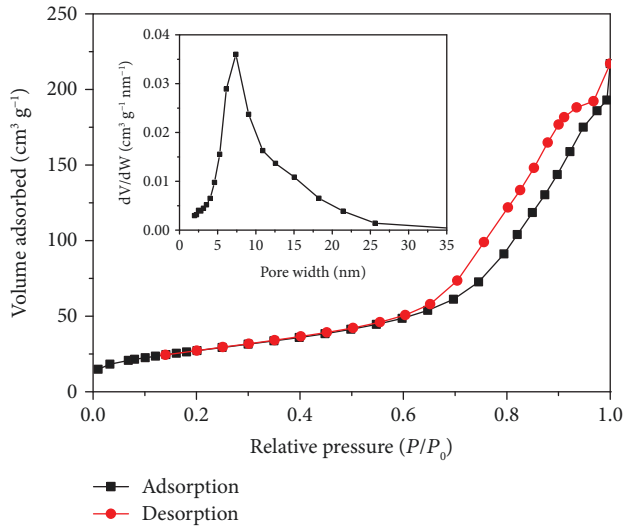

Figure 3: N_2 adsorption-desorption isotherms of the calcined product at 77 K.

prepared products demonstrate superior lithium storage properties (1358 mA h g^{-1} at 100 mA g^{-1} in the initial cycle and 750 mA h g^{-1} after 80 charge/discharge cycles) mostly due to the nanosized and porous structure, which substantially facilitate electronic/ionic transport and afford good structural stability upon cycling. This work provides a cost-

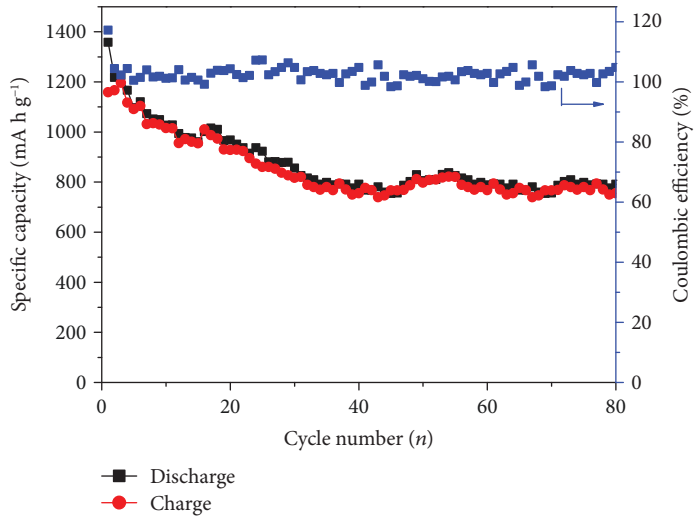

Figure 4: Cycling performance and corresponding coulombic efficiency at a current density of 100 mA g^{-1}.

effective route for the synthesis of porous materials; we hope it can also be expanded to other materials in a wider field.

Data Availability

The data used to support the findings of this study are available from the corresponding author upon request.

Conflicts of Interest

The authors declare that there is no conflict of interest regarding the publication of this paper.

Authors' Contributions

Chunyan Zhang and Nianqiao Qin contributed equally to this work.

Acknowledgments

This work is supported by the Key Research Project of the Natural Science Foundation of Anhui Provincial Universities (Grant Nos. KJ2019A0216, KJ2019A0200, and KJ2018A0161) and the Scientific Research Foundation of Anhui Agricultural University (Grant No. Wd2018-05).

References

[1] R. Ding, K. Liu, X. Liu, Z. Li, C. Wang, and M. Chen, "Hollow Co_3O_4 nanosphere surrounded by N-doped graphitic carbon filled within multilayer-sandwiched graphene network: a high-performance anode for lithium storage," *Inorganic Chemistry*, vol. 58, no. 5, pp. 3416–3424, 2019.

[2] Y. Li, Y. Fu, W. Liu, Y. Song, and L. Wang, "Hollow Co-Co_3O_4@CNTs derived from ZIF-67 for lithium ion batteries," *Journal of Alloys and Compounds*, vol. 784, pp. 439–446, 2019.

[3] W. Liu, Y. Fu, Y. Li, S. Chen, Y. Song, and L. Wang, "Three-dimensional carbon foam surrounded by carbon nanotubes and Co-Co_3O_4 nanoparticles for stable lithium-ion batteries," *Composites Part B: Engineering*, vol. 163, pp. 464–470, 2019.

[4] H. H. Fan, L. Zhou, and H. H. Li, "2D Fe_2O_3 nanosheets with bi-continuous pores inherited from Fe-MOF precursors: an advanced anode material for Li-ion half/full batteries," *2D Materials*, vol. 6, no. 4, article 045022, 2019.

[5] C. Zhang, J. Dai, P. Zhang et al., "Porous Fe_2O_3/ZnO composite derived from MOFs as an anode material for lithium ion batteries," *Ceramics International*, vol. 42, no. 1, pp. 1044–1049, 2016.

[6] W. Qi, X. Li, H. Li et al., "Sandwich-structured nanocomposites of N-doped graphene and nearly monodisperse Fe_3O_4 nanoparticles as high-performance Li-ion battery anodes," *Nano Research*, vol. 10, no. 9, pp. 2923–2933, 2017.

[7] F. Wang, C. Wang, H. Chen et al., "A composite of Fe_3O_4@ C and multilevel porous carbon as high-rate and long-life anode materials for lithium ion batteries," *Nanotechnology*, vol. 30, no. 33, article 335701, 2019.

[8] Y. Ding, B. Liu, R. Cai et al., "One-pot synthesis of α-Fe_2O_3 nanospindles as high-performance lithium-ion battery anodes," *Nano*, vol. 13, no. 2, article 1850018, 2018.

[9] Y. Zhang, Q. Li, J. Liu et al., "Hierarchical Fe_2O_3@C@M-nO_2@C multishell nanocomposites for high performance lithium ion batteries and catalysts," *Langmuir*, vol. 34, no. 18, pp. 5225–5233, 2018.

[10] Z. Li, Y. Mao, Q. Tian, W. Zhang, and L. Yang, "Extremely facile preparation of high-performance Fe_2O_3 anode for lithium-ion batteries," *Journal of Alloys and Compounds*, vol. 784, pp. 125–133, 2019.

[11] M. S. Balogun, Z. Wu, Y. Luo et al., "High power density nitridated hematite (α-Fe_2O_3) nanorods as anode for high-performance flexible lithium ion batteries," *Journal of Power Sources*, vol. 308, pp. 7–17, 2016.

[12] M. Chen, E. Zhao, Q. Yan, Z. Hu, X. Xiao, and D. Chen, "The effect of crystal face of Fe_2O_3 on the electrochemical performance for lithium-ion batteries," *Scientific Reports*, vol. 6, no. 1, article 29381, 2016.

[13] J. Li, X. Wang, G. Zhao et al., "Metal–organic framework-based materials: superior adsorbents for the capture of toxic

and radioactive metal ions," *Chemical Society Reviews*, vol. 47, no. 7, pp. 2322–2356, 2018.

[14] F. Ke, Y. Li, C. Zhang et al., "MOG-derived porous FeCo/C nanocomposites as a potential platform for enhanced catalytic activity and lithium-ion batteries performance," *Journal of Colloid and Interface Science*, vol. 522, pp. 283–290, 2018.

[15] C. Zhang, F. Ke, H. Xiao, H. Zhang, Y. Tian, and Y. Shen, "Well-designed hollow and porous Co_3O_4 microspheres used as an anode for Li-ion battery," *Journal of Solid State Electrochemistry*, vol. 23, no. 8, pp. 2477–2482, 2019.

[16] L. Zhang, H. B. Wu, S. Madhavi, H. H. Hng, and X. W. (. D.). Lou, "Formation of Fe_2O_3 microboxes with hierarchical shell structures from metal–organic frameworks and their lithium storage properties," *Journal of the American Chemical Society*, vol. 134, no. 42, pp. 17388–17391, 2012.

[17] C. Nie, X. Zhang, H. Ren et al., "Synthesis of manganese-based Prussian blue nanocubes with organic solvent as high-performance anodes for lithium-ion batteries," *European Journal of Inorganic Chemistry*, vol. 2019, no. 28, pp. 3277–3286, 2019.

[18] S. Li, S. Sun, H. Wu, C. Wei, and Y. Hu, "Effects of electron-donating groups on the photocatalytic reaction of MOFs," *Catalysis Science & Technology*, vol. 8, no. 6, pp. 1696–1703, 2018.

[19] H. Hu, H. Zhang, Y. Chen, Y. Chen, L. Zhuang, and H. Ou, "Enhanced photocatalysis degradation of organophosphorus flame retardant using MIL-101(Fe)/persulfate: effect of irradiation wavelength and real water matrixes," *Chemical Engineering Journal*, vol. 368, pp. 273–284, 2019.

[20] X. Li, Y. Ma, G. Cao, and Y. Qu, "FeO_x @ carbon yolk/shell nanowires with tailored void spaces as stable and high-capacity anodes for lithium ion batteries," *Journal of Materials Chemistry A*, vol. 4, no. 32, pp. 12487–12496, 2016.

[21] J. Nai and X. W. Lou, "Hollow structures based on Prussian blue and its analogs for electrochemical energy storage and conversion," *Advanced Materials*, article 1706825, 2018.

Hindawi
Journal of Nanomaterials
Volume 2019, Article ID 3128179, 13 pages
https://doi.org/10.1155/2019/3128179

Research Article

Synthesis and Study of an Efficient Metal-Organic Framework Adsorbent (MIL-96(Al)) for Fluoride Removal from Water

Xingang Wang,[1,2] Hui Zhu,[1,2] Tongshuai Sun,[1,2] Yinbo Liu,[1,2] Ting Han,[1,2] Jingxian Lu,[1,2] Hongliang Dai,[1,2,3] and Linzhi Zhai[1,2]

[1]*School of Environmental and Chemical Engineering, Jiangsu University of Science and Technology, No. 2 Mengxi Road, Zhenjiang 212018, China*
[2]*Marine Equipment and Technology Institute, Jiangsu University of Science and Technology, Zhenjiang 212003, China*
[3]*School of Energy and Environment, Southeast University, No. 2 Sipailou, Nanjing 210096, China*

Correspondence should be addressed to Hongliang Dai; daihongliang@just.edu.cn and Linzhi Zhai; zhailinzhi@just.edu.cn

Received 25 April 2019; Revised 17 July 2019; Accepted 2 August 2019; Published 4 September 2019

Guest Editor: Fei Ke

Long-term consumption of drinking water that contains excessive amounts of fluoride can endanger human health; therefore, the preparation and application of a high-efficiency defluorination adsorbent for advanced purification of drinking water are of significant interest. This study presents a metal-organic framework adsorbent (MIL-96(Al)) with the granular structure of rice, which was generated by hydrothermal reaction. The specific surface area of MIL-96(Al) was ~220 $m^2\ g^{-1}$, and it showed a good thermal stability. Several experiments were conducted wherein conditions, including adsorbent dosage, initial concentration, pH, and coexisting anions, were varied to understand the defluorination performance of the material. Results showed that pH (6–9) and coexisting anions had little effect on the removal efficiency of fluoride. The adsorption isotherm can be described by the Langmuir model, and the theoretical fluoride adsorption capacity of MIL-96(Al) was up to 42.19 mg Fg^{-1} at 298 K, which is much higher than that of the commonly used activated alumina. The adsorption process of fluoride is endothermic and follows pseudo second-order kinetics. In addition, MIL-96(Al) was shown to still achieve ~61.8% of the adsorption capacity after seven regenerations. This study shows that MIL-96(Al) is a good application prospect and could be widely used to remove fluoride from water.

1. Introduction

Fluoride is closely related to activities of human life and the metabolism of bone tissue. Excessive fluoride in natural water is predominantly caused by the discharge of fluoride-rich wastewater effluent or surface water washing of fluoride-containing ore over long periods [1, 2]. Excessive fluoride in the human body can mineralize calcium hydroxyphosphate to calcium fluorophosphate, which causes a significant change in the fluoride-phosphorus ratio resulting in spurs, periosteal hyperplasia, osteoporosis, osteosclerosis, and bone deformation [3, 4]. Long-term intake of high-fluoride food by children will result in enamel hypoplasia, tooth damage, and fluoride deposition, causing a series of deformities in the bones [5, 6]. The World Health Organization (WHO) stipulates that the maximum fluoride concentration within drinking water should be 1.5 mg L^{-1} [7]; however, this is exceeded in some developing countries, especially in tropical countries. Therefore, it is generally recommended that the maximum concentration of fluoride in drinking water be 1.0 mg L^{-1} [8]. There are several methods that can be used to remove fluoride from water, such as precipitation, adsorption, electrocoagulation, ion exchange, reverse osmosis, and electrodialysis [9]. The equipment cost and energy consumption of the electrochemical methods are relatively large, the electrode is easy to passivate, and the selectivity of this method needs to be improved; the processing speed of the precipitation methods is slow, and the water quality of the effluent is not easy to reach the standard; the cost of the surface assimilation techniques needs to be reduced. Among

these methods, the adsorption method is widely used for defluorination; however, there is still an urgent need for a low-energy consumption, simple, fast, efficient, and economical adsorbent [10].

Aluminum (Al) is an abundant and inexpensive metal element and has a stronger bond strength with fluoride than many other adsorbents; therefore, activated alumina is the most commonly used metal adsorbent and is recognized by the WHO and the United States Environmental Protection Agency (USEPA) as the best fluoride removal adsorbent [11–13]. Al^{3+} also has excellent adsorption properties for other low-concentration contaminants [14]. Activated alumina has a large specific surface area; however, its adsorption capacity is only 0.8–2.0 mg g^{-1} for fluoride, and it also requires adjustment of the pH of the reaction system, which increases the cost of water treatment [15]. For example, according to Dhillon et al.'s research, a Fe-Ca-Zr hybrid metal oxide nanomaterial has a large adsorption capacity of 250 mg Fg^{-1}, but has a high pH requirement. [16]. In Venditti et al.'s study, industrial wastewater was treated with aluminum chloride containing Actifluo (Brenntag). Some pretreatment is also required, and the fluoride content in the treated wastewater is still relatively high [17]. In addition, coexisting anions in the water interfere with activated alumina, inhibiting the removal of fluoride from the water [18]. Of particular concern is that Al can leach into the water, which may cause harm to people's memory and intelligence and could even cause brain damage [19, 20]. Powdered activated carbon also has a good fluoride removal performance; however, the fluoride removal process must be carried out under acidic conditions, increasing costs. To overcome these problems, a stable, convenient, and efficient Al-based defluorination adsorbent with a large adsorption capacity is required.

Metal-organic frameworks (MOFs) are crystalline porous materials with a periodic network structure composed of a porous metal center (metal ions or metal clusters) and a bridged organic ligand [21]. MOFs are also known as a coordination complex (coordination polymer) and have a high void ratio and a regular surface structure, which is different from general inorganic porous materials and organic complexes, and excellent chemical and thermal stability [22, 23]. These characteristics mean that MOFs have many potential applications and are widely used in industries, for example, catalysis, sensors, gas adsorption, removal of hazardous materials, and potential drug delivery and biomedical applications [24–30]. As far as we know, the application of MOF due to poor water stability in water treatment is not much in the literature; for example, AlFu MOF was studied by Karmakar et al. Researches on the use of Al-based MOF or even MOF to adsorb fluoride from water are relatively rare [31, 32]. This is probably because traditional MOFs are not suitable for use as defluorination adsorbents, and complex water quality conditions have a series of uncontrollable effects, where the combination of metal ions and fluorion results in a series of complex reactions [33]. Aluminum (Al) ions and fluorion complex in water to adsorbed fluoride and fluorion in water are mainly removed by means of physical adsorption, chemical adsorption, sweeping, and ion exchange of ligands. Due to the unique octahedral nature of the Al center [34], Al-MOF is used as a defluorination adsorbent, allowing Al ions to fully contact fluorion, resulting in improved fluoride removal.

Many previous studies have attempted to modify activated alumina and investigated several new adsorbents; however, the modifications resulted in no clear improvement in fluoride removal efficiency. In this study, a MOF (MIL-96(Al)), as a fluoride removal adsorbent, was synthesized and provides more active sites that react with fluoride, resulting in improved performance. The adsorption properties of MIL-96(Al) were explored under conditions varying by dosage, initial concentration, pH, and coexisting anions. The adsorption isotherms, thermodynamics, kinetics, regeneration of material, and postregeneration performance were also investigated. A more effective and promising defluorination adsorbent was produced, and the results shed light on the adsorption mechanisms of various adsorbents for defluorination.

2. Materials and Methods

2.1. Materials. Aluminum nitrate nonahydrate ($Al(NO_3)_3{\cdot}9H_2O$) and 1,3,5-benzentricarboxylate (1,3,5-BTC or H_3BTC) were provided by Sinopharm Chemical Reagent Co., Ltd. (Shanghai, China). Sodium fluoride was provided by Tianjin Kaitong Chemical Reagent Co., Ltd. (Tianjin, China). Alizarin complexone (fluoride reagent, molecular formula: $C_{19}H_{15}NO_8$) was provided by Tianjin Komiou Chemical Reagent Co., Ltd. (Tianjin, China). All of the chemical reagents used were of analytical grade and used as received without further purification.

2.2. Fabrication of MIL-96(Al). Synthesis of MIL-96(Al) was achieved by the reaction of Al^{3+} and a ligand at high temperature. $Al(NO_3)_3{\cdot}9H_2O$ (2.628 g) and 1,3,5-BTC (0.21 g) were added to pure water (10 mL) and stirred until the solid was completely dissolved. This solution was added to a 50 mL reactor with a polytetrafluoroethylene liner. The mixture was hydrothermally reacted for 24 hours in a blast drying oven at 483 K, and the resulting MIL-96(Al) product was washed three times with pure water and dried in an oven at 333 K [35].

2.3. Characterization. The microstructure of the sample was observed using an S-4800 field-emission scanning electron microscope (FE-SEM). Transmission electron microscopy (TEM) imaging analysis was performed using a Tecnai 12 instrument. X-ray diffraction (XRD) was performed using a Bruker D8 Advance diffractometer to investigate the crystal structure of the sample. The surface properties and valence states of the samples were determined using an ESCALAB 250Xi X-ray photoelectron spectrometer. The Autosorb-i Q3 specific surface area and pore size analyzer and the ZRY-2P thermogravimetric analyzer were used to determine the specific surface area (BET) and produce thermal analysis (TG) data, respectively. Infrared (IR) testing of samples was performed on a VERTEX 70.

2.4. Fluoride Adsorption Experiment. To explore the adsorption performance of the sample in defluorination, a series of

experiments were carried out. In these experiments, the fluoride-containing wastewater we used was prepared using sodium fluoride and pure water. The solution was filtered using a 0.45 μm membrane syringe filter before measuring the fluoride concentration in the water and determined by spectrophotometry with an Alizarin complexone, and the absorbance value was measured using an ultraviolet-visible spectrophotometer (UV755B, Precision Scientific Instrument, Shanghai) at a wavelength of 620 nm. Finally, the fluoride concentration in the solution was obtained according to the standard curve of fluoride. To investigate the effect of the dosage of MIL-96(Al) in defluoridation, different quality MIL-96(Al) was added to F^- solution with a concentration of 10 mg L^{-1}, respectively. The solution was placed in a constant temperature shaker shaking at 298 K at 150 rpm for 2.5 hours and then filtered to determine the absorbance value to calculate the removal rate.

The initial concentration of fluoride in the water had a different effect on the adsorption of MIL-96(Al). Therefore, 0.5 g L^{-1} adsorbent was added to the F^- solution with a concentration of 5 to 50 mg L^{-1}, shaking at 298 K at 150 rpm for 2.5 hours. The pH may also have effects on the adsorption of the adsorbent, so 0.5 g L^{-1} of MIL-96(Al) was added to the F^- solution with a concentration of 10 mg L^{-1}. The pH of the solution was adjusted to 3-11 by HCl and NaOH. At the same time, another set of experiments was carried out, and the common anions of Cl^-, SO_4^{2-}, NO_3^-, and CO_3^{2-} were quantitatively added to the F^- solution with a concentration of 10 mg L^{-1} with different concentrations of anions, and 0.5 g L^{-1} of MIL-96 (Al) was added. The three sets of experiments were shaken at 298 K at 150 rpm for 2.5 hours and then filtered to determine the absorbance value to investigate the effect.

The measurement of the adsorption isotherm of the fluoride was carried out in a 250 mL Erlenmeyer flask. 0.5 g L^{-1} of MIL-96 (Al) was added to the F^- solution with a concentration range of 5 to 150 mg L^{-1} solutions separately. The solutions were shaken at 150 rpm for 2.5 hours at 298 K, 303 K, and 308 K, respectively. The Freundlich and Langmuir isothermal models are two widely used adsorption isotherm models [36, 37]. The D-R isotherm model is proposed by Dubinin and Radushkevich, which is also often used to study whether the adsorption process is physical or chemical adsorption. Therefore, these three models were used to analyze the adsorption process [38].

$$\text{Freundlich model}: \lg q_e = \lg K + \frac{1}{n} \lg c_e, \quad (1)$$

$$\text{Langmuir model}: \frac{c_e}{q_e} = \frac{1}{q^0 b} + \frac{c_e}{q^0}, \quad (2)$$

$$\text{D} - \text{R model}: \ln q_e = \ln q^0 - \beta\varepsilon^2, \quad (3)$$

$$\varepsilon = RT \ln\left(1 + \frac{1}{c_e}\right), \quad (4)$$

$$E = \frac{1}{\sqrt{(2\beta)}}, \quad (5)$$

where c_e (mg L^{-1}) is the concentration of fluoride remaining in the solution when the adsorption equilibrium is reached, q_e (mg g^{-1}) is the equilibrium adsorption amount, q^0 (mg g^{-1}) is the single-layer saturated adsorption amount, and K, n, and b are constants.

In the study of the adsorption kinetics of MIL-96 (Al), 0.5 g L^{-1} of the adsorbent was added to the F^- solution with a concentration of 20 mg L^{-1}, and the solution was shaken at 298 K and 308 K at 150 rpm for 2.5 hours. The kinetic data in this process was fitted using pseudo first-order, pseudo second-order, and Elovich models.

$$\text{Pseudo first} - \text{order equation}: \frac{dq_t}{dt} = k1(q_e - q_t), \quad (6)$$

$$\text{After calculus}: \ln(q_e - q_t) = \ln q_e - k1t, \quad (7)$$

$$\text{Pseudo second} - \text{order equation}: \frac{dq_t}{dt} = k2(q_e - q_t)^2, \quad (8)$$

$$\text{After calculus}: \frac{t}{q_t} = \frac{1}{k2{q_e}^2} + \frac{t}{q_e}, \quad (9)$$

$$\text{Elovich models}: q_t = \alpha + k_e \ln t, \quad (10)$$

where q_t (mg g^{-1}) is the amount of fluoride adsorbed at time t, q_e (mg g^{-1}) is the amount of adsorption at equilibrium, k_1 (min^{-1}) and k_2 (g mg^{-1} min^{-1}) are the rate constants, and $k_2{q_e}^2$ represents the initial adsorption rate. Both k_e and α are Elovich constants [37].

The thermal selection parameters of the adsorption process can be calculated by the following formula.

$$\Delta G^0 = \Delta H^0 - T\Delta S^0, \quad (11)$$

$$\Delta G^0 = -RT\text{In}K_c, \quad (12)$$

where K_c is the equilibrium constant at a certain temperature, $K_c = q_e/c_e$, indicating the affinity of adsorption. So the above formula can be combined to get

$$\ln\frac{q_e}{c_e} = -\frac{-\Delta H^0}{RT} + \frac{\Delta S^0}{R}. \quad (13)$$

ΔG^0, ΔH^0, and ΔS^0 represent the free energy, free enthalpy change, and free entropy change, respectively, and can be plotted by $\ln(q_e {c_e}^{-1})$ versus $1/T$, and then, the Gibbs free energy change ΔG^0 is obtained according to the obtained slope and intercept [39].

2.5. Regeneration of MIL-96(Al). Regeneration of the adsorbent can greatly reduce costs. Therefore, the heating desorption regeneration method and solvent method were applied for regeneration [40]. The adsorbent used was separated by a centrifuge and then placed in an oven. The heating desorption regeneration method involved heating the spent adsorbent at different temperatures for 12 hours. The solvent method involved soaking the spent adsorbent with NaOH solution, HCl solution, H_2SO_4 solution, and HNO_3 solution

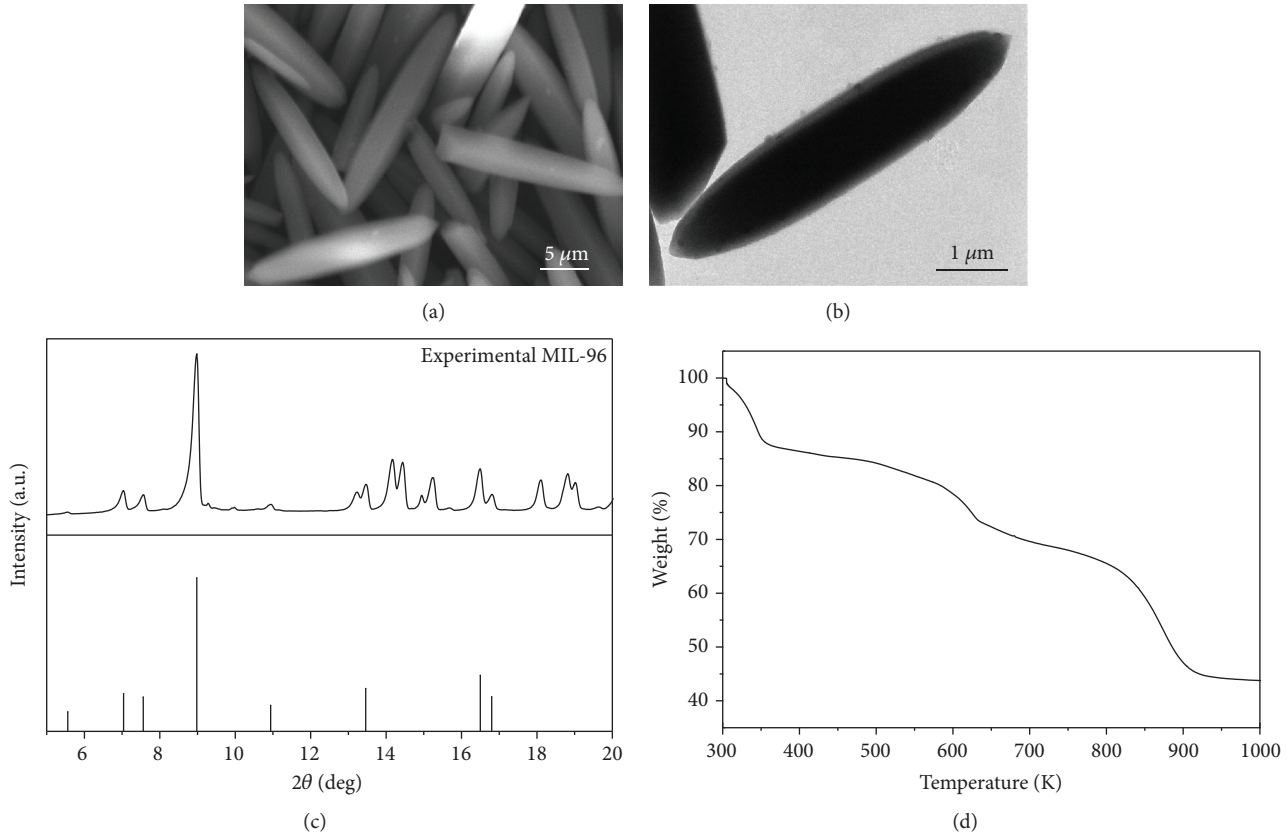

Figure 1: The SEM image of MIL-96(Al) (a), the TEM image of MIL-96(Al) (b), the XRD patterns of MIL-96(Al) (c), and the loss of TG for MIL-96(Al) (d).

for 12 hours. The adsorbent was then collected and washed by centrifugation.

3. Results and Discussion

3.1. Characterization of a Rice Granular Defluorination Adsorbent. To obtain a high-performance defluorination adsorbent, the prepared material was analyzed to verify that the material was MIL-96(Al). The material should have similar characteristics to rice: smooth, uniform in size, and highly crystalline [35]. The SEM image of the prepared MIL-96(Al) (Figure 1(a)) shows that the prepared material had good dispersibility, a similar morphology to rice grains with a uniform size, a regular shape and smooth surface, and a length of 4–6 μm and width of 1–2 μm. Figure 1(b) is the TEM image of the material, which shows that the sample was a solid structure, similar to the SEM image, and was used to preliminarily determine that the prepared material was MIL-96(Al).

Figure 1(c) shows the XRD pattern of the material; the peak intensity was high, indicating high crystallinity; this is supported by the SEM image of the material. The material was indexed to the structure of the MIL-96 ($Al_{12}O(OH)_{18}(H_2O)_3(Al_2(OH)_4)(BTC)_6{\cdot}24H_2O$) [35]. In previous studies, MIL-96(Al) was successfully prepared by the solvothermal method and the peak value of the XRD pattern corresponds well to the value in this study, indicating that the crystal form was well prepared. Figure 1(d) presents the TG curve of MIL-96(Al) under N_2. As the temperature was initially increased and the boiling point of 1,3,5-benzenetricarboxylic acid is about 583 K, the mass loss (~15%) below 373 K was mainly attributed to the evaporation of free water and the loss (~5%) between 373 and 583 K was the precipitation of bound water. As the temperature reached the boiling point of 1,3,5-benzenetricarboxylic acid, the organic skeleton of the material began to decompose; during this process, mass loss was not obvious. However, when the temperature reached 823 K, the structure collapsed, as seen in the image. This indicated that the material was relatively stable at the typical temperatures used to treat wastewater. The BET surface area was about 220 m^2 g^{-1} [33, 35].

X-ray photoelectron spectroscopy (XPS) was employed to investigate the valence state of different elements in MIL-96(Al). It determined that the prepared material contained the four elements Al, N, C, and O (Figure 2(a)). Figure 2(b) shows that Al 2p peaks appeared at 74.75–74.85 eV, indicating that the Al present was trivalent and was Al oxide, matching the binding energy of Al^{+3} well [41]. The peak of O 1s in the metal oxide is between 528 and 531 eV, which is the O in Al oxide (Figure 2(c)) [34]. It can also clearly see both the aliphatic carbon (at ca. 285 eV) and the two kinds of strongly oxidized carbon at the higher binding energies up to ca. 289 eV (Figure 2(d)). There are three different kinds of

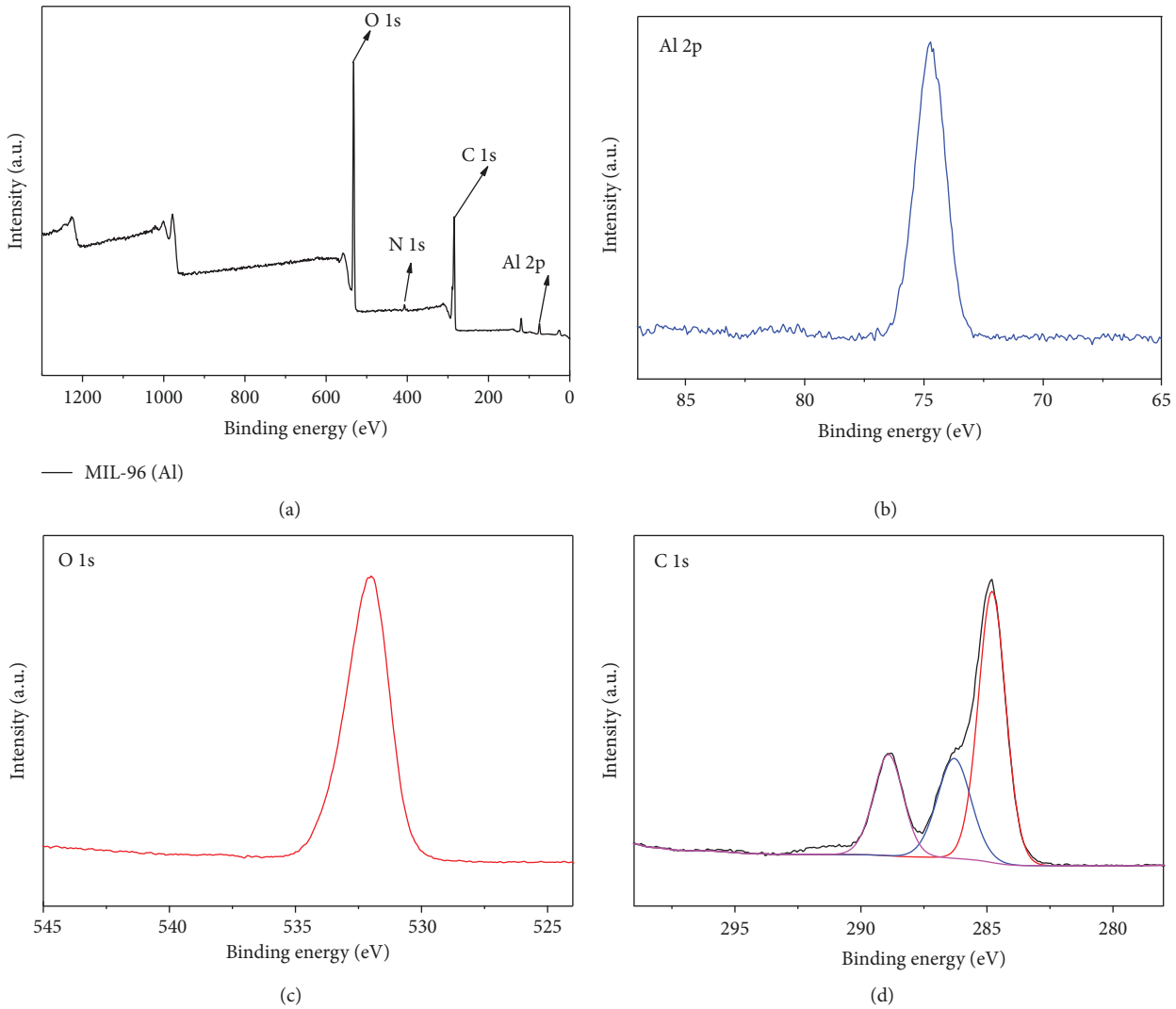

Figure 2: The XPS spectra of MIL-96(Al) (a), Al 2p (b), O 1s (c), and C 1s (d) for MIL-96(Al).

carbon in MIL-96(Al): (a) the carbon in the phenyl ring, (b) COO carboxylate groups connected to aluminum cations, and (c) likely carbon of COOH groups. The last probably constitutes an impurity in MIL-96(Al) due to the BTC precursor.

3.2. Experimental Study on MIL-96(Al) Fluoride Adsorption. The equilibration time for maximum adsorption of fluoride and the effect of dosage and initial concentration on the defluoridation were determined. The removal efficiency was relatively high during the first 50 minutes, and the removal ended after approximately 90 minutes (Figure 3(a)). It is possible that there were more adsorption sites and fluorion on the surface when the adsorbent was added, and the adsorption rate rose rapidly. When the dosage of the adsorbent remains unchanged, the higher concentration will promote the competitive combination of fluorion and the adsorption site, and the adsorption saturation will be reached more quickly. Furthermore, this phenomenon indicated that the surface of MIL-96(Al) is heterogeneous and rich in activated binding sites [42]. And in Figure 3(b), it can be seen that the dosage of the adsorbent 0.5 g L^{-1} was suitable for the treatment of 10 mg L^{-1} of fluoride solution.

Figure 4(a) shows the system under different pH conditions. Under acidic conditions, the removal rate reaches 100% because in the acidic environment, some F^- will react with H^+ in water. The formation of HF, in the form of molecules in water, coupled with the action of the adsorbent, can achieve a 100% removal rate. Interestingly, under alkaline conditions, the removal rate also increased. It is possible that the hydroxide in the solution combines with the Al ions, bridging the organic skeleton of the material causing flocculation, which then causes the fluorion in the water to separate from the liquid phase, resulting in a significant increase in the removal rate [43]. Similarly, blank experiments adjusting the pH were carried out. Under acidic conditions, the concentration of fluoride in the solution was significantly reduced, while the concentration did not change significantly under alkaline conditions. However, during the treatment of wastewater with a strong acid and alkali, the acid and alkali were generally recovered first; the pH is controlled and then treated, so the adsorbent is not affected. The effect of

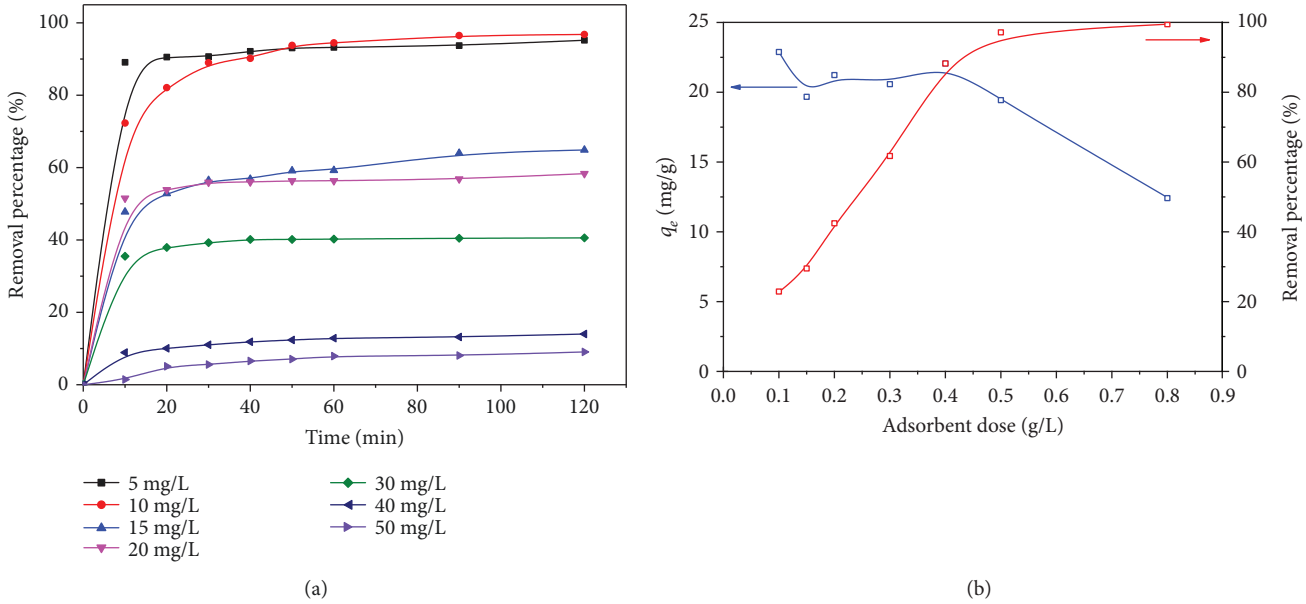

Figure 3: The effect of concentration on removal percentage when the dosage of MIL-96(Al) is 0.5 g/L at about 298 K (a) and the effect of adsorbent dosage on the adsorption capacity and removal percentage of MIL-96(Al) to fluoride when the concentration is 10 mg/L (b).

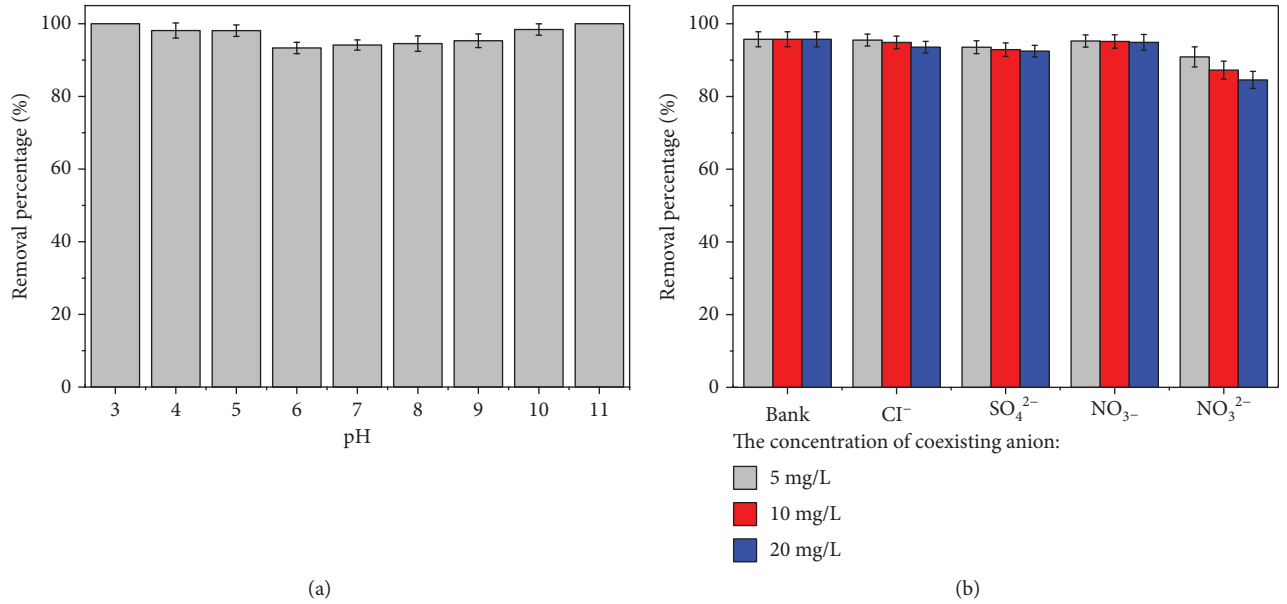

Figure 4: The effect of pH on removal percentage (a) and the effect of anions on the removal rate (b) (the dosage of MIL-96(Al): 0.5 g L^{-1}, the concentration of fluoride: 10 mg L^{-1}).

coexisting anions on the removal rate can be seen in Figure 4(b). CO_3^{2-} interfered with fluoride adsorption through the competition of fluoride active adsorption sites on MIL-96(Al), and high concentration of CO_3^{2-} led to a decrease in fluoride adsorption efficiency, but the actual impact was not very big. Other common coexisting anions only had very small effect on the fluoride removal of the adsorbent, indicating that MIL-96(Al) had higher selectivity for removing fluoride and stronger anti-interference ability.

3.3. Isothermal Adsorption Model of MIL-96(Al). The variation in the equilibrium adsorption amount with the equilibrium concentration is described by the adsorption isotherm. The adsorption isotherms shed light on the interaction between the adsorbate and adsorbent and were therefore determined for this system (Table 1 and Figure 5) and could be judged from the line type as the Langmuir isotherm. As the initial concentration increases, so too does the amount of adsorption; also, an increase in temperature increases the adsorption capacity of the adsorbent.

Table 1: The data of isotherm at different temperatures.

C_0 (mg L^{-1})	298 K		303 K		308 K	
	C_e (mg L^{-1})	q_e (mg g^{-1})	C_e (mg L^{-1})	q_e (mg g^{-1})	C_e (mg L^{-1})	q_e (mg g^{-1})
5.00	0.00	10.00	0.00	10.00	0.00	10.00
10.00	0.33	19.35	0.32	19.36	0.00	20.00
15.00	4.77	20.47	3.34	23.32	1.62	26.76
20.00	8.38	23.24	7.84	24.32	4.97	30.06
30.00	16.82	26.36	16.25	27.50	14.59	30.82
40.00	25.90	28.20	25.25	29.50	22.92	34.15
50.00	35.45	29.10	33.38	33.23	31.37	37.27
60.00	43.79	32.42	43.06	33.87	40.88	38.24
80.00	62.29	35.42	61.57	36.86	59.57	40.86
100.00	81.35	37.30	79.86	40.28	79.09	41.83
120.00	99.85	40.30	98.75	43.15	98.66	44.68
150.00	129.75	40.50	128.36	43.28	127.58	44.83

C_0 (mg L^{-1}) is the initial concentration of fluoride in the solution, C_e (mg L^{-1}) is the concentration of fluoride remaining in the solution, and q_e (mg g^{-1}) is the equilibrium adsorption amount.

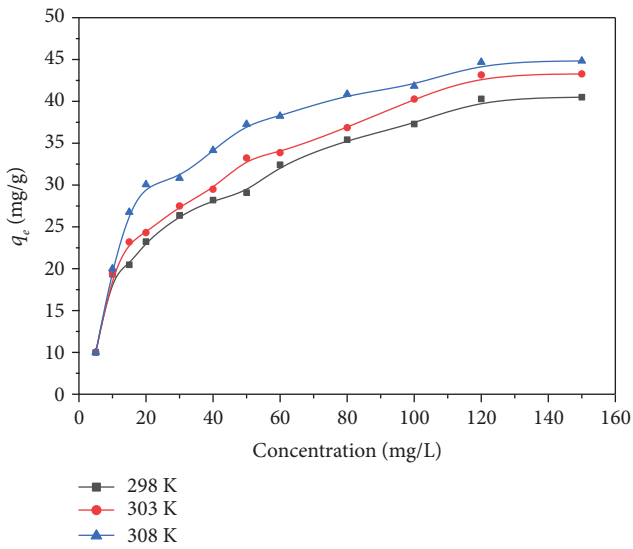

Figure 5: The adsorption isotherms of F under different reaction temperatures.

The adsorption process was analyzed by three adsorption isotherm models, Freundlich, Langmuir, and D-R models, in detail. Tables 2 and 3 present the fitting results of the Freundlich and Langmuir models. The correlation coefficient R^2 of the Langmuir model was greater than that of the Freundlich model, demonstrating that the adsorption of fluoride by MIL-96(Al) was more consistent with the Langmuir model and suggesting monolayer adsorption. At the same time, according to the shape of the adsorption isotherm, it can be judged as the Langmuir model. Although the Freundlich model is poorly correlated, the value of $1/n$ is also between 0.1 and 0.5, indicating that the adsorption process is also prone to occur. Furthermore, the value of $1/n$ decreased with increasing temperature, which indicated that higher temperature assisted the adsorption process. The theoretical maximum value for fluoride adsorption was 42.194 mg g^{-1} at 298 K. In the Langmuir model, q^0 and b are characteristic parameters of adsorption performance. The larger q^0 is, the larger the adsorption capacity is under the same conditions, and the larger b is, the faster the adsorption rate is. With the increase in temperature, q^0 and b were also increased. The adsorption capacity and adsorption rate of MIL-96(Al) increased. R_L also is an important dimensionless constant separation factor in the Langmuir model, and it indicates the shape of the isotherm accordingly and can be expressed by the following formula: $R_L = 1/(1 + b \times c_0)$, where b is a constant and c_0 is the initial concentration of fluoride. When $0 < R_L < 1$, adsorption readily proceeds, whereas when $R_L = 0$, adsorption is an irreversible process. When $R_L = 1$, the isotherm is linear and adsorption is reversible, and when $R_L > 1$, the adsorption process is difficult to verify [44]. The R_L values under different concentration conditions were between 0 and 1, indicating that the adsorption process was relatively easy. The D-R isothermal model does not assume a uniform adsorbent surface or a constant adsorption energy. Based on the fitting results of the Freundlich and Langmuir models, it can be determined whether there was physical or chemical adsorption. When $E = 8 - 16$ kJ mol^{-1}, the adsorption process is triggered by ion exchange; when $E < 8$ kJ mol^{-1}, the adsorption process is physical adsorption and physical forces such as van der Waals and hydrogen bonding may affect the adsorption mechanism; and when $E > 16$ kJ mol^{-1}, the adsorption process is chemical adsorption. Table 4 presents the fitting result of the D-R isothermal model. The average adsorption energy was during 8–16 kJ mol^{-1}, showing that the adsorption is mainly caused by ion exchange during the process [38].

3.4. Adsorption Kinetics of MIL-96(Al). Another important indicator of the adsorption capacity of adsorbents on adsorbates is the adsorption rate. Figure 6(a) shows that, initially, the adsorption of fluoride onto MIL-96(Al) increases rapidly,

Table 2: Fitted result by the Freundlich model at different temperatures.

Temperature (K)	Parameter			Linear equation
	K	$\frac{1}{n}$	R^2	$\lg q_e = 1\mathrm{g}K + \left(\frac{1}{n}\right) \lg c_e$
298	14.4644	0.1777	0.9849	$\lg q_e = 0.2134 \lg c_e + 1.1603$
303	16.9785	0.2564	0.9581	$\lg q_e = 0.1906 \lg c_e + 1.2299$
308	24.1434	0.1250	0.9486	$\lg q_e = 0.1250 \lg c_e + 1.3827$

Table 3: Fitted results by the Langmuir model at different temperatures.

Temperature (K)	Parameter			Linear equation
	b	q^0 (mg Fg^{-1})	R^2	$\frac{c_e}{q_e} = \left(\frac{1}{q^0 b}\right) + \left(\frac{c_e}{q^0}\right)$
298	0.1139	42.1941	0.9880	$\frac{c_e}{q_e} = 0.0237c_e + 0.2080$
303	0.1220	44.8430	0.9877	$\frac{c_e}{q_e} = 0.0223c_e + 0.1828$
308	0.1729	46.0829	0.9958	$\frac{c_e}{q_e} = 0.0217c_e + 0.1255$

Table 4: Fitted result by the D-R model at different temperatures.

Temperature (K)	Parameter			Linear equation
	E (kJ mol^{-1})	q^0 (mg Fg^{-1})	R^2	$\ln q_e = \ln q^0 - \beta\varepsilon^2$
298	11.6248	41.4381	0.8704	$\ln q_e = -0.0037\varepsilon^2 + 3.7242$
303	11.7851	44.4916	0.9039	$\ln q_e = -0.0036\varepsilon^2 + 3.7953$
308	11.7851	46.0211	0.9638	$\ln q_e = -0.0036\varepsilon^2 + 3.8291$

with the adsorption amount reaching 80% or more of the equilibrium adsorption amount after 20 minutes. As the oscillation time continued to increase, the adsorption amount increased slowly. When the oscillation time reached 90 min, no significant change in the adsorption amount was observed; therefore, under the experimental conditions, the adsorption equilibrium time of fluoride adsorption onto MIL-96(Al) was determined to be 90 min [45]. It can be seen from the figure that as the temperature increases, both the adsorption rate and the adsorption capacity increase, indicating that the process is an endothermic process.

The dynamic process was fitted using the pseudo first-order equation, pseudo second-order equation, and Elovich model (Figure 6(b)–6(d)). The parameters obtained by fitting the above three kinetic models are shown in Table 5. The fitting results obtained by the three models show a good correlation; however, the relative error of the R^2 of the pseudo first-order kinetics fit was bigger. Therefore, this adsorption process did not follow the pseudo first-order equation. The linear correlation coefficient of the pseudo second-order equation fitting is close to 1 (0.9989), and the relative error of the equilibrium adsorption amount is small, which is better than the fitting result of the pseudo first-order equation. Therefore, the adsorption process was determined to follow the pseudo second-order equation and it is mainly chemical adsorption.

3.5. Adsorption Thermodynamics of MIL-96(Al). Adsorption thermodynamics, which investigates the adsorption capacity with a change in the adsorption temperature, is important for determining the adsorption capacity; thus, it is used in practical applications. From Table 6, ΔH^0 was shown to be a positive number. It is known that the adsorption process for fluoride is endothermic, and it was experimentally verified that an increase in temperature was advantageous for adsorption to the adsorbent surface and the process is endothermic in kinetic studies. ΔS^0 was also shown to be a positive number, meaning that the irregular interlayer adsorption of the solid-liquid system interface is enhanced during the adsorption of fluoride and the disorder of the adsorbate-adsorbent system is increased. $\Delta S^0 > 0$ indicates that the adsorption reaction is an entropy-driven process. For solid-liquid exchange adsorption, the exchange of solute molecules from the liquid phase to the solid-liquid interface loses some of the free energy, resulting in a decrease in entropy. Therefore, the adsorption of fluoride ions onto the surface of the adsorbent should also be a process of entropy reduction, but the result of this experiment is that the entropy is less

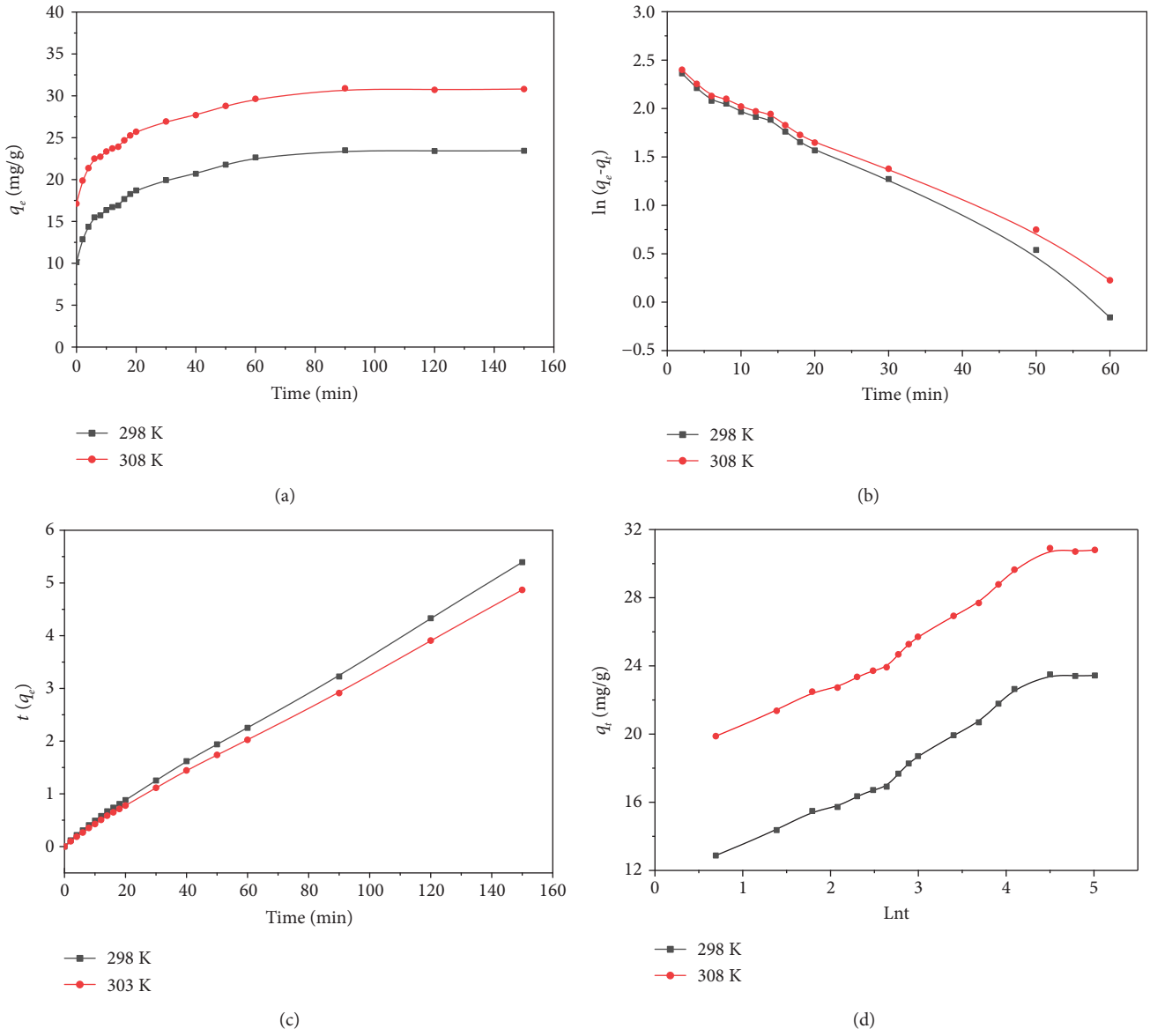

Figure 6: (a) Adsorption rate curves of fluoride. (b) Fitted result by the pseudo first-order equation. (c) Fitted result by the pseudo second-order equation in the second-order kinetic model. (d) Fitted result by the Elovich model.

than 0, so that in the adsorption process, other substances must be released to increase the entropy value. The release of matter causes the increase in entropy to cancel out the decrease in entropy caused by fluoride ion adsorption, causing the final smoke of the system to become positive. It is also possible to introduce that the adsorption process is an ion exchange process. ΔG^0 was shown to be smaller than zero, meaning that the reaction process was spontaneous; however, it is not in the standard state for practical applications and physical adsorption also existed in the case of chemical adsorption. Increasing the temperature lowers ΔG^0, indicating that the spontaneity of the adsorption process was proportional to the temperature [44].

3.6. Regeneration of MIL-96(Al). The experimental study found that traditional regeneration, such as of hydrochloric acid, sodium hydroxide, and ethanol, did not achieve the desired effect on material regeneration and a higher concentration of NaOH had a better regeneration effect. In this study, 0.1 mol L^{-1} and 0.2 mol L^{-1} NaOH solution were used as the analytical solution to soak the saturated adsorbent for 12 h and yielded promising results. The removal performance of MIL-96(Al) in seven cycles was shown in Figure 7. It can be seen that as the number of regenerations increased, the volume followed a downward trend. After being used seven times, the fluoride removal rate dropped to ~61.8% and the removal effect decreased by ~40%, as OH^- in the solution exchanged with F^- on the adsorbent, transferring the fluorion into the analytical solution. An increase in the concentration of the solution could also contribute to the rate of exchange. However, the analytical solution is strongly alkaline and the Al on the adsorbent will

Table 5: Fitted results by different kinetic models.

Dynamic mode	Parameter				
	K	k_1	q_e (mg g^{-1})	R^2	Kinetic equation
Pseudo first-order equation	298	0.0400	10.9539	0.9895	$\ln(q_e - q_t) = -0.0400t + 2.3937$
	308	0.0349	10.9135	0.9931	$\ln(q_e - q_t) = -0.0349t + 2.3900$
	K	k_2	q_e (mg g^{-1})	R^2	Kinetic equation
Pseudo second-order equation	298	0.00942	28.4091	0.9986	$\frac{t}{qt} = 0.0352t + 0.1315$
	308	0.00971	31.4465	0.9989	$\frac{t}{qt} = 0.0318t + 0.1041$
	K	k_e	α	R^2	Kinetic equation
Elovich model	298	2.7764	10.3370	0.9776	$q_t = 2.7764 \ln t + 10.3370$
	308	2.8554	17.1600	0.9789	$q_t = 2.8554 \ln t + 17.1600$

Table 6: The thermodynamic parameters for the adsorption.

Parameter					
C_0 (mg g^{-1})	ΔH^0 (kJ mol^{-1})	ΔS^0 (J mol^{-1} K^{-1})	ΔG^0 (kJ mol^{-1})		
			298 K	303 K	308 K
20	59.263	206.578	-2.297	-3.330	-4.363
30	22.718	79.770	-1.053	-1.451	-1.850
40	23.861	80.537	-0.139	-0.542	-0.944

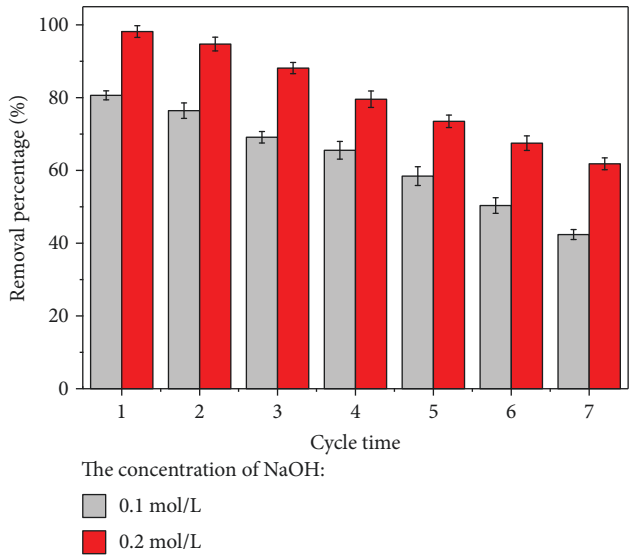

Figure 7: Seven consecutive adsorption cycles of MIL-96(Al) (the dosage of MIL-96(Al): 0.5 g L^{-1}, the concentration of fluoride and coexisting anion: 10 mg L^{-1}).

undergo a redox reaction with NaOH; therefore, after regeneration, the performance of the adsorbent dropped but was still far better than that of the commercially available activated alumina [45]. The material has a larger specific surface area, higher adsorption capacity, and a convenient synthesis method compared to many other adsorbents (Table 7). At present, there are some adsorbents with outstanding performance. The preparation of AlFu MOF is more complicated [31], but its excellent performance will become the target of our future research. MIL-96(Al) also has good adsorption performance after regeneration and has shown good potential as a novel fluoride removal adsorbent.

3.7. Adsorption Mechanism. The IR spectrum of MIL-96(Al) before and after adsorption of fluoride is shown in Figure 8(a). This provides insight into the adsorption mechanism of fluoride onto this material. The vibrational band at 1,400–1,600 cm^{-1} was assigned to the carboxyl functional group before the adsorption of fluoride. For the bound C-O group, ν_{asym} and ν_{sym} were between 1,459 and 1,399 cm^{-1} and the strong absorption bands were at 1,596 and 1,671 cm^{-1}, indicating that the BTC species was a coordinated Al atom [35]. There was fluctuation between 1,200 and 1,350 cm^{-1}, and the corresponding peak in the stretching model of Al-OH appears at 1,330 cm^{-1}. However, this peak disappeared after adsorption and another distinct characteristic peak appeared at 1,123 cm^{-1}; this was attributed to the formation of Al-F bonds, showing that the absorption of fluoride by this material was mainly dependent on the exchange of -OH bonded to Al in the structure of the material [51]. Figure 8(b) shows the possible adsorption process of MIL-96(Al) for fluoride removal. The F^- in water substituted -OH on the adsorbent and combined with the Al atom to achieve the purpose of defluorination, which was a method by means of metal sites in MOFs to remove fluoride. Similarly, after adsorption, the adsorbent can be regenerated by replacing the F^- using -OH supplied by high-concentration NaOH solution.

Table 7: Comparison of different adsorbents in literatures.

Adsorbents	MgOC	Activated alumina	MCLRB	MOCA	COCA	MIL-96(Al)
Adsorption capacity ($mg\,Fg^{-1}$)	4.44	2.07	22.35	2.85	7.77	42.19
Synthetic method	Calcination	Calcination	Inverse suspension	Calcination	Calcination	Hydrothermal
BET ($m^2\,g^{-1}$)	45.5	185.6	21.24	170.4	189.3	220.0
Cycle times	N.R.	N.R.	7	N.R.	N.R.	7
Refs.	[46]	[47]	[48]	[49]	[50]	This work

N.R.: nonreported; MgOC: magnesia/chitosan composite; MCLRB: mixed-rare earth magnetic chitosan beads; MOCA: manganese-oxide-coated alumina; COCA: copper oxide-coated alumina.

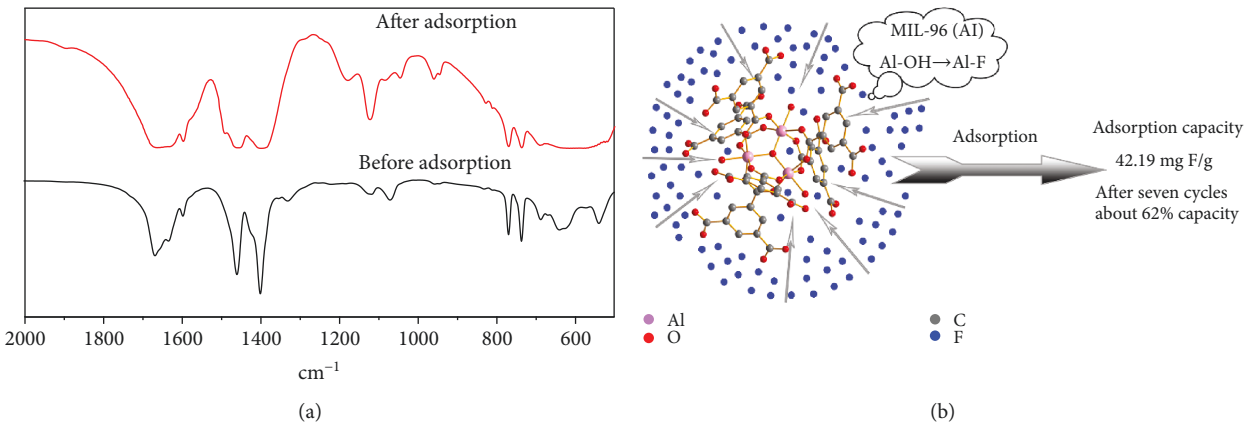

Figure 8: The IR spectra of MIL-96(Al) before and after adsorption of fluoride (a) and the adsorption process of MIL-96(Al) (b).

4. Conclusions

The rice-like MIL-96(Al) was fabricated successfully by hydrothermal reaction and showed better fluoride removal performance than many other adsorbents. The adsorption isotherm of MIL-96(Al) matched with the Langmuir model, and the theoretical fluoride adsorption capacity was up to $42.19\,mg\,g^{-1}$ at 298 K. The process was shown to be monolayer adsorption; the adsorption kinetics and thermodynamics followed pseudo second-order kinetics, typical of an endothermic chemisorption process. The initial concentration affected the defluorination efficiency, but this can be adjusted by controlling the dosage. The pH of the initial solution had a small effect on the removal of fluoride by MIL-96(Al) and was stable in the pH range of 6–9. Various common anions in water influenced the removal slightly, indicating that MIL-96(Al) has good selectivity for defluorination. Regeneration of the adsorbent can reduce the application cost significantly. OH^- within the NaOH solution can exchange the F^- on the adsorbent; thus, a $0.2\,mol\,L^{-1}$ NaOH solution was used to regenerate the MIL-96(Al) well, which showed good adsorption properties even after seven cycles. Testing indicated that MIL-96(Al) has great potential for defluorination of drinking water and industrial wastewater.

Data Availability

The data used to support the findings of this study are included within the article.

Conflicts of Interest

The authors declare that they have no conflicts of interest.

Acknowledgments

This study was funded by the Social Development Project of Zhenjiang (No. 2016014), the Qing Lan Project for Young Core Teachers in University of Jiangsu Province, the China Postdoctoral Science Foundation (No. 2019M652274), the Foundation from Marine Equipment and Technology Institute for Jiangsu University of Science and Technology, China (HZ20190004), and the Natural Science Foundation of China (Nos. 51908252, 41601304). In addition, the English in this document has been checked by a company that provides professional English language editing services.

References

[1] J. Cai, X. Zhao, Y. Zhang, Q. Zhang, and B. Pan, "Enhanced fluoride removal by La-doped Li/Al layered double hydroxides," *Journal of Colloid and Interface Science*, vol. 509, pp. 353–359, 2018.

[2] M. K. So, Y. Miyake, W. Y. Yeung et al., "Perfluorinated compounds in the Pearl River and Yangtze River of China," *Chemosphere*, vol. 68, no. 11, pp. 2085–2095, 2007.

[3] H. Wu, H. Zhang, Q. Yang, D. Wang, W. Zhang, and X. Yang, "Calcined chitosan-supported layered double hydroxides: an efficient and recyclable adsorbent for the removal of fluoride from an aqueous solution," *Materials*, vol. 10, no. 11, article 1320, 2017.

[4] I. N. Dias, J. P. Bassin, M. Dezotti, and V. J. P. Vilar, "Fluorene oxidation by solar-driven photo-Fenton process: toward mild pH conditions," *Environmental Science and Pollution Research*, vol. 25, no. 28, pp. 27808–27818, 2018.

[5] A. Bhatnagar, E. Kumar, and M. Sillanpaa, "Fluoride removal from water by adsorption—a review," *Chemical Engineering Journal*, vol. 171, no. 3, pp. 811–840, 2011.

[6] C. Prathibha, B. Sharma, L. A. A. Chunduri, S. K. Aditha, T. (. M.). Rattan, and K. Venkataramaniah, "Nano calcium aluminum mixed oxide: a novel and effective material for defluoridation of drinking water," *Separation Science and Technology*, vol. 50, no. 13, pp. 1915–1924, 2015.

[7] H. G. Gorchev and G. Ozolins, "WHO guidelines for drinking-water quality," *WHO Chronicle*, vol. 38, no. 3, pp. 104–108, 1984.

[8] Z. Ruan, Y. Tian, J. Ruan et al., "Synthesis of hydroxyapatite/-multi-walled carbon nanotubes for the removal of fluoride ions from solution," *Applied Surface Science*, vol. 412, pp. 578–590, 2017.

[9] M. Mohapatra, S. Anand, B. K. Mishra, D. E. Giles, and P. Singh, "Review of fluoride removal from drinking water," *Journal of Environmental Management*, vol. 91, no. 1, pp. 67–77, 2009.

[10] S. Ayoob, A. K. Gupta, and V. T. Bhat, "A conceptual overview on sustainable technologies for the defluoridation of drinking water," *Critical Reviews in Environmental Science and Technology*, vol. 38, no. 6, pp. 401–470, 2008.

[11] M. K. Adak, A. Sen, A. Mukherjee, S. Sen, and D. Dhak, "Removal of fluoride from drinking water using highly efficient nano-adsorbent, Al(III)-Fe(III)-La(III) trimetallic oxide prepared by chemical route," *Journal of Alloys and Compounds*, vol. 719, pp. 460–469, 2017.

[12] W. X. Gong, J. Qu, R. P. Liu, and H. C. Lan, "Fluoride removal from water by adsorption—a review," *Chemical Engineering Journal*, vol. 189, pp. 126–133, 2012.

[13] Y. Ku and H. M. Chiou, "The adsorption of fluoride ion from aqueous solution by activated alumina," *Water, Air, and Soil Pollution*, vol. 133, no. 1/4, pp. 349–361, 2002.

[14] E. Tchomgui-Kamga, V. Alonzo, C. P. Nanseu-Njiki, N. Audebrand, E. Ngameni, and A. Darchen, "Preparation and characterization of charcoals that contain dispersed aluminum oxide as adsorbents for removal of fluoride from drinking water," *Carbon*, vol. 48, no. 2, pp. 333–343, 2010.

[15] B. Grzmil and J. Wronkowski, "Removal of phosphates and fluorides from industrial wastewater," *Desalination*, vol. 189, no. 1-3, pp. 261–268, 2006.

[16] A. Dhillon, M. Nair, S. K. Bhargava, and D. Kumar, "Excellent fluoride decontamination and antibacterial efficacy of Fe–Ca–Zr hybrid metal oxide nanomaterial," *Journal of Colloid and Interface Science*, vol. 457, pp. 289–297, 2015.

[17] F. Venditti, F. Cuomo, G. Giansalvo, M. Giustini, G. Cinelli, and F. Lopez, "Fluorides decontamination by means of aluminum polychloride based commercial coagulant," *Journal of Water Process Engineering*, vol. 26, pp. 182–186, 2018.

[18] M. Pontié, C. Diawara, A. Lhassani et al., "Chapter 2 Water defluoridation processes: a review. Application: nanofiltration (NF) for future large-scale pilot plants," *Advances in Fluorine Science*, vol. 2, pp. 49–80, 2006.

[19] H. Jin, Z. Ji, J. Yuan et al., "Research on removal of fluoride in aqueous solution by alumina-modified expanded graphite composite," *Journal of Alloys and Compounds*, vol. 620, pp. 361–367, 2015.

[20] N. Chen, C. Feng, and M. Li, "Fluoride removal on Fe–Al-impregnated granular ceramic adsorbent from aqueous solution," *Clean Technologies and Environmental Policy*, vol. 16, no. 3, pp. 609–617, 2014.

[21] K. Uma, G. T. Pan, and T. C. K. Yang, "The preparation of porous sol-gel silica with metal organic framework MIL-101(Cr) by microwave-assisted hydrothermal method for adsorption chillers," *Materials*, vol. 10, no. 6, p. 610, 2017.

[22] M. Eddaoudi, J. Kim, N. Rosi et al., "Systematic design of pore size and functionality in isoreticular MOFs and their application in methane storage," *Science*, vol. 295, no. 5554, pp. 469–472, 2002.

[23] H. Furukawa, K. E. Cordova, M. O'Keeffe, and O. M. Yaghi, "The chemistry and applications of metal-organic frameworks," *Science*, vol. 341, no. 6149, p. 974, 2013.

[24] F. Wang, W. Liu, S. J. Teat et al., "Chromophore-immobilized luminescent metal-organic frameworks as potential lighting phosphors and chemical sensors," *Chemical Communications*, vol. 52, no. 67, pp. 10249–10252, 2016.

[25] E. Haque, J. W. Jun, and S. H. Jhung, "Adsorptive removal of methyl orange and methylene blue from aqueous solution with a metal-organic framework material, iron terephthalate (MOF-235)," *Journal of Hazardous Materials*, vol. 185, no. 1, pp. 507–511, 2011.

[26] E. Adatoz and S. Keskin, "Application of MD simulations to predict membrane properties of MOFs," *Journal of NanoMaterials*, vol. 2015, Article ID 136867, 9 pages, 2015.

[27] S. Wang, C. M. McGuirk, A. d'Aquino, J. A. Mason, and C. A. Mirkin, "Metal-organic framework nanoparticles," *Advanced Materials*, vol. 30, no. 37, article 1800202, 2018.

[28] Z. Sumer and S. Keskin, "Computational screening of MOF-based mixed matrix membranes for CO_2/N_2 separations," *Journal of NanoMaterials*, vol. 2016, Article ID 6482628, 12 pages, 2016.

[29] M. Lismont, L. Dreesen, and S. Wuttke, "Metal-organic framework nanoparticles in photodynamic therapy: current status and perspectives," *Advanced Functional Materials*, vol. 12, no. 3, pp. 2094–2105, 2018.

[30] T. M. Al-Jadir and F. R. Siperstein, "The influence of the pore size in metal–organic frameworks in adsorption and separation of hydrogen sulphide: a molecular simulation study," *Microporous and Mesoporous Materials*, vol. 271, pp. 160–168, 2018.

[31] S. Karmakar, J. Dechnik, C. Janiak, and S. De, "Aluminium fumarate metal-organic framework: a super adsorbent for fluoride from water," *Journal of Hazardous Materials*, vol. 303, pp. 10–20, 2016.

[32] X. Zhao, D. Liu, H. Huang, W. Zhang, Q. Yang, and C. Zhong, "The stability and defluoridation performance of MOFs in fluoride solutions," *Microporous and Mesoporous Materials*, vol. 185, pp. 72–78, 2014.

[33] Y. Xue, W. Sun, Q. Wang, L. Cao, and J. Yang, "Sparsely loaded Pt/MIL-96(Al) MOFs catalyst with enhanced activity for H2-SCR in a gas diffusion reactor under 80 ˚C," *Chemical Engineering Journal*, vol. 335, pp. 612–620, 2018.

[34] X. Yang, S. Deng, F. Peng, and T. Luo, "A new adsorbent of a Ce ion-implanted metal-organic framework (MIL-96) with high-efficiency Ce utilization for removing fluoride from

water," *Dalton Transactions*, vol. 46, no. 6, pp. 1996–2006, 2017.

[35] T. Loiseau, L. Lecroq, C. Volkringer et al., "MIL-96, a porous aluminum trimesate 3D structure constructed from a hexagonal network of 18-membered rings and μ3-oxo-centered trinuclear units," *Journal of the American Chemical Society*, vol. 128, no. 31, pp. 10223–10230, 2006.

[36] C. Zhang, Y. Li, T. J. Wang, Y. Jiang, and J. Fok, "Synthesis and properties of a high-capacity iron oxide adsorbent for fluoride removal from drinking water," *Applied Surface Science*, vol. 425, pp. 272–281, 2017.

[37] I. Langmuir, "The adsorption of gases on plane surfaces of glass, mica and platinum," *Journal of Chemical Physics*, vol. 40, no. 9, pp. 1361–1403, 1918.

[38] R. A. Anayurt, A. Sari, and M. Tuzen, "Equilibrium, thermodynamic and kinetic studies on biosorption of Pb(II) and Cd(II) from aqueous solution by macrofungus (Lactarius scrobiculatus) biomass," *Chemical Engineering Journal*, vol. 236, pp. 341–347, 2014.

[39] P. N. Dave and L. V. Chopda, "Application of iron oxide nanomaterials for the removal of heavy metals," *Journal of Nanotechnology*, vol. 2014, Article ID 398569, 14 pages, 2014.

[40] D. L. Childers, J. Corman, M. Edwards, and J. J. Elser, "Sustainability challenges of phosphorus and food: solutions from closing the human phosphorus cycle," *Bioscience*, vol. 61, no. 2, pp. 117–124, 2011.

[41] Y. L. Yan, M. A. Helfand, and C. R. Clayton, "Evaluation of the effect of surface roughness on thin film thickness measurements using variable angle XPS," *Applied Surface Science*, vol. 37, no. 4, pp. 395–405, 1989.

[42] Y. Yu, L. Yu, and J. Paul Chen, "Adsorption of fluoride by Fe–Mg–La triple-metal composite: adsorbent preparation, illustration of performance and study of mechanisms," *Chemical Engineering Journal*, vol. 262, pp. 839–846, 2015.

[43] L. Luo, K. Chen, Q. Liu et al., "Zinc(II) and cadmium(II) complexes with 1,3,5-benzenetricarboxylate and imidazole-containing ligands: structural variation via reaction temperature and solvent," *Crystal Growth and Design*, vol. 13, no. 6, pp. 2312–2321, 2013.

[44] E. K. Putra, R. Pranowo, J. Sunarso, N. Indraswati, and S. Ismadji, "Performance of activated carbon and bentonite for adsorption of amoxicillin from wastewater: mechanisms, isotherms and kinetics," *Water Research*, vol. 43, no. 9, pp. 2419–2430, 2009.

[45] N. Kannan and M. M. Sundaram, "Kinetics and mechanism of removal of methylene blue by adsorption on various carbons—a comparative study," *Dyes and Pigments*, vol. 51, no. 1, pp. 25–40, 2001.

[46] C. Sairam Sundaram, N. Viswanathan, and S. Meenakshi, "Defluoridation of water using magnesia/chitosan composite," *Journal of Hazardous Materials*, vol. 163, no. 2-3, pp. 618–624, 2009.

[47] S. H. Dhawane, A. A. Khan, K. Singh, A. Tripathi, R. Hasda, and G. Halder, "Insight into optimization, isotherm, kinetics, and thermodynamics of fluoride adsorption onto activated alumina," *Environmental Progress & Sustainable Energy*, vol. 37, no. 2, pp. 766–776, 2018.

[48] P. Liang, R. An, R. Li, and D. Wang, "Comparison of La^{3+} and mixed rare earths-loaded magnetic chitosan beads for fluoride adsorption," *International Journal of Biological Macromolecules*, vol. 111, pp. 255–263, 2018.

[49] S. M. Maliyekkal, A. K. Sharma, and L. Philip, "Manganese-oxide-coated alumina: a promising sorbent for defluoridation of water," *Water Research*, vol. 40, no. 19, pp. 3497–3506, 2006.

[50] A. Bansiwal, P. Pillewan, R. B. Biniwale, and S. S. Rayalu, "Copper oxide incorporated mesoporous alumina for defluoridation of drinking water," *Microporous and Mesoporous Materials*, vol. 129, no. 1-2, pp. 54–61, 2010.

[51] N. Zhang, X. Yang, X. Yu et al., "Al-1,3,5-benzenetricarboxylic metal–organic frameworks: a promising adsorbent for defluoridation of water with pH insensitivity and low aluminum residual," *Chemical Engineering Journal*, vol. 252, pp. 220–229, 2014.

Hindawi
Journal of Nanomaterials
Volume 2019, Article ID 7425787, 7 pages
https://doi.org/10.1155/2019/7425787

Research Article

Synthesis, Characterization, and In Vitro Drug Delivery of Chitosan-Silica Hybrid Microspheres for Bone Tissue Engineering

Niu Niu,[1] Shu-Hua Teng,[1] Hua-Jian Zhou,[1] and Hai-Sheng Qian[2]

[1]*School of Materials Science and Engineering, China University of Mining and Technology, Xuzhou 221116, China*
[2]*School of Food and Biological Engineering, Hefei University of Technology, Hefei 230009, China*

Correspondence should be addressed to Shu-Hua Teng; shteng425@cumt.edu.cn and Hai-Sheng Qian; shqian@hfut.edu.cn

Received 25 June 2019; Accepted 29 July 2019; Published 14 August 2019

Guest Editor: Fei Ke

Chitosan-silica (CS-SiO_2) hybrid microspheres were prepared through the combined process of sol-gel and emulsification-crosslinking. Their composition, morphology, *in vitro* bioactivity, and drug release behavior were investigated. The results showed that, when 20 wt% SiO_2 was incorporated, the as-prepared CS-SiO_2 hybrid microspheres exhibited a regular spherical shape, a high dispersity, and a uniform microstructure. Their average particle diameter was determined to be about 24.0 μm. The in situ deposited inorganic phase of the hybrid microspheres was identified as amorphous SiO_2, and its actual content was determined by the TG analysis. As compared with the pure chitosan microspheres, the CS-SiO_2 hybrid microspheres displayed a greatly improved *in vitro* bioactivity. Vancomycin hydrochloride (VH) was selected as a model drug. It was demonstrated that the CS-SiO_2 hybrid microspheres presented a good capacity for both loading and sustained release of VH. Moreover, the increase of the SiO_2 content efficiently slowed down the drug release rate of the CS-SiO_2 hybrid microspheres.

1. Introduction

In the past few decades, microspheres have been widely used in the fields of catalysis, adsorption, drug delivery, etc. [1–5]. In particular, when serving as drug carriers, microspheres exhibit good targeting ability to specific organs/tissues and sustained and controlled release behaviors as well as various administration methods (oral, injection, filler, nasal drops, etc.) [6], thus presenting more development potentials in some specific application areas than the other types of drug carriers.

Much effort has been made to investigate the preparation processes, in vitro/in vivo evolution, or clinical performance of different kinds of the microsphere-based drug carriers [7–9]. These carrier materials mainly involve natural polymers (starch, gelatin, chitosan, cellulose, etc.) [7, 10, 11], synthetic polymers (polyvinyl alcohol, polylactic acid, poly(lactic-co-glycolic acid), etc.) [12, 13], and inorganic materials (silica, hydroxyapatite, ferroferric oxide, etc.) [14, 15]. Chitosan is one of the commonly used natural biopolymers with good sphere-forming capability, chemical stability, biocompatibility, and biodegradability [16, 17]. However, when used as a drug carrier for bone tissue engineering, the poor mechanical strength and bioactivity of the chitosan microspheres have greatly limited their clinical applications.

In this paper, silica (SiO_2) xerogel, an important inorganic biomaterial possessing good mechanical properties and bioactivity, was incorporated into the chitosan (CS) microspheres to form the chitosan-silica (CS-SiO_2) hybrid microspheres. The influence of the SiO_2 contents on the composition and morphology of the chitosan microspheres was investigated. Moreover, the feasibility of the CS-SiO_2 hybrid microspheres as a drug carrier for bone tissue engineering was preliminarily evaluated by *in vitro* bioactivity and drug delivery behavior.

2. Experimental Procedure

2.1. Preparation of the CS-SiO_2 Hybrid Microspheres. Chitosan with a medium molecular weight and a degree of deacetylation of 75-85% was purchased from Sigma-Aldrich

(Shanghai, China) and used as received. Vancomycin hydrochloride (VH) was obtained from Shanghai Macklin Biochemical Co. Ltd. (Shanghai, China). All the other chemical reagents used in this study were of analytical pure grade and supplied by Sinopharm Chemical Reagent Co. Ltd. (Shanghai, China).

The CS-SiO_2 hybrid microspheres were prepared in a water-in-oil (W/O) emulsion system, and the water/oil ratio was kept at 10 : 1. Firstly, the CS powder was dissolved in acetic acid to obtain a 2% (*w*/*v*) CS solution. Then, a certain amount of the SiO_2 sol prepared by the hydrolysis of tetramethoxysilane (TMOS) in the presence of HCl was added to the CS solution. Subsequently, the resultant CS-SiO_2 hybrid sol was dropped into soybean oil containing 1% (*w*/*v*) sorbitan monooleate (Span 80) as the surfactant and stirred at 37°C for 0.5 h to generate a stable W/O emulsion. Thereafter, 0.5 mL of glutaraldehyde (25% aqueous solution) was then added into the system to solidify the CS-SiO_2 droplets, followed by adding the NaOH solution to allow the precipitation of the CS matrix. Finally, the hybrid microspheres were obtained by the successive process of centrifugation and repeated washing and air-drying. The CS-SiO_2 hybrid microspheres with 20 wt% and 40 wt% of SiO_2 (theoretical weight percentages) were prepared just by changing the amount of the added SiO_2 sol, and the samples were designated as CS-20%SiO_2 and CS-40%SiO_2, respectively. For the control group, the pure CS microspheres were also prepared using a similar procedure.

2.2. Characterization of the CS-SiO_2 Hybrid Microspheres. The morphology of the hybrid microspheres was observed with scanning electron microscopy (SEM, SU8220). A portion of the as-prepared CS-20%SiO_2 hybrid microspheres were calcined at 600°C for 4 h in a muffle furnace, and the residual powders after calcination were analyzed by SEM and transmission electron microscopy (TEM, JEOL-2010). Fourier transform infrared spectroscopy (FT-IR, PerkinElmer 983G) was applied to identify the chemical groups of the hybrid microspheres using the KBr pellet method. The crystallization behavior of the microspheres was investigated by X-ray diffraction (XRD) analysis (D8 Advance). In addition, the thermal analysis of the microspheres was carried out by thermogravimetry/differential scanning calorimetry (TG/DSC, STA 449 F3 Jupiter).

2.3. In Vitro Bioactivity of the CS-SiO_2 Hybrid Microspheres. The *in vitro* bioactivity test was performed by soaking 0.1 g of the microspheres in 5 mL simulated body fluid (SBF, pH 7.4) at 37°C. The SBF solution was refreshed every other day. After 3 days of culture, the microspheres were collected by centrifugation, washed 3 times with deionized water, and lyophilized. The dried microspheres were subjected to the SEM analysis.

2.4. Drug Loading and In Vitro Release of the CS-SiO_2 Hybrid Microspheres. The procedures of drug loading and release were performed according to the literature [18]. Briefly, the drug-loading experiment was carried out by dispersing 0.1 g of the microspheres into 20 mL of the PBS solution containing 5 mg/mL of VH. After being incubated at 37°C for 24 h, the mixture was centrifuged and the clear supernatant was collected for analysis by UV (6100S, METASH) at 281 nm. For the drug release test, the VH-loaded microspheres (0.1 g) were immersed in 10 mL of PBS at 37°C. At selected intervals, 3 mL aliquots were withdrawn and analyzed with the UV spectrophotometer. All the tests were performed in duplicate, and the data were reported as mean ± standard deviation (SD).

3. Results and Discussion

Figure 1 displayed the SEM images of the CS and CS-SiO_2 hybrid microspheres, which revealed that the SiO_2 content exerted a great influence on the dispersity and morphology of the hybrid microspheres. Among these specimens, the CS-20%SiO_2 hybrid microspheres exhibited the most desirable morphology with good spherical shape and high dispersity (Figure 1(b)). Their average particle diameter was determined to be about 24.0 μm. It was also found that there were a few fragments existing in the CS-20%SiO_2 samples, probably due to the increase in the brittleness of the microspheres with the introduction of the SiO_2 phase. Even though most of the pure CS microspheres also presented an approximately spherical form, they are more or less agglomerated together. This was inferred that the uniform hybrid of CS with SiO_2 effectively strengthened the CS microspheres, thus producing a relatively stiff network. Moreover, it was indicated by comparing the insets of Figures 1(a) and 1(b) that, after the addition of SiO_2, the microspheres exhibited a relatively rough surface. However, as the content of silica increased up to 40 wt%, the viscosity of the CS-SiO_2 hybrid sol will be enhanced correspondingly, eventually resulting in an increased average particle size to 28.0 μm and a slight adhesion between particles (Figure 1(c)).

The FT-IR spectra of pure CS and CS-SiO_2 hybrid microspheres were illustrated in Figure 2(a). The pure CS microsphere showed a wide band in the region of 3300-3500 cm^{-1}, assigning to the stretching vibrations of the N-H groups and/or the O-H groups. It was also observed that characteristic signals at 1662 and 1569 cm^{-1} may be attributed to C-O stretching and N-H stretching, respectively [19]. Moreover, the characteristic absorption peaks of the Si-O-Si groups at 448 and 793 cm^{-1} appeared in the spectra of the CS-SiO_2 hybrid microspheres [20], and the intensity of those peaks increased gradually with the increase of the SiO_2 content. A broad adsorption band of the CS-SiO_2 hybrid microspheres was centered at 1041 cm^{-1}, which was associated with the stretching vibrations of Si-O-C groups overlapping with those of the Si-O-Si groups [21]. The presence of this band confirmed the hybridization of silica with CS [22]. Figure 2(b) shows the XRD patterns of the microspheres. Pure CS microspheres exhibited a diffraction peak centered at about 19°. As observed in the XRD pattern of the CS-SiO_2 hybrid microspheres, no obvious diffraction peak was assigned to the SiO_2 phase, indicating its amorphous structure. However, with the increase of the SiO_2 content, the diffraction peak of

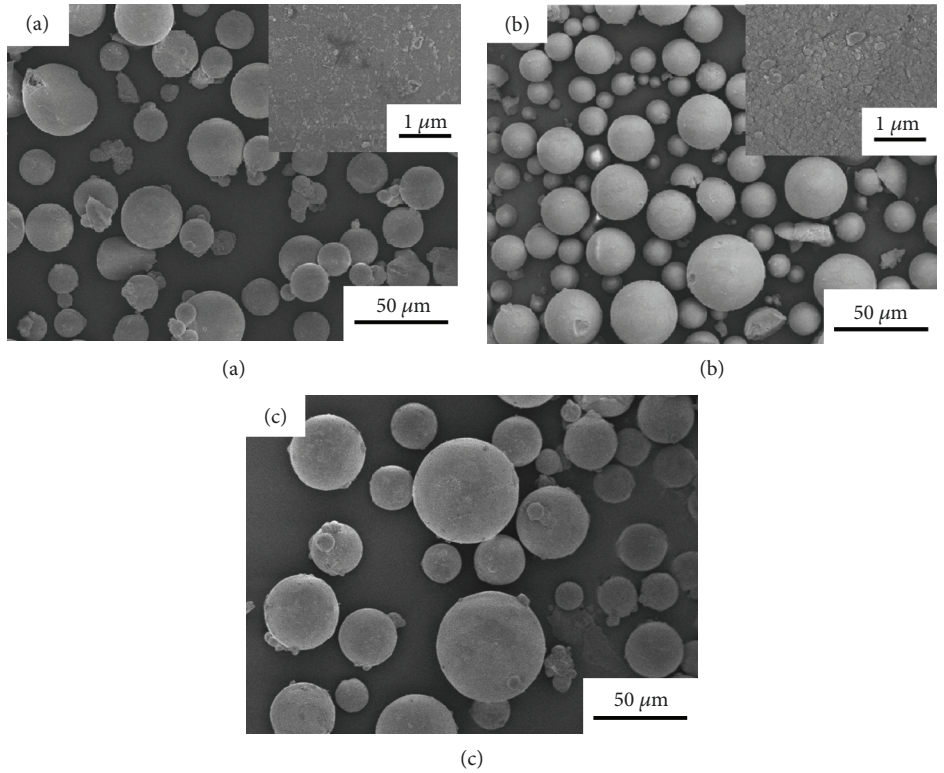

FIGURE 1: SEM images of (a) pure CS, (b) CS-20%SiO_2, and (c) CS-40%SiO_2 hybrid microspheres. The insets of (a) and (b) showed the high-magnification SEM images of the pure CS and CS-20%SiO_2 microspheres, respectively.

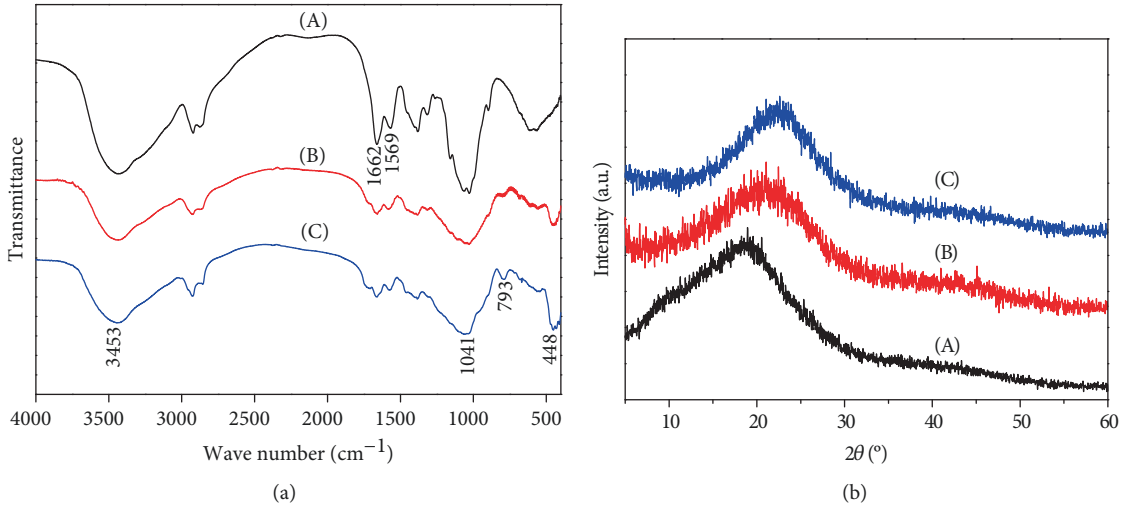

FIGURE 2: (a) FT-IR spectra and (b) XRD patterns of (A) pure CS, (B) CS-20%SiO_2, and (C) CS-40%SiO_2 hybrid microspheres.

CS was found to shift to a higher 2θ value and became less sharp, indicating the possible interaction between the SiO_2 and CS phases. In combination with the FI-IR and XRD results, it was confirmed that the inorganic phase in the CS-SiO_2 hybrid microspheres prepared herein was amorphous silica.

The thermal behavior of the CS-SiO_2 hybrid microspheres was investigated by TG/DSC. As shown in Figure 3(a), both the CS and CS-SiO_2 hybrid microspheres had almost exactly the same weight loss steps. The large weight loss occurring in the region of 200-600°C was probably associated with the decomposition of CS as well as the progressive polycondensation and dehydration of silica xerogel [23], corresponding to the strong exothermic peak in the DSC curves (Figure 3(b)). After deducting the residual amount of the pure CS microspheres (~3 wt%), the SiO_2 contents of the CS-20%SiO_2 and CS-40%SiO_2 hybrid microspheres were determined from the TG curves

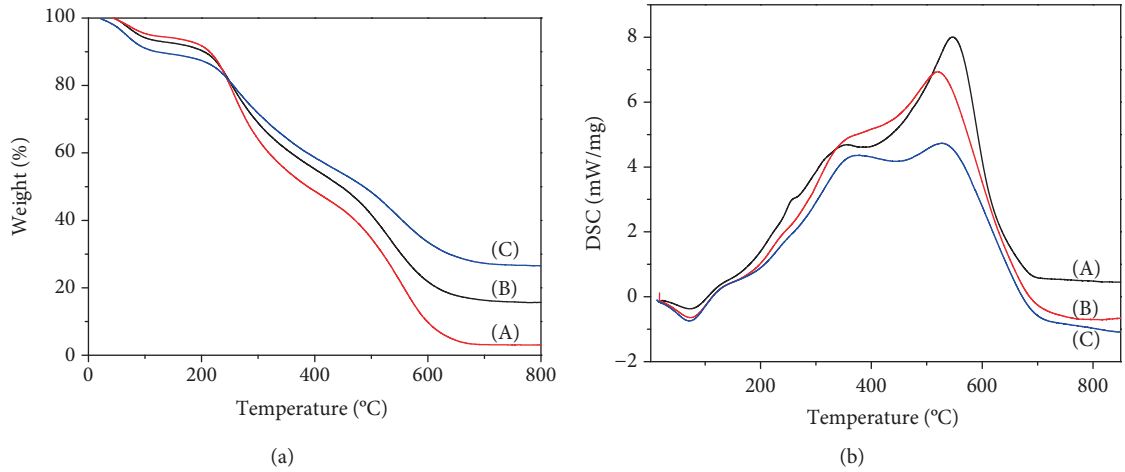

(a) (b)

Figure 3: (a) TG and (b) DSC races of (A) pure CS, (B) CS-20%SiO_2, and (C) CS-40%SiO_2 hybrid microspheres.

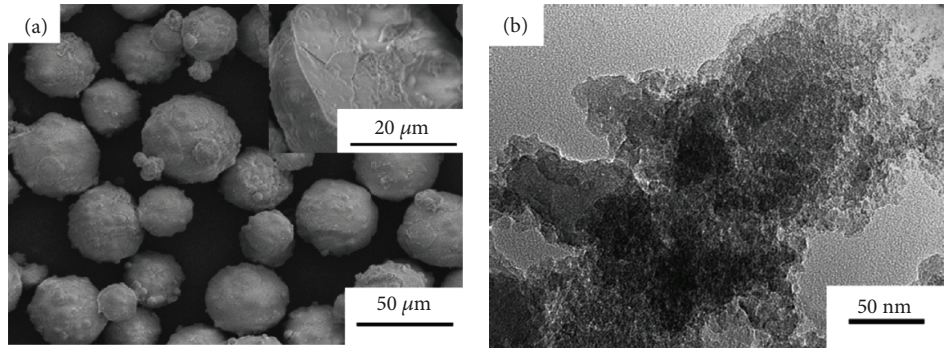

(a) (b)

Figure 4: (a) SEM and (b) TEM images of the CS-20%SiO_2 hybrid microspheres after calcination at 600°C for 4 h.

to be about 13 wt% and 23 wt%, respectively, lower than their theoretical values. This was probably attributable to the partial loss of SiO_2 with the squeezed water during the crosslinking process. The addition of NaOH had a negligible effect on the final content of SiO_2, which was confirmed by our experiments.

To further verify the uniform hybrid of silica xerogel within the CS matrix, the CS-20%SiO_2 hybrid microspheres were calcined at 600°C for 4 h. As shown in Figure 4(a), after removal of CS by calcination, the microspheres maintained the spherical shape well and the particle size had a little change before and after calcinations although the surface turned out to be rougher. In addition, it was observed from the cross-sectional SEM image of the calcined microspheres shown in the inset of Figure 4(a) that their internal structure was very similar with the surface one, and no obvious collapse occurred during calcination. The TEM image of the crashed microspheres after calcination presented a porous structure composed of many closely packed nanopores (Figure 4(b)), which was consistent with the morphology of porous SiO_2 reported by other authors [24]. From the above analysis, it was confirmed that the SiO_2 phase was homogeneously hybridized with CS.

In vitro bioactivity is considered as one of the most important characteristics of the biomaterials for bone tissue regeneration. It was usually evaluated *in vitro* by the formation ability of bone-like apatite on the surface of the materials after immersion in the SBF solution for a period of time [25]. It was observed in Figure 5(a) that only a small amount of the mineral phase was deposited on the pure CS microspheres after 3 days of immersion. In contrast, the CS-20%SiO_2 hybrid microspheres showed a vigorous precipitation of bone-like apatite nanoparticles on the surface (Figure 5(b)), and the morphology of the particles was very similar with those reported in the SiO_2-related literatures [26, 27]. Such a result indicated the greatly improved biomineralization capacity of the CS microspheres by the uniform hybrid with silica xerogel.

Vancomycin hydrochloride (VH) was selected as a model drug and loaded into the microspheres. It was revealed in Table 1 that the CS microspheres exhibited good drug entrapment efficiency and drug-loading capacity mainly due to their strong interaction with the drug molecules *via* hydrogen bonding or ionic interaction. However, both drug entrapment efficiency and drug-loading capacity of the microspheres decreased gradually with the increase of the SiO_2 content. Even though the SiO_2 xerogel had been reported to also have strong adsorption ability of drugs by virtue of the abundant –OH groups on their surface [28], the mechanical strengthening effect of silica as an inorganic

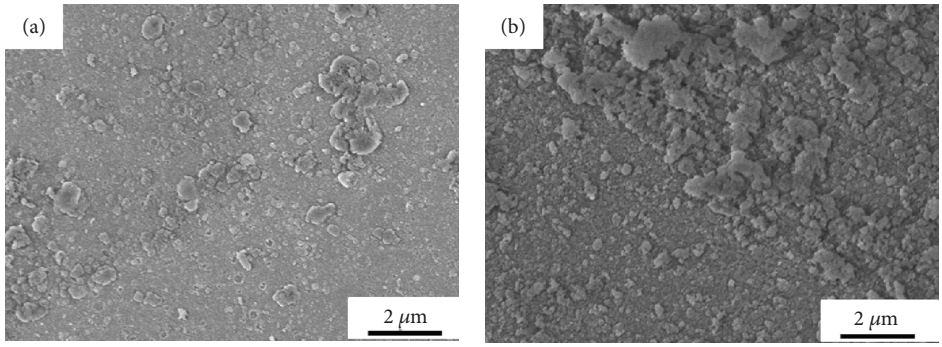

(a) (b)

Figure 5: SEM images of (a) pure CS and (b) CS-20%SiO_2 hybrid microspheres after being soaked in the SBF solution for 3 d.

Table 1: Drug encapsulation efficiency and drug-loading capacity of the microspheres.

Samples	Drug encapsulation efficiency (%)	Drug-loading capacity (%)
CS	19.2 ± 1.5	7.7 ± 0.3
CS-20%SiO_2	17.6 ± 1.1	7.1 ± 0.2
CS-40% SiO_2	16.8 ± 0.9	6.7 ± 0.2

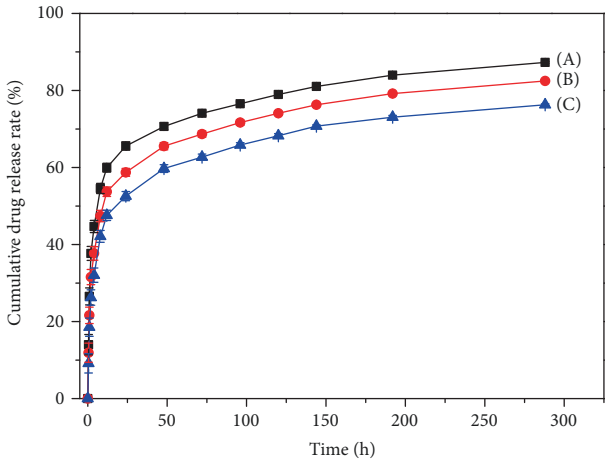

Figure 6: Drug release profiles of (A) pure CS, (B) CS-20%SiO_2, and (C) CS-40%SiO_2 hybrid microspheres.

phase for the CS microspheres would restrain their swelling behavior. Namely, the CS-SiO_2 hybrid microspheres with a higher SiO_2 content will have a higher adsorption ability but only a limited diffusion capability of drugs into the weakly swollen microspheres.

The cumulative release profiles of VH from the CS and CS-SiO_2 hybrid microspheres were depicted in Figure 6. It was implied that the release behaviors of all the microspheres typically consisted of two stages. The first stage was the burst release of VH within 12 h, which was attributed to the rapid dissolution of VH adsorbed on the surface of the microsphere or embedded in the surface layer. After 12 h of test, the cumulative amounts of VH released from the pure CS, CS-20%SiO_2, and CS-40%SiO_2 microspheres were determined as 60.0%, 53.7%, and 49.1%, respectively. In contrast, at the second stage, the VH release from 12 up to 288 h was slowed down greatly *via* gradual diffusion of the entrapped drug through the microsphere network. Moreover, the release rate during this period was decreased with the increase of the SiO_2 content, indicating that the CS-SiO_2 hybrid microspheres were more effective in releasing the drugs in a sustained manner than the pure CS microspheres. The improved drug release behavior of the CS-SiO_2 hybrid microspheres can be ascribed to their good morphologies as well as the presence of SiO_2. On the one hand, the regular shape and high dispersity of the hybrid microspheres allowed the drug to diffuse out of the microspheres more controllably and constantly. On the other hand, the abundant –OH groups as well as the strengthening effect of the SiO_2 xerogel in the hybrid microspheres would be beneficial to the sustained release of drugs. In addition, even after 288 h of test, the release of VH from all the three samples was still maintained at a comparable rate, and the cumulative amount of VH released from the pure CS, CS-20%SiO_2, and CS-40%SiO_2 microspheres reached to be about 87.2%, 82.4%, and 76.3%, respectively.

4. Conclusions

A combined process of sol-gel and emulsification-crosslinking was applied to fabricate the CS-SiO_2 hybrid microspheres in a water-in-oil emulsion. The SEM observation presented that the CS-20%SiO_2 hybrid microspheres with an average particle diameter of about 24.0 μm had the most desirable morphology. The phase composition of the microspheres was confirmed by the FT-IR, XRD, and TG/DSC measurements. After being soaked in the SBF solution for 3 days, the CS-SiO_2 hybrid microspheres were covered with bone-like apatite particles, indicating their good *in vitro* bioactivity Moreover, the CS-SiO_2 hybrid microspheres exhibited a slightly lower drug-loading capacity but a more sustained release behavior than their CS equivalents, thus potentially severing as a suitable drug carrier for bone tissue engineering.

Data Availability

The data used to support the findings of this study are included within the article. Any more specific details in the data will be delivered by the corresponding authors upon request.

Conflicts of Interest

The authors declare that they have no conflicts of interest.

Acknowledgments

This work was financially supported by the Fund for the Frontier Research of the Discipline (No. 2015XKQY03).

References

[1] K. Wei, K. Li, L. Yan et al., "One-step fabrication of g-C_3N_4 nanosheets/TiO_2 hollow microspheres heterojunctions with atomic level hybridization and their application in the multi-component synergistic photocatalytic systems," *Applied Catalysis B: Environmental*, vol. 222, pp. 88–98, 2018.

[2] C. Lei, M. Pi, C. Jiang, B. Cheng, and J. Yu, "Synthesis of hierarchical porous zinc oxide (ZnO) microspheres with highly efficient adsorption of Congo red," *Journal of Colloid and Interface Science*, vol. 490, pp. 242–251, 2017.

[3] E. Tawagi, T. Ganesh, H. L. M. Cheng, and J. P. Santerre, "Synthesis of degradable-polar-hydrophobic-ionic co-polymeric microspheres by membrane emulsion photopolymerization: in vitro and in vivo studies," *Acta Biomaterialia*, vol. 89, pp. 279–288, 2019.

[4] W.-N. Wang, W. Dong, C.-X. Huang, B. Liu, S. Cheng, and H. Qian, "UCNPs@$Zn_{0.5}Cd_{0.5}S$ core-shell and yolk-shell nanostructures: selective synthesis, characterization, and near-infrared-mediated photocatalytic reduction of Cr(VI)," *Journal of Nanomaterials*, vol. 2018, Article ID 1293847, 9 pages, 2018.

[5] J. Huang, W. Lin, L. Xie, and W. Ho, "Facile synthesis of $Zn_xCd_{1-x}S$ solid solution microspheres through ultrasonic spray pyrolysis for improved photocatalytic activity," *Journal of Nanomaterials*, vol. 2017, Article ID 6356021, 8 pages, 2017.

[6] V. D. Prajapati, G. K. Jani, and J. R. Kapadia, "Current knowledge on biodegradable microspheres in drug delivery," *Expert Opinion on Drug Delivery*, vol. 12, no. 8, pp. 1283–1299, 2015.

[7] Y.-G. Bi, Z.-T. Lin, and S.-T. Deng, "Fabrication and characterization of hydroxyapatite/sodium alginate/chitosan composite microspheres for drug delivery and bone tissue engineering," *Materials Science and Engineering: C*, vol. 100, pp. 576–583, 2019.

[8] W. Chen, A. Palazzo, W. E. Hennink, and R. J. Kok, "Effect of particle size on drug loading and release kinetics of gefitinib-loaded PLGA microspheres," *Molecular Pharmaceutics*, vol. 14, no. 2, pp. 459–467, 2017.

[9] E. Garin, Y. Rolland, S. Laffont, and J. Edeline, "Clinical impact of ^{99m}Tc-MAA SPECT/CT-based dosimetry in the radioembolization of liver malignancies with ^{90}Y-loaded microspheres," *European Journal of Nuclear Medicine and Molecular Imaging*, vol. 43, no. 3, pp. 559–575, 2016.

[10] S. Javanbakht, P. Nezhad-Mokhtari, A. Shaabani, N. Arsalani, and M. Ghorbani, "Incorporating Cu-based metal-organic framework/drug nanohybrids into gelatin microsphere for ibuprofen oral delivery," *Materials Science and Engineering: C*, vol. 96, pp. 302–309, 2019.

[11] A. Huang, X. Li, X. Liang et al., "Solid-phase synthesis of cellulose acetate butyrate as microsphere wall materials for sustained release of emamectin benzoate," *Polymers*, vol. 10, no. 12, p. 1381, 2018.

[12] Q. Wang, A. Xiao, Y. Liu et al., "One-step preparation of nano-in-micro poly(vinyl alcohol) embolic microspheres and used for dual-modal T_1/T_2-weighted magnetic resonance imaging," *Nanomedicine: Nanotechnology, Biology and Medicine*, vol. 14, no. 8, pp. 2551–2561, 2018.

[13] K. Shalumon, C. Y. Kuo, C. B. Wong, Y. M. Chien, H. A. Chen, and J. P. Chen, "Gelatin/nanohyroxyapatite cryogel embedded poly(lactic-co-glycolic acid)/nanohydroxyapatite microsphere hybrid scaffolds for simultaneous bone regeneration and load-bearing," *Polymers*, vol. 10, no. 6, p. 620, 2018.

[14] K. Wang, Y. Wang, X. Zhao et al., "Sustained release of simvastatin from hollow carbonated hydroxyapatite microspheres prepared by aspartic acid and sodium dodecyl sulfate," *Materials Science and Engineering: C*, vol. 75, pp. 565–571, 2017.

[15] Z. Yang, B. Cui, Y. Bu, and Y. Wang, "Preparation of flower-dewdrops Fe_3O_4/carbon-SiO_2 microsphere for microwave-triggered drug delivery," *Journal of Alloys and Compounds*, vol. 775, pp. 826–835, 2019.

[16] S.-H. Teng, M.-H. Liang, P. Wang, and Y. Luo, "Biomimetic composite microspheres of collagen/chitosan/nano-hydroxyapatite: in-situ synthesis and characterization," *Materials Science and Engineering: C*, vol. 58, pp. 610–613, 2016.

[17] S. A. Agnihotri, N. N. Mallikarjuna, and T. M. Aminabhavi, "Recent advances on chitosan-based micro- and nanoparticles in drug delivery," *Journal of Controlled Release*, vol. 100, no. 1, pp. 5–28, 2004.

[18] K. Xue, S.-H. Teng, N. Niu, and P. Wang, "Biomimetic synthesis of novel polyvinyl alcohol/hydroxyapatite composite microspheres for biomedical applications," *Materials Research Express*, vol. 5, no. 11, article 115401, 2018.

[19] A. Salama and P. Hesemann, "Synthesis of *N*-guanidinium-chitosan/silica hybrid composites: efficient adsorbents for anionic pollutants," *Journal of Polymers and the Environment*, vol. 26, no. 5, pp. 1986–1997, 2018.

[20] E.-J. Lee, S.-H. Teng, T.-S. Jang et al., "Nanostructured poly(ε-caprolactone)–silica xerogel fibrous membrane for guided bone regeneration," *Acta Biomaterialia*, vol. 6, no. 9, pp. 3557–3565, 2010.

[21] A. A. El hadad, D. Carbonell, V. Barranco, A. Jiménez-Morales, B. Casal, and J. C. Galván, "Preparation of sol–gel hybrid materials from γ-methacryloxypropyltrimethoxysilane and tetramethyl orthosilicate: study of the hydrolysis and condensation reactions," *Colloid and Polymer Science*, vol. 289, no. 17-18, pp. 1875–1883, 2011.

[22] H. Hassan, A. Salama, A. K. el-ziaty, and M. el-Sakhawy, "New chitosan/silica/zinc oxide nanocomposite as adsorbent for dye removal," *International Journal of Biological Macromolecules*, vol. 131, pp. 520–526, 2019.

[23] F.-W. Chen, S.-H. Teng, S.-H. Xia, P. Wang, and G.-Q. Pan, "One-pot synthesis of polyvinyl alcohol/silica composite microspheres in a surfactant-free system for biomedical applications," *Journal of Sol-Gel Science and Technology*, vol. 79, no. 3, pp. 525–529, 2016.

[24] Z. Chen, Z. Hu, J. Wang et al., "Synthesis of mesoporous silica-carbon microspheres via self-assembly and in-situ

carbonization for efficient adsorption of Di-*n*-butyl phthalate," *Chemical Engineering Journal*, vol. 369, pp. 854–862, 2019.

[25] H. W. Kim, J. H. Song, and H. E. Kim, "Nanofiber generation of gelatin–hydroxyapatite biomimetics for guided tissue regeneration," *Advanced Functional Materials*, vol. 15, no. 12, pp. 1988–1994, 2005.

[26] B. H. Yoon, H. E. Kim, and H. W. Kim, "Bioactive microspheres produced from gelatin–siloxane hybrids for bone regeneration," *Journal of Materials Science: Materials in Medicine*, vol. 19, no. 6, pp. 2287–2292, 2008.

[27] S.-H. Teng, P. Wang, and J.-Q. Dong, "Bioactive hybrid coatings of poly(ε-caprolactone)–silica xerogel on titanium for biomedical applications," *Materials Letters*, vol. 129, pp. 209–212, 2014.

[28] H. S. Jamwal and G. S. Chauhan, "Designing silica-based hybrid polymers and their application in the loading and release of fluorescein as a model drug and diagnostic agent," *Advances in Polymer Technology*, vol. 37, no. 2, pp. 411–418, 2018.

Hindawi
Journal of Nanomaterials
Volume 2019, Article ID 3617050, 12 pages
https://doi.org/10.1155/2019/3617050

Research Article

Synthesis and Properties of Red Mud-Based Nanoferrite Clinker

Hongfang Sun,[1] **Chuyu Chen**,[1] **Li Ling**,[1] **Shazim Ali Memon**,[2] **Zhu Ding**,[1] **Weiwen Li**,[1] **Lu-ping Tang**,[3] **and Feng Xing**[1]

[1]*Guangdong Provincial Key Laboratory of Durability for Marine Civil Engineering, College of Civil and Transportation Engineering, Shenzhen University, Shenzhen 518060, China*
[2]*Department of Civil Engineering, Nazarbayev University, Astana 010000, Kazakhstan*
[3]*Division of Building Technology, Chalmers University of Technology, Gothenburg 41296, Sweden*

Correspondence should be addressed to Feng Xing; xingf@szu.edu.cn

Received 1 May 2019; Accepted 8 July 2019; Published 29 July 2019

Guest Editor: Yunpan Ying

Red mud, an industrial waste obtained from alumina plants, is usually discharged into marine or disposed into a landfill polluting the surrounding water, atmosphere, and soil. Thus, disposal of red mud is an environmental concern and it should be recycled in an effective way. Since red mud consists of iron- and aluminum-rich phases, it can potentially be processed into cementitious material and can be used for a construction purpose. This research investigated the synthesis of nanoferrite (NF) clinker by using red mud as a raw material through chemical combustion technology for potential use in cement-based composite. Before the synthesis of NF, red mud was characterized by using XRF, XRD, and SEM techniques. From characterization results, the stoichiometric ratio of raw materials was calculated and experimentally optimized. The sample was then tested at various temperatures (815, 900, 1000, and 1100°C) to find the optimum synthesis temperature. Finally, the hydraulic activity of NF was verified and the contribution to mechanical properties was determined by replacing cement with NF at various substitution levels (0, 5, 10, and 20 wt%). Test results showed that the optimum condition for the synthesis of NF was found when the ratio of $CaCO_3$/red mud was 1.5 and the sintering temperature was 815°C. The synthesized NF had an average diameter of 300 nm, and the main composition was brownmillerite (C_4AF) with distinct hydraulic reaction. When NF was used as a substitute of Portland cement in mortar, the flexural strength with a 5% replacement level improved by 15%. Therefore, it can be concluded that the synthesis of NF provides an alternative approach to recycle red mud and could significantly help in reducing environmental pollution.

1. Introduction

Red mud, produced by the Bayer process, is an industrial waste obtained during the production of aluminum. For every ton of alumina produced, approximately 1.6 tons of red mud is released and it is estimated that more than 66 million tons of this waste is annually generated worldwide [1, 2]. The red mud is usually discharged into marine [3] or disposed into land [4] polluting the surrounding water, atmosphere, and soil, especially in the areas where this industry is located [5]. Therefore, steps must be taken to recycle this waste in an eco-friendly way.

Based on the composition of red mud, it can be recycled and used in a variety of fields. For example, it can be used as a recovery of metals or can be used as a potential alternative catalyst since it mainly consists of a mixture of oxides of Fe, Al, and Ti and a smaller amount of Si, Ca, and Na [6, 7]. Red mud can also act as a pigment since its iron-rich phases have a red color [8]. However, a large amount of red mud still needs to be recycled and more effective applications should be developed. Recently, the application of red mud as building materials has attracted the research community [9]. Calcined red mud usually consists of elements Si, Al, and Fe and has shown pozzolanic reactivity [10]. Thus, it has a potential to be used as a cementitious material. Till to date, a variety of red mud-based cements have been fabricated, such as Portland cement [11], self-compacting cement [12], and alkali-activated cement [13]. However, it could greatly enlarge the

application area of red mud if new cement-based composites containing red mud are developed.

Ferrite cement has a variety of excellent properties such as high strength, impermeability, antifreeze, and corrosion resistance. Consequently, it can be used for various applications, such as emergency repair, winter construction, antiseepage, plugging, underground foundation, and high-strength concrete production [14]. However, the hydration rate of ferrite cement is slow (several years or even decades to fully hydrate) [15], which greatly limits its popularity. One of the effective approaches to accelerate the early hydration is to reduce the particle size of ferrite cement [16], especially down to nanoscale [17–20]. The most commonly used technique to reduce the particle size of ferrite cement is grinding, which consumes a lot of energy. The ground particles usually have a wide particle size distribution with an irregular shape which might not be conducive to the workability of concrete. Furthermore, it is an uphill task to reduce the particle size to a nanometer scale [21]. Therefore, it is necessary to develop an effective and economical way to refine the particle size of ferrite cement.

In this research, iron-rich red mud was used to synthesize nanoferrite (NF) clinker through a chemical combustion method at a much lower temperature (≦1150°C) than traditional ferrite cement (1250-1300°C). The production conditions were theoretically designed and experimentally optimized. After optimization, the hydration activity and mechanical properties of NF admixture were determined.

2. Materials and Methods

2.1. Materials. Red mud and limestone were used as raw materials while urea and nitric acid were used as a fuel to produce NF. Red mud is an industrial waste produced by the Bayer process. The purity of $CaCO_3$ in limestone and H_2NCOCH_2 in urea were greater than 95.5% and 99%, respectively, while the content of HNO_3 in concentrated nitric acid was 65-68%. The raw material (limestone), urea, and concentrated nitric acid were purchased from Xilong Scientific Co. Ltd. (Guangzhou, China). In order to investigate the hydration and mechanical properties of NF, P·I type ordinary Portland cement (OPC) produced by China United Cement Qufu Co. Ltd. (Qufu, China) and having the following composition (Table 1) was used.

2.2. Synthesis of NF. The production procedure of NF is as follows: Firstly, raw materials (red mud and limestone) and fuel (urea and nitric acid) were mixed and placed in a muffle furnace. The heating temperatures of the samples in the muffle furnace were set at 815, 900, 1000, and 1100°C, respectively. The temperature of the samples was raised from room temperature to the set temperature (815, 900, 1000, and 1100°C) and held for 15 minutes. Then, the samples were rapidly taken out and allowed to cool in the air. Finally, the cooled samples were ground to obtain the final NF powder. The mass ratios of red mud to $CaCO_3$ in the raw materials were 1 : 0.5, 1 : 0.6, 1 : 0.7, 1 : 0.8, 1 : 0.9, 1 : 1, and 1 : 2 while the raw materials-to-fuel ratio was 0.24 : 1. The role of the fuel was to provide the raw materials with the heat required for reaction so as to lower the sintering temperature and to refine the product. The mass ratio of urea to nitric acid in fuel was 2.02 : 1.

Table 1: Composition of Portland cement (%).

SiO_2	Al_2O_3	Fe_2O_3	CaO	MgO	SO_3
22.12	4.51	3.45	64.92	3.35	0.4

2.3. Testing

2.3.1. Scanning Electron Microscopy (SEM). In this research, the secondary electron (SE), backscattered electron (BSE), and energy dispersive X-ray spectroscopy (EDS) in SEM were used to evaluate the morphology and composition of red mud and NF before and after hydration. The SEM observation was performed on FEI Quanta 250 (FEI Inc., Hillsboro, OR, USA) with a field emission gun and an accelerating voltage of 15 kV. The SE images provide the information on the morphology of the surface while BSE images combined with EDS mapping provide the cross-sectional microstructure and information about the chemistry of the analyzed samples.

The unhydrated and hydrated NF were observed directly by the SE technique. For BSE, the raw red mud powder and unhydated NF were prepared by adopting the following procedure. At first, mix the same mass of red mud and epoxy resin (containing a curing agent) to form viscous slurry. The slurry was poured into a cylindrical mold (10 mm diameter and 55 mm height) and cured at room temperature for 24 hours. The solidified sample was then cut by a low-speed diamond saw to expose the fresh surface. Thereafter, the surface was polished using diamond pastes of gradations 9, 6, 3, 1, and 0.25 μm on top of Texmet papers.

In order to observe hydrated NF samples through BSE, the following procedure was adopted. Take the weight of NF powder and deionized water in a mass ratio of 1.0, and mix for 2 minutes. The mixture was poured into a mold ($10 \times 10 \times 10\,mm^3$), consolidated, and cured at room temperature (20 ± 2°C). After curing for 3, 7, 14, 28, and 56 days, the samples were taken out for testing (only the 28-day sample was used for SEM observation while samples cured at other ages as well as 28 days were used for XRD examination). The 28-day samples were then cut into 2 cm thick pieces and vacuum-saturated with epoxy for 24 h at room temperature. Thereafter, the specimens were cut with a slow speed diamond saw to expose a fresh surface by following the procedure as mentioned in the previous paragraph. Before loading the specimen into the SEM chamber, the specimens were sputter coated using gold to form a conductive surface.

2.3.2. X-Ray Diffraction (XRD). To obtain the mineralogical composition of red mud powder and NF before and after hydration, XRD was performed on a Bruker D8 instrument (Bruker, Karlsruhe, Germany) using a CuKα X-radiation ($\lambda = 1.5406$ Å) at 40 kV and 40 mA while Jade program 6.5 was used for quantitative analysis.

2.3.3. X-Ray Fluorescence (XRF). The elemental composition of red mud powder was evaluated using a Bruker S4 Explorer

XRF instrument (Bruker AXS, Germany) equipped with an X-ray tube with an operating voltage of 50 kV and a current of 50 mA. The exit spot at the end of the beamline was adjusted by the slit to $50 \times 60\ \mu m^2$. The sample was kept 1 m away from the slit at a 45° angle to the X-ray beam, while the detector was 3-10 cm away at an angle of 45° with the sample. The effective exposure time of each sample in the experiment was 600 s.

2.3.4. BET Surface Area. The specific surface area of unhydrated NF powder was tested by a BET instrument in a fully automated TriStar II Surface Area and Porosity Analyzer from Micromeritics Instrument Corporation. Before the experiment, each sample was degassed in a vacuum at 105°C for more than 6 hours. In this experiment, nitrogen was used as the adsorption gas.

2.3.5. Mechanical Properties. In order to evaluate the mechanical properties of NF material, the compressive and flexural strength tests were conducted. For these tests, cement mortar samples having a size of $10 \times 10 \times 40\ mm^3$ were prepared with NF at different levels of cement substitution (0, 5, 10, 15, and 20 wt% replacement of OPC by NF). The water-to-binder ratio and the binder-to-sand ratio used were kept as 0.35 and 1, respectively, while the dosage of the superplasticizer was 0.55%. In order to reduce the influence of large sand particle size on the test specimens, the sand having a size of more than 1 mm was removed by sieving. A YZH-300 testing machine (Luda Machinery Instrument Co. Ltd., Zhejiang, China) was used to determine the mechanical properties at the age of 3, 7, 14, and 28 days. The strength value represented the average of three specimens.

3. Results and Discussion

3.1. Synthesis of NF

3.1.1. Characterization of Red Mud Raw Material. During the synthesis of NF, red mud acted as an iron and aluminum source while limestone acted as a calcium source. They reacted with the assistance of heat provided by both furnace and fuel (urea and nitric acid). It is known that the composition and characterization of limestone and fuel (urea and nitric acid) are simple, and the only factor that needs to be considered is the purity of the samples. However, the characterization of red mud raw material, which is a complex mixture of more than ten kinds of compounds, is not an easy task. The precise characterization of red mud is an important step before its applications are considered. According to the available literature [22], most of the time, red mud is usually characterized by only XRD or XRF methods. However, XRD spectrum of the red mud sample is difficult to analyze due to the presence of multiphases in red mud, which leads to overlapping peaks. As far as XRF is concerned, it can only identify the relative proportion of elements instead of phases, although it is important for the stoichiometric calculation. Therefore, in order to accurately characterize the composition of red mud, firstly, an element mapping technique (EDS combined with BSE in SEM) was used to narrow down the range of elements. Then, phase identification and quantitative analysis were performed by the XRD. Finally, for a verification purpose, the results were compared with XRF.

Figure 1 presents a typical BSE image and corresponding element mapping results of red mud. It is clear that red mud powder contains a large amount of Fe and Al elements as well as some Na, Si, Ca, and O. The mapping results of elements H and C are not shown here since it is believed that part of them came from epoxy resin and was introduced during a sample preparation process. Moreover, element H was also beyond the detection limit of this technique. However, actually, they might possibly exist in red mud. Therefore, it was speculated that elements with possible positive valency were C, Si, H, and the aforementioned metals, while the element with negative valence was O. Therefore, red mud might contain components possibly having Al-Si-Na-O (-H and/or -C), Al-O (-H and/or -C), Fe-O (-H and/or -C), and Ca-O (-H and/or -C). It is suggested that Ti-O (-H and/or -C) and Fe-Ti-O (-H and/or -C) might also have formed. Based on the above analysis, the XRD spectrum was obtained and analyzed to further characterize the composition of red mud.

Based on the elemental range as shown in Figure 1, the phase identification and quantitative analysis of red mud were performed through XRD and the results are presented in Figure 2 and Table 2. It can be seen that Fe-related phases in red mud are in the forms of Fe_2O_3 (33.4%), Fe_3O_4 (1.4%), and FeOOH (2.8%, decomposition temperature of 400°C) [23]. The Al-related phases consist of AlO(OH) (10.7%, decomposition temperature of 430°C) [24], $Na_{7.88}(Al_6Si_6O_{24})(CO_3)_{0.93}$ (6.8%, decomposition temperature of 520°C) [25], Al_2TiO_5 (3.4%, decomposition temperature of 800°C) [26], and $Na_{0.33}Ca_{0.67}Al_{11.67}Si_{2.33}O_8$ (1.3%, decomposition temperature of 800°C) [27]. Moreover, a small amount of Ca-related phases was detected in the forms of $CaCO_3$ (5.0%) and $Na_{0.33}Ca_{0.67}Al_{11.67}Si_{2.33}O_8$ (1.3%). Minor SiO_2 (6.4%) and TiO_2 (4.5%) were also found. Based on the above analysis, it can be seen that all Al-related phases $Na_{7.88}(Al_6Si_6O_{24})(CO_3)_{0.93}$, $Na_{0.33}Ca_{0.67}Al_{1.67}Si_{2.33}O_8$, and Al_2TiO required extra heat to synthesize NF. As far as Fe-related phases are concerned, FeOOH required extra heat to synthesize NF while the other forms of Fe (Fe_2O_3 and Fe_3O_4) can directly be used to form NF. Therefore, decomposition temperature of both Fe- and Al-related phases was above 800°C and was set to be the minimal temperature required for sintering NF. It should also be noticed that SiO_2 and CaO components obtained from either red mud or decomposition reaction (such as decomposition of $CaCO_3$ at 900°C) may also produce belite with hydraulic activity.

In order to verify the XRD results presented in Table 2, the composition of red mud was converted to oxide composition and compared with XRF results as shown in Table 3. The comparison indicates that the XRD and XRF results are in good agreement with percentage errors in most cases within 10%. Despite Na_2O having an error of 23.5%, the difference between the content determined by XRF (11.7%) and XRD (8.95%) is acceptable. This mutual verification confirmed the accuracy of the composition of analyzed

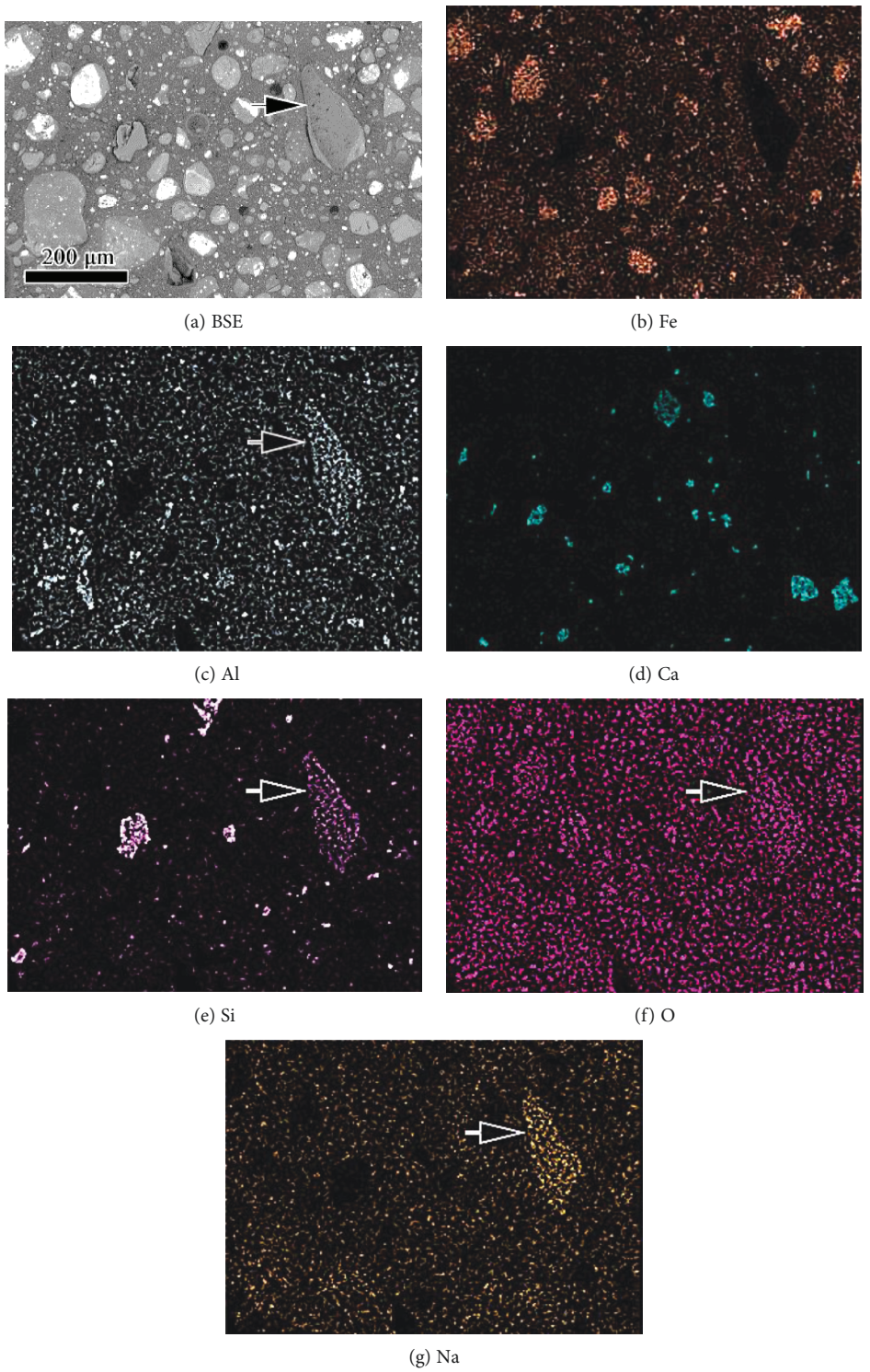

Figure 1: BSE and element mapping results of red mud powder. The arrows indicate particles simultaneously containing elements Na, Al, Si, and O.

red mud raw material, which forms foundation for the synthesis of NF.

3.1.2. Stoichiometric Calculation of NF Synthesis with Red Mud. In order to experimentally synthesize NF, stoichiometric calculation of raw materials was performed. According to the composition of NF (target compound was Ca_2FeAlO_5, abbreviated to C_4AF) [28], the raw materials are required to consist of oxides of CaO, Fe_2O_3, and Al_2O_3, part of which can be provided by red mud while the remaining has to be provided by supplementary materials.

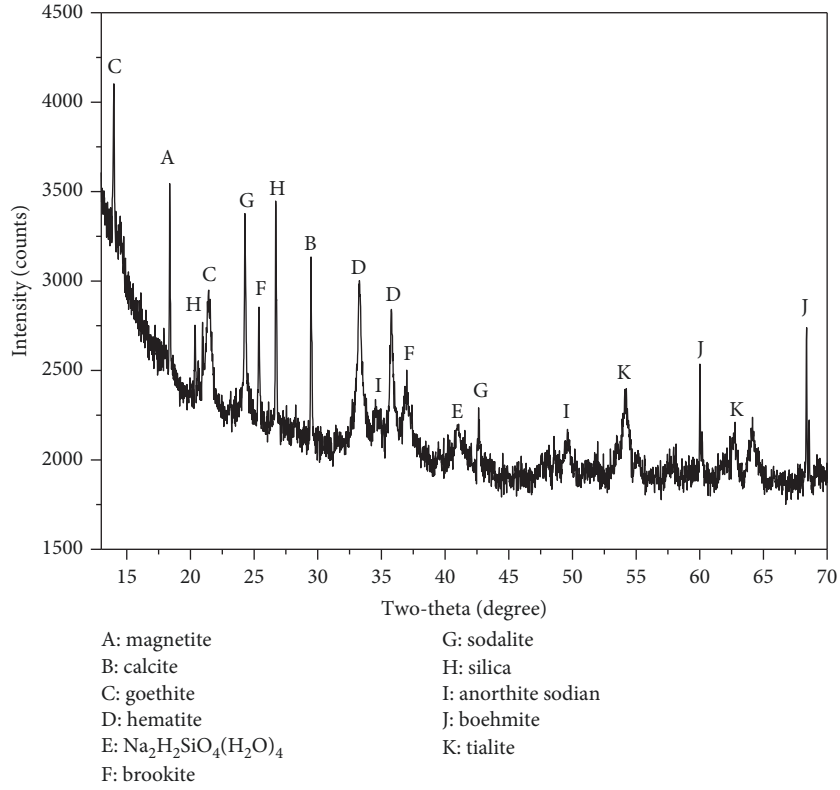

Figure 2: XRD spectrum of red mud.

Table 2: Composition of red mud from quantitative XRD analysis.

Compositions of red mud	Content (%)
Silica (SiO_2)	6.4
Sodalite ($Na_{7.88}(Al_6Si_6O_{24})(CO_3)_{0.93}$)	6.8
Sodium dihydrogen silicate tetrahydrate ($Na_2H_2SiO_4(H_2O)_4$)	24.3
Anorthite sodian ($Na_{0.33}Ca_{0.67}Al_{1.67}Si_{2.33}O_8$)	1.3
Calcite ($CaCO_3$)	5.0
Magnetite (Fe_3O_4)	1.4
Hematite (Fe_2O_3)	33.4
Boehmite (AlO(OH))	10.7
Goethite (FeOOH)	2.8
Brookite (TiO_2)	4.5
Tialite (Al_2TiO_5)	3.4

Table 3: Comparison between XRD and XRF results of red mud.

Oxide	Fe_2O_3	Al_2O_3	SiO_2	Na_2O	TiO_2	CaO
XRF result (%)	37.69	24.4	16.8	11.7	5.33	2.83
XRD result (%)	37.38	22.36	16.23	8.95	5.99	2.80
Deviation (%)	0.82	8.36	3.39	23.50	12.4	1.06

Assuming that CaO, Fe_2O_3, and Al_2O_3 are decomposed completely from red mud during the synthesis of NF [29], according to the following formula [30]:

$$4CaO + Fe_2O_3 + Al_2O_3 \longrightarrow 4CaO \cdot Fe_2O_3 \cdot Al_2O_3, \quad (1)$$

it can be seen that theoretically in 100 g of red mud, maximum 37.38 g of Fe_2O_3 and 52.33 g of CaO can be used to produce C_4AF with the assistance of 25.23 g of Al_2O_3. By looking at the oxide composition of red mud in Table 3, it seems that extra Fe_2O_3 exists in red mud while the quantity of CaO (2.83 g) required is far from enough. However, it should be noticed that during sintering, SiO_2 may consume CaO to generate silicate. Thus, more calcium source should be added so that it can possibly react with both Fe_2O_3 and SiO_2. It is worth noting that at the synthesis temperature of C_4AF (1000-1100°C) [31], it is possible to generate hydraulic C_2S, which does not have a negative effect on C_4AF. The production of C_2S is based on the following formula:

$$2CaO + SiO_2 \longrightarrow 2CaO \cdot SiO_2. \quad (2)$$

It can be seen that in 100 g red mud, stoichiometrically, 16.80 g SiO_2 reacts with 31.36 g CaO to synthesize C_2S. Therefore, in total, 81.30 g of extra CaO is required to form C_4AF and C_2S, corresponding to 145.18 g of $CaCO_3$. In other words, the mass ratio of $CaCO_3$ added to red mud is about 1.5, and at this mass ratio, theoretically, 114.4 g of C_4AF and 48.16 g of C_2S can be generated.

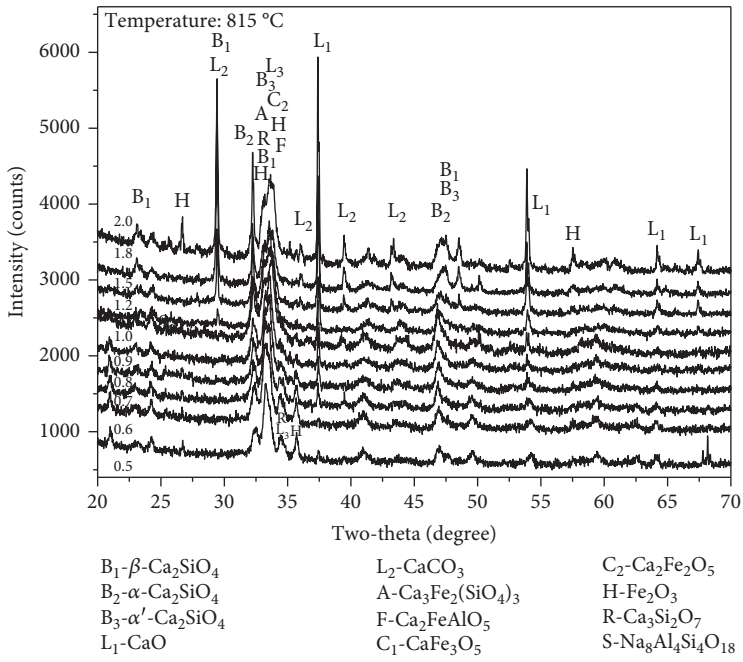

Figure 3: XRD spectra of NF produced at different $CaCO_3$/red mud ratios.

Table 4: Variation in content of major phases in NF at different $CaCO_3$/red mud ratios (%).

$CaCO_3$/red mud (wt%)	0.5	0.6	0.7	0.8	0.9	1.0	1.2	1.5	1.8	2.0
Ca_2FeAlO_5 (brownmillerite)	**19.2**	**21.7**	**23.4**	**32.1**	**39.0**	**36.3**	**41.5**	**47.2**	**39.8**	**34.9**
$Ca_2Fe_2O_5$ (srebrodolskite)	14.1	22.5	26.1	30.9	18.0	19.2	13.3	10.4	10.3	9.0
$CaFe_3O_5$ (calcium iron oxide)	6.4	4.3	4.4	3.7	3.9	4.4	5.4	2.8	2.5	3.7
$Ca_3Fe_2(SiO_4)_3$ (andradite)	2.1	3.5	2.7	0.6	2.6	2.7	0.6	1.7	0.3	2.1
Fe_2O_3 (hematite)	14.8	17.2	12.8	9.4	5.5	3.3	5.0	2.5	2.3	3.4
β-Ca_2SiO_4 (dicalcium silicate)	14.0	9.5	6.3	5.2	7.0	7.5	6.9	7.4	7.2	6.2
α-Ca_2SiO_4 (dicalcium silicate)	2.3	3.5	3.9	4.2	6.1	0.5	0.8	0.9	0.7	0.6
α'-Ca_2SiO_4 (dicalcium silicate)	1.5	0.2	0.2	0.1	0.2	1.4	0.2	0.3	0.2	0.2
Ca_2SiO_4 (sum(α+α'+β)) (dicalcium silicate)	**17.8**	**13.2**	**10.4**	**9.5**	**13.3**	**9.4**	**8.0**	**8.6**	**8.1**	**7.0**
$Ca_3Si_2O_7$ (rankinite)	12.9	12.5	12.8	8.3	11.5	16.8	15.8	10.5	11.0	8.2
$CaCO_3$ (calcite)	0.6	0.1	0.1	0.1	0.1	2.2	2.5	6.2	15.1	16.2
CaO (lime)	1.6	1.1	2.8	3.4	3.9	3.2	7.0	8.8	9.8	13.8
$(CaO)_{12}(Al_2O_3)_7$ (mayenite)	0	0	0.5	0.1	0.3	1.2	0.4	0.6	0.1	0
$NaAlSi_4$ (sodium aluminium silicon)	1.2	1.8	1.7	1.0	1.7	3.2	0.6	0.7	0.7	1.7
$Na_8Al_4Si_4O_{18}$ (sodium aluminum silicate)	9.7	1.8	2.3	0.9	0.3	0	0	0	0	0

In order to verify the above theoretical analysis, the ratios of $CaCO_3$/red mud were experimentally adjusted to around 1.5 as 0.5, 0.6, 0.7, 0.8, 0.9, 1.0, 1.2, 1.5, 1.8, and 2.0, respectively, and optimized. Since the heating temperature might also influence the final composition of NF, the influence of various temperatures (815, 900, 1000, and 1100°C) was also investigated.

3.1.3. Influence of $CaCO_3$/Red Mud Raw Materials. The raw materials and the fuel were mixed to synthesize NF. The influence of $CaCO_3$/red mud on NF composition is shown in Figure 3 and Table 4, respectively, while the change in the content of main phases in NF with varying $CaCO_3$/red mud ratios is shown in Figure 4. It can be seen that with the increase in the ratio of $CaCO_3$/red mud from 0.5 to 2.0, the content of the target product Ca_2FeAlO_5 (brownmillerite, C_4AF) firstly increased and then decreased. The peak value of 47.2% was achieved when the ratio of $CaCO_3$/red mud reached 1.5. The intermediate products of Ca_2FeAlO_5, i.e. $Ca_2Fe_2O_5$ and $CaFe_3O_5$, can also be seen. The content of $Ca_2Fe_2O_5$ firstly increased from 14.1% to 30.9% and then decreased to 9.0%, while the content of $CaFe_3O_5$ did not

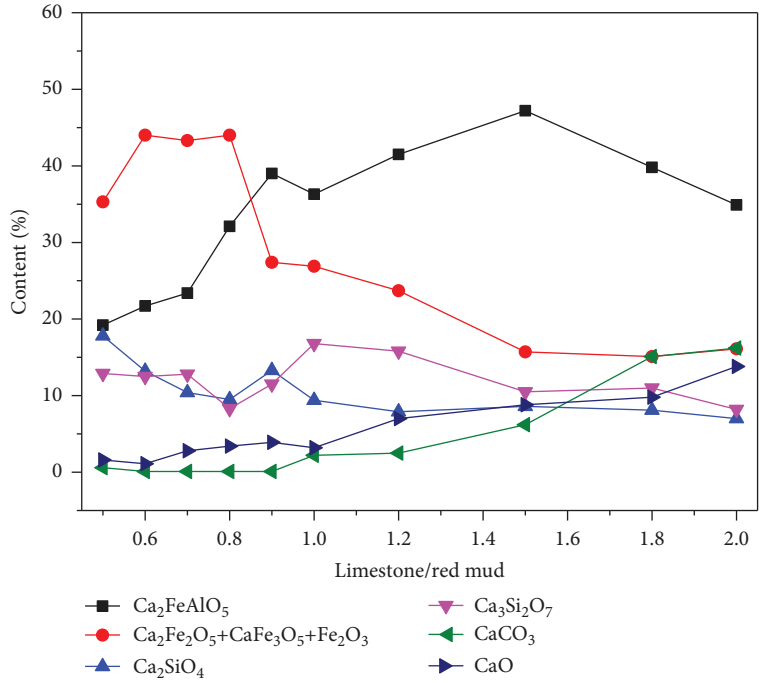

Figure 4: Variation in contents of major phases in NF at different $CaCO_3$/red mud ratios.

change much and remained at about 4%. In addition, the product containing Fe phase also had $Ca_3Fe_2(SiO_4)_3$; however, its content was minor (less than 4%).

As far as silicate products are concerned, three types of dicalcium silicates (abbreviated as C_2S), namely β, α, and α', were found in NF. Among these three types, β showed the highest content ranging from 5.2 to 14.0%, while the content of α and α' types was less than 6.1%. Since all three types of C_2S have hydration activity, therefore, a total amount of C_2S would be used for discussion. With the increase in the level of $CaCO_3$ raw materials, the total C_2S content decreased slightly. At a $CaCO_3$/red mud ratio of 1.5, the C_2S content was 8.1% while the total amount of the hydraulic contents (C_4AF+C_2S) was about 55%. The silicate also contained a certain amount of $Ca_3Si_2O_7$ (abbreviated as C_3S_2); however, it did not change much (range 8-16%) with the increase in the ratio of $CaCO_3$/red mud. It can also be seen from Figure 4 that at the 1.5 $CaCO_3$/red mud ratio, the content of C_3S_2 was found to be 10.5%. Although C_3S_2 does not have hydration activity, its volume expands in the carbonization environment [32], which can be beneficial to control the cracking and strength decrease caused by carbonization shrinkage.

The results (Figure 3 and Table 4) also show the presence of $CaCO_3$ residue and CaO (decomposition product of $CaCO_3$) in NF. Their content increased ($CaCO_3$: 0.1-16.2%; CaO: 1.1-13.8%) with the increase of the ratio of $CaCO_3$/red mud. At a $CaCO_3$/red mud ratio of 1.8 and higher, the content of $CaCO_3$ and CaO increased sharply, indicating that the effective use of raw materials was drastically reduced. At the 1.5 $CaCO_3$/red mud ratio, the $CaCO_3$ and CaO contents were found to be 6.2% and 8.8%, respectively. The contents of $NaAlSi_4$ and $Na_8Al_4Si_4O_{18}$, which are the residuals from red mud and having no hydration activity, were below 2%. Therefore, their influence on NF was negligible.

From the stoichiometric calculation of NF synthesis shown in Section 3.1.2, it can be seen that at the 1.5 $CaCO_3$/red mud ratio, the theoretical content of C_4AF in NF was 63.2%. However, the actual content of C_4AF in the synthesized NF was 47.2%, which was approximately 16% lower than the theoretical value. This is due to the reason that part of Fe in NF is in the form of $Ca_2Fe_2O_5$, $Ca_3Fe_2(SiO_4)_3$, and $CaFe_3O_5$ while the remaining unreacted part remained as Fe_2O_3. It should be mentioned here that the total amount of element Fe in Fe-related phases was 16.03%, which was close to the theoretical value of 14.55%, confirming the reliability of quantitative analysis. However, it is suggested that the conversion efficiency of raw materials to NF could be further improved by using the current experimental conditions. With regard to element Al, it was almost completely consumed to generate C_4AF. It is also noticed that the actual content of C_2S is 8.1%, which is quite different from the calculated value of 26.59%. The difference between the theoretical and experimental values is attributed to the formation of 10.5% $Ca_3Si_2O_7$(C_3S_2) and 1.7% $Ca_3Fe_2(SiO_4)_3$, which in turn influenced Si-related phases. It is believed that Si-related phases in red mud were too stable to completely release SiO_2 required for the synthesis of NF.

In conclusion, at a $CaCO_3$/red mud ratio of 1.5, the content of C_2S+C_4AF in NF reached the maximum value. A further increase in $CaCO_3$ content in the raw materials resulted in the decrease of required C_4AF and unnecessary production of CaO and $CaCO_3$ residue. Hence, in the following sections, the ratio of $CaCO_3$/red mud would be taken as

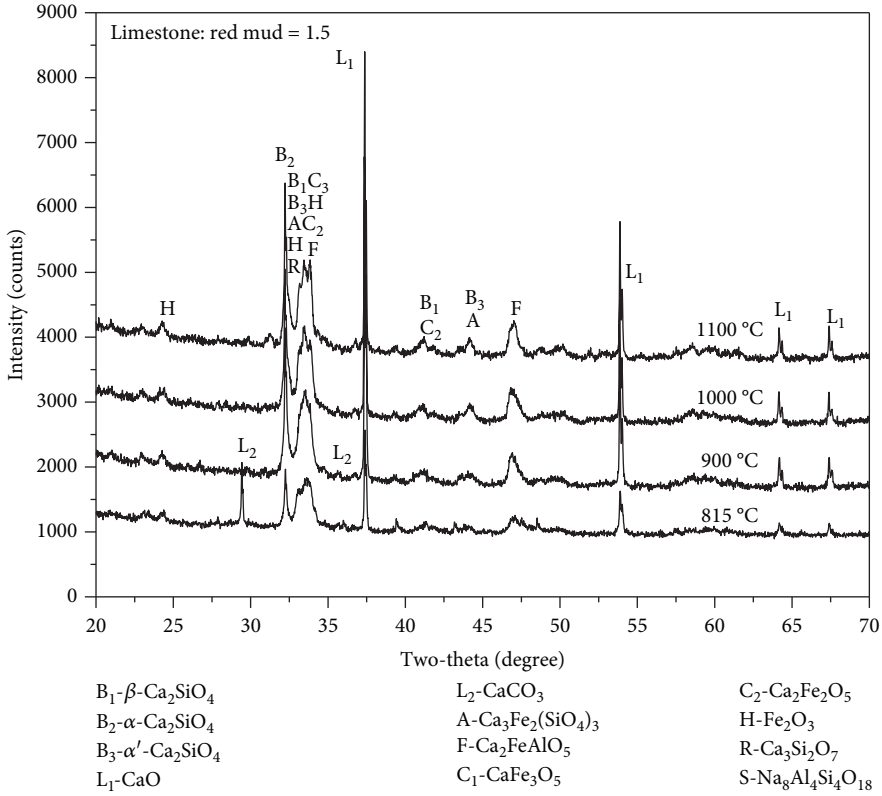

Figure 5: XRD spectra of NF produced at different heating temperatures.

1.5 and the heating temperature would be varied to evaluate the possibility of improving conversion efficiency of raw materials.

3.1.4. Influence of Heating Temperature. In order to study the effect of the heating temperature on NF prepared with a $CaCO_3$/red mud ratio of 1.5, the XRD of NF samples synthesized at 815, 900, 1000, and 1100°C, respectively, was evaluated. The results are presented in Figure 5. It can be seen that the peak intensity corresponding to brownmillerite (Ca_2FeAlO_5) increased slightly with the increase in temperature. However, above 900°C, the change was not significant. It is known that the synthesis temperatures of α-C_2S, α'-C_2S, and β-C_2S are higher than 1450, 725, and 500°C, respectively [33]. Therefore, the α-C_2S level increased sharply with the increase in temperature while α'-C_2S and β-C_2S were not influenced significantly by the increase in temperature.

In addition, it can be observed that above 900°C, the peak of $CaCO_3$ disappeared, while the peak of CaO gradually increased when the heating temperature was higher than 900°C, suggesting that extra heat was required to decompose $CaCO_3$ into CaO. The peak intensities of other products shown in Figure 5 remained unchanged. Therefore, it can be deduced that from the perspective of energy saving and efficiency, the temperature required to convert raw materials to target product (synthesis of NF) is 815°C.

3.1.5. Morphology and Fineness of NF. The morphology of typical NF synthesized at an optimal $CaCO_3$/red mud ratio of 1.5 and heating temperature of 815°C is shown in Figure 6. It can be seen from Figure 6(a) that the sintered NF has a particle size of approximately 300 nm and its shape is nearly spherical. The comparison of BSE images of NF (Figure 6(b)) and PC (Figure 6(c)) for PC also shows that the size of the NF was much smaller than that of the PC particles.

3.2. Hydration of NF. After determining the optimal synthesis temperature of NF, SEM and XRD techniques were used to determine the hydration products of NF. The SE image after 28 days of NF hydration presented in Figure 7(a) shows that the morphology of the main hydration product is flaky. The BSE image of hydrated NF presented in Figure 7(b) shows that the prepared NF had been significantly hydrated at the age of 28 days. It suggests that the reduction of the particle size of ferrite to nanoscale could effectively accelerate hydration when compared with a traditional ferrite material, which has not shown significant hydration at the age of 28 days [34].

The XRD spectra of NF hydrated at the age of 3, 7, 14, 28, and 56 days are presented in Figure 8. At this time, a large number of early hydration products $C(A,F)H_{10}$ and a small amount of $C_2(A,F)H_8$ were formed. This confirmed that the prepared NF had hydrated significantly at 3 days. At this age, the content of C_2S in NF decreased and the content of hydration product $Ca(OH)_2$ increased, indicating that C_2S had also hydrated. However, during the first 56 days, the content of C_2S decreased slowly, which confirmed that the early hydration of C_2S was still slow. At

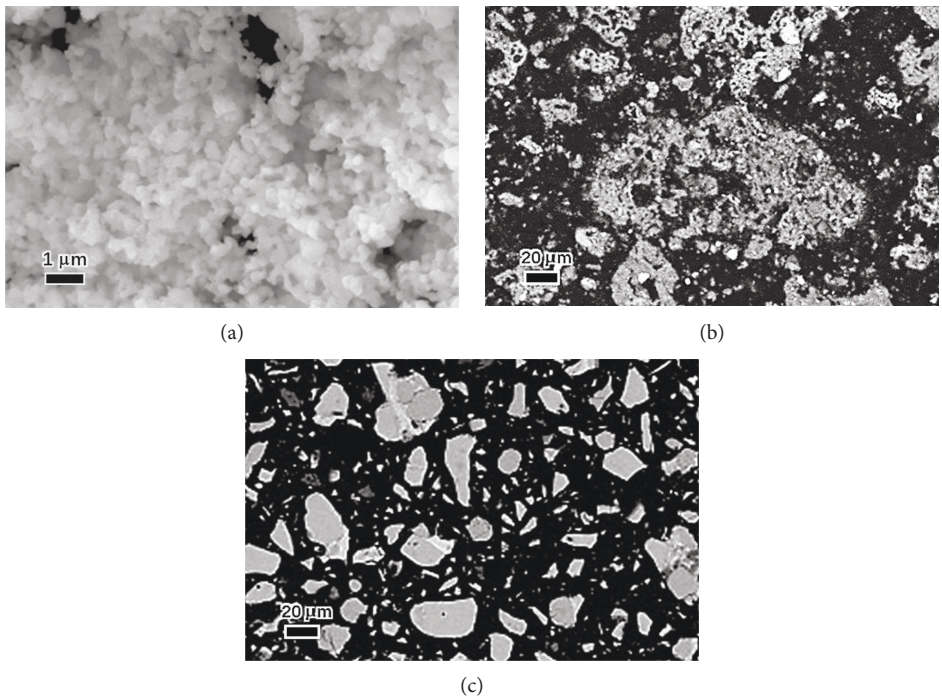

(a) (b)

(c)

Figure 6: SEM images of NF produced at $CaCO_3$/red mud of 1.5 and temperature of 815°C. (a) NF (SE). (b) NF (BSE). (c) PC (BSE).

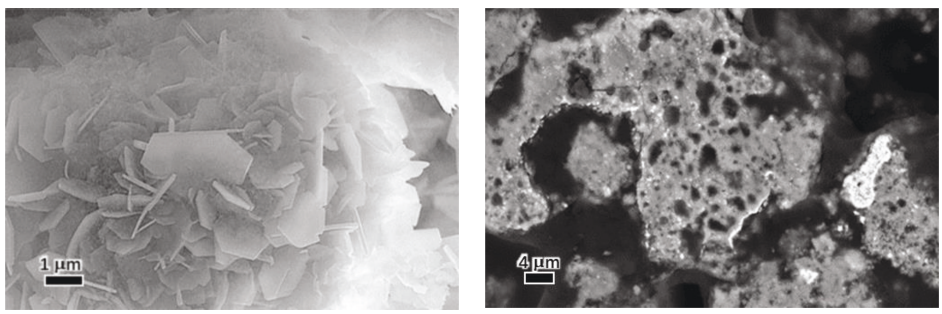

(a) (b)

Figure 7: SEM images of hydrated NF at the age of 28 days. (a) Micrograph by SE. (b) Cross-sectional image by BSE.

the age of 7 days, the content of $C(A,F)H_{10}$ decreased and the content of $C_2(A,F)H_8$ increased due to the gradual transformation of $C(A,F)H_{10}$ to $C_2(A,F)H_8$ crystals. At 14 days, the content of $C(A,F)H_{10}$ decreased and the content of $C_2(A,F)H_8$ increased further. Meanwhile, $C_3(A,F)H_6$ started to appear [35]. At 28 days, the content of $C_3(A,F)H_6$ further increased while the contend of $Ca(OH)_2$ decreased. At this age, a diffraction peak of $CaCO_3$ appeared due to carbonation. At the age of 56 days, the $C(A,F)H_{10}$ crystal almost disappeared, $C_2(A,F)H_8$ content decreased significantly, and $C_3(A,F)H_6$ content increased significantly. This indicated that $C(A,F)H_{10}$ and $C_2(A,F)H_8$ were so unstable that they transformed into more stable $C_3(A,F)H_6$ at later ages and is consistent with the findings presented in references [15, 36].

3.3. Mechanical Properties of NF. In order to further investigate the properties of NF as an admixture, the mechanical properties of cement mortars were determined by replacing a specific content of PC by 0, 5, 10, 15, and 20% of NF, respectively. The results of mechanical properties at the age of 3, 7, 14, and 28 days are presented in Figure 9. The figure indicates that the flexural and compressive strengths of all samples increased with the increase in the age of testing. As the replacement level of NF increased from 0% to 20%, the flexural and compressive strengths first increased and then decreased, reaching the maximum compressive and flexural strengths at 5% substitution level. Moreover, specimens prepared with 5% replacement level achieved the highest flexural and compressive strengths than the control mix (specimens with 0% replacement) at all ages. Compared with the control specimens, the flexural and compressive strengths of the 5% substitution specimens increased by 15.4% and 9.0%, respectively, at the age of 3 days, and by 9.0% and 6.7%, respectively, at 28 days. The increase in strength is much higher than that of mortar prepared with 5% traditional ferrite

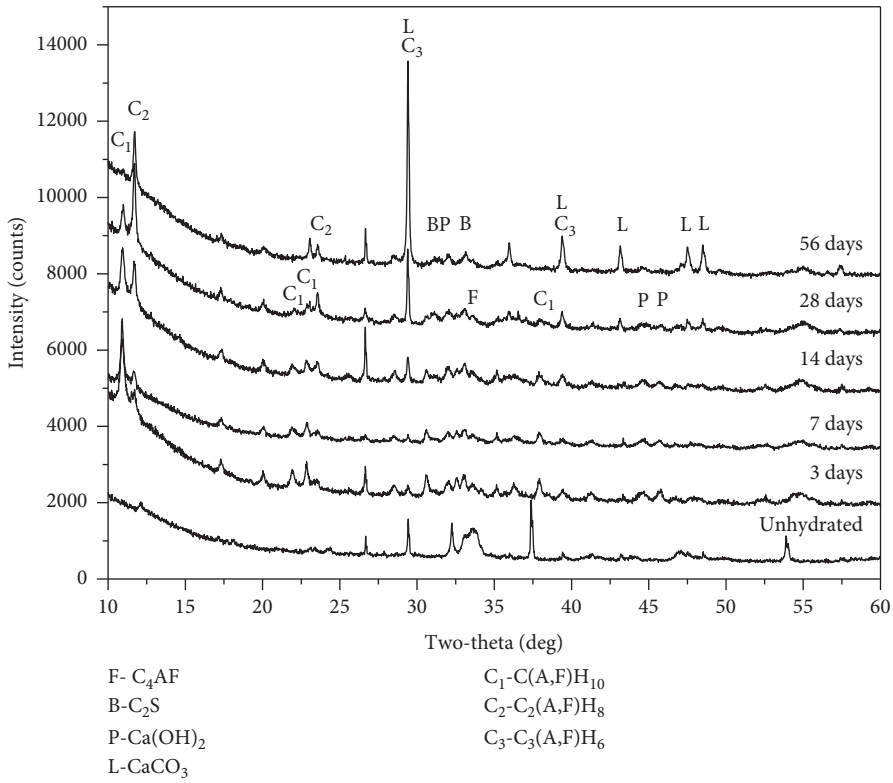

Figure 8: XRD spectra of hydrated NF cured at different ages.

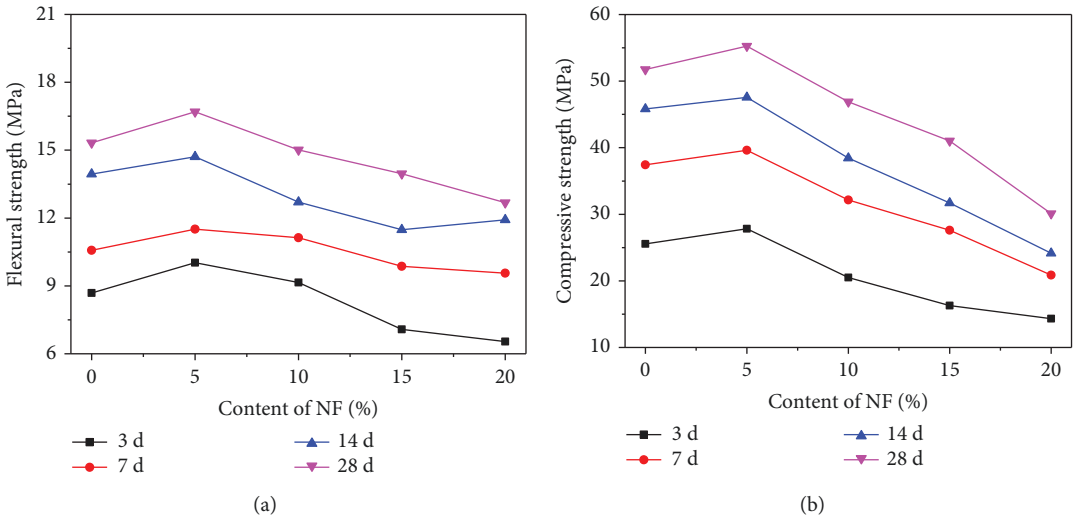

Figure 9: The flexural and compressive strength of cement mortars prepared with different contents of NF.

additive produced by red mud (compressive strength enhanced by 5% at 28 days) [37] as well as mortar prepared with 3.5% as-received red mud (compressive strength enhanced by 0% at 3 days and by 4.5% at 28 days) [38]. It indicates that reprocessing of red mud and nanocrystallization could effectively improve the mechanical properties on cementitious materials. Unfortunately, at other replacement levels, such as 10%, 15%, and 20%, the overall flexural strength and compressive strength were lower than control specimens. Therefore, with increasing NF content in cement mortar, the mechanical properties of cement mortar did not always increase but achieved maximum mechanical strength at the 5% replacement level.

The increase in strength at 5% NF when compared with that of control specimen is believed to be due to the following reasons: (1) NF particles having nanoscale size were effective in filling and improving packing density of mortar, and this in turn reduced the porosity of the system. (2) The

appropriate amount of nanomaterials could improve the interfacial transition zone (ITZ) between sand and cement paste [39].

As mentioned earlier, when the dosage of NF exceeded 5%, the flexural and compressive strengths of mortar decreased. This can be attributed to the following reasons: (1) The hydration of C_2S and C_4AF in NF was still slower than that of PC, resulting in lower flexural and compressive strengths than the control mortar during the tested period (until 28 days). (2) It is believed that the NF particles might not have been sufficiently dispersed especially at high dosage and the aggregation of nanoparticles existed as defects in mortar and caused decrease in flexural and compressive strengths.

Therefore, the amount of NF dosage plays an important role in the strength development of cement mortar. Hence, higher compressive strength can be expected if the dispersion technique of NF in PC cement could be improved. However, further investigation is required and proposed for future research.

4. Conclusions

In this research, NF was synthesized by a chemical combustion method using red mud as one of the raw materials. By using stoichiometric calculation and experimental verification, the optimal conditions for NF preparation were found at a $CaCO_3$/red mud ratio of 1.5 and a heating temperature of 815°C. The synthesized NF particles were roughly spherical in shape with an approximate size of 300 nm. The dominant composition of NF was found to be C_4AF (47.2%) and C_2S (8.6%). The decrease in the particle size of ferrite enhanced early hydration. Flaky hydration products of $C(A,F)H_{10}$ and $C_2(A,F)H_8$ were formed and at later ages were gradually converted into a more stable cubic $C_3(A,F)H_6$. NF could enhance the mechanical properties when it was used as a replacement of cement in cement-based composite. At the 5% replacement level of cement with NF, the flexural and compressive strengths increased by 15% and 9%, respectively.

From the aspect of energy consumption and quality of product, NF was synthesized at a much lower temperature (≦1150°C) than traditional ferrite cement (1250-1300°C); thus, it would save a lot of sintering energy. The synthesized NF particles have a porous structure and are loosely agglomerated hence requiring slight grinding before it can be used as an admixture. This would greatly reduce the post grinding energy and further reduce the production cost. Additionally, the produced NF particles have a round shape with a relatively uniform particle size distribution, which is beneficial for the workability of concrete. In the future work, effort would be put to reduce the cost of fuels in order to reduce the overall production cost.

In general, red mud can be converted into hydraulic NF through a chemical combustion method and it provides a new approach for the utilization of red mud in construction industry.

Data Availability

The data used to support the findings of this study are included within the article.

Conflicts of Interest

The authors declare that there is no conflict of interest regarding the publication of this paper.

Acknowledgments

This research work was supported by the National Natural Science Foundation of China (Grant Nos. 51878412, 51520105012, 51878413, 51678368, and 51508338), the (Key) Project of Department of Education of Guangdong Province (Grant No. 2014KZDXM051), and the Shenzhen R&D Fund (Grant No. JCYJ20170818100641730). We also thank the Guangdong Provincial Key Laboratory of Durability for Marine Civil Engineering, College of Civil and Transportation Engineering, Shenzhen University, for providing facilities and equipment.

References

[1] S. Patel and B. K. Pal, "Current status of an industrial waste: red mud an overview," *Ijltemas*, vol. 4, no. 8, pp. 1–6, 2015.

[2] J. Ortega, M. Cabeza, A. Tenza-Abril, T. Real-Herraiz, M. Climent, and I. Sánchez, "Effects of red mud addition in the microstructure, durability and mechanical performance of cement mortars," *Applied Sciences*, vol. 9, no. 5, p. 984, 2019.

[3] V. Dethlefsen and H. Rosenthal, "Problems with dumping of red mud in shallow waters. A critical review of selected literature," *Aquaculture*, vol. 2, pp. 267–280, 1973.

[4] H. Zhang, H. Li, Y. Zhang, D. Wang, J. Harvey, and H. Wang, "Performance enhancement of porous asphalt pavement using red mud as alternative filler," *Construction and Building Materials*, vol. 160, pp. 707–713, 2018.

[5] S. Baseden and D. Grey, "Environmental study of the disposal of red mud waste," *Marine Pollution Bulletin*, vol. 7, no. 1, pp. 4–7, 1976.

[6] Y. Çengeloğlu, E. Kir, and M. Ersöz, "Recovery and concentration of Al(III), Fe(III), Ti(IV), and Na(I) from red mud," *Journal of Colloid and Interface Science*, vol. 244, no. 2, pp. 342–346, 2001.

[7] S. Sushil and V. S. Batra, "Catalytic applications of red mud, an aluminium industry waste: a review," *Applied Catalysis B: Environmental*, vol. 81, no. 1-2, pp. 64–77, 2008.

[8] J. Carneiro, D. M. Tobaldi, W. Hajjaji et al., "Red mud as a substitute coloring agent for the hematite pigment," *Ceramics International*, vol. 44, no. 4, pp. 4211–4219, 2018.

[9] C. Klauber, M. Gräfe, and G. Power, "Bauxite residue issues: II. Options for residue utilization," *Hydrometallurgy*, vol. 108, no. 1-2, pp. 11–32, 2011.

[10] C. Shi, P. E. Grattan-Bellew, and J. A. Stegemann, "Conversion of a waste mud into a pozzolanic material," *Construction and Building Materials*, vol. 13, no. 5, pp. 279–284, 1999.

[11] D. V. Ribeiro, J. A. Labrincha, and M. R. Morelli, "Potential use of natural red mud as pozzolan for Portland cement," *Materials Research*, vol. 14, no. 1, pp. 60–66, 2011.

[12] W. C. Tang, Z. Wang, Y. Liu, and H. Z. Cui, "Influence of red mud on fresh and hardened properties of self-compacting concrete," *Construction and Building Materials*, vol. 178, pp. 288–300, 2018.

[13] P. Krivenko, O. Kovalchuk, A. Pasko et al., "Development of alkali activated cements and concrete mixture design with high volumes of red mud," *Construction and Building Materials*, vol. 151, pp. 819–826, 2017.

[14] L. Zhang, M. Su, and Y. Wang, "The research and application of ferrite cement with high strength," *China Concrete And Cement Products*, no. 6, pp. 11–15, 1994.

[15] Y. Hong, "Preparation and properties of aluminoferrite cement clinker based on the slag of Ti-Si-V-Fe alloy-making from Titania-rich BF slag," in *Material Science*, p. 69, Wuhan University of Science and Technology, China National Knowledge Infrastructure, 2014.

[16] K. Behfarnia and N. Salemi, "The effects of nano-silica and nano-alumina on frost resistance of normal concrete," *Construction and Building Materials*, vol. 48, pp. 580–584, 2013.

[17] H. R. Jiang, Y. K. Zeng, M. C. Wu, W. Shyy, and T. S. Zhao, "A uniformly distributed bismuth nanoparticle-modified carbon cloth electrode for vanadium redox flow batteries," *Applied Energy*, vol. 240, pp. 226–235, 2019.

[18] H. Li, L. Luo, P. Kunal et al., "Oxygen reduction reaction on classically immiscible bimetallics: a case study of RhAu," *The Journal of Physical Chemistry C*, vol. 122, no. 5, pp. 2712–2716, 2018.

[19] H. Li, K. Shin, and G. Henkelman, "Effects of ensembles, ligand, and strain on adsorbate binding to alloy surfaces," *The Journal of Chemical Physics*, vol. 149, no. 17, article 174705, 2018.

[20] C. Duan, F. Li, M. Yang, H. Zhang, Y. Wu, and H. Xi, "Rapid synthesis of hierarchically structured multifunctional metal–organic zeolites with enhanced volatile organic compounds adsorption capacity," *Industrial & Engineering Chemistry Research*, vol. 57, no. 45, pp. 15385–15394, 2018.

[21] M. Katsioti, P. E. Tsakiridis, P. Giannatos, Z. Tsibouki, and J. Marinos, "Characterization of various cement grinding aids and their impact on grindability and cement performance," *Construction and Building Materials*, vol. 23, no. 5, pp. 1954–1959, 2009.

[22] L. Y. Li and G. K. Rutherford, "Effect of bauxite properties on the settling of red mud," *International Journal of Mineral Processing*, vol. 48, no. 3-4, pp. 169–182, 1996.

[23] P. F. Rossi, G. Caracciolo, and G. Busca, "Evolution of the surface of haematite prepared by thermal decomposition of goethite: a microcalorimetric study," *Colloids and Surfaces*, vol. 32, no. 1-2, pp. 75–85, 1988.

[24] S. Ananthakumar, G. Krishnapriya, A. D. Damodaran, and K. G. K. Warrier, "Thermal decomposition characteristics of boehmite gels under microwave heating and associated microstructural features," *Materials Letters*, vol. 35, no. 1–2, pp. 95–99, 1998.

[25] J. Felsche and S. Luger, "Phases and thermal decomposition characteristics of hydro-sodalites $Na_{6+x}[AlSiO_4]_6,(OH)_x \cdot nH_2O$," *Thermochimica Acta*, vol. 118, no. 1, pp. 35–55, 1987.

[26] A. Tsetsekou, "A comparison study of tialite ceramics doped with various oxide materials and tialite–mullite composites: microstructural, thermal and mechanical properties," *Journal of the European Ceramic Society*, vol. 25, no. 4, pp. 335–348, 2005.

[27] J. Ye, W. Zhang, and D. Shi, "Effect of elevated temperature on the properties of geopolymer synthesized from calcined ore-dressing tailing of bauxite and ground-granulated blast furnace slag," *Construction and Building Materials*, vol. 69, no. 11, pp. 41–48, 2014.

[28] D. Herfort, G. K. Moir, V. Johansen, F. Sorrentino, and H. B. Arceo, "The chemistry of Portland cement clinker," *Advances in Cement Research*, vol. 22, no. 4, pp. 187–194, 2010.

[29] C. Wu and D. Liu, "Mineral phase and physical properties of red mud calcined at different temperatures," *Journal of Nanomaterials*, vol. 2012, Article ID 628592, 6 pages, 2012.

[30] H. Zhang, "Cement section 1:portland cement," in *Book of Building Materials in Civil Engineering*, pp. 46–423, Woodhead Publishing, Sawston, UK, 2011.

[31] M. Singh, S. N. Upadhayay, and P. M. Prasad, "Preparation of special cements from red mud," *Waste Management*, vol. 16, no. 8, pp. 665–670, 1996.

[32] J. Chang and H. Wu, "Study on carbonation mechanism of steel slag," *Journal of the Chinese Ceramic Society*, vol. 38, no. 7, pp. 1185–1190, 2010.

[33] W. Zhao and J. Chang, "Sol–gel synthesis and in vitro bioactivity of tricalcium silicate powders," *Materials Letters*, vol. 58, no. 19, pp. 2350–2353, 2004.

[34] Y. Guo, M. Su, J. Deng, and Y. Wng, "Study on hydration characteristics of iron phase in iron aluminate cement," *China Academic Journal Electronic Publishing House*, vol. 17, no. 4, pp. 296–301, 1989.

[35] B. Dou, "Sythesis and research on properties of nano-cement clinker minerals," in *Material Engineering*, p. 56, Hebei United University, China National Knowledge Infrastructure, 2014.

[36] C. Gosselin, "Microstructural development of calcium aluminate cement based systems with and without supplementary cementitious materials," in *Institute of Materials*, p. 234, EPFL, Lausanne, Switzerland, 2009.

[37] I. Vangelatos, G. N. Angelopoulos, and D. Boufounos, "Utilization of ferroalumina as raw material in the production of Ordinary Portland Cement," *Journal of Hazardous Materials*, vol. 168, no. 1, pp. 473–478, 2009.

[38] P. E. Tsakiridis, S. Agatzini-Leonardou, and P. Oustadakis, "Red mud addition in the raw meal for the production of Portland cement clinker," *Journal of Hazardous Materials*, vol. 116, no. 1-2, pp. 103–110, 2004.

[39] H. Li, H. Xiao, J. Yuan, and J. Ou, "Microstructure of cement mortar with nano-particles," *Composites Part B: Engineering*, vol. 35, no. 2, pp. 185–189, 2004.

Hindawi
Journal of Nanomaterials
Volume 2019, Article ID 2326042, 12 pages
https://doi.org/10.1155/2019/2326042

Research Article

Study on Photocatalytic Antibacterial and Sustained-Release Properties of Cellulose/TiO_2/β-CD Composite Hydrogel

Hui Zhang, Jiangying Zhu, Yanqiang Hu, Aonan Chen, Liang Zhou, Hui Gao, Yamei Liu, and Shengquan Liu

School of Forestry and Landscape Architecture, Anhui Agricultural University, Hefei 230036, China

Correspondence should be addressed to Shengquan Liu; liusq@ahau.edu.cn

Received 27 March 2019; Revised 30 May 2019; Accepted 28 June 2019; Published 24 July 2019

Guest Editor: Yunpan Ying

A novel cellulose/TiO_2/β-CD hydrogel with high photocatalytic antibacterial activity and sustained release of drug was prepared. TiO_2 sol with a diameter of about 9 nm in this hydrogel was the photoantibacterial agent. β-CD can significantly enhance photoantibacterial activity and the sustained-release effect of this hydrogel. The structure and property of this hydrogel composite were characterized by Fourier transform infrared spectroscopy (FTIR), X-ray diffraction (XRD), scanning electron microscopy (SEM), and transmission electron microscopy (TEM). *Escherichia coli* and *Staphylococcus aureus* were selected as model bacteria to evaluate the antibacterial activity of the composite hydrogel under natural light irradiation and darkness, respectively. The in vitro release experiment used curcumin as a model drug in PBS buffer solution. The influence of β-CD on the antibacterial activity and sustained-release effect of the composite hydrogel was investigated. The results showed that the hydrogel composite presented a good photoantibacterial property, while the antibacterial activity can be neglected under the condition of no light. The complete release of curcumin from the composite was achieved after 120 h. Therefore, the hydrogel system has the characteristics of low cost and high effect, which could be used for an antibacterial sustained-release material.

1. Introduction

Cellulose is one of the most abundant biomass materials and possesses many promising properties, which has been widely used in all areas of society. The application of cellulose-based materials has received great attention in recent years [1, 2].

Hydrogels are three-dimensional, cross-linked polymeric networks which possess an ability to swell in water without getting dissolved in it [3]. With the advantages of renewability, biocompatibility, biodegradability, and thermal and chemical stabilities, cellulose-based hydrogels can be used for wound healing [4], tissue engineering [5], and drug carrying [6].

However, due to a lack of bactericidal property and the inherent incompatibility between hydrophobic drugs and the hydrophilic nature of the cellulose net, the release of hydrophobic drugs from cellulose-based hydrogels cannot be controlled for a long duration [7].

β-CD contains a peculiar hydrophobic cavum and could form inclusion complexes with various guest molecules. Zhang et al. have synthesized cellulose hydrogels by the addition of β-CD cross-linked with epichlorohydrin (ECH) in a NaOH/urea aqueous solution; these hydrogels could complex 5-FU with β-CD that restrains the release from the hydrogels because the inclusion interactions are too strong to let 5-FU complex into the cavity of β-CD [8]. However, this hydrogel still lacks a bactericidal property, and the influence of β-CD with a cross-linker on the hydrogel formed has not been studied.

The addition of TiO_2 sol can improve the antimicrobial performance of the cellulose-based hydrogel. TiO_2 sol has been widely used in the fields of photovoltaics, photocatalysis, and antibiosis. It is now well established that TiO_2 produces electrons and holes upon exposure to light, subsequently leading to the formation of reactive oxygen species (ROS). These oxygen species are highly reactive

with both cell membrane and cytoplasmic materials. And the point of attack depends on the particle location upon excitation. Such oxidative reactions can affect cell integrity and the chemical arrangement of surface structures and are the main mechanisms of their photocatalytic antibacterial activities [9–11].

Nonetheless, photocatalytic antibacterial efficiency is still not high due to the rapid recombination of the electron and hole of TiO_2 particles [12]. To improve the effect of TiO_2, β-cyclodextrins (β-CD) are added as a photocatalytic promoter based on their hydrophobic inner cavity, the charge transfer rate from the photoexcited semiconductor to electron acceptors is accelerated, and the photocatalytic substrates onto the TiO_2 surface are concentrated [13].

To form a hydrogel from dissolved cellulose, a cross-linking process is required. The aim of the cross-linking process is to improve the insolubility, mechanical strength, stiffness, and rigidity of the polymer. One of the most common cross-linkers used is epichlorohydrin (ECH) [14]. Even though ECH is toxic in nature, its toxicity is diminished after a rinsing process [15]. For this reason, ECH was used to cross-link a cellulose-based composite hydrogel in this manuscript.

In this study, a novel cellulose/TiO_2/β-CD hydrogel composite was prepared. As illustrated in Scheme 1, we prepared the hydrogel by adding TiO_2 sol, which was synthesized in advance by a sol-gel method and a β-CD-to-cellulose solution; then, the mixture was cross-linked with epichlorohydrin (ECH). The structure and properties of the obtained hydrogel composite were characterized by Fourier transform infrared spectroscopy (FTIR), X-ray diffraction (XRD), scanning electron microscopy (SEM), and transmission electron microscopy (TEM). *Escherichia coli* and *Staphylococcus aureus* were selected as model bacteria to evaluate the bactericidal activity of the hydrogel under natural light and darkness, respectively. The in vitro release experiment chose hydrophobic curcumin as the model drug in the PBS buffer solution (pH = 7.4). This hydrogel system possesses the characteristics of a simple preparation process, low cost, and high effect, which may be used as an antibacterial and sustained-release material.

2. Experimental

2.1. Materials. Tetrabutyl titanate, β-CD (MW = 1134.98), disodium hydrogen phosphate (Na_2HPO_4), sodium chloride (NaCl), potassium chloride (KCl), sodium hydroxide (NaOH), urea, and curcumin were obtained from Aladdin Reagent Database Inc. (Shanghai, P.R. China). 1,3-Diphenylisobenzofuran (DPBF) was purchased from Acros Organics (Geel, Belgium). Qualitative filter paper was obtained from Titan Reagent Database Inc. (Shanghai, P.R. China). All reagents were of analytical grade and were used without further purification. Double-distilled water was used in the whole experiment.

2.2. Synthesis of TiO_2 Sol. TiO_2 sol with a solid content of 25% was synthesized by the hydrolysis of tetrabutyl titanate. In brief, 3.5 mL of tetrabutyl titanate was added to a solution containing 47 mL of water and 8 mL of acetic acid. After magnetic stirring for 2 h, the nearly transparent appearance of sol was obtained. The sol was stored in a sealed vial to age overnight, and then the sol was stored in a fridge set at 4°C for a maximum period of one month, to prevent excessive ageing.

2.3. Cellulose/TiO_2/β-CD Hydrogel Preparation. The cellulose solution was prepared according to methods reported by literature. 4 g of qualitative filter paper was dissolved in 81 mL of deionized water containing 7 g of NaOH and 12 g of urea which were filtered with a G2 sand filter. The solution was stirred for 5 min and stored in a refrigerator for 12 h; the solution was then brought back to room temperature, stirred extensively to obtain a colorless and transparent solution, and then centrifuged for 15 min (7200 rpm) at 15°C. Then, β-CD was added at concentrations of 1.0, 2.0, 3.0, 4.0, 5.0, 6.0, 7.0, 8.0, 9.0, and 10 wt%, and the TiO_2 sol was added to the β-CD/cellulose solutions with the concentration of 5% (v/v). 10 mL of ECH was added into the cellulose/TiO_2/β-CD mixture solution and reacted for 30 min under room temperature and then kept at 50°C for 5 h to obtain the composite hydrogel [8, 16].

2.4. Characterization. The FTIR spectra of the cellulose/-TiO_2/β-CD hydrogel were collected with a Bruker Tensor II Fourier transform infrared spectrometer. The test specimens were prepared by the KBr-disc method. The particle sizes of the TiO_2 were measured by a Nano ZS (Malvern Co., U.K.). The phase structure and purity of the TiO_2 were examined by X-ray diffraction (XRD) using a MAP18XAHF with a diffract meter with Cu Kα radiation ($\lambda = 1.54$ Å) at a scanning rate of 2°/min. The morphology and microstructure were characterized by a SEM instrument (Hitachi S-4800, Japan) and an EDX (Oxford Instruments Link ISIS). The fractured surfaces of the hydrogels were sputtered with gold before they were observed and photographed. The UV-vis absorbance was measured by using a UV-1800 spectrophotometer (Shimadzu, Japan).

2.5. Swelling Experiments. The swelling capacity of the cellulose/TiO_2/β-CD hydrogel with respect to time was carried out. The experiment was performed using a definite quantity of the material, which was transferred to a previously weighed tea bag and then placed in a beaker containing 100 mL of distilled water at room temperature for 24 h to attain equilibrium. The samples were collected from the distilled water at regular intervals. Before the weights of the hydrogel were recorded, the surfaces of the hydrogels had been wiped with filtered paper to remove water. The sample weights were recorded as the average of three measurements.

2.6. Antibacterial Studies. The antibacterial activity of the final product was screened by the disc diffusion method using *Escherichia coli* and *Staphylococcus aureus*. Cellulose/-TiO_2/β-CD hydrogels were cut into a disc shape with a diameter of 10 mm (360 mg by weight), which was the same size as the samples. Next, fresh precultures of *Escherichia coli* and *Staphylococcus aureus* were spread on the agar plate, and the samples were placed on top and incubated at 37°C

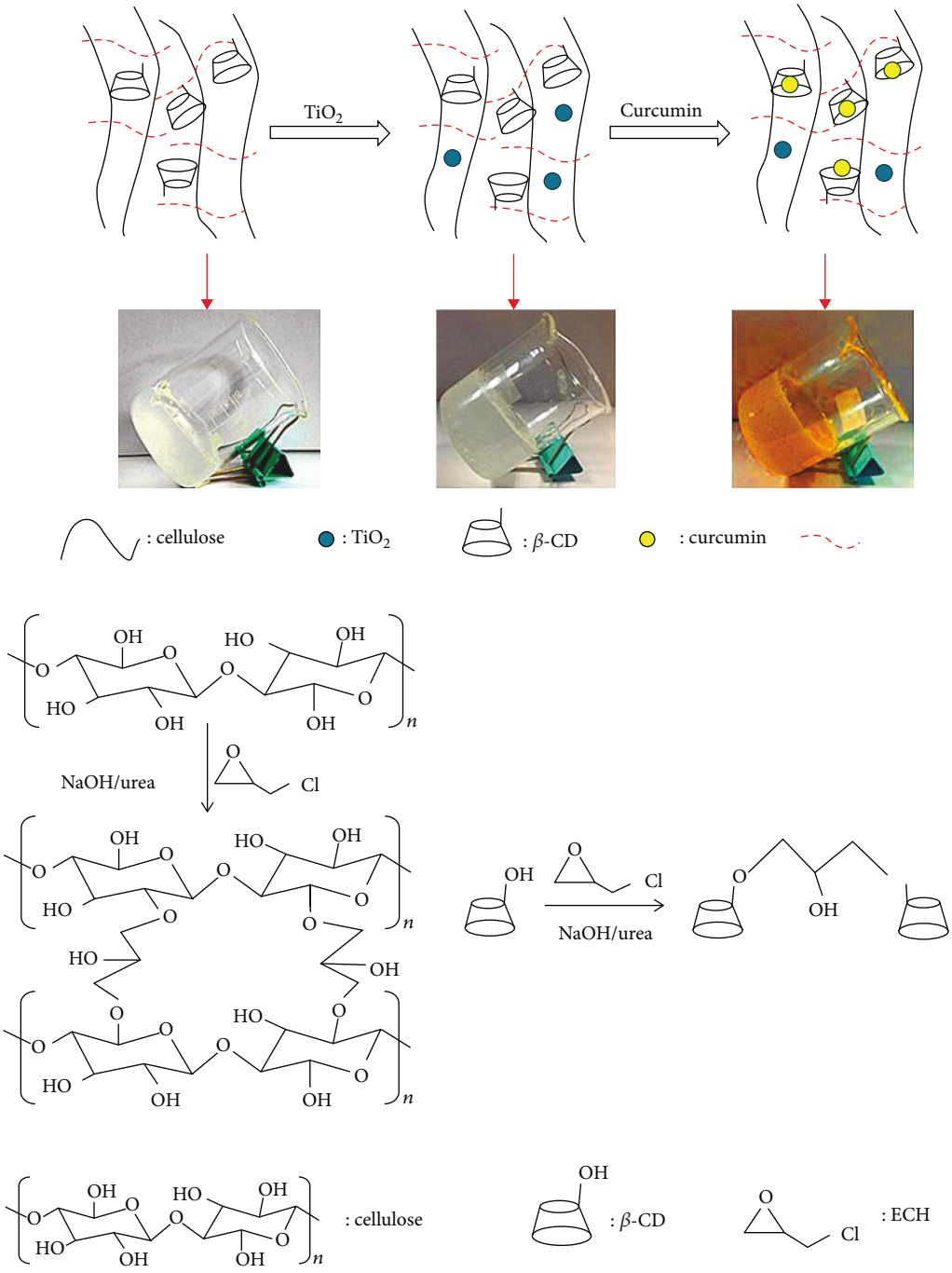

Scheme 1: Schematic illustration of the curcumin-carrying composite hydrogel and the proposed mechanism for the cross-linking reaction of ECH with β-CD and cellulose.

for 24 h exposed to natural light. Finally, the inhibition zones were measured. To test the contribution of β-CD to the antimicrobial activity, the ring of inhibition was measured for different composites with the same cellulose/-TiO_2 concentrations. In addition, the dark reaction and the blank experiments of the composite hydrogels were also done. In blank experiments, the antibacterial effect of the cellulose/β-CD (4 wt%) hydrogel without TiO_2 sol and with 1 mL, 2 mL, and 3 mL TiO_2 sol was compared with light irradiation.

The ROS generated from the cellulose/TiO_2/β-CD hydrogel with different concentrations of β-CD under natural light irradiation was determined by decomposing 1,3-diphenylisobenzofuran (DPBF) in ethanol at 410 nm, which can be measured by using a UV-1800 spectrophotometer.

2.7. Drug Loading and In Vitro Release. Curcumin was chosen as the model drug for sustained release by a swelling equilibrium method [17]. Curcumin loading was carried out by dispersing 100 mg of the dried cellulose/TiO_2/β-CD

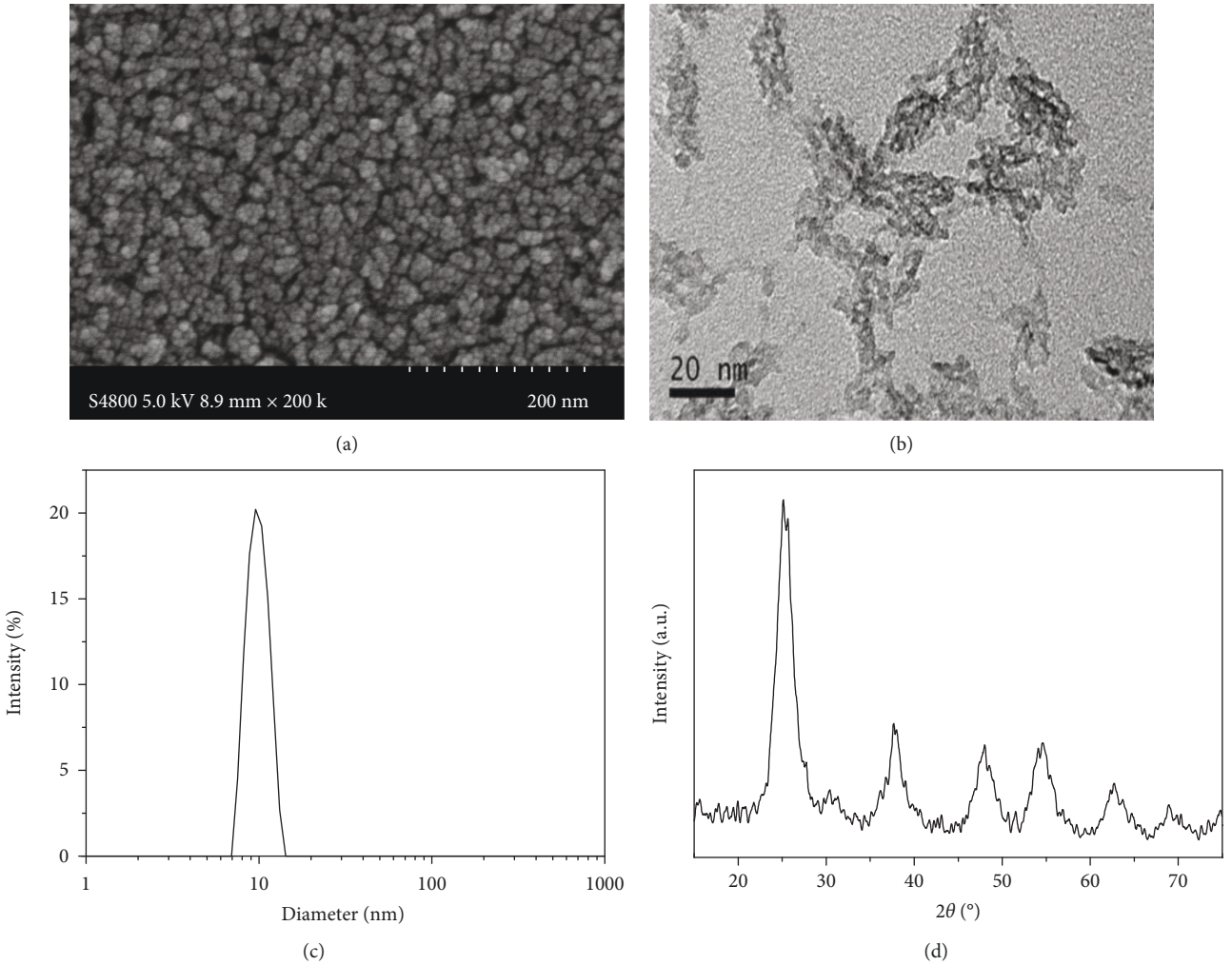

Figure 1: (a) SEM image, (b) TEM image, (c) size distribution curve, and (d) XRD pattern of the prepared TiO_2 sol.

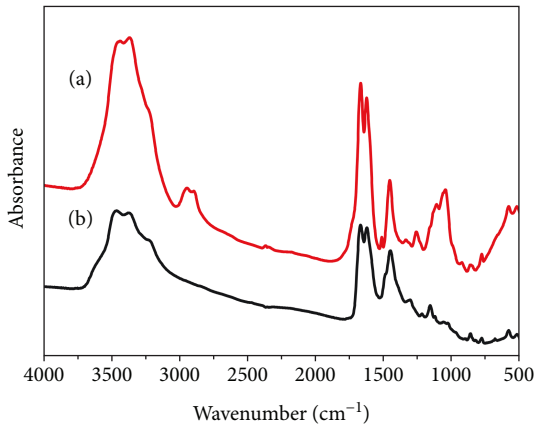

Figure 2: FTIR spectra of the cellulose/TiO_2/β-CD hydrogel before (a) and after (b) cross-linking by ECH.

hydrogel in a mixture of 1 mg/mL curcumin aqueous solution and 50 mL phosphate buffer solution (PBS, pH = 7.4) and then stirring for 24 h to reach the equilibrium state at 37°C. The mixed solution was centrifuged, and the supernatant was collected and subjected to UV-vis analysis at λ_{max} = 440 nm [18]. The loading efficiency was calculated using the following:

$$\text{Loading efficiency}(\%) = \frac{\text{total curcumin} - \text{free curcumin}}{\text{total curcumin}}. \quad (1)$$

Then, the hydrogel was fetched out and vacuum dried at 45°C. The in vitro release was carried out at 37°C in phosphate buffer solution (PBS, pH = 7.4). The release study was performed by immersing the above drug-loaded hydrogel in a glass bottle filled with PBS. After specified time intervals (12 h), it was centrifuged and the supernatant solution was collected and subjected to UV-vis analysis at λ_{max} = 440 nm. The percentage amount of curcumin released was calculated and plotted versus time according to the following [19]:

$$\text{Drug release}(\%) = \frac{\text{released curcumin}}{\text{total curcumin}}. \quad (2)$$

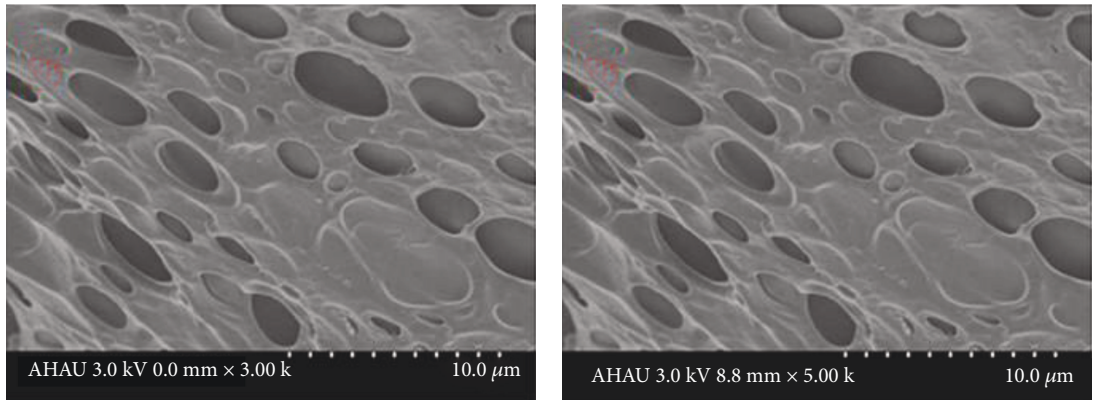

(a) (b)

Figure 3: SEM images of the cellulose/TiO_2 hydrogel (a) and cellulose/TiO_2/β-CD hydrogel (b).

3. Results and Discussion

3.1. Characterization of TiO_2 Sol. The TiO_2 sol was prepared by the sol-gel method. The SEM and TEM analyses of the prepared TiO_2 sol exhibiting an irregular shape are shown in Figures 1(a) and 1(b). The size distribution of TiO_2 sol determined by dynamic light scattering (DLS) is presented in Figure 1(c). The average particle size of TiO_2 sol is about 9 nm. It is well known that the small size of TiO_2 sol has a much higher active surface energy, and it can be used as a highly efficient photoantibacterial agent.

The XRD pattern of TiO_2 sol (Figure 1(d)) exhibits six major reflection peaks at 2θ of 25.2°, 38.5°, 48.0°, 55.0°, 62.6°, and 70.3°, which can be well indexed to the (101), (112), (200), (211), (204), and (220) planes of anatase TiO_2 (JCPDS Card No. 21-1272), respectively [20].

3.2. Preparation of Cellulose/TiO_2/β-CD Composite Hydrogel. A cellulose solution with a concentration of 4.0 wt% was prepared according to the previous method. The cellulose/-TiO_2/β-CD composite hydrogel was synthesized with different concentrations of TiO_2 sol and β-CD in the cellulose solution with ECH as a cross-linking agent. The proper quantity of TiO_2 sol to the volume ratio of the cellulose solution is 5% (v/v). This ratio is adopted in the following results.

As plenty of hydroxyls in β-CD could react with ECH, the content of β-CD may impact the gelation properties of the composite hydrogel. The hydrogel was very soft when the β-CD content was below 3 wt%, and the hydrogel became harder as the β-CD content was higher than 4 wt%.

3.3. Characterizations of the Hydrogel Composite. The FTIR spectra of the obtained cellulose/TiO_2/β-CD hydrogel before and after cross-linking by ECH can be seen in Figure 2. The FTIR of β-CD showed strong absorption peaks at 3400 cm^{-1} (O-H), 2929 cm^{-1} (C-H), 1635 cm^{-1} (H-O-H bending), and 1156 cm^{-1} (C-O). In the spectra of ECH cross-linked with the cellulose/TiO_2/β-CD hydrogel, the strength of the absorption peaks at 2929 cm^{-1} was obviously diminished maybe by the decreases of the hydrophobic saturated C-H groups with the hydrogel cross-linked by ECH [21]. And the strengths of absorption peaks at 3400 and 1052 cm^{-1} for the hydroxyl groups and hydrogen bonds were obviously diminished, indicating that a lot of the hydroxyls both in cellulose and β-CD reacted with the ECH cross-linking agent that occurred in the cellulose/TiO_2/β-CD sample.

To investigate the influence of β-CD on the structure of the composite hydrogel, the surface morphology of cellulose/TiO_2 and cellulose/TiO_2/β-CD hydrogels were observed using SEM, and the result can be seen in Figure 3. Interpenetrated porous and network structures of both hydrogels were clearly observed in Figure 3. It can be observed that the network structure formed with β-CD was more dense, and the hydrogel formed without β-CD was looser. This phenomenon could be explained by the observation that β-CD in the composite hydrogel could actively participate in the cross-linking reaction, just as it was mentioned previously.

The pore diameters of the cellulose/TiO_2 hydrogel and cellulose/TiO_2/β-CD hydrogel ranged from 200 to 300 nm (Figure 3(a)) and 100 to 200 nm (Figure 3(b)), respectively, as it is feasible for a material with smaller pores to get a larger specific surface area, which facilitated the uptake of a large amount of solvent. Furthermore, the porous architecture of the material could also load all kinds of drugs and control drug release. Therefore, the cellulose/TiO_2/β-CD hydrogel might be a good carrier for sustained and controlled drug release.

In order to prove that TiO_2 was successfully introduced into the composite hydrogels and get the accurate data, the SEM-EDS and EDX mapping techniques were used to determine precisely the microstructure, component, and content of TiO_2 in Figure 4. The elemental EDX mapping of the sample clearly demonstrated the existence of Ti and O in the hydrogel with 4 wt% of β-CD, and the distribution of these elements was quite uniform and the TiO_2 content obtained is about 35 wt%. Similar results were obtained for different morphologies of the hydrogels with 3 wt% and 5 wt% of β-CD in Figures 4(e)–4(l). All data fully documented that TiO_2 was successfully introduced into the composite hydrogels.

The hydrogels were further examined by TEM. Figure 5(a) is the TEM image of the cellulose/TiO_2 hydrogel without β-CD, and Figure 5(b) is the cellulose/TiO_2/β-CD hydrogel. It was observed that TiO_2 exhibits a sphere

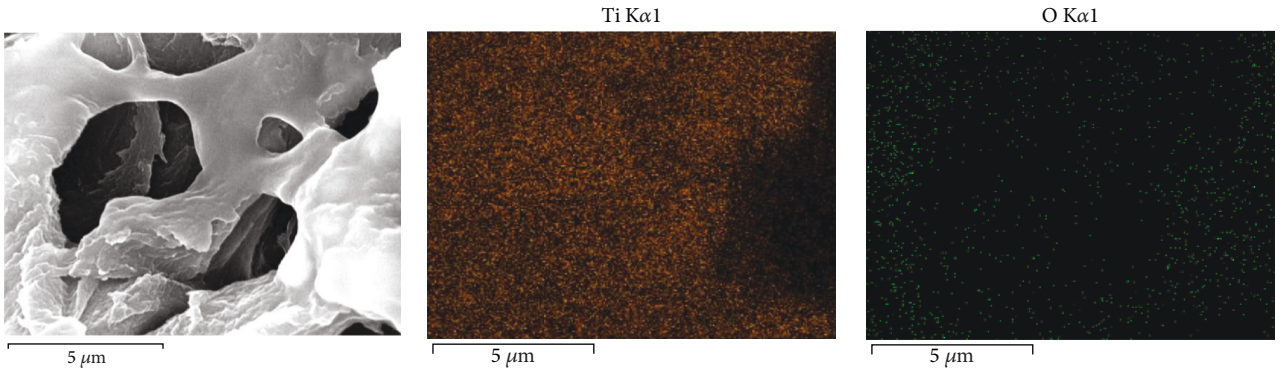

(a) (b) (c)

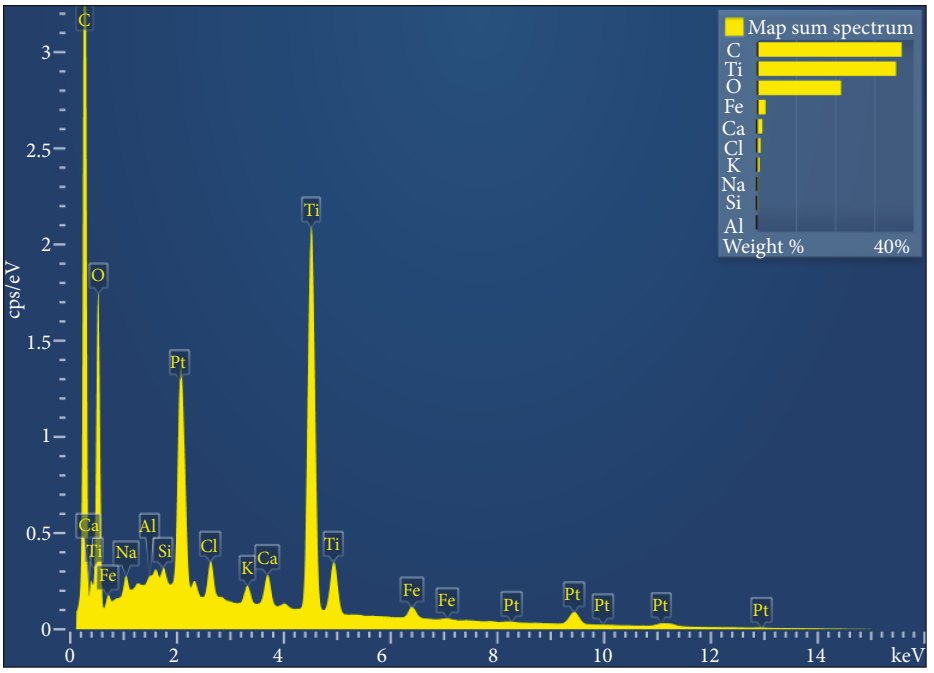

(d)

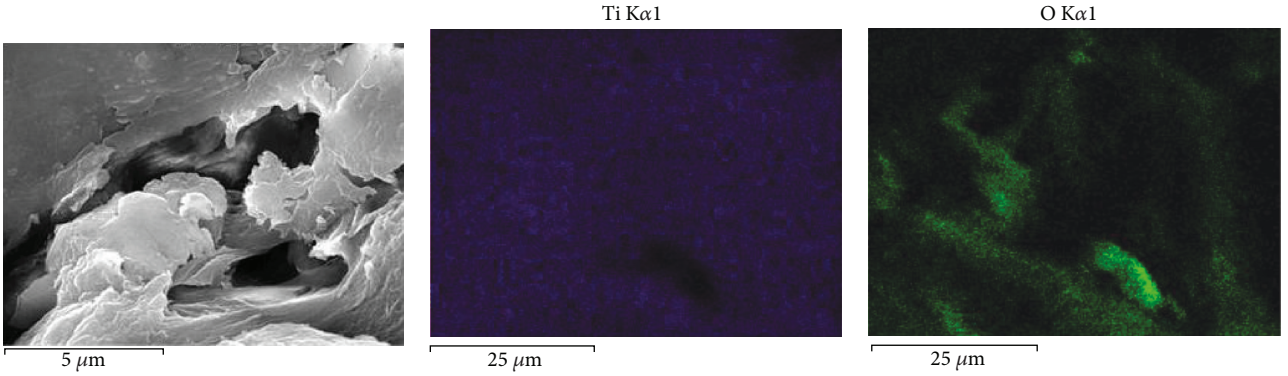

(e) (f) (g)

Figure 4: Continued.

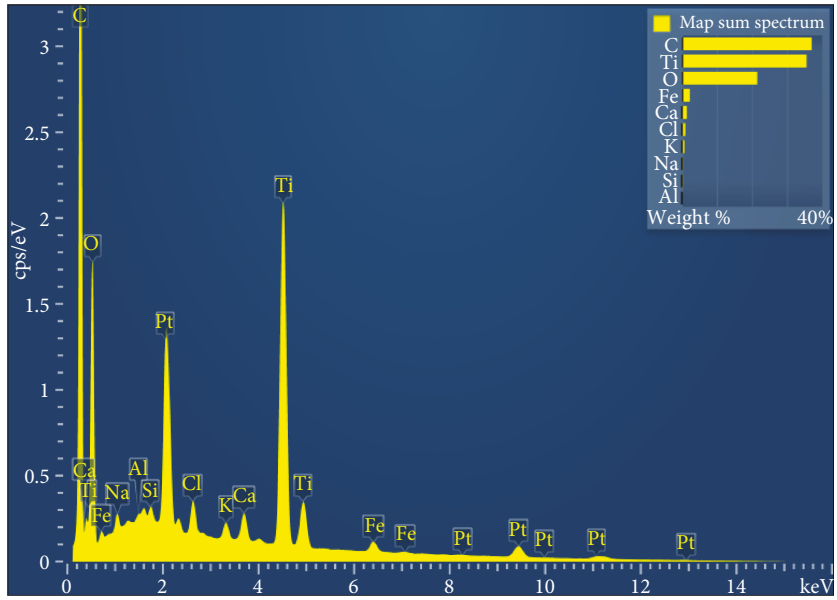

(h)

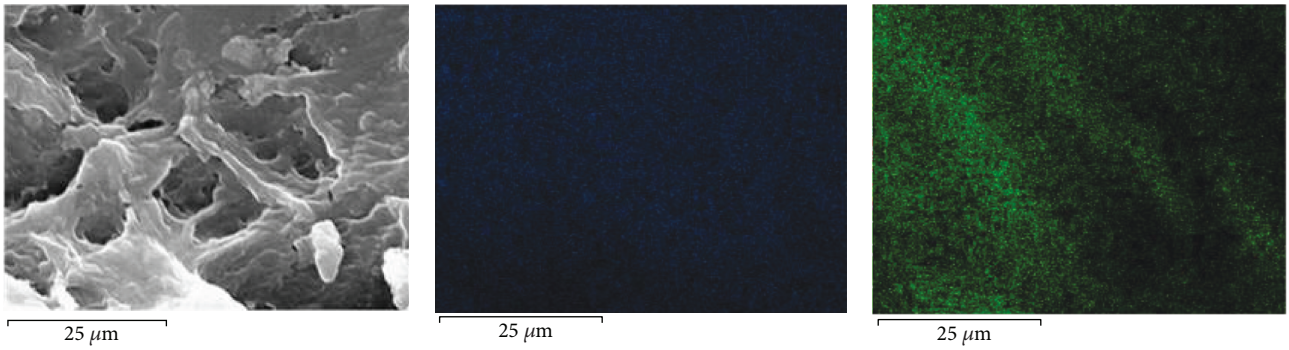

(i) (j) (k)

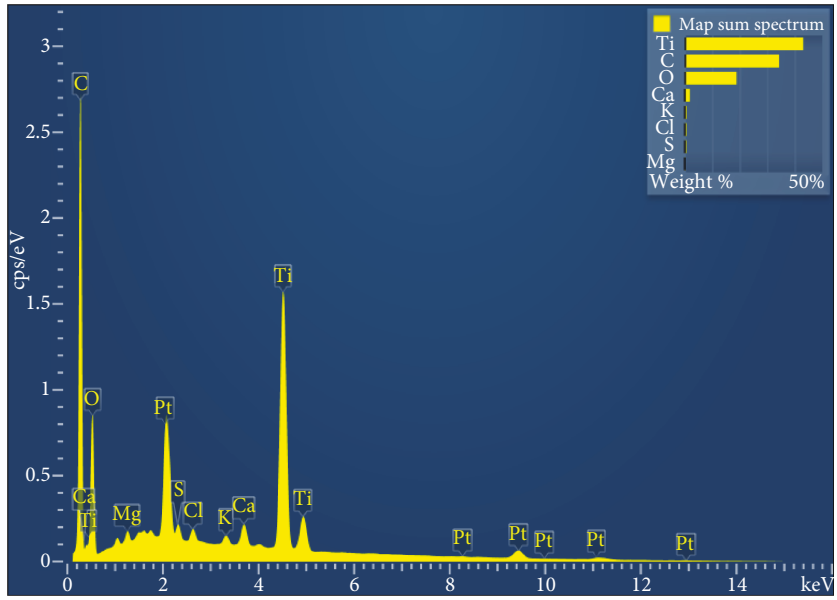

(l)

Figure 4: SEM-EDX mapping of the element distribution of hydrogel with 4 wt% of β-CD ((b) Ti, (c) O). Similar images of hydrogel with 3 wt% (e–h) and 5 wt% β-CD (i–l).

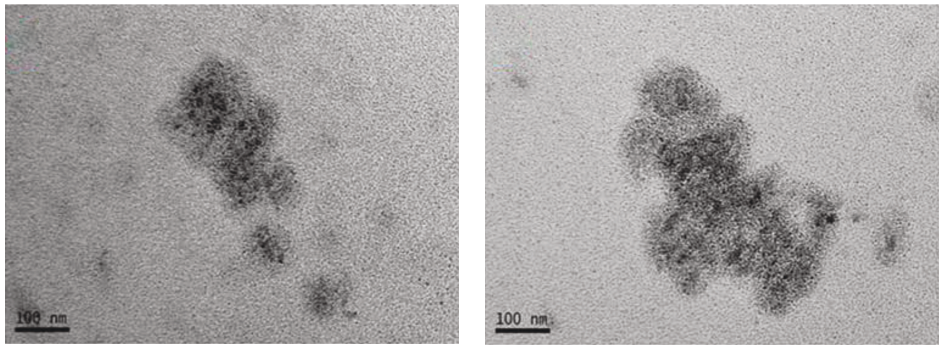

(a) (b)

Figure 5: TEM images of the cellulose/TiO_2 hydrogel (a) and the cellulose/TiO_2/β-CD hydrogel (b).

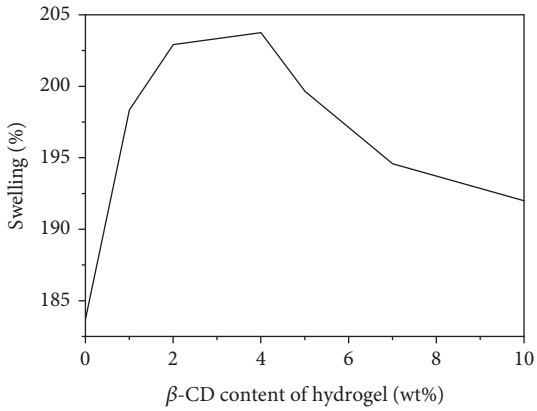

Figure 6: Effect of β-CD content on the swelling behavior of the hydrogel.

with a diameter less than 10 nm, and it is uniformly dispersed in both composite hydrogels without agglomeration. This demonstrates that cellulose, TiO_2, and β-CD were combined very well.

3.4. Swelling Properties. The equilibrium swelling degree is an important parameter to evaluate the property of the hydrogel [22]. Figure 6 shows the water uptake curves of the cellulose/TiO_2/β-CD hydrogel investigated with the β-CD content ranging from 1 wt% to 10 wt%; the sample was incubated in water for 24 h before investigating. It was found that as the amount of β-CD increased from 1 wt% to 4 wt%, the swelling percentage gradually increased. In particular, when a content of 4 wt% of β-CD was used in the hydrogel, the optimal swelling percentage is obtained, for which the swelling percentage level reaches the highest value of 203.6% among all investigated samples. This can be ascribed to the structure and properties of β-CD with a hydrophilic exterior. However, the further increase of the β-CD content in the hydrogel leads to the deterioration of their water uptake capacity. It should be due to an increased cross-linking degree upon increasing the dosage of β-CD. Thus, it can be concluded that grafting moderate amounts of β-CD onto the cellulose/TiO_2 hydrogel network may increase its swelling capacity.

3.5. Antibacterial Studies. The antibacterial activity of hydrogels was tested by the inhibition zone method against two representatives clinically relevant bacterial strains, namely *Staphylococcus aureus* (Gram-positive) and *Escherichia coli* (Gram-negative) under natural light irradiation. In agar plate wells, cellulose/TiO_2 hydrogels with 0 wt%, 3 wt%, 4 wt%, and 5 wt% of β-CD were used (Figure 7). The inhibition zones of all the three samples were formed in the test, indicating the good antibacterial activities of hydrogels against *Staphylococcus aureus* and *Escherichia coli*.

The widths of the inhibition rings of the hydrogel with different concentrations of β-CD exposed to natural light are summarized in Table 1. With the increase of β-CD in the hydrogel, the width of the inhibition ring increases; the results indicated that the bacterial growth inhibition capacity of the hydrogels was increased along with the consistency of β-CD, owing to the addition of the hydrophobic inner cavity of β-CD and the acceleration of the charge transfer rate from the photoexcited TiO_2 to the electron acceptors.

Moreover, blank experiments of the cellulose/β-CD (4 wt%) hydrogel without TiO_2 were also carried. As expected, the cellulose/β-CD (4 wt%) hydrogel without TiO_2 did not show any antibacterial activity against either bacteria (Figure 8, 1). The antibacterial activity was increased with the increase of TiO_2 concentration (Figure 8, 2-4). The widths of the inhibition rings of the hydrogel with 1 mL, 2 mL, and 3 mL TiO_2 were 20.32, 22.52, and 24 mm, respectively. These results demonstrate that TiO_2 sol plays a vital role in enhancing the antibacterial activity.

TiO_2 has been reported to be a suitable material for antimicrobial activities and this effect of TiO_2 originates from the generation of reactive oxygen species (ROS) formed with light irradiation [23]. Photocatalytic antibacterial efficiency of TiO_2 is still not high due to the rapid recombination of the electron and hole. β-CD/TiO_2 could show a significant enhancement of the photocatalytic activity mainly because β-CD could trap the photogenerated holes resulting in the lower e^-/h^+ recombination [24]. An illustration of the possible mechanism for the formation of ROS and electron transfers is given in Figure 9.

To test the capability of TiO_2 in generating ROS such as singlet oxygen ($^1O_2$) and hydroxyl radical ($OH^\bullet$) in the cellulose/TiO_2/β-CD hydrogel under natural light irradiation, we used 1,3-diphenylisobenzofuran (DPBF) as a detector [25]. ROS was determined by the decomposition of DPBF correlated to the decay of the absorption at 410 nm

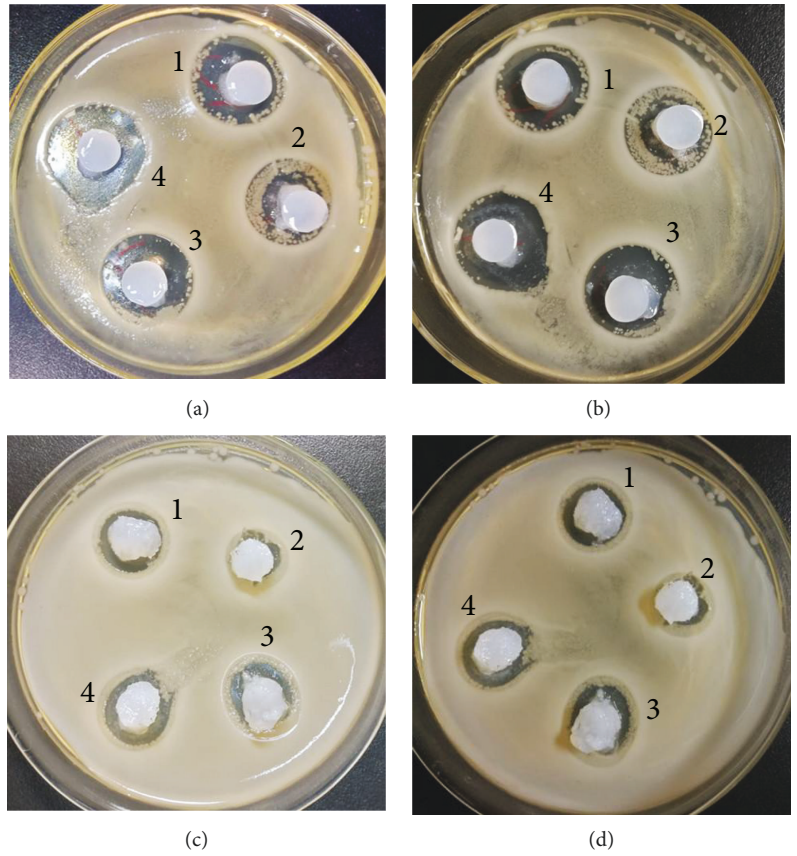

Figure 7: Antibacterial activity against *Staphylococcus aureus* and *Escherichia coli* with visible light illumination (a, b) and without light illumination (c, d). In each picture, 1-4 indicate the contents of β-CD at 0 wt%, 3 wt%, 4 wt%, and 5 wt%, respectively.

Table 1: The widths of the inhibition rings of the hydrogel with different concentrations of β-CD against *Staphylococcus aureus* and *Escherichia coli* exposed to natural light.

Content of β-CD (wt%)	The widths of the inhibition rings of the hydrogel (mm)	
	Staphylococcus aureus	*Escherichia coli*
0	19.48	17.59
3	19.50	18.40
4	21.14	19.52
5	22.59	21.89

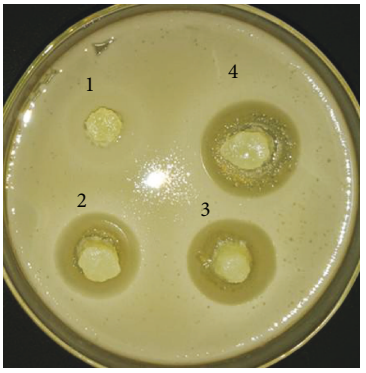

Figure 8: The cellulose/β-CD hydrogel with different concentrations of TiO_2.

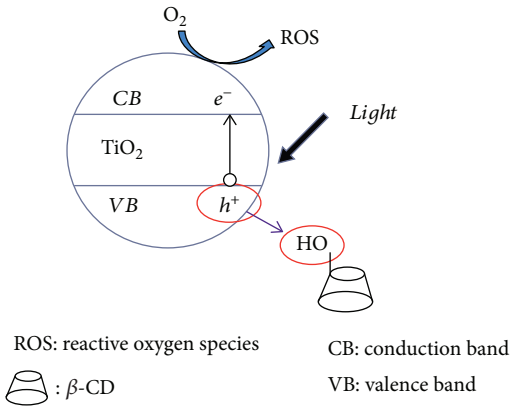

Figure 9: Proposed mechanism for the enhanced photocatalytic activity of β-CD/TiO_2.

(Figures 10(a) and 10(b)). Figure 10(a) plots the ROS output of the cellulose/TiO_2/β-CD hydrogel as a function of irradiation time. About 9.1×10^{-8} mol DPBF was completely decomposed in 2 h, reflecting a very high yield of ROS.

We also investigated the ability of the cellulose/β-CD hydrogel to regenerate ROS under the same experimental conditions; no effect of degradation of DPBF was detected even after 24 h. The ROS production measurements with different concentrations of β-CD under irradiation of light for 2 h was also performed (Figure 10(c)). The hydrogel had a

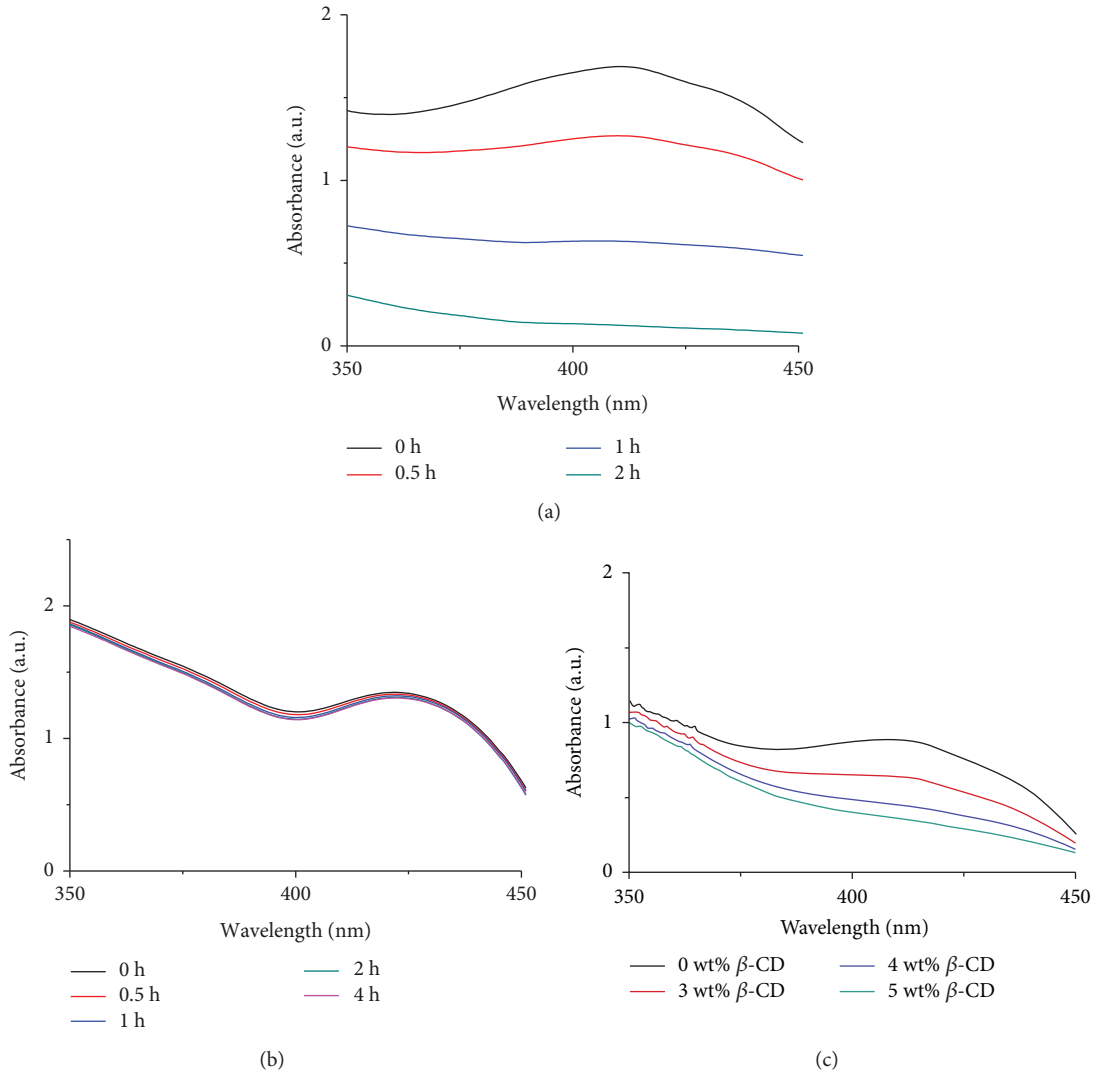

Figure 10: Decomposition of DPBF correlated with the decay of absorption at 410 nm: (a) cellulose/TiO_2/β-CD hydrogel, (b) cellulose/β-CD hydrogel, and (c) cellulose/TiO_2 hydrogel with different concentrations of β-CD under irradiation of light for 2 h.

significant ROS output with 5 wt% β-CD. The ROS output decreased slightly with 4 wt% β-CD and significantly decreased with 3 wt% and 0 wt%. This fact implies that β-CD could evidently increase the antimicrobial activity of the hydrogel.

3.6. Drug Encapsulation Efficiency (DEE). Based on the residual cavities of β-CD in the composite hydrogel, hydrophobic curcumin was chosen as a model drug to study the drug-loading property of the cellulose/TiO_2/β-CD hydrogel. In order to reach the encapsulation capacity saturation of curcumin, curcumin was encapsulated by the hydrogel in the dark for 48 h at room temperature (Table 2). The amount of the curcumin laden in the hydrogel can be determined by a UV-vis spectrophotometer at a wavelength of 440 nm. The curcumin encapsulation efficiency was determined to be 18.79 wt% for the sample of the hydrogel without the addition of β-CD. When the amount of β-CD increased to 5 wt%, the curcumin encapsulation efficiency went up to 22.77%. Hence, this hydrogel has the potential to be a drug carrier.

Table 2: Variation of DEE (%) with respect to change in content of β-CD.

Content of β-CD (wt%)	DEE (%)
0	18.78
1	24.22
2	23.74
3	20.71
4	21.68
5	22.77

The drug encapsulated within the hydrogel gets stabilized by hydrogen bonding between hydroxyl groups of drug molecules and hydroxyl groups of the hydrogel network and by hydrophobic interaction between the respective hydrophobic moieties of the drug and β-CD of the hydrogel. Since cross-linking between the polymeric chains is unfavourable for hydrogen bonding between the drug molecules and the hydrogel network, the hydrogel network without β-CD also

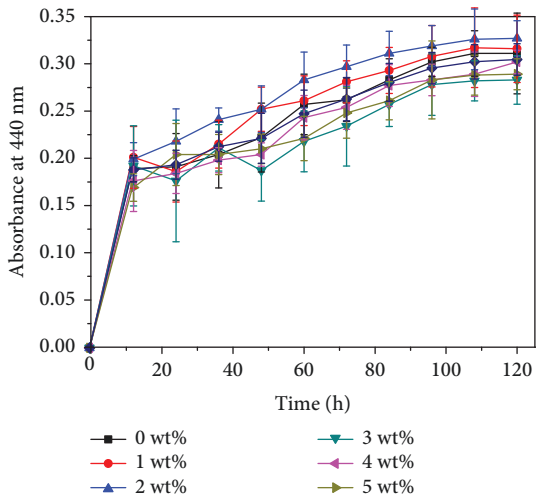

FIGURE 11: Cumulative release of curcumin from the cellulose/TiO_2/β-CD hydrogels at 37°C.

has an appreciable encapsulation capacity. The DEE of the hydrogels increase first with an increase in the β-CD concentration. With a further increase in β-CD concentration, two antagonistic phenomena seem to interplay with an increase in β-CD concentration: (a) an increase in the number of hydrophobic cavities within the hydrogel which support the drug encapsulation and (b) an increase in the potency of ECH-β-CD interactions which decreases the drug-β-CD interactions at the same time [26]. So the curcumin encapsulation efficiency was decreased to 20.71% with 3 wt% β-CD and went up to 22.77% with 5 wt% β-CD.

3.7. Release of Curcumin from Hydrogel. In vitro curcumin release kinetic of the curcumin-loaded cellulose/TiO_2/β-CD composite hydrogels was investigated. Curcumin can be detected by a UV-vis spectrophotometer at a wavelength of 440 nm in PBS buffer solution (pH 7.4). As a control group, curcumin released from the cellulose/TiO_2 hydrogel was also carried out to evaluate the role of β-CD in sustained-release progress.

As can be seen from the curcumin release kinetics (Figure 11), there was a fast release of curcumin at the initial stage, which was ascribed to the quick dissolution of curcumin from the surface of the hydrogel and diffusion out into the PBS medium. As swelling continued, curcumin could be slowly diffused out from the microporous hydrogel, which results in a more smooth release curve of curcumin. About 120 h later, the in vitro drug release reached equilibrium. As the concentration of β-CD was arranged in a sequence from 0 to 5.0 wt%, the drug cumulative release was arranged in the reverse order. At 10 h, about 38% of curcumin was released from the hydrogel with a concentration of 0 wt% β-CD. With an increase of β-CD content in the hydrogel, the cumulative release slowed down. The release of hydrogel-1 wt% (β-CD) after 10 h was 33%, while that of hydrogel-5 wt% (β-CD) was 23%. The increase in time consumption may be ascribed to the hydrophobic forces that played a role in the binding of curcumin and β-CD. This result demonstrates that curcumin encapsulated in the cavities of β-CD in the cellulose/TiO_2/β-CD hydrogel can be released through a long-term mechanism.

4. Conclusions

A novel cellulose/TiO_2/β-CD composite hydrogel with high antimicrobial activity and sustained drug release effect was developed. The as-prepared TiO_2 sol displays good photoantimicrobial ability under natural light irradiation. β-CD in this hydrogel can improve the performance of antibacterial activity and the sustained-release effect. The hydrogel could be used as a biomaterial for some hydrophobic drugs which could complex with β-CD. Hence, the hydrogel composite system has a potential application for biological materials.

Data Availability

The data used to support the findings of this study are available from the corresponding author upon request.

Conflicts of Interest

The authors declare that there is no conflict of interest regarding the publication of this paper.

Acknowledgments

This work is supported by the National Key R&D Program of China (2017YFD0600201), the Youth Science Fund Project of Anhui Agricultural University (2014zr015), and the National Undergraduate Innovation and Entrepreneurship Program (201610364010).

References

[1] X. Y. Qiu and S. W. Hu, ""Smart" materials based on cellulose: a review of the preparations, properties, and applications," *Materials*, vol. 6, no. 3, pp. 738–781, 2013.

[2] N. Sun, T. Wang, and C. Liu, "Preparation, characterization and photocatalytic study of wood-flour/β-cyclodextrin/TiO_2 hybrid composite," *Wood Science and Technology*, vol. 50, no. 6, pp. 1243–1260, 2016.

[3] J. Nie, B. Pei, Z. Wang, and Q. Hu, "Construction of ordered structure in polysaccharide hydrogel: A review," *Carbohydrate Polymers*, vol. 205, pp. 225–235, 2019.

[4] S. P. Lin, H. N. Kung, Y. S. Tsai, T. N. Tseng, K. D. Hsu, and K. C. Cheng, "Novel dextran modified bacterial cellulose hydrogel accelerating cutaneous wound healing," *Cellulose*, vol. 24, no. 11, pp. 4927–4937, 2017.

[5] C. Boyer, L. Figueiredo, R. Pace et al., "Laponite nanoparticle-associated silated hydroxypropylmethyl cellulose as an injectable reinforced interpenetrating network hydrogel for cartilage tissue engineering," *Acta Biomaterialia*, vol. 65, pp. 112–122, 2018.

[6] H. X. Jiang, K. Tovar-Carrillo, and T. Kobayashi, "Ultrasound stimulated release of mimosa medicine from cellulose hydrogel matrix," *Ultrasonics Sonochemistry*, vol. 32, pp. 398–406, 2016.

[7] N. Zainuddin, I. Ahmad, H. Kargarzadeh, and S. Ramli, "Hydrophobic kenaf nanocrystalline cellulose for the binding

of curcumin," *Carbohydrate Polymers*, vol. 163, pp. 261–269, 2017.

[8] L. Zhang, J. Zhou, and L. Zhang, "Structure and properties of β-cyclodextrin/cellulose hydrogels prepared in NaOH/urea aqueous solution," *Carbohydrate Polymers*, vol. 94, no. 1, pp. 386–393, 2013.

[9] L. Gabrielyan, A. Hovhannisyan, V. Gevorgyan, M. Ananyan, and A. Trchounian, "Antibacterial effects of iron oxide (Fe_3O_4) nanoparticles: distinguishing concentration-dependent effects with different bacterial cells growth and membrane-associated mechanisms," *Applied Microbiology and Biotechnology*, vol. 103, no. 6, pp. 2773–2782, 2019.

[10] M. Bhushan, Y. Kumar, L. Periyasamy, and A. K. Viswanath, "Facile synthesis of Fe/Zn oxide nanocomposites and study of their structural, magnetic, thermal, antibacterial and cytotoxic properties," *Materials Chemistry and Physics*, vol. 209, pp. 233–248, 2018.

[11] L. P. Liu, X. N. Yang, L. Ye et al., "Preparation and characterization of a photocatalytic antibacterial material: graphene oxide/TiO_2 bacterial cellulose nanocomposite," *Carbohydrate Polymers*, vol. 174, pp. 1078–1086, 2017.

[12] P. Kokila, M. Rameshbabu, and V. Senthil Kumar, "Antibacterial and phitocatalytic activity of pomegranate rind extract doped TIO_2 nanoparticles by sol-gel method," *International Journal of Development Research*, vol. 7, no. 1, pp. 10947–10950, 2017.

[13] I. Willner, Y. Eichen, and B. Willner, "Supramolecular semiconductor receptor assemblies: improved electron transfer at TiO_2-β-cyclodextrin colloid interfaces," *Research on Chemical Intermediates*, vol. 20, no. 7, pp. 681–700, 1994.

[14] K. M. Salleh, S. Zakaria, M. S. Sajab et al., "Chemically cross-linked hydrogel and its driving force towards superabsorbent behaviour," *International Journal of Biological Macromolecules*, vol. 118, pp. 1422–1430, 2018.

[15] I. M. Garnica-Palafox, F. M. Sánchez-Arévalo, C. Velasquillo et al., "Mechanical and structural response of a hybrid hydrogel based on chitosan and poly(vinyl alcohol) cross-linked with epichlorohydrin for potential use in tissue engineering," *Journal of Biomaterials Science, Polymer Edition*, vol. 25, no. 1, pp. 32–50, 2014.

[16] L. Zhang, J. Cai, and J. Zhou, "Novel solvent compounds and its preparation and application," 2005, CN 03128386.1.

[17] T. S. Anirudhan, P. L. Divya, and J. Nima, "Synthesis and characterization of novel drug delivery system using modified chitosan based hydrogel grafted with cyclodextrin," *Chemical Engineering Journal*, vol. 284, pp. 1259–1269, 2016.

[18] Y. M. Wang, J. Wang, Z. Y. Yuan et al., "Chitosan cross-linked poly(acrylic acid) hydrogels: drug release control and mechanism," *Colloids and Surfaces B: Biointerfaces*, vol. 152, pp. 252–259, 2017.

[19] V. S. Ghorpade, A. V. Yadav, and R. J. Dias, "Citric acid cross-linked β-cyclodextrin/carboxymethylcellulose hydrogel films for controlled delivery of poorly soluble drugs," *Carbohydrate Polymers*, vol. 164, pp. 339–348, 2017.

[20] H. Zhang, R. H. Shi, A. J. Xie et al., "Novel TiO_2/PEGDA hybrid hydrogel prepared in situ on tumor cells for effective photodynamic therapy," *ACS Applied Materials & Interfaces*, vol. 5, no. 23, pp. 12317–12322, 2013.

[21] N. Sun, T. Wang, and X. Yan, "Synthesis and investigation of a self-assembled hydrogel based on hydroxyethyl cellulose and its *in vitro* ibuprofen drug release characteristics," *RSC Advances*, vol. 7, no. 16, pp. 9500–9511, 2017.

[22] X. L. Hu, C. Sun, B. Peng et al., "Swelling property of PVA hydrogels with different concentration and specifications and its influencing factors," *International Journal of Clinical and Experimental Medicine*, vol. 9, no. 2, pp. 708–716, 2016.

[23] D. Yang, G. X. Yang, Q. Q. Sun et al., "Carbon-dot-decorated TiO_2nanotubes toward photodynamic therapy based on water-splitting mechanism," *Advanced Healthcare Materials*, vol. 7, no. 10, article 1800042, 2018.

[24] P. Sakthivel and P. Velusamy, "Modification of the photocatalytic performance of various metal oxides by the addition of β-cyclodextrin under visible light irradiation," *Journal of Water Process Engineering*, vol. 16, pp. 329–337, 2017.

[25] J. Y. Zhang, S. Chen, P. Wang et al., "$NaYbF_4$ nanoparticles as near infrared light excited inorganic photosensitizers for deep penetration in photodynamic therapy," *Nanoscale*, vol. 9, no. 8, pp. 2706–2710, 2017.

[26] M. Maswal, O. A. Chat, and A. A. Dar, "Rheological characterization of multi-component hydrogel based on carboxymethyl cellulose: insight into its encapsulation capacity and release kinetics towards ibuprofen," *Colloid & Polymer Science*, vol. 293, no. 6, pp. 1723–1735, 2015.